NORTHWESTERN UNIVERSITY

Intracavity Fast Light for Rotation Sensing and Gravitational Wave Detection

A DISSERTATION

SUBMITTED TO THE GRADUATE SCHOOL
IN PARTIAL FULFILLMENT OF THE REQUIREMENTS

for the degree

DOCTOR OF PHILOSOPHY

Field of Physics and Astronomy

BY

Mary Katherine Salit

EVANSTON, ILLINOIS

June 2009

ACKNOWLEDGEMENTS

I had the privilege of working with Ken Salit from my first day in the lab, and a lot of what is in this thesis, he taught me. He kept me honest, made me work harder than I sometimes would've liked, made me think so hard it hurt, and when I really needed it, made me laugh. He also made me fall in love with him, and want to spend the rest of my life learning from and working beside and thinking and laughing with him. The day I saw him in my new lab was the luckiest day of my life.

Our advisor, Selim Shahriar, showed me what it takes to be a scientist. He taught me optimism and perseverance, how to give a talk and how to think about some of the hardest problems humans have stumbled on – as simply as possible. I grew up a lot, under his guidance.

I learned from everyone else I worked with in his group over the last six years as well, post-docs and graduate students alike, and I am grateful to each of them. I want to mention in particular the two then-post-docs that I worked with the longest, however: Gour Pati, and Venkatesh Gopal. For the rest of my career I will try to imitate their never-ending patience and positive attitudes, and I will use the experimental techniques I learned by watching them. I spent my first two years looking over Dr. Pati's shoulder, and I can't imagine a better way to become an experimentalist.

I owe a debt of gratitude to all of the teachers and professors I've had over the last dozen years, but I particularly want to thank Prof. Alan Thorndike at the University of Puget Sound, for making me take myself seriously as a physics student.

Finally I would like to thank my parents, for all their support and for making it possible for me to be where I am now.

ABSTRACT

Intracavity Fast Light for Rotation Sensing and Gravitational Wave Detection

Mary Salit

Many optical sensors, including ring laser gyroscopes and interferometric gravitational wave detectors, can be made more sensitive if the index of refraction within the system is carefully tailored. Research into slow light and fast light has, in the last decade, led to methods for controlling the index which have direct applications in sensing. An ideal fast light medium is a transparent material with an anomalous dispersion profile. This same type of material, inserted into an optical resonator, causes the resonance frequency to vary more rapidly with changes in the resonator length than it otherwise would. There is in principle no theoretical limit to the increase in sensitivity; the practical limits are imposed by experimental constraints on our ability to control the index over a broad spectral region.

New experimental and theoretical evidence for the utility of fast light in optical sensing is presented here.

Table of Contents

CHAPTER 1 - INTRODUCTION....5

CHAPTER 2 - OPTICAL RESONATORS....10

CHAPTER 3 - CLASSICAL DISPERSION....28

CHAPTER 4 - QUANTUM MECHANICAL DISPERSION....45

CHAPTER 5 - INTERFEROMETRIC GYROSCOPES....73

CHAPTER 6 - INTRACAVITY DISPERSION....87

CHAPTER 7 - DISPERSION IN ACTIVE CAVITIES....103

CHAPTER 8 - GRAVITATIONAL WAVE DETECTION....148

CHAPTER 9 - EXPERIMENTAL RESULTS....180

CHAPTER 10 - CONCLUSIONS....216

CHAPTER 1 - INTRODUCTION

Optical interference effects are a remarkably powerful tool for sensors. Because the wavelength of light is just a few hundred nanometers, it only takes optical path length changes on that scale to dramatically change the amount of light on a detector. We can use interferometers to show the nano-scale texture of surfaces which look flat, or detect tiny variations in the position of a reflector or length of an optical fiber due to vibration or strain in materials. We can also detect changes in the environment which affect materials through which the light passes. Magnetic fields, for example, shift the energy levels of atoms, which changes their refractive index at a given frequency and polarization. Pressure and temperature changes affect the density of the atoms in a material, and this too increases or decreases the refractive index of the material and thus the optical path length of the light. Any effect which changes the optical path length for a particular beam by an amount on the order of half a wavelength of the light will be detectable with a simple two-beam configuration such as a Michelson or Mach-Zehnder interferometer[1].

Optical resonators, also known as optical cavities, are a slightly more complex kind of optical interferometer. They allow us to measure the interference of beams which have traversed the same path over and over again. They are, for this reason, even more sensitive than simple two-beam interferometers to changes in that path. Changes, even much smaller than the wavelength of light, can be detected in the length of an optical cavity, because the light traverses the cavity so many times. The cavity is likewise sensitive to any changes in the refractive index of a material within it. Every laser is an optical resonator, and of course lasers are also in use as sensors. We generally detect changes in their length or in the index of their materials as changes in lasing frequency.

In all materials, the index of refraction depends somewhat on the frequency of the light passing through it. This variation of index with frequency is called the dispersion of the material. In some materials, such as atomic gasses with sharp resonant absorption or gain features, this variation of index with frequency can be quite large, and can be controlled artificially. The dispersion of an intracavity material has an effect on the sensitivity of any resonator-based sensor.

The research presented here is about finding ways to use controllable intracavity dispersion to improve the performance of resonator-based interferometric optical sensors.

Dispersion has another effect on light as well. Pulses of light do not have a single frequency, but can be described as the sum of light fields at many frequencies. In a dispersive medium, each of these frequencies experiences a different index, and hence a different phase shift. For this reason the peak of a pulse, which is the point at which all of the waves of all of these different frequencies add in phase, can travel faster (in a "fast light material") or slower (in a "slow light material") than the free-space speed of light. The particular form of the index of refraction in which we are interested has been studied before in the context of fast light. In a material with the appropriate index, this effect reshapes light pulses in such a way as to make them travel faster than they would in free space without violating any laws of physics – no photon actually travels faster than the speed of light. It is demonstrated later in this thesis, that the same kind of dispersion which tends to increase the sensitivity of resonator-based sensors also gives rise to these superluminal pulse velocities. It is for this reason that we refer to the enhanced sensors which use them as fast-light sensors.

In the past few decades, researchers studying fast light and slow light have found new ways of producing these media, ways of controlling the index of refraction of various materials by combining laser beams of different frequencies inside those materials[2,3,4,5].

We will discuss the use of these techniques to create the kind of customized index of refraction which, when placed inside an optical cavity, changes the resonance behavior of that cavity in a way that is desirable for sensing applications[6]. We will concentrate, in the present work, on two particular types of sensors: optical gyroscopes and interferometric gravitational wave detectors.

Though the materials which we use are fast light materials in the sense that the group velocity for pulses within the appropriate bandwidth is greater than c, for purposes of this research, the details of fast-light propagation are not relevant in themselves. Our proposed applications involve continuous waves, rather than pulses. The dispersion profile characterizes the relationship between frequency and wavelength in general. It is because of this connection to wavelength that the dispersion can affect the behavior of continuous wave beams inside optical cavities; that behavior depends strongly on wavelength.

In particular, the wavelength of a continuous wave probe beam inside a fast light material can be made to change very little as the frequency is changed. Later chapters will show that by changing the relationship between frequency and wavelength in this way, we change the behavior of the cavity, making it resonate over a larger range of frequencies, and making the effect of changes in the length of the cavity on its resonance frequency larger. By the same token, a cavity filled with a slow light material should resonate over a narrower range of frequencies, and be less sensitive to changes in its length, as we will discuss in detail later. The demonstration of these behaviors is the substance of this thesis.

We have studied the effect of putting a slow light or a fast medium into a cavity both experimentally and theoretically, and confirmed experimentally that slow light narrows the linewidth of the cavity and causes its resonance frequency to change very little when its length is changed, while fast light broadens its linewidth, and that the degree of broadening is controllable, a result which might prove useful in several schemes that have been proposed for gravitational wave detection. Finally, we have shown theoretically that a fast light medium in a cavity will increase the sensitivity of the cavity to length changes, a relevant result for optical gyroscopes. We hope to use these results to design more sensitive optical gyroscopes and broader bandwidth cavities for use in gravitational wave detectors.

The experimental results are reported in detail in their own chapter at the end of this work. We begin by first reviewing the fundamental principles of optical cavities, and of dispersion and index of refraction, including the argument for why superluminal pulse velocities are consistent with the laws of physics as we know them. We then discuss the effects of a dispersive material on the resonance of a passive cavity (that is, a cavity which does not contain an optical gain medium, as contrasted with an active or laser cavity). We show how a fast-light material may be used to turn a passive cavity into a so-called White Light Cavity (WLC). These cavities can only be made truly "white light," in the sense of resonating any and all optical frequencies, in theory. In practice, however, we can make cavities which have a broader resonance bandwidth and are more sensitive to changes in their length than an empty cavity, and we support this theoretical conclusion with experimental data.

Next we turn our attention to schemes for exploiting these properties of the WLC for gravitational wave detection. We will review the principles of interferometric gravitational wave detection with special attention to the detector designs which can benefit the most from the incorporation of a WLC.

We then consider the related idea of the "Active White Light Cavity." This is a cavity which incorporates within it an active gain material which, when not saturated by too strong a field, produces a gain which is greater than any losses light experiences on one round trip within the cavity. An active cavity is also known as a laser, and produces a strong, narrowband lasing output. Because the output of a laser is always narrow-band, an Active WLC does not resonate "White Light" in any meaningful sense, but so strong are its similarities in other ways to the passive WLC that referring to it by the same name is almost irresistible. We might also call it a "Superluminal Laser," because the dispersive materials within it give rise to superluminal pulse velocities. This name is slightly misleading in its own way, however, as we generally consider only cases where continuous wave light, rather than pulses, is circulating within the cavity, so nothing is actually traveling at superluminal speeds.

We discuss the resonance properties of the Active WLC, in particular the sensitivity of the resonance frequency of such a cavity to changes in its length, and then we move on to a discussion of the usefulness of these properties for laser gyroscopy. We review the basic theory of optical gyroscopes, and show that this sensitivity to length changes does in fact make an Active WLC a more sensitive optical gyroscope, and explore the prospects for and engineering challenges of realizing such a gyroscope.

Finally, we conclude with the summary of our results, both theoretical and experimental, and a discussion of the directions for future work that these results imply. The WLC and Active WLC are potentially very powerful sensing technologies with applications beyond the gyroscope and gravitational wave detection devices described here.

CHAPTER 2 - OPTICAL RESONATORS

Let us begin by briefly reviewing the basic theory of optical resonators: As this work is concerned with resonator-based sensors, it is worth reminding ourselves at the outset of the fundamental concepts. A more detailed review of the properties and behaviors of cavities may be found in, for instance, references 7 and 8. We need, for now, a single equation, describing the intensity of the field in the cavity as a function of its length, and of the wavelength of the circulating light. We will take a few pages here at the beginning to derive it from first principles, and then explore some of its implications.

The simplest kind of optical resonator is a two-mirror cavity. Some light transmits through one partially reflecting mirror, called the input coupler, and a portion of that light is reflected back again from a second partially reflecting mirror, called the output coupler. It travels back toward the first where it is reflected again, and so on, bouncing between the mirrors indefinitely and losing only a small fraction of its energy with each bounce. Figure 2.1 depicts the path of the light when the mirrors are not perfectly parallel.

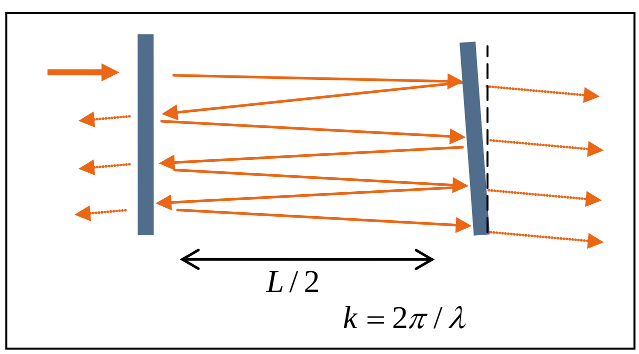

Figure 2.1: Multiple reflections in a two-mirror Fabry-Perot cavity

If the mirrors are perfectly parallel, the light will be reflected directly back along its original path, and all of these reflected fields will occupy the same space, which means they will necessarily interfere with one another. The interference may be constructive, as depicted in Figure 2.2a, or it may be destructive, as in Figure 2.2b. If it is constructive, the intracavity field grows as the incoming light adds in phase with the reflected fields.

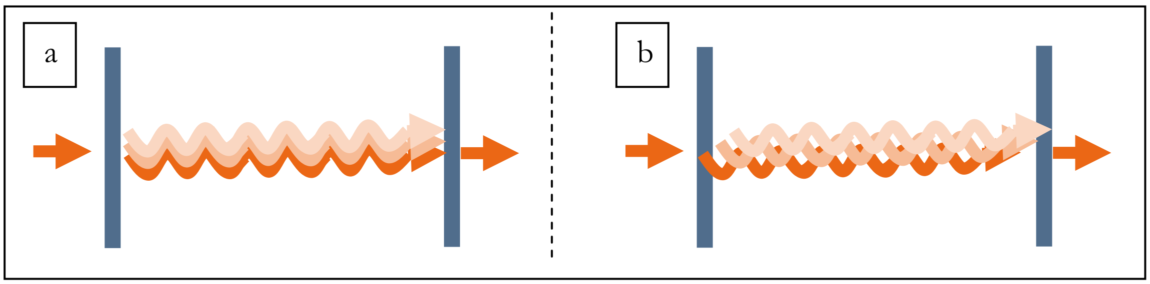

Figure 2.2: Interference in a two-mirror Fabry-Perot Cavity

Let us write the field transmitted through the first mirror as:

$$E_1 = \mathrm{Re}\left[t_1 E_0 e^{-i\omega t}\right]$$

Here t_1 is the transmissivity of the input mirror, E_0 is the amplitude of the electric field before the input mirror, and ω is the optical frequency. We will choose the phase to be zero at the position of the second mirror, for the beam which has traveled once through the cavity and has not yet reflected from any mirror—we will call this the first pass beam.) The field which has transmitted through the first mirror, reflected from the second mirror, then from first, and traveled back to the position of the second mirror is then

$$E_2 = \mathrm{Re}\left[t_1 (r_1 r_2) e^{ikL} E_0 e^{-i\omega t}\right]$$

Where r_1 and r_2 are the reflectivities of the input and output mirrors, respectively, and $k = 2\pi / \lambda$ is the wavenumber of the light.

We want to add up the transmitted first pass beam, the first reflection, and all successive reflections, which are all simultaneously present, assuming we are continuously feeding light into the cavity. We can drop the "real part" notation at this point, so long as we remember to properly compute the magnitude of the complex result.

The total field inside the cavity at the location of the second mirror is

$$\begin{aligned}
&E_{cav} = t_1 E_0 e^{-i\omega t} \\
&+ r_2 r_1 e^{ikL} t_1 E_0 e^{-i\omega t} \\
&+ (r_2 r_1)^2 e^{3ikL} t_1 E_0 e^{-i\omega t} \\
&+ (r_2 r_1)^3 e^{4ikL} t_1 E_0 e^{-i\omega t} \\
&+ \ldots \\
&= t_1 E_0 e^{-i\omega t} \sum_{n=0}^{\infty} (r_2 r_1 e^{ikL})^n
\end{aligned}$$

This is a geometric series, and the sum converges to give:

Equation 2.1: $$E_{cav} = \frac{t_1 E_0 e^{-i\omega t}}{1 - r_2 r_1 e^{ikL}} \Rightarrow \left|E_{cav}\right|^2 = \frac{\left|t_1\right|^2}{1 - 2 r_2 r_1 \cos kL + \left|r_1 r_2\right|^2}$$

What does it mean physically for this sum to converge? It tells us that the intracavity field, which is growing as incoming light adds constructively with an ever increasing number of reflections, approaches a constant, steady-state value. A fixed amount of light, so much energy per unit time, is constantly entering the cavity through the input coupler. The amount of light leaving the cavity through the output coupler, on the other hand, depends on the field strength inside the cavity. The output field is a certain fraction of the total intracavity field, given by the reflectivity of the output coupler. Therefore the output intensity grows as the intracavity field builds up. As we will see in a moment, the limiting intracavity field value that we find by adding up this infinite series is the value that makes the output field equal in magnitude to the input field, assuming the input and output couplers have equal reflectivity. This limiting value of the output may be smaller than the input if the reflectivities are not matched, but it may never be greater, as this would be a violation of the law of conservation of energy.

Let us calculate the output intensity of the cavity explicitly. We obtain it by multiplying the intracavity field strength with the output mirror transmissivity and inserting the appropriate constant to convert from units of electric field to units of intensity.

Equation 2.2: $$I_{out=}\frac{\left|t_2 E_{cav}\right|^2}{2\eta}=\frac{1}{2\eta}\left(\frac{\left(t_1 t_2 E_0\right)^2}{1-2r_1 r_2\cos(kL)+(r_2 r_1)^2}\right)$$

Here, η, the conversion constant, is the impedance of free space.

A thorough understanding of Equation 2.2 tells us a great deal about the behavior of cavities, but we will restate it in a more general form, before discussing the implications further. To describe resonators with more than two mirrors, we need only modify the derivation slightly. Consider the system depicted in Figure 2.3

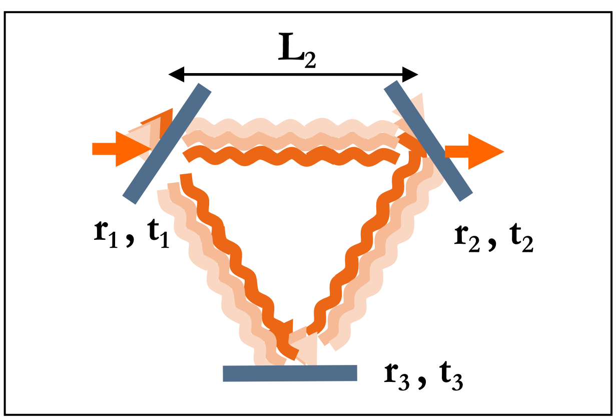

Figure 2.3: A three mirror ring cavity

Mirror 1 is still the input coupler in this case, and Mirror 2 is again the output coupler. If we now call the round trip distance around the perimeter and back to the input coupler L, and again set the phase to be zero just before the second mirror, it is easy to see that the field at this point is:

$$E_1 = \mathrm{Re}\left[t_1 E_0 e^{-i\omega t} \right]$$

And after one round trip:

$$E_2 = \mathrm{Re}\left[t_1 (r_1 r_2 r_3) e^{ikL} E_0 e^{-i\omega t} \right]$$

If we follow the same logic as before, we arrive at

Equation 2.3: $\left|E_{cav}\right|^2 = \left(\dfrac{\left|t_1 E_0\right|^2}{1 - 2r_1 r_2 r_3 \cos(kL) + \left|r_2 r_1 r_3\right|^2} \right) \Rightarrow I_{out} = \dfrac{1}{2\eta} \left(\dfrac{\left|t_1 t_2 E_0\right|^2}{1 - 2r_1 r_2 r_3 \cos(kL) + \left|r_2 r_1 r_3\right|^2} \right)$

We can easily extend this to any number of mirrors. In general, we for N mirrors have

Equation 2.4: $\left|E_{cav}\right|^2 = \left(\dfrac{\left|t_1 E_0\right|^2}{1 - 2r_{net} \cos(kL) + \left|r_{net}\right|^2} \right) \Rightarrow I_{out} = \dfrac{1}{2\eta} \left(\dfrac{\left|t_1 t_2 E_0\right|^2}{1 - 2r_{net} \cos(kL) + \left|r_{net}\right|^2} \right)$

Where $r_{net} = \prod_{i=1 to N} r_i$ is the product of the reflectivities of all N mirrors, and L is always the total perimeter, the input coupler is always labeled as mirror one, and the output coupler as mirror two.

This expression tells us how the output intensity and intracavity field depend on wavelength (or frequency, given that $c = \omega / k = \lambda \nu$) If we plot the output intensity, for instance, for a two mirror cavity with the two mirrors having matched reflectivities, we get graphs like these in Figure 2.4

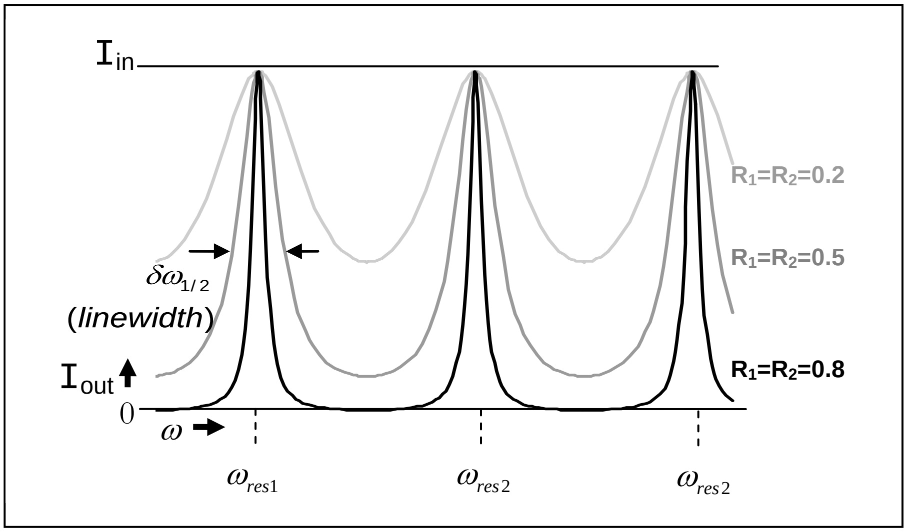

Figure 2.4: Transmission through a two-mirror cavity with matched reflectivities as a function of frequency.

The graphs for multi-mirror cavities are much the same. The choice of reflectivities determines both the width of the peaks and the depth of the "valleys". The output intensity of an empty cavity at resonance can never be greater than input intensity, though it can be smaller, for instance, if the mirrors in a two mirror cavity have different reflectivities, or if the reflection or propagation within the cavity is lossy. By contrast, the intracavity field, which lacks the factor of t_2, may be arbitrarily large.

The frequency range of the resonance, that is, the difference in frequency between the points on either side of the peak at which the output is half the input (which we will henceforth refer to as the linewidth of the cavity, $\delta\omega_{1/2}$) is a property in which we are particularly interested, for purposes of this work. Figure 2.4 illustrates the dependence of this width on the net reflectivity of the cavity mirrors. We will discuss this linewidth in greater depth in a moment.

First, let us understand Equation 2.4 qualitatively. Consider that $\cos(kL)$ term in the denominator. When $kL = 2\pi m$ for some integer m, $\cos(kL) = 1$, and the denominator becomes

$\left(1+r_{net}^{2}\right)-2r_{net}$, which approaches zero as r_{net} approaches one. If r_{net} is close to one, then, we see that we can get a small denominator, and therefore a large magnitude of E_{cav}, by choosing the cavity length and the wavelength of the light such that $kL = 2\pi m$. Since $k = 2\pi/\lambda$, we may equivalently write this resonance condition as $L = m\lambda$. Physically, this says that resonance requires that the round-trip path length of the cavity be an integer multiple of the wavelength of the light. This will cause the reflections to add constructively as illustrated in Figure 2.3.

We know that the frequency of light in free space is given by the equation $c = \lambda\nu$, so that the angular frequency is given by $\omega = 2\pi c/\lambda$. From this we can see that

Equation 2.5: $\omega_{res}[m] = \dfrac{2\pi c}{\lambda_{res}} = \dfrac{2\pi mc}{L}$

This is a key equation for the purposes of this work, because it tells us how the resonant frequency of a cavity depends on its length. Resonator based sensors, including gyroscopes and, indirectly, gravitational wave detectors, use this relationship to allow us to measure small length changes by measuring changes in resonant frequency.

This equation also tells us the spacing between different resonance frequencies of the cavity. The difference between subsequent resonant frequencies, $\omega_{res}[m+1]/2\pi - \omega_{res}[m]/2\pi$ is called the free spectral range (FSR) of the cavity. (The factor of 2π is to convert the resonant frequencies from angular frequency units to natural frequency units, consistent with the conventional definition of FSR, which is in natural frequency units.)

Equation 2.6: $FSR = \dfrac{\omega_{res}[m+1]}{2\pi} - \dfrac{\omega_{res}[m]}{2\pi} = \dfrac{c}{L}$

Note that some sources derive this for a two mirror cavity and define L as the distance between the two mirrors, and not the total round trip path length. Thus one sometimes sees a version of this equation which differs by a factor of two. We use the round trip path length so that we can write the expression in this form, which is more general in that it describes multi-mirror cavities as well as two-mirror cavities.

We thus see that we may derive the free spectral range of a cavity from Equation 2.4, along with the peak transmission, minimum transmission, the dependence of those resonance frequencies on the cavity length, and the effect of varying the mirror reflectivities. Equation 2.4 even tells us the effect of an intracavity medium on the resonance behavior, if we are careful to use $k_{medium} = nk_{vacuum}$ (where n is the index of refraction of the medium) where necessary. What's more, computing $\mathrm{Re}\left[E_{cav}\right]$ directly tells us the strength of the intracavity electric field.

Let us take a moment now to understand the linewidth of the cavity, and how it depends on the mirror reflectivity. Consider a beam which has reflected fifty times from each mirror. This beam has traveled a total distance of $50(L)$. The phase shift it has picked up in traveling this far is $50(kL)$. Now let us say that the light has a wavenumber k such that $kL = 2\pi(m+0.99)$ (for some integer m). In this case, the first reflection, which differs in phase from the incoming light by kL, adds mostly constructively with it, being shifted by almost an integer multiple of 2π, as do the second and third passes. However, this beam which has reflected fifty times has picked up a phase shift of $50\times kL \;\; = 50\times 2\pi(m+0.99) \;\; = 100\pi\left(m+.99\right)$ $= 100\pi m + 99\pi$. That is an odd integer multiple of π, which tells us that this fiftieth reflection is exactly out of phase with the incoming light, though the first reflection was almost in phase. The question, then, is what the magnitude of that fiftieth reflection is. If it is comparable to the amplitude of the incoming light, then it will interfere destructively with it (and further reflections will cancel destructively with the other early reflections) and there will be no cavity build-up. If, on the other hand, the fiftieth (and subsequent) reflections are much smaller in amplitude than the first pass beam, then they cannot, through destructive interference, reduce the total field inside the cavity significantly. Of course, the numbers chosen for this example were arbitrary. The point is that no matter how close a beam is to the resonant wavelength, if it is even slightly off, it will become out of phase with the input beam after some number of bounces. If the reflectivity of the mirrors is small enough, however, this out–of-phase field will by then be negligible in amplitude. For this reason, slightly off resonant beams can still build up inside a cavity if the reflectivity of the cavity mirrors is low. This accounts for the broader linewidth at low reflectivities. We can verify from $|E_{cav}|^2$ expression in Equation 2.4 that the intracavity field is also smaller in these low-reflectivity cavities on resonance, all other things being equal. So low reflectivity mirrors in general give smaller intracavity fields but allow build-up over a broader frequency range.

Note that the longer L is, the more kL will differ from $2\pi m$ after one round trip, for a k which is slightly off resonance. For this reason, the linewidth of the cavity depends on its length as well. Longer cavities have narrower linewidths, since changing the frequency slightly has more effect on the round-trip phase than it would in a shorter cavity. We therefore expect the linewidth to decrease if the cavity length is increased. In short, the longer the cavity, and the higher the reflectivity of its mirrors, the narrower its linewidth.

We can find the linewidth of the cavity graphically from plots like those in Figure 2.4, but it is very useful to have an explicit analytical expression for it. Let $\delta\phi_{1/2}$ be the difference between the round trip phase on resonance, and that when the cavity output drops to half its resonant value: $\delta\phi_{1/2} = 2\pi m - kL$ for an appropriate integer m. Then Equation 2.4 says that

Equation 2.7: $$I_{out}/I_{in} = \left(\frac{|t_1|^2 |t_2|^2}{1 - 2|r_{net}|\cos(\delta\phi_{1/2}) + |r_{net}|^2}\right) = 1/2$$

Making use of a trigonometric identity allows us to rewrite this as:

Equation 2.8: $$\frac{|t_1|^2 |t_2|^2}{1 - 2|r_{net}|\left(1 - 2\sin^2\left(\delta\phi_{1/2}/2\right)\right) + |r_{net}|^2} = 1/2$$

With a little algebra, this reduces to:

Equation 2.9: $$\frac{|t_1|^2 |t_2|^2}{4|r_{net}|\sin^2\left(\delta\phi_{1/2}/2\right) + \left(1 - |r_{net}|\right)^2} = 1/2$$

And now by defining an additional variable, we can write

Equation 2.10: $$\frac{|t_1|^2 |t_2|^2}{\left(1 + F\sin^2\left(\delta\phi_{1/2}/2\right)\right)\left(1 - |r_{net}|\right)^2} = 1/2 \qquad where\, F = \frac{4|r_{net}|}{\left(1 - |r_{net}|\right)^2}$$

Finally, solving for $\delta\phi_{1/2}$ gives us:

Equation 2.11: $$\delta\phi_{1/2} = 2\sin^{-1}\left(\sqrt{\frac{1}{F}\left(\frac{2|t_1|^2 |t_2|^2}{\left(1 - |r_{net}|\right)^2} - 1\right)}\right)$$

Since we know that $\phi = kL = \omega L/c$, so that ϕ and ω are linearly related, we can say that for a constant L, a change in phase $\delta\phi$ always corresponds to a change in frequency $\delta\omega = \frac{d\omega}{d\phi}\delta\phi = \frac{c}{L}\delta\phi$. This allows us to conclude that the change in frequency which drops the cavity output to half of its input value is

Equation 2.12: $$\delta\omega_{1/2} = \frac{c}{L}\delta\phi_{1/2} = \frac{c}{L}$$

Substituting in our expression for $\delta\phi_{1/2}$ gives us a linewidth (in angular frequency) of

Equation 2.13: $$\delta\omega_{1/2} = \frac{c}{L}\delta\phi_{1/2} = \frac{c}{L}2\sin^{-1}\left(\sqrt{\frac{1}{F}\left(\frac{2|t_1|^2|t_2|^2}{\left(1-|r_{net}|\right)^2}-1\right)}\right)$$

This is a rather ugly expression, so let us choose $r_{net} = r_1 r_2$, and $r_1 = r_2 = r$. Then $|t_1|^2 = |t_2|^2 = \left(1-|r|^2\right) = \left(1-|r_{net}|\right)$, and , and Equation 2.11 reduces to

Equation 2.14: $$\delta\phi_{1/2} = 2\sin^{-1}\left(\sqrt{\frac{1}{F}}\right) \cong 2\sqrt{\frac{1}{F}} = 2\sqrt{\frac{\left(1-|r_{net}|\right)^2}{4|r_{net}|}} = \frac{1-|r_{net}|}{\sqrt{|r_{net}|}}$$

This expression assumes that F is large enough that $\sin\left(1/\sqrt{F}\right) \cong 1/\sqrt{F}$. The linewidth (in angular frequency) is then:

Equation 2.15: $$\delta\omega_{1/2} = \frac{c}{L}\frac{2}{\sqrt{F}} = \frac{2c}{L}\left(\frac{1-|r_{net}|}{\sqrt{|r_{net}|}}\right)$$

If we convert this to units of natural frequency, we get

Equation 2.16: $$\delta\nu_{1/2} = \frac{c}{L}\frac{2}{\sqrt{F}} = \frac{c}{L}\left(\frac{1-|r_{net}|}{\pi\sqrt{|r_{net}|}}\right) = \frac{FSR}{F} \quad where F = \frac{\pi\sqrt{|r_{net}|}}{1-|r_{net}|}$$

Again, in this expression, $r_{net} = r_1 r_2 = r^2$. This is a popular expression for the linewidth[8], since most practical cavities justify the assumptions we made in deriving it.. However, Equation

2.13 is the more general result. The script letter $\mathcal{F} = \sqrt{F}/2$ is called the cavity finesse, and is a way of measuring the amount of light a cavity can store.

All of this information is, again, implicit in Equation 2.4. However, there is one, somewhat subtle, question which Equation 2.4 cannot answer. We said earlier that energy conservation requires that the transmitted intensity from an empty, passive cavity, even on resonance, never be greater than the input intensity, however large the intracavity field may be. What if the cavity is not resonant with the incoming light? Where then does the energy go? The only possible answer that is consistent with energy conservation is that the light is reflected from the cavity instead of transmitted through it. To prove mathematically that this is what happens, we must calculate the phase of the light which transmits back out through the input coupler. We can characterize this field using the same methods by which we derived Equation 2.4, but we need to add up the fields traveling toward the input mirror (mirror 1) at a point just inside that mirror, and then multiply that field by t_1:

Equation 2.17:

$$E_{back} = E_0 t_1^2 \left(r_{net}/r_1\right) e^{-i\omega t} e^{ik(L-L_2)} \sum_{N=1}^{\infty} \left(r_{net} e^{ikL}\right)^N = \frac{E_0 t_1^2 \left(r_{net}/r_1\right) e^{-i\omega t} e^{ik(L-L_2)}}{1 - r_{net} e^{ikL}}$$

Here we divide r_{net} by r_1 to reflect the fact that the first pass beam, which has traversed the cavity only once, has reflected off every mirror except the input coupler, and we subtract L_2 (which here is the distance from the input coupler to mirror 2 as illustrated in Figure 2.3) from L to be consistent with our convention that the phase of the light is zero at the output coupler.

This transmitted field adds with the portion of the input beam reflected from the input coupler to produce a total field of

Equation 2.18: $$E_{cav-ref} = \frac{E_0 t_1^2 \left(r_{net} / r_1\right) e^{-i\omega t} e^{ik(L-L_2)}}{1 - r_{net} e^{ikL}} - r_1 E_0 e^{-i\omega t} e^{ik(-L_2)}$$

The minus sign in front of r_1 is due to the phase of π which light picks up in reflecting off the interface between the glass of the mirror and the empty space inside the cavity, a "dense to rare" reflection[9]. (Here we are neglecting the additional reflection from the outer surface of the mirror. In practice, one usually coats this outer surface so as to minimize reflections, while the inner surface is designed to be relatively high reflecting.)

We have labeled this field $E_{cav-ref}$ because it is the total field traveling back away from the input coupler, reflected by the cavity as a whole. The cavity may be treated, mathematically, as a single mirror, positioned and oriented as the input coupler is, with a complex reflectivity, which is defined as the ratio of this net backward traveling field to the input field:

Equation 2.19: $$r_{cav} = E_{cav-ref} \Big/ \left(E_0 e^{-i\omega t} e^{ik(-L_2)}\right) = \frac{t_1^2 \left(r_{net} / r_1\right) e^{ikL}}{1 - r_{net} e^{ikL}} - r_1$$

Let us apply this to the two mirror case illustrated by Figure 2.2. We will calculate the reflectivity on resonance, with $kL = 2\pi m$ (an even multiple of π) and anti-resonance, with $kL = \pi(2m+1)$ (an odd multiple of π).

Let us choose $r_1 = r_2 = 0.9$, so that $r_{net} = r_1 r_2 = (0.9)^2 = 0.81$, and $t_1^2 = 1 - r_1^2 = \left(1 - 0.81\right)$. Equation 2.19 reduces in this case to

$$r_{cav} = \frac{\left(1-0.81\right)\left(0.81/0.9\right) e^{ikL}}{1 - 0.81 e^{ikL}} - 0.9$$

If we now choose $kL = 2\pi m$, we find:

$$r_{cav} = \frac{(1-0.81)(0.81/0.9)}{1-0.81} - 0.9 = 0$$

Hence we see that no light is reflected from the cavity when it is on resonance. The output intensity is in this case equal to the input intensity; the cavity is one hundred percent transmitting.

If we next choose $kL = \pi(2m+1)$, we find:

$$r_{cav} = \frac{(-1+0.81)(0.81/0.9)}{1+0.81} - 0.9 = 0.9\left(\frac{0.81-1}{0.81+1} - 1\right) \cong -0.994$$

In this case the cavity is almost, but not exactly, one hundred percent reflecting. The negative sign indicates a phase shift on reflection of 180 degrees. This phase shift varies with the resonance condition of the cavity, from zero when the cavity is on resonance (where the magnitude of the reflectivity is also zero, in this case) to 180 degrees at anti-resonance. The result that the reflectivity does not go to one is consistent with the result we saw earlier in Figure 2.4, where we showed that the transmissivity does not go all the way to zero, and depends on the reflectivity of the mirrors of which the cavity is comprised.

In general, the effective reflectivity and transmissivity obey the equation $|r_{cav}|^2 + |t_{cav}|^2 = 1$, exactly like an ordinary mirror except that the quantities are complex, due to the variable phase shift the cavity imposes on the light it reflects. The relationship $|r_{cav}|^2 + |t_{cav}|^2 = 1$ tells us that while a passive cavity can store light, it cannot (except through losses due to mirror heating which we have been neglecting) actually reduce or increase the amount of energy in the system. Energy is conserved.

Let us conclude our review of cavities with a brief discussion of what happens when we put a gain medium inside of one. As we noted in the introduction, a cavity with a gain medium inside it is also known as an active cavity, by contrast with the passive empty cavity. If the percentage gain within the cavity initially exceeds the percentage loss, then each reflection is as a result stronger than the last, and the active cavity becomes a laser. We will discuss lasers in much greater detail in Chapter 7, but we introduce them here in order to compare them with passive cavities.

Recall that the steady state for a passive cavity requires that the incoming light be equal in energy to the outgoing light. Unlike a passive cavity, a laser need not have an input to produce an output. In fact, a laser cavity generally lacks an input coupler, having only one partially reflecting mirror. The "incoming" light is, in this case, just the additional field produced by the gain medium on each reflection, and the outgoing light is again a fixed fraction of the circulating field. The laser, like the passive cavity, reaches a steady state with a finite intracavity field after infinite reflections. This is because as the field inside the cavity grows, the gain medium necessarily begins to saturate, giving smaller percentage gains as the total field strength increases. The steady state is reached when the percentage gain due to the partially saturated medium is equal to the percentage loss, ideally through the output coupler only. This saturation occurs because, in order to provide gain, the medium within the cavity needs to have a population inversion[7] — its atoms must be in an excited state. The stronger and stronger field drives the atoms out of the excited state more and more rapidly, and the rate at which they are leaving the excited state eventually exceeds the rate at which they are being pumped back into it by whatever pumping mechanism the gain medium depends upon. A population inversion cannot be maintained without a pumping mechanism. The excited atoms are subject to spontaneous decay, and will naturally fall back to the ground state if left to themselves. The energy in the laser output comes, not from any input beam, but from the pumping mechanism, which usually derives its power, ultimately, from the electrical grid, and it is this power we must measure to ensure that energy is being conserved.

The fluorescence of the gain medium due to that spontaneous decay also serves as the initial "input" to the resonator, the first pass beam which the medium then amplifies. Unlike the inputs to passive resonators, however, it never has to pass through an input coupler. It is inside the cavity to begin with. The fluorescence is a result of the spontaneous decay, and the decay is a result of interactions of the atoms with the vacuum fluctuations in the electric field, so we can say that the initial input field to the laser cavity is really that vacuum fluctuation field.

A laser has a Free Spectral Range of c/L just a passive cavity does, and for the same reason, though we must be very careful in this case to interpret L as the optical path length and not just a physical distance, since the gain medium will have an index of refraction which will affect that optical length, although in most cases the effect is slight. (We will discuss this effect in much greater detail later in Chapter 7.) The round trip optical path length must, in a laser as in a passive cavity, be an integer multiple of the wavelength of the circulating field in order for the reflections to add coherently, and c/L is the difference between frequencies which fulfill that condition. Equation 2.5 applies to lasers as well as passive cavities. The laser may be single mode, lasing only at the resonant frequency which is closest to the peak gain frequency, or it may be multimode, lasing at multiple resonant frequencies at the same time. Which a given laser will be depends on the type of gain medium in a way that we will also explore in Chapter 7.

The linewidth of the laser, however, does not depend on the mirror reflectivities and the FSR as linewidth of the passive cavity does. Since, in a laser in steady state, the gain is equal to the loss, we know that the fiftieth reflection, or indeed the fifty-thousandth, will be just as strong as the first. Therefore, any field with a wavelength even slightly different from the resonant wavelength will eventually suffer from destructive interference, as the strong out-of-phase later reflections begin to cancel with the early reflections. The linewidth of a laser is therefore, classically, zero. Only a single frequency, the resonant one, will interfere constructively no matter how many reflections it undergoes. Any frequency which differs, by however infinitesimal an amount, from the resonant frequency will be subject to destructive interference. Quantum mechanically however, there is room for small deviations. The spontaneous decay process introduces quantum noise into the intracavity field, and that noise shows up as frequency fluctuations in the output field. Experimentally, too, there is another source of noise. The mirrors and the medium are subject to vibrations and thermal variations which cause the optical path length to fluctuate, and this shows up as frequency fluctuations in the output as well. Nevertheless, the linewidth of a laser is, regardless of the reflectivity of its mirrors, very narrow in comparison to that of a comparable empty cavity.

Our qualitative discussion of the properties of laser resonators allows us to conclude that they are similar to passive cavities in that they have resonant frequencies which depend on the round trip optical path length, and that on resonance they reach a steady state determined by the law of conservation of energy. Unlike passive cavities, they need no input beam, and their linewidths are unrelated to the reflectivity of their mirrors. For a quantitative treatment of these topics, please see Chapter 7 and reference 10.

There is much more to know about passive cavities as well: their spatial modes, stability criteria, impedance matching conditions, storage times, etc which may be found in, for instance, reference 7, but these details are not necessary for understanding the research presented here.

The most important results of this chapter, for the research to follow, are the linewidth, given by Equation 2.13 (and in simplified form, Equation 2.16) and the dependence of the resonant frequencies on length, given by Equation 2.5. Both are derivable from Equation 2.4, which is our master equation for empty cavities.

CHAPTER 3 - CLASSICAL DISPERSION

The research presented here involves modifying the resonance properties of cavities by incorporating dispersive media into them, so, having reviewed the resonance properties of cavities, we will now review dispersive media.

The index of refraction of a material is determined by the frequency dependent response of its atoms to light propagating through it. Quantum mechanically, of course, the resonant frequencies of those atoms depend on their energy levels, and the energy levels themselves depend on the structure of the material. We will discuss the quantum mechanical models in a separate section, because the details are important to the technologies which allow us to manipulate the index of refraction of certain materials. For now, however, we will limit ourselves to a classical model, which is somewhat more transparent, to make the relationship between the frequency, phase, and wavelength of electromagnetic radiation in a medium, and the index of refraction of that medium, as clear as possible.

The atoms in materials radiate, because their electron shells oscillate in response to the incident field, and these oscillating dipoles necessarily radiate[9]. When we add the dipole radiation due to a single atom to the incident wave, we get a total field that looks like the incident field, but delayed and potentially different in magnitude, as illustrated in

Figure **3.1**.

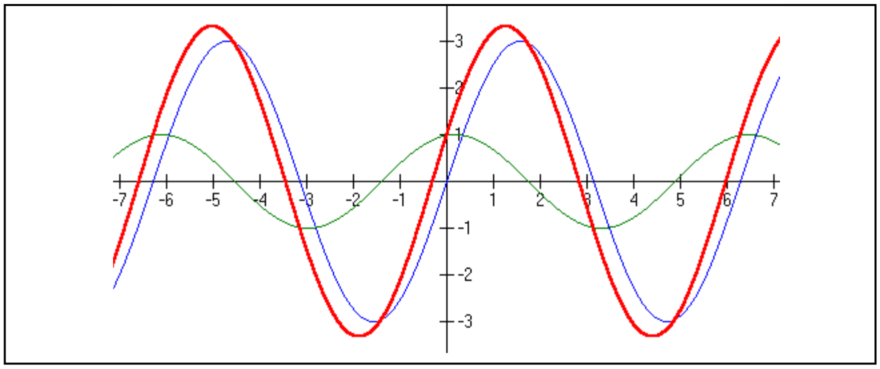

Figure 3.1 Incident wave blue, dipole radiation smaller and green, resultant wave larger and red

The next atom then sees this modified electric field then causes the next atom to oscillate in a slightly different way than the first did. The incident field itself still propagates at the free space velocity of light, but the total field, in the single-atom case, is a wave which has been shifted in phase so that each crest reaches a given point slightly later than it would have in the absence of the material, as if the material had slowed the wave down to a velocity v_p, and the index of refraction of the material is defined in terms of this change: $n = c / v_p$

How much the phase of the light radiated by the atoms (and thus the phase of the total field which includes that light) lags behind the phase of the incident light depends on how close the incident frequency is to the resonant frequency of the atoms.

Classically, we can model the atoms as harmonic oscillators, as electrons bound to atomic nuclei by springs instead of by the Coulomb force. This is not a very physical picture, but the model gives us a way to incorporate a key property of real atoms – the fact that they have resonant frequencies – which otherwise can only be accounted for quantum mechanically.

An electron on a spring, then, obeys the equation:

Equation 3.1: $m\ddot{x} + m\gamma\dot{x} + m\omega_0^2 x = qE_0 \cos(\omega t)$

Here m is the mass of the electron, q its charge, ω_0 the resonant frequency of the atom, and γ is the damping, which is physically caused by spontaneous decay. $E_0 \cos(\omega t)$ is the forcing field. We can solve this equation by treating x, which represents the distance from the electron to the proton, as the real part of a variable obeying a complex equation[9]:

Equation 3.2: $m\ddot{\tilde{x}} + m\gamma\dot{\tilde{x}} + m\omega_0^2\tilde{x} = q\tilde{E}_0 e^{i\omega t}$

We plug in the ansatz $\tilde{x} = \tilde{x}_0 e^{i(\omega t - \alpha)}$, and find that this solves the equation so long as $\tilde{x}_0$ obeys

Equation 3.3: $\tilde{x}_0 = \frac{q\tilde{E}_0}{m}\frac{e^{+i\alpha}}{\omega_0{}^2 - \omega^2 - i\gamma\omega}$

The fact that this solution for $\tilde{x}$ has an imaginary part means the motion of the electron is out of phase with the electric field, lagging behind by an angle given by

Equation 3.4: $\tan\alpha = \gamma\omega / (\omega_0^2 - \omega^2)$

The time dependent dipole moment of the atom, p, is then given by

Equation 3.5: $p = \mathrm{Re}\left[\tilde{p}\right] \quad and \quad \tilde{p} = q\tilde{x}(t)$

Strictly, the dipole moment of the atom is a real, not a complex quantity, and is not proportional to the electric field, another real quantity. The two have the same time dependence, but are out of phase. However, relating each of them to a complex quantity with both a phase and a magnitude allows us to write the simple relationship

Equation 3.6: $\tilde{p} = \varepsilon_0 \chi_j \tilde{E} \quad where\, \tilde{E} = E_0 e^{i\omega t}$

Here χ_j is a dimensionless complex number, and its phase is the phase difference α between the electric field and the dipole moment of the atom. ε_0 is a conversion constant, because $\tilde{p}$ has units of dipole moment, and $\tilde{E}$ has units of electric field. Both the magnitude and phase of χ_j can be determined from

Equation 3.7: $\chi_j = \frac{q\tilde{x}_0}{\tilde{E}_0} = \frac{q^2}{m(-\omega^2 + i\gamma_j\omega + \omega_{0j}^2)}$

The susceptibility for the medium is the average of these single-oscillator susceptibilities. Different atoms in the medium have slightly different effective restoring forces and damping constants, so we add up these individual susceptibilities and divide by the total volume, to arrive at a bulk polarization of the material, P, which has units of dipole moment per unit volume and is defined by

Equation 3.8: $P = \mathrm{Re}\left[\tilde{P}\right]$ *where* $\tilde{P} = \left(\varepsilon_0/V\right)\sum_j \chi_j \tilde{E} = \varepsilon_0 \chi \tilde{E}$

So that

Equation 3.9 $\chi = \frac{\tilde{P}\varepsilon_0}{\tilde{E}}$

Finally we note that the field radiated by the oscillating dipoles is $\pi/2$ radians out of phase with the motion of the dipoles themselves[9], so that when χ is entirely imaginary, equal to $|r|e^{i\pi/2}$ for some magnitude $|r|$, the field the dipoles radiate is actually π radians or one hundred and eighty degrees out of phase with the incident light, and interferes destructively with it. An imaginary χ then, indicates that the material is absorbing the incident field (and radiating the energy away in random directions through spontaneous decay.) We can see from Equation 3.7 that χ is purely imaginary when $\omega = \omega_0$, i.e., when the incident field frequency matches the resonant frequency of the atoms. If the susceptibility is complex rather than purely imaginary, there will still be some absorption, but it will be less than the maximum value obtained when exactly on resonance, as the dipole field will not be exactly out of phase with the incident field.

Note that for $\omega > \omega_0$, α is greater than $\pi / 2$ and the phase lag becomes indistinguishable, for infinite, continuous waves, from a phase lead, as illustrated in Figure 3.2:

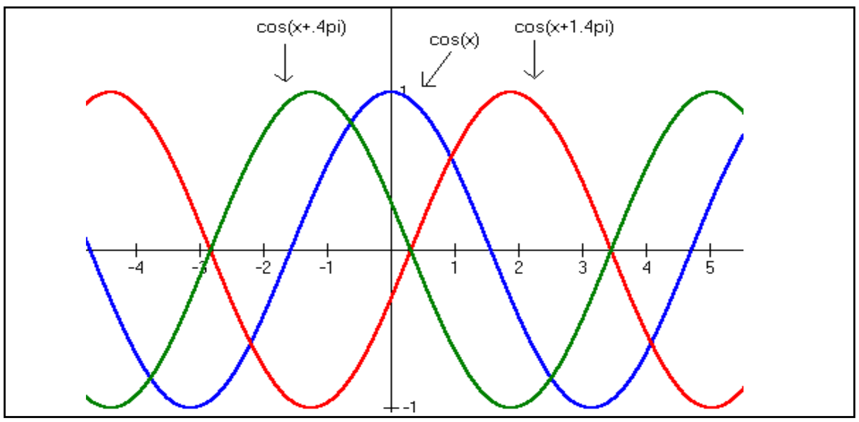

Figure 3.2: Continuous waves with different phase shifts, illustrating the fact that a phase lag greater than pi is indistinguishable from a phase lead

For this reason it is possible to have an index of refraction less than one, and the implied apparent velocity greater than the free space speed of light.

Now that we have a qualitative understanding of index of refraction, let us develop a quantitative model. The first part of this derivation is general, and does not depend on the specific model of susceptibility which we have developed so far. It will be equally applicable to the quantum mechanical models for susceptibility that we will develop later.

We begin with Maxwell's equations:

Equation 3.10: $$\nabla\times\vec{H}=\frac{d\vec{D}}{dt};\ \nabla\times\vec{E}=-\frac{d\vec{B}}{dt};\ \nabla\times\vec{B}=0;\ \nabla\times\vec{D}=\rho$$
$$where\ \vec{D}=\varepsilon_0\vec{E}+\vec{P},\ \ \vec{B}=u_0\vec{H}$$

We derive the wave equation :

$$\nabla\times\nabla\times\vec{E}=-\nabla\times\frac{d\vec{B}}{dt}$$
$$\Rightarrow-\nabla^2\vec{E}-\nabla(\nabla\bullet\vec{E})=\mu_0\frac{d}{dt}(\nabla\times\overline{H})$$
$$\Rightarrow-\nabla^2\vec{E}-\frac{1}{\varepsilon_0}\nabla(\nabla\bullet(\overline{D}-\vec{P}))=\mu_0\frac{d^2}{dt^2}(\varepsilon_0\vec{E}+\vec{P})$$

And since $\nabla\bullet(\overline{D}-\overline{P}))$ =0, we can write

Equation 3.11: $$\Rightarrow-\nabla^2\vec{E}-\mu_0\varepsilon_0\frac{d^2\vec{E}}{dt^2}=\mu_0\frac{d^2\vec{P}}{dt^2}$$

Recall from Equation 3.8 that $\tilde{P}=\varepsilon_0\chi\tilde{E}$. We then define another variable

Equation 3.12: $$\varepsilon\equiv\varepsilon_0\left(1+\chi\right)$$

Then we can write the wave equation as

Equation 3.13: $$\nabla^2\tilde{E}=\varepsilon\mu_0\frac{\partial^2\tilde{E}}{\partial t^2}$$

We try an ansatz

Equation 3.14: $$\tilde{E}=\tilde{E}_0e^{i(\tilde{k}z-\omega t)}$$

This solves the differential equation if

Equation 3.15: $$\tilde{k}=\sqrt{\tilde{\varepsilon}\mu_0}\omega\equiv\kappa_R+i\kappa_I$$

At the point in time and space where the wave has a crest, the field is given by $\tilde{E}_0e^{i((\kappa_R+i\kappa_I)z_{crest}-\omega t_{crest})}=\tilde{E}_0e^{-\kappa_I z_{crest}}e^{i(\kappa_R z_{crest}-\omega t_{crest})}=f\tilde{E}_0e^{i(\kappa_R z_{crest}-\omega t_{crest})}$, (where $f=e^{-i\kappa_I z_{crest}}$ is the factor by which any absorption has reduced the magnitude of the field. This location is only a "crest" if the phase is zero, i.e. $\kappa_R z_{crest} - \omega t_{crest} = 0$, and we can find the rate at which the crest travels by writing $z_{crest} = \omega t_{crest} / \kappa_R$ and thus

Equation 3.16: $$\frac{dz_{crest}}{dt_{crest}} = \frac{\omega}{\kappa_R} = v_p$$

Note that in vacuum $v_p = \omega / \kappa_R \equiv 1/\sqrt{\varepsilon_0 \mu_0} = c$. In a medium $v_p = \omega / \kappa_R \equiv 1/\sqrt{\varepsilon_0 \mu_0 (1+\chi)}$, so we have the index of refraction of a medium given by

Equation 3.17: $$n = \frac{c}{v_p} = \frac{c\kappa_R}{\omega} = \mathrm{Re}\left[\sqrt{(1+\tilde{\chi})}\right]$$

We see from this equation that the index tells us the velocity of the phase fronts. As a consequence, it also tells us about the wavelength of the light in the material. If the phase velocity is reduced, but waves are still entering the material at the same rate (as they must if the source continues to emit at the same frequency) then the phase fronts will necessarily become closer together. The usual analogy is a line of soldiers fording a stream. A soldier enters the water and slows down; the soldier behind him, still on land, closes the distance between them, and then enters the water and travels at the same rate so the distance remains constant while they are both in the water. On exiting, the first soldier moves quickly again and opens up the distance before the soldier behind him emerges. The same effect means that an index of refraction greater than one, resulting in a phase velocity less than c, will cause phase fronts to bunch together within a material. An index greater than one, and a phase velocity greater than c, will allow the waves to separate. The wavelength in the material is given by

Equation 3.18: $$\frac{\omega}{k_{medium}} = V_p = \frac{c}{n} \Rightarrow \lambda_{medium} = \frac{2\pi}{k_{medium}} = \frac{2\pi c}{n\omega} = \lambda_0 / n(\lambda_0)$$

Here λ_0 is the free space wavelength.

The spatial phase picked up by the light is then

Equation 3.19: $$k_{medium} L = n k_0 L$$

Because of this, it is sometimes said that the effect of the index is to alter the optical path length, through the material, by a factor of n. Physically, though, it is the wavelength of the light and not the path length that is affected.

We can also derive the absorption coefficient, the fraction of intensity lost as a function of length:

Equation 3.20: $$|E|^2 = \left|\tilde{E}_0 \left(e^{-\kappa_I z}\right)\right|^2$$

Therefore the fraction of intensity lost per unit length is e^{α_L} :

Equation 3.21: $$\alpha_L = -2\kappa_I = -2\,\mathrm{Im}\left[\omega\sqrt{\mu_0\varepsilon_0\left(1+\chi\right)}\right]$$

These equations, Equation 3.20 and Equation 3.21 are completely general, independent of our model for χ.

Let us now, however, plug in the expression from χ that we obtained from our classical model (assuming a uniform sample with number density "N".)

Equation 3.22: $$n = Re\left[\sqrt{1+\frac{N q^2}{m(-\omega^2 + i\gamma\omega + \omega_0^2)}}\right] \approx 1 + \frac{1}{2}\frac{Nq^2(\omega_0 - \omega)}{m\left(\left(\omega_0^2 - \omega^2\right)^2 + \gamma^2\omega^2\right)}$$

If we plot this, the result is a graph like Figure 3.3 below.

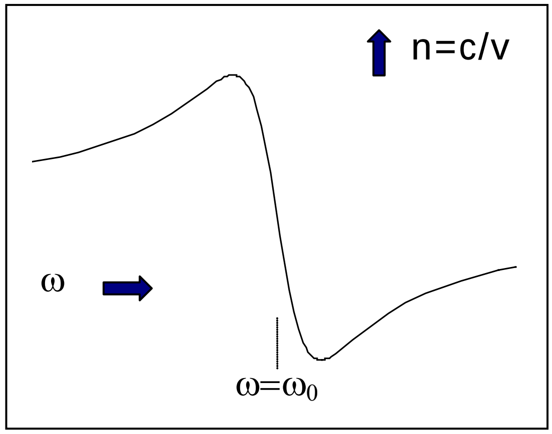

Figure 3.3 Lineshape of index of refraction vs. frequency derived using classical "electrons on springs" model.

Next we calculate the absorption:

Equation 3.23:

$$\alpha = -2\,\mathrm{Im}\left[\omega\sqrt{\mu_0\varepsilon_0\left(1+\frac{N\,q^2}{m(-\omega^2+i\gamma\omega+\omega_0^2)}\right)}\right] \approx -2\omega\sqrt{\mu_0\varepsilon_0}\left(1-\frac{1}{2}\frac{Nq^2\gamma\omega}{m\left(\left(\omega_0^2-\omega^2\right)^2+\gamma^2\omega^2\right)}\right)$$

Plotting this gives a lineshape like that shown below in Figure 3.4.

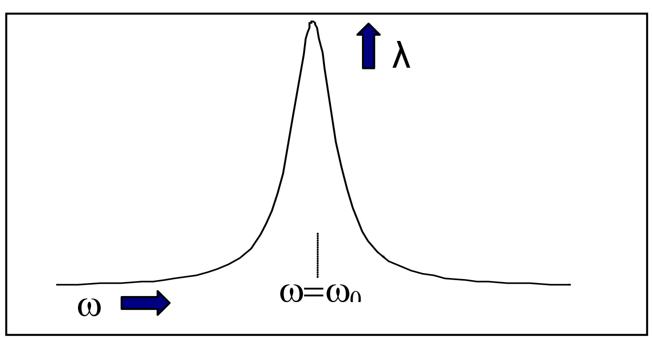

Figure 3.4: Lineshape of absorption vs. frequency derived using classical "electrons on springs" model.

Plotting these lineshapes in this form makes it obvious that they are related: the lineshape of the index resembles the derivative of that of the absorption. This relationship is not limited to this particular model or type of system. It is a consequence of the Kramers-Kronig relations, which are completely general, following from a statement of causality in the frequency domain. We derive them briefly here, beginning with a definition of the time-dependent polarizability of a material, without assuming, this time, a form for the solution.

Equation 3.24: $P(t)=\varepsilon_0\int_{-\infty}^{\infty}E(t')\chi(t-t')dt'$

The polarization response function must obey causality, i.e. the effect cannot precede the cause. W can state that mathematically with the condition that for $t<0,\ E=0$. Therefore

Equation 3.25: $\chi(t)=0\ \ \textit{for}\ \ t<0$ or $\chi(t-t')=0$ for $t<t'$

This can be expressed using the "step function":

Equation 3.26: $\chi(t)=\theta(t)\chi(t)$ where $\textit{where}\ \theta(t)=\begin{cases}0 & t<0\\ 1 & t>0\end{cases}$

If we now plug this expression into Equation 3.24: $P(t)=\varepsilon_0\int_{-\infty}^{\infty}E(t')\chi(t-t')dt'$, we have an expression of causality in the time domain, which may be Fourier transformed in order to explore its consequences in the frequency domain.

Equation 3.27:

$$\chi(\omega)=F\{\theta(t)\chi(t)\}=\int_{-\infty}^{\infty}\theta(t)\chi(t)e^{i\omega t}dt\ \ \textit{where}\ \chi(t)=\int_{-\infty}^{\infty}\chi(\omega')e^{i\omega' t}d\omega'$$

We attempt to carry through these integrals:

Equation 3.28: $\chi(\omega)=\int_{-\infty}^{\infty}dt\int_{-\infty}^{\infty}d\omega'\theta(t)\chi(\omega')e^{i(\omega-\omega')t}=\int_{-\infty}^{\infty}d\omega'\chi(\omega')\int_{-\infty}^{\infty}dt\theta(t)e^{i(\omega-\omega')t}$

The last expression there is just the Fourier transform of the step function, which is well known, so we can write

Equation 3.29: $$\chi(\omega)=\int_{-\infty}^{\infty}d\omega'\chi(\omega')\theta(\omega-\omega')$$

Now we must use that well-known Fourier transform:

Equation 3.30: $$\theta(\omega)=F\{\theta(t)\}=\frac{1}{2}\delta(\omega)+\frac{i}{2\pi\omega}$$

Plugging this in gives us

Equation 3.31: $$\chi(\omega)=\int_{-\infty}^{\infty}d\omega'\chi(\omega')\frac{1}{2}\delta(\omega-\omega')+i\int_{-\infty}^{\infty}d\omega'\frac{\chi(\omega')}{2\pi(\omega-\omega')}$$

Evaluating the first integral and solving for the susceptibility, we finally arrive at:

Equation 3.32: $$\chi(\omega)=\frac{i}{\pi}\int_{-\infty}^{\infty}\frac{\chi(\omega')}{\omega-\omega'}d\omega'$$

This is the statement of causality in the frequency domain. If we keep mind that $\chi(\omega)$ is a complex number, we can see from this statement that it relates the real and imaginary parts of $\chi(\omega)$, which we have already seen correspond to the index of refraction and the absorption of the material, respectively. Writing both the left and right sides of this equation as explicit sums of a real term and in imaginary term allows us to write the relationship between the real part χ' and imaginary part χ'' as

Equation 3.33: $$\chi''(\omega)=-\frac{2\omega}{\pi}\int_{0}^{\infty}\frac{\chi'(\omega')}{\omega'^2-\omega^2}d\omega'$$

and

Equation 3.34: $$\chi'(\omega)=-\frac{2}{\pi}\int_{0}^{\infty}\frac{\omega'\chi''(\omega')}{\omega'^2-\omega^2}d\omega'$$

The physical interpretation of these equations is slightly subtle. The connection to causality was described by John Toll in reference[11]. The figure to which he refers resembles the illustration in Figure 3.5.

> "This figure illustrates schematically the basic reason for the logical connection of causality and dispersion. An input A which is zero for times t less than zero is formed as a superposition of many Fourier components such as B, each of which extends from $t=-\infty$ to $t=\infty$. These components produce the zero- input signal by destructive interference for t<0. It is impossible to design a system which absorbs just the component B without affecting other components, for in this case the output would contain the complement of B during times before the onset of the input wave, in contradiction with causality. Thus causality implies that absorption of one frequency must be accompanied by a compensating shift in phase of other frequencies; the required phase shifts are prescribed by the dispersion relation."

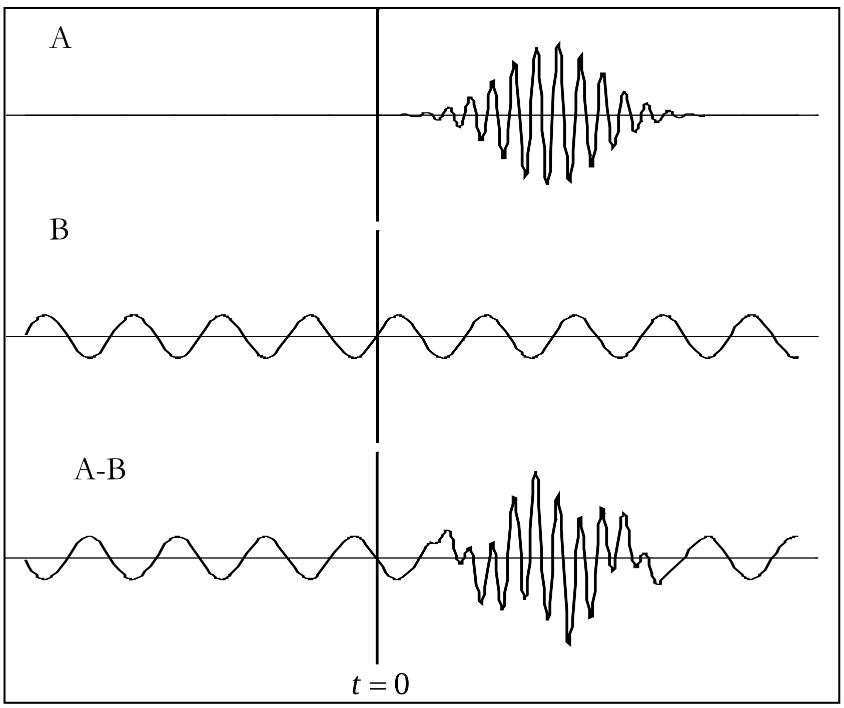

Figure 3.5: A) Input pulse, zero before time t=0 B) A single Fourier component of the pulse C) The pulse with one component removed and no compensating phase shift – the signal would have to be non-zero before t=0, in violation of causality.

Thus, it is a universal consequence of causality that the real and imaginary parts of the susceptibility, corresponding to the index of refraction and the absorption, are related.

The techniques described later in this thesis for using dispersive materials to modify the behavior of optical cavities and interferometers rely on specially tailored index of refraction profiles. We produce these by exploiting this connection between absorption (and gain, which is simply negative absorption) and index. An absorption peak is associated with the lineshape displayed in Figure 3.3. A gain peak will produce the opposite lineshape, with a positive slope in the center. Combinations of absorption and gain features with controllable frequency spacing and magnitudes allow us to produce almost any slope for the dispersion profile that we choose. We now discuss the relevance of that slope.

Now that we have established the effect of the medium as a function of frequency, we can see what happens to a pulse of light made of many different frequency components as it propagates through the medium. If each frequency component receives a different phase shift, the point at which the different components add in phase can move at a rate different than that of any of the underlying frequency components. Consider, for instance, the sum of three frequencies. If those frequencies all propagate in the same way, the pulse will propagate with them. However, if they receive different phase shifts, different phase fronts will line up, and the pulse will be located at a different point in space, after the same time.

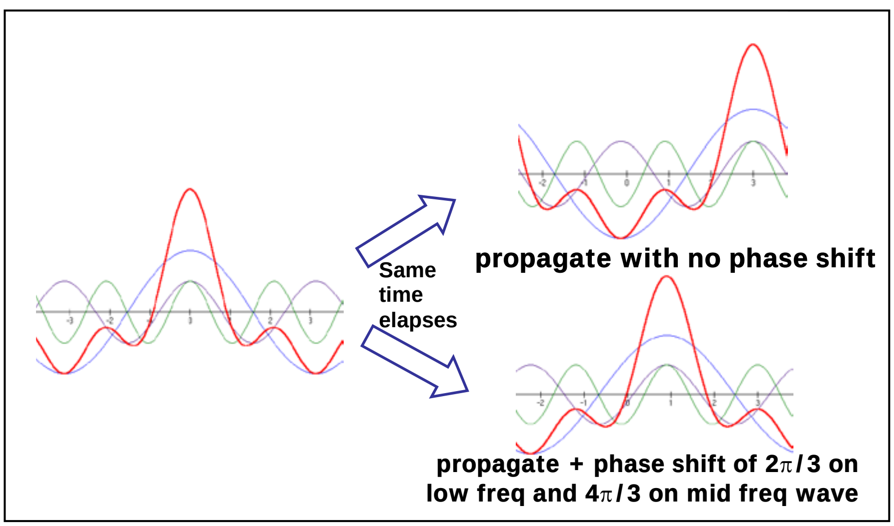

Figure 3.6: Pulse location at two different times with and without frequency dependent phase shifts.

At what rate, then does the pulse propagate? Let us consider the location of the pulse. At what point do all of the frequency components have the same phase?

For waves of the form:

Equation 3.35: $E(z,t) = Ae^{i(kz-\omega t)} + c.c.$ where $k = n\omega / c$

The phase at any point in space and time is given by:

Equation 3.36: $\phi(\omega) = \mathrm{kz}\text{-}\omega\mathrm{t} = \dfrac{n(\omega)\omega z}{c} - \omega t$

The requirement that they add in phase can be expressed mathematically by the statement that the phase does not vary with frequency (at a particular point in space and time), i.e. that

Equation 3.37: $\dfrac{d\phi}{d\omega} = 0$ or $\dfrac{dn}{d\omega}\dfrac{\omega z}{c} + \dfrac{nz}{c} - t = 0$

The "z" and "t" in this equation tell us the location of the pulse as a function of time, so its velocity is given by:

Equation 3.38: $v_g = \dfrac{\Delta z}{\Delta t} = \dfrac{c}{n + \omega\, dn / d\omega} = \dfrac{d\omega}{dk}$

Just as we defined the index of refraction as the ratio of the phase velocity and the free space speed of light, we can now define a "group index":

Equation 3.39: $v_g = \dfrac{c}{n_g}$ $where\ n_g = n + \omega \dfrac{dn}{d\omega}$

So we see that the slope of the index, $dn / d\omega$, determines the group index of the material. A positive slope necessarily gives rise to a group index greater than one, and a group velocity less than the speed of light. For that reason, materials with index functions that have positive slopes (normal dispersion) are known as "slow light materials," especially if this dispersion occurs at frequencies at which the material is transparent. On the other hand, if $dn/d\omega$ is negative, and $|\omega\, dn/d\omega| < n$, the group index will be less than one but greater than zero, resulting in a group velocity greater than the speed of light. For this reason the materials which fulfill this condition are known as "fast light" materials, again, especially if the material is transparent over the spectral range of the dispersion. Finally, if the dispersion is negative and the slope is very large, it is possible for the group index to become negative. In this case the pulse appears to propagate backwards.

Since the index of refraction is in general frequency dependent, it is possible for a material to be a slow light material at one frequency and a fast light material at another frequency. Indeed, we have demonstrated this behavior, and we discuss it in the experimental results section later in this document.

The idea of slow light is not controversial, but the notion of fast light raises questions. How is it possible for a pulse to travel faster than the speed of light in vacuum, given that the theory of relativity forbids every kind of faster than light travel?

In fact the process is best viewed, not as a speeding up of the pulse, but as a re-shaping of it.[12][13] If the rear part of the pulse is attenuated, and the leading part is amplified or even just attenuated less, the apparent center of the pulse shifts forward. Smooth pulses, such as Gaussians, can be shifted forward arbitrarily, because they have infinitely long "tails" in either direction – they are in fact infinitely long, and to send a true Gaussian pulse would take an infinite time. Such a smooth pulse cannot carry information. In practice, at any rate, there must be a sharp cut-off somewhere, a time at which the laser was turned on. At this point the pulse is not smooth. And the peak of the pulse cannot be shifted beyond this starting time. Zero field is zero field, and no amplification or attenuation affects it. No photon ever travels faster than c. Another way of looking at is that this sharp cut-off involves many frequency components, and the bandwidth of the anomalous dispersion is limited. Inevitably there will be components of the pulse outside that bandwidth.

It is possible to imagine the peak of a pulse exiting a material before the peak of the input pulse enters it. What if a shutter in front of the material were closed at this point, and the input pulse were prevented from entering? This experiment has been tried with the RF equivalent of fast light[14]. This phenomenon is perfectly possible, though the trailing edge of the output pulse is distorted, becoming an oscillatory signal. Reference 15 models this behavior mathematically, and presents evidence that:

> The apparent difficulty here stems from the natural assumption that the output peak is causally related to the input peak. [...] In order for event A to be the cause of event B, it must be that preventing A also prevents B. Both experiment and theory show that preventing the peak in the input does not prevent the peak in the output, therefore the peaks are not causally related. The peak in the output is however causally related to earlier parts of the input, since cutting off the input sufficiently early will prevent the output peak from appearing.[15]

It is impossible to use fast light to send information at speeds greater than c. Nevertheless the shift forward in time is real, as we show experimentally in Chapter 9.

This chapter has reviewed the general theoretical basis of index of refraction, in terms of the wave equation, and reviewed its relationship, through the Kramers-Kronig relations, to the frequency dependent absorption function of the medium. We have explored the consequences of the variation of index with frequency for pulse propagation. We will use this information later in our discussion of methods for creation of custom tailored refractive indices. Finally we have developed a simple classical model for the index of atoms with a single resonant frequency by considering the behavior of electrons on springs, in order to get an idea of the general shape of the index and absorption for a typical atomic medium. More elaborate index functions require quantum mechanical models, and we develop some of these in the next section.

CHAPTER 4 - QUANTUM MECHANICAL DISPERSION

Two Level Systems

In order to understand the more complicated index profiles which will make possible the modifications we want to make to cavity resonance properties, we need quantum mechanics. We review briefly, here, the quantum mechanical models of absorption and index of refraction for two and three level atomic systems.

First we will discuss two level interactions. We will assume that, if the atom has any other energy levels, they are not coupled, and are unavailable to the system. We are assuming, in other words, that the electric field which drives the transition between the two levels we will be treating here is far off resonance for the other transitions, and that no other fields are present. We first solve the Schrödinger equation to illustrate the behavior of this kind of system, and then show how the index of refraction of the material may be calculated from the atomic wavefunctions. Finally we will generalize the approach to derive the index profiles for multi-level systems, in particular three level systems consisting of two lower energy metastable states which do not couple optically, and a single excited state which couples optically, albeit at two different resonant frequencies, to both. (These are known as "Lambda" systems, from the resemblance of their level diagram, as in Figure 4.5, to the Greek letter lambda.) It is this kind of atom, illuminated by light fields of at least two frequencies, which will ultimately serve as our controllable dispersive medium. Both slow and fast light can be created in such a material.

These calculations, however, are numerical and often opaque. The methods we use for modeling these systems are most transparent when applied to the two level system. We can confirm that our approach agrees with the results predicted by the simple classical model developed in the last section, and develop a clear understanding of this most common type of dispersion, before attempting to model more complex systems.

Consider, then, an electron in the energy well of an atom, initially in its ground state.

Equation 4.1: $\psi(x,t=0)=\psi_1(x)$

It interacts with an electromagnetic field of the form

Equation 4.2: $\vec{E}(x,t)=E_0\hat{x}\cos(kz)\cos(\omega t+\phi)$

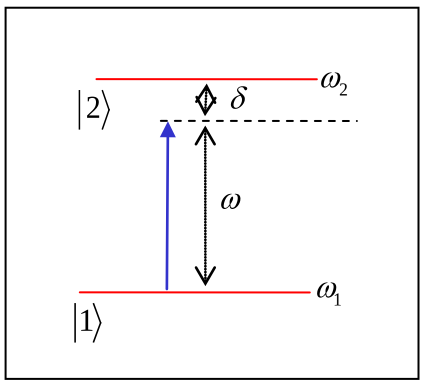

Figure 4.1: Energy level diagram for a two level system

In the presence of the field, the electron will have energy

Equation 4.3: $\hat{H}=\hat{H}_0+\hat{H}_1$, *where* $\hat{H}_0=\dfrac{\hat{p}^2}{2m}+V(\vec{r}),\ \hat{H}_1=-\hat{\vec{p}}\bullet\hat{\vec{E}}$

The dipole moment of the electron is given by its charge times its distance from the nucleus. This expression of the energy assumes that the wavelength of the light is long enough that the field is, at any time, approximately constant over the region of the wavefunction for the electron. Now we plug in:

Equation 4.4: $\hat{p}=\mu_0\hat{x}$ (electron lies along x axis), so that $\hat{H}_1=-\mu_0E_0\hat{x}\cos(kz)\cos(\omega t)$

(Note that the carets are intended to indicate operators, not unit vectors.) Since we have assumed that only two levels are available, we can write the wavefunction of the electron at any time as a superposition of those two levels.

Equation 4.5: $\left|\psi(x,t)\right\rangle = c_1(t)\left|\psi_1\right\rangle + c_2(t)\left|\psi_2\right\rangle \quad where\ c_1(t) = \left\langle\psi|\psi_1\right\rangle, c_2(t) = \left\langle\psi|\psi_2\right\rangle$

The Schrödinger equation for the system is then:

Equation 4.6: $i\hbar\frac{d}{dt}\begin{bmatrix} c_1(t) \\ c_2(t) \end{bmatrix} = \begin{bmatrix} \left\langle\psi_1\middle|\hat{H}\middle|\psi_1\right\rangle & \left\langle\psi_2\middle|\hat{H}\middle|\psi_1\right\rangle \\ \left\langle\psi_1\middle|\hat{H}\middle|\psi_2\right\rangle & \left\langle\psi_2\middle|\hat{H}\middle|\psi_2\right\rangle \end{bmatrix}\begin{bmatrix} c_1(t) \\ c_2(t) \end{bmatrix}$

We know that

Equation 4.7: $\left\langle\psi_m\middle|\hat{H}_0\middle|\psi_n\right\rangle = E_m\delta_{mn}$

where E_m is the energy of the m^th level. We then write

Equation 4.8: $\hat{H}_1 = -p_0E_0\hat{x}\cos(kz)\cos(\omega t+\phi) \approx \frac{-p_0E_0}{2}\hat{x}\left(e^{i(\omega t+\phi)} + e^{-i(\omega t+\phi)}\right) = f(t)\hat{x}$

Where we have made use of our assumption that the field is approximately constant over the spatial extent of the wavefunction, at any given time. Thus:

Equation 4.9: $\left\langle\psi_m\middle|\hat{H}_1\middle|\psi_n\right\rangle = f(t)\left\langle\psi_m\middle|\hat{x}\middle|\psi_m\right\rangle$

Since $\left|\psi_1\right\rangle$ and $\left|\psi_2\right\rangle$ are eigenfunctions of the unperturbed, spherically symmetric Hamiltonian, we know from symmetry that

Equation 4.10: $\left\langle\psi_1\middle|\hat{x}\middle|\psi_1\right\rangle = \left\langle\psi_2\middle|\hat{x}\middle|\psi_2\right\rangle = 0$

We will define

Equation 4.11: $$x_{12} = \langle \psi_1 | \hat{x} | \psi_2 \rangle = \langle \psi_2 | \hat{x} | \psi_1 \rangle^*$$

We assume this quantity to be real and non-zero. We further define the "Rabi frequency" as

Equation 4.12: $$\Omega_0 = \frac{-d_0 E_0 x_{12}}{\hbar}$$

We now have

Equation 4.13: $$\hat{H} = \hbar \begin{bmatrix} \omega_1 & \Omega_0 \left(e^{i(\omega t+\phi)} + e^{-i(\omega t+\phi)} \right) \\ \Omega_0 \left(e^{-i(\omega t+\phi)} + e^{i(\omega t+\phi)} \right) & \omega_2 \end{bmatrix}$$

We now make the "rotating wave approximation" [16], ignoring the complex conjugate terms since they do not strongly couple the levels.

Equation 4.14: $$H \approx \hbar \begin{bmatrix} \omega_1 & \frac{\Omega_0}{2} e^{-i(\omega t+\phi)} \\ \frac{\Omega_0}{2} e^{i(\omega t+\phi)} & \omega_2 \end{bmatrix}$$

It is this expression for the Hamiltonian that we plug into the Schrödinger equation given as Equation 4.6. In order to solve this equation, we will make some changes of variable. The goal here is find an effective Hamiltonian which is time independent. First, we introduce a "Q" matrix, where

Equation 4.15: $$\hat{Q} = \begin{bmatrix} e^{i(\theta_1 t+\eta_1)} & 0 \\ 0 & e^{i(\theta_2 t+\eta_2)} \end{bmatrix} \text{ such that } \hat{Q}^{-1} = \hat{Q}^*$$

We note that

Equation 4.16: $$\dot{\hat{Q}} = i\hat{M}\hat{Q}$$

We now act on both sides of Equation 4.6 with this Q matrix.

Equation 4.17: $$\hat{Q}\frac{d\left|\psi\right\rangle}{dt} = -\frac{i}{\hbar}\hat{Q}\hat{H}\left|\psi\right\rangle$$

We take the derivative and insert an identity operator $\hat{I} = \hat{Q}^{-1}\hat{Q}$:

Equation 4.18: $$\frac{d\left\{\hat{Q}\left|\psi\right\rangle\right\}}{dt} - \dot{\hat{Q}}\left|\psi\right\rangle = -\frac{i}{\hbar}\hat{Q}\hat{H}\hat{Q}^{-1}\hat{Q}\left|\psi\right\rangle$$

We now define two more new variables:

Equation 4.19: $$\left|\tilde{\psi}\right\rangle = \begin{bmatrix} \tilde{c}_1(t) \\ \tilde{c}_2(t) \end{bmatrix} = \hat{Q}\left|\psi\right\rangle \quad and \quad \hat{H}' = \hat{Q}\hat{H}\hat{Q}^{-1}$$

Equation 4.18 now becomes:

Equation 4.20: $$\frac{d\left|\tilde{\psi}\right\rangle}{dt} = \frac{-i}{\hbar}\hat{H}'\left|\tilde{\psi}\right\rangle + i\hat{M}\left|\tilde{\psi}\right\rangle = \frac{-i}{\hbar}\left[\hat{H}' - \hbar\hat{M}\right]\left|\tilde{\psi}\right\rangle$$

We can now write a new equation that strongly resembles the original Schrödinger equation:

Equation 4.21:

$$i\hbar\frac{d\left|\tilde{\psi}\right\rangle}{dt} = \tilde{H}\left|\tilde{\psi}\right\rangle$$

$$where \;\; \tilde{H} = \hat{H}' - \hbar\hat{M} = \hbar\begin{bmatrix} (\omega_1 - \theta_1) & \frac{\Omega_0}{2}e^{i\omega t + i\phi}e^{i[(\theta_1 t + \eta_1) - (\theta_2 t + \eta_2)]} \\ \frac{\Omega_0}{2}e^{-i\omega t - i\phi}e^{-i[(\theta_1 t + \eta_1) - (\theta_2 t + \eta_2)]} & (\omega_2 - \theta_2) \end{bmatrix}$$

However, if we now choose:

Equation 4.22: $$\theta_1 - \theta_2 = \omega$$

We eliminate the time dependence. We can further choose, arbitrarily

Equation 4.23: $\theta_1 = \omega_1,\ \eta_1 = 0,\ \eta_2 = \phi$

This simplifies our effective Hamiltonian to

Equation 4.24: $\tilde{H} = \hbar \begin{bmatrix} 0 & \Omega_0/2 \\ \Omega_0/2 & -\delta \end{bmatrix}$ $\textit{where}\ \delta = \omega - (\omega_1 - \omega_2)$

We also have

Equation 4.25: $|\tilde{\psi}\rangle = \hat{Q}|\psi\rangle = \begin{bmatrix} c_1(t)e^{i\omega_1 t} \\ c_2(t)e^{i(\omega_1-\omega)t+i\phi} \end{bmatrix} = \begin{bmatrix} \tilde{c}_1(t) \\ \tilde{c}_2(t) \end{bmatrix}$

Our Schrödinger equation now requires that we take the time derivative of $|\tilde{\psi}\rangle$.

Equation 4.26: $i\hbar \dfrac{d|\tilde{\psi}\rangle}{dt} = i\hbar \begin{bmatrix} \dot{\tilde{c}}_1 \\ \dot{\tilde{c}}_2 \end{bmatrix}$

We can set this equal to the result of acting upon this wavefunction with the effective Hamiltonian:

Equation 4.27: $\tilde{H}|\tilde{\psi}\rangle = \hbar \begin{bmatrix} 0 + \dfrac{\Omega_0}{2}\tilde{c}_2 \\ \dfrac{\Omega_0}{2}\tilde{c}_1 - \delta\tilde{c}_2 \end{bmatrix}$

Setting Equation 4.26 and Equation 4.27 equal, we find

Equation 4.28: $\dot{\tilde{c}}_1 = -i\dfrac{\Omega_0}{2}\tilde{c}_2,\quad \dot{\tilde{c}}_2 = -i\dfrac{\Omega_0}{2}\tilde{c}_1 + i\delta\tilde{c}_2$

Taking the derivative of the $\dot{\tilde{c}}_1$ equation gives us

Equation 4.29:

$$\ddot{\tilde{c}}_1 = -i\frac{\Omega_0}{2}\dot{\tilde{c}}_2 = -i\frac{\Omega_0}{2}\left(-i\frac{\Omega_0}{2}\tilde{c}_1 + i\delta\tilde{c}_2\right) = -i\frac{\Omega_0}{2}\left(-i\frac{\Omega_0}{2}\tilde{c}_1 + i\delta\frac{2i}{\Omega_0}\dot{\tilde{c}}_1\right) = \left(-\frac{\Omega_0^2}{4}\tilde{c}_1 + i\delta\dot{\tilde{c}}_1\right)$$

This has the form of a simple harmonic oscillator equation, with the general solution:

Equation 4.30: $$\tilde{c}_1(t) = \frac{1}{\sqrt{2}}\left[Ae^{-i\Omega_A t} + Be^{i\Omega_B t}\right]$$

Below, we plug this into the equation and solve for the undetermined constants.

Equation 4.31:

$$-\frac{\Omega_0^2}{4}\tilde{c}_1(t) = -\frac{\Omega_0^2}{4\sqrt{2}}\left[Ae^{-i\Omega_A t} + Be^{i\Omega_B t}\right];\quad i\delta\dot{\tilde{c}}_1(t) = \frac{\delta}{\sqrt{2}}\left[\ \Omega_A Ae^{-i\Omega_A t} - \Omega_B Be^{i\Omega_B t}\right]$$
$$\ddot{\tilde{c}}_1(t) = \frac{1}{\sqrt{2}}\left[-\Omega_A^2 Ae^{-i\Omega_A t} - \Omega_B^2 Be^{i\Omega_B t}\right]$$
$$\rightarrow -\Omega_A^2 = \delta\,\Omega_A - \frac{\Omega_0^2}{4} \ \ \&\ \ -\Omega_B^2 = -\delta\,\Omega_B - \frac{\Omega_0^2}{4}$$

The result is

Equation 4.32: $$\Omega_A = \left(-\delta \pm \sqrt{\delta^2 + \Omega_0^2}\right)\Big/2,\ \ \Omega_B = \left(\delta \pm \sqrt{\delta^2 + \Omega_0^2}\right)\Big/2$$

If we plug these in and assume the atom is initially in the ground state so that

Equation 4.33: $$A(0) + B(0) = \sqrt{2},\ \ A(0) - B(0) = 0, \rightarrow A(0) = B(0) = 1/\sqrt{2}$$

We get the following time evolution for the system:

Equation 4.34: $$\tilde{c}_1(t) = \frac{1}{2}\left[e^{-i\left(-\delta \pm \sqrt{\delta^2+\Omega_0^2}\right)t/2} + e^{i\left(\delta \pm \sqrt{\delta^2+\Omega_0^2}\right)t/2}\right] = e^{i\delta t}\cos\left(\sqrt{\delta^2 + \Omega_0^2}\,t/2\right)$$

The excited state amplitude obeys the same equation (as we see by taking the derivative of the $\dot{\tilde{c}}_2$ expression in Equation 4.1):

Equation 4.35: $$\ddot{\tilde{c}}_2 = -i\frac{\Omega_0}{2}\left(-i\frac{\Omega_0}{2}\tilde{c}_2\right) + i\delta\dot{\tilde{c}}_2$$

The initial conditions tell us, then, that

Equation 4.36: $$\tilde{c}_2(t) = \frac{1}{2}\left[e^{-i\left(-\delta\pm\sqrt{\delta^2+\Omega_0^2}\right)t/2} - e^{i\left(\delta\pm\sqrt{\delta^2+\Omega_0^2}\right)t/2}\right] = i\,e^{i\delta t}\sin\left(\sqrt{\delta^2+\Omega_0^2}\,t/2\right)$$

Equation 4.34 and Equation 4.36 give the solution for the behavior of a two level system under resonant excitation in the absence of decay. They apply in a frame of reference that is said to "rotate with the field" [16] so that the Hamiltonian is time independent. We can recover the behavior in the non-rotating frame by solving Equation 4.25 for $|\psi\rangle$. Inverting the transformation gives us

Equation 4.37: $$|\psi\rangle = \hat{Q}^{-1}|\tilde{\psi}\rangle = \begin{bmatrix} \tilde{c}_1(t)e^{-i\omega_1 t} \\ \tilde{c}_2(t)e^{-i(\omega_1-\omega)t-i\phi} \end{bmatrix} = \begin{bmatrix} c_1(t) \\ c_2(t) \end{bmatrix}$$

We have solved the system. The phase of the ground and excited state coefficients oscillate rapidly, but the magnitude of those coefficients changes sinusoidally with a frequency $\sqrt{\delta^2+\Omega_0^2}/2$. This is known as the effective Rabi frequency. It is the rate at which the population of the ground state oscillates in the presence of a driving field.

This solution is, however, physically unrealistic for optical excitation. This model treats the field classically, and does not include the coupling of the atom to the vacuum fluctuations in the electromagnetic field which cause spontaneous decay in real atoms. The decay rate is proportional to the cube of the field energy difference between two states, and is on the scale of tens of nanoseconds for optically coupled transitions[17]. Strictly, the best way to include this effect is to quantize the field and analyze the system in a fully quantum, rather than semi-classical, way. However, it is possible to include the effect in our semi-classical calculations using an empirical "decay matrix," and that is the approach we will take here.

In order to include decay empirically, however, we need to re-write the problem in the density matrix formalism. This formalism is described in greater detail in reference 16.and 17. It allows us to consider the behavior of a statistical sample of atoms, rather than calculating the behavior of each individually, and to include random, spontaneous decay statistically. The density matrix is defined by

Equation 4.38: $$\hat{\rho} = \sum_m W_m \left|\psi_m\right\rangle\left\langle\psi_m\right|$$

The sum is over all atomic states populated by atoms in the sample, and the weight factor indicates what fraction of the atoms in the collection are in each state.

The diagonal elements of this matrix $\rho_{jj} = \sum_m W_m \left|c_j\right|^2$ represent the average populations of the energy levels. The off diagonal elements $\rho_{jk} = \sum_m W_m c_j c_k^*$ represent the average phase of superpositions of the two states labeled by the indices. Those off diagonal elements will be zero if all atoms in the collection are in an eigenstate, or if they are all in superpositions but all with different phases.

In this formalism, the equation of motion is written:

Equation 4.39: $$\dot{\hat{\rho}} = -\frac{i}{\hbar}\left[\hat{H}, \hat{\rho}\right] + \dot{\hat{\rho}}_{\text{decay}}$$

The first term is simply the Schrödinger equation restated in the new notation[16]. The second term is empirical, and accounts for the statistical nature of decay.

To solve this equation of motion it is useful to work again in the rotated frame, in which the Hamiltonian is time-independent. To find the density matrix in the rotated frame, we must simply performing the averaging over the $|\tilde{\psi}\rangle$ instead of $|\psi\rangle$ and we find

Equation 4.40:
$$\tilde{\rho} = \begin{pmatrix} \tilde{\rho}_{11} & \tilde{\rho}_{12} \\ \tilde{\rho}_{21} & \tilde{\rho}_{22} \end{pmatrix} = \sum_m W_m |\tilde{\psi}_m\rangle\langle\tilde{\psi}_m| = \hat{Q}\hat{\rho}\hat{Q}^{-1},\ \ where\ |\tilde{\psi}_m\rangle = \hat{Q}|\psi_m\rangle$$

So that

Equation 4.41:
$$\tilde{\rho}_{11} = \rho_{11},\ \ \tilde{\rho}_{12} = \rho_{12}e^{-i\omega t},\ \ \tilde{\rho}_{21} = \rho_{21}e^{i\omega t},\ \ \tilde{\rho}_{22} = \rho_{22}$$

It can be shown[16] that the equation of motion (the Optical Bloch Equation) is now

Equation 4.42:
$$\dot{\tilde{\rho}} = -\frac{i}{\hbar}\left[\tilde{H}, \tilde{\rho}\right] + \dot{\tilde{\rho}}_{\text{decay}}$$

The decay matrix is determined phenomenologically to be[16]:

Equation 4.43:
$$\dot{\tilde{\rho}}_{decay} = \begin{bmatrix} \Gamma\tilde{\rho}_{22} & -\frac{\Gamma}{2}\tilde{\rho}_{21} \\ -\frac{\Gamma}{2}\tilde{\rho}_{12} & -\Gamma\tilde{\rho}_{22} \end{bmatrix}$$

The presence of decay means the system now eventually settles into a steady state motion which does not depend on its initial condition. The system indeed resembles the damped, driven harmonic oscillator we used for our classical model, with the decay playing the role of the damping force. All motions which are not caused by the driving force will eventually be damped out. So the oscillation that we found at $\sqrt{\delta^2 + \Omega_0^2}/2$ represents only a transient behavior. These oscillations are damped by the interaction with vacuum fluctuations, and on a timescale determined by the inverse of Γ, the amplitude of the oscillations decays. The steady state is time dependent in that the motion of the electron follows that of the driving field, but it is time-independent in the rotating frame in which the field is constant.

The steady state is that which satisfies the condition:

Equation 4.44:
$$\dot{\tilde{\rho}} = -\frac{i}{\hbar}\left[\tilde{H},\tilde{\rho}\right] + \dot{\tilde{\rho}}_{\text{decay}} = 0$$

In general, it is more convenient to solve this numerically (or using a symbolic equation solver such as Wolfram's *Mathematica*) than by hand. The solution in this case is:

Equation 4.45:
$$\tilde{\rho}_{11} = 1 - \frac{\Omega^2}{2\Omega^2+\Gamma^2+4\delta^2}, \quad \tilde{\rho}_{12} = \frac{i(\Omega\Gamma - 2i\Omega\delta)}{2\Omega^2+\Gamma^2+4\delta^2},$$
$$\tilde{\rho}_{21} = \frac{-i(\Omega\Gamma + 2i\Omega\delta)}{2\Omega^2+\Gamma^2+4\delta^2}, \quad \tilde{\rho}_{22} = \frac{\Omega^2}{2\Omega^2+\Gamma^2+4\delta^2}$$

As we mentioned above, the off diagonal elements tell us about the average number of atoms in superposition states, and whether or not those superpositions are generally in phase. The relevance of this phase for dispersion calculations is well illustrated by the solutions to, for example, the infinite square well:

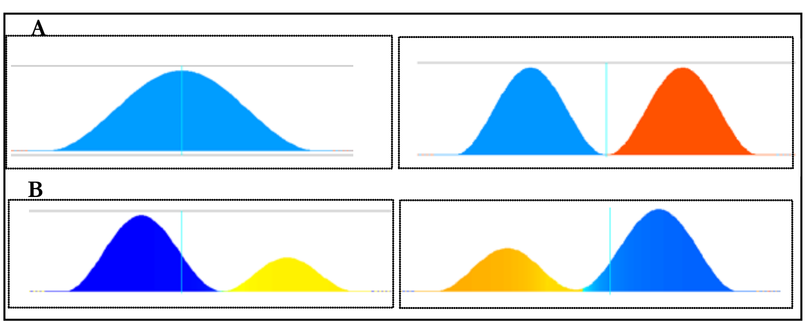

Figure 4.2: A) Probability distributions for particles in ground state and first excited state of infinite square well. B) Probability distributions for superpositions of ground and first excited states: two different phases.

The position of the electron, and thus the dipole moment of the atom, changes with the phase of the superpositions. Eigenstates of the unperturbed Hamiltonian are symmetric and thus atoms in these have zero dipole moment. If the sample includes atoms in superposition states, but the phase of the superposition states is random, the average dipole moment, which gives the polarization of the material, will again be zero.

If, on the other hand, the atoms, following the field, are all stretched into the same superposition state, these off diagonal components will not be zero, and their values will tell us about the phase difference between the motion of the atomic dipole and that of the field. Recall that the index of refraction is determined by the difference in phase between the field radiated by the atomic dipoles in the medium and the driving field. The phase of the radiated field is, in general, 90 degrees out of phase with the motion of the dipoles themselves[9].

To calculate the index of refraction and the absorption coefficient explicitly, we must make use of a theorem provable from the density matrix formalism:

Equation 4.46: $$\langle \hat{x} \rangle = Tr(\rho \hat{x}) = x_0(\rho_{21} + \rho_{12})$$

This applies to any operator, not the just the position operator. However, it is the average position of the electron with which we are primarily concerned. We have already seen, in the previous chapter, how knowing the average position of the electrons relative to their nuclei, and hence the average dipole moment, allows us to calculate the polarization response of the material, and how this response function can be plugged into the wave equation to allow us to calculate the index of refraction and the absorption coefficient.

We expect this value for the average position to be a real number with a sinusoidal time dependence, matching the time dependence of the driving field. However, because it will be out of phase with the driving field, we cannot express this number as a scalar multiple of the driving field unless we use phasor notation. We "complexify" x by dropping the complex conjugate, so that:

Equation 4.47: $\langle \hat{x} \rangle_C = x_0(\rho_{21})$

The phase of this complex number tells us the relative phase between the motion of the field and that of the electron.

The dipole moment of an individual atom in the rotating frame is then $ex_0\tilde{\rho}_{21}$. If this is simply a positive scalar multiple of i (keeping in mind that e, the charge on the electron, is negative), it means the phasor is of the form $|ex_0\rho_{21}|Exp[i\pi/2]$, and the dipole motion is $\pi/2$ radians (90 degrees) out of phase with the driving field. The radiated field is thus 180 degrees out of phase with the driving field. That this is the case when $\delta = 0$ can be seen from Equation 4.45. On resonance, then, the radiated field adds destructively with the driving field. This shows qualitatively that an imaginary $ex_0\tilde{\rho}_{21}$ is associated with absorption. If $ex_0\tilde{\rho}_{21}$ were proportional to $-i$, the radiated field would then add in phase with the driving field, and the result would be gain, which is mathematically equivalent to negative absorption. If $ex_0\tilde{\rho}_{21}$ is real, then the dipole motion will itself be in phase with the driving field, meaning the radiated field is 90 degrees out of phase with it. The net field produced lags behind the original driving field by an amount that depends on the relative strengths of the original field and the reradiated field. This shows qualitatively that the real part of $\tilde{\rho}_{21}$ is associated with index of refraction.

To demonstrate these effects mathematically, we need only calculate the polarization:

Equation 4.48: $$P_C = Np_C = Ne\langle x\rangle_C = Nex_0(\rho_{21}) = \varepsilon_0\chi E_C \quad where\, E_C = E_0 e^{i\omega t}$$

The subscript "C" is intended to indicate that these are complex phasors and not real quantities. (In the previous chapter we used a tilde for this purpose, however since we have used that same notation already in this chapter to indicate quantities which are expressed in the rotating frame, we must change our convention slightly.) The real quantities are given by the sum of the phasor with its complex conjugate.

We have already determined ρ_{21}, so Equation 4.48 allows us to calculate the average dipole moment of the ensemble, which tells us the polarization and thus, according to Equation 3.9 the susceptibility of the medium:

Equation 4.49: $$\chi = \frac{Nex_0(\rho_{12})}{\varepsilon_0 E_C} \quad where\, E_C = E_0 e^{i\omega t}$$

From this point on, the calculation of the index is exactly the same as it was in the classical case. The expressions (Equation 3.17 and Equation 3.21) which we derived in the previous chapter relating the index and absorption to the polarization were general, and they apply here as well. Therefore, we conclude that:

Equation 4.50: $$n = \frac{c}{v_p} = \frac{c\kappa_R}{\omega} = \mathrm{Re}\left[\sqrt{(1+\chi)}\right] = \mathrm{Re}\left[\sqrt{1+\frac{Nex_0(\rho_{21})}{\varepsilon_0 E_C}}\right]$$

Therefore:

Equation 4.51: $n \approx 1 + \frac{1}{2} \frac{Nex_0 \operatorname{Re}\left[\frac{-i(\Omega\Gamma + 2i\Omega\delta)}{2\Omega^2 + \Gamma^2 + 4\delta^2}\right]}{\varepsilon_0 E_C}$

We need only specify our driving field strength and frequency (which determine $\Omega, E_C, and\ \delta$) and the decay rate and resonant frequency of our atomic energy levels in order to completely determine the index for a two level system.

Similarly, the absorption is given by:

Equation 4.52: $\alpha_L = -2\kappa_I = -2\operatorname{Im}\left[\omega\sqrt{\mu_0\varepsilon_0(1+\chi)}\right] = -2\operatorname{Im}\left[\omega\sqrt{\mu_0\varepsilon_0\left(1+\frac{Nex_0(\rho_{21})}{\varepsilon_0 E_C}\right)}\right]$

Therefore:

Equation 4.53: $\alpha_L \approx -2\omega\sqrt{\mu_0\varepsilon_0}\left(1+\frac{1}{2}\operatorname{Im}\left[\frac{Nex_0\left(\frac{-i(\Omega\Gamma+2i\Omega\delta)}{2\Omega^2+\Gamma^2+4\delta^2}\right)}{\varepsilon_0 E_C}\right]\right)$

Plotting the expression for the index gives us:

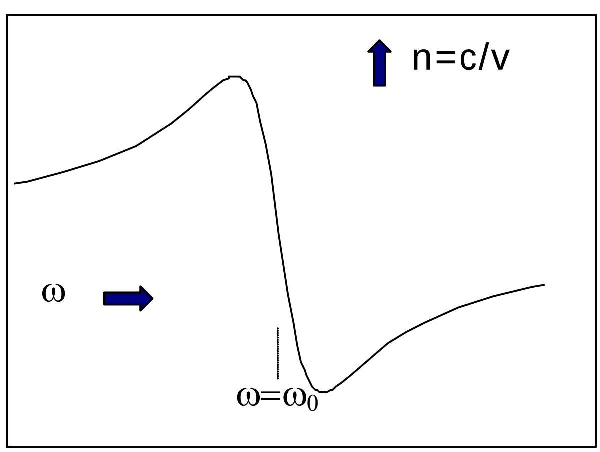

Figure 4.3: Lineshape of index of refraction vs. frequency derived using two-level quantum mechanical model.

For the absorption coefficient, we get:

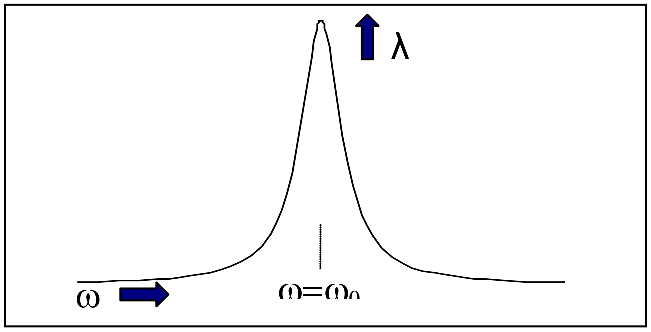

Figure 4.4: Lineshape of absorption vs. frequency derived using two-level quantum mechanical model.

These lineshapes clearly agree with the results derived using the classical model. This is the same approach we will now use (with less derivation) to model the behavior of three level systems.

Three Level Systems

We now turn our attention to a specific type of three level system. The lower two levels must be long-lived, and must not couple optically to one another. Under these conditions, both can be considered ground states, in the sense that they are both stable, low energy states into which the atom can decay, though one is of course lower in energy than the other. These systems are known as “Lambda” systems for the way their energy level diagrams are conventionally drawn, illustrated below in Figure 4.5. A more detailed description of the behavior of these systems, including a fully quantized model, can be found in Reference 18.

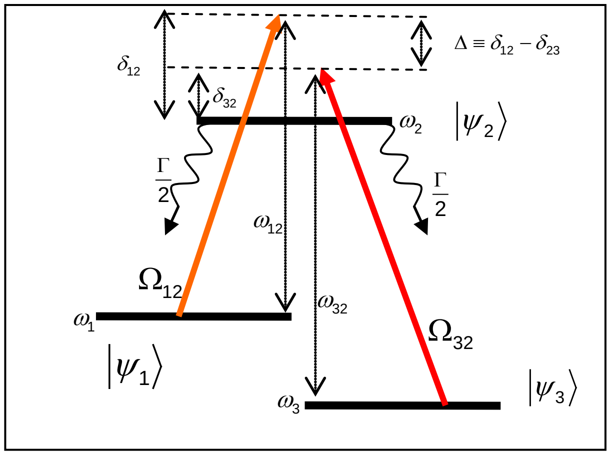

Figure 4.5: Energy level diagram for a Lambda System.

In this system, some purely quantum mechanical effects become possible. For instance, it is possible for the system to be in a superposition of the ground states such that transition amplitudes from the two lower states are equal in magnitude and opposite in sign, and the total transition probability to the upper state is zero. The result is that the atom does not absorb at either frequency under this condition, even if both beams are on resonance.

The condition for this is:

Equation 4.54: $$\dot{c}_2(t) \propto \langle \psi_2 | \hat{H} | \psi \rangle = \langle \psi_2 | \hat{H}(t) \left(c_1 | \psi_1 \rangle + c_3 | \psi_3 \rangle \right) = 0$$

Note that the $|\psi_1\rangle$ state has an $e^{-i\omega_1 t}$ time dependence and the $|\psi_3\rangle$ state, $e^{-i\omega_3 t}$, so that the time dependence of the first term in this equation is $e^{i(\omega_2-\omega_1)t-i\omega_{12}t}$ and of the second, $e^{i(\omega_2-\omega_3)t-i\omega_{32}t}$. If we want these to cancel for all time, the detunings have to match $\delta_{12} = \delta_{32} \rightarrow \Delta = 0$.

Since $|\psi_1\rangle$ and $|\psi_3\rangle$ are eigenstates of the unperturbed atom, however, and not of the atom + field system, the atom cannot simply remain in either one. What happens instead is known as "coherent population transfer" (CPT). The atom passes back and forth among superposition states of $|\psi_1\rangle$ and $|\psi_3\rangle$ (with a small, constant component in $|\psi_2\rangle$) for which $\dot{c}_2 = 0$ always. In this way the population can be transferred from one metastable state to another without absorption or spontaneous emission. The process requires the presence of two beams with equal detunings. Transitions of this kind between metastable states are known as "two photon transitions" or "Raman transitions." The drop in the absorption that results when the detunings are matched is known as "electromagnetically induced transparency" (EIT.) We will see that a superposition of the ground states achieved through this CPT process is in fact the steady state for a three level system under this kind of excitation. If the system is first optically pumped and if the average detuning $\left(\delta_{12} + \delta_{32}\right)/2$ is larger than the normal absorption linewidth for either transition, then this process can result in gain rather than just transparency, a phenomenon known as "Raman gain."

To model this behavior mathematically, we first describe the two fields:

Equation 4.55: $E_{12} = \hat{\varepsilon}_{12} E_{012} \cos(k_a z - \omega_a t + \phi_a)$ and $E_{32} = \hat{\varepsilon}_{32} E_{032} \cos(k_b z - \omega_b t + \phi_b)$

The Hamiltonian should consist of the atomic energy terms and a dipole interaction term $H_1 = \hat{\vec{p}} \cdot \hat{\vec{E}}$:

Equation 4.56:

$$\hat{H}_0 + \hat{H}_1 = \hbar \begin{pmatrix} \omega_1 & \Omega_{12}\cos(k_{12}z - \omega_{12}t + \phi_{12}) & 0 \\ \Omega_{12}\cos(k_{12}z - \omega_{12}t + \phi_{12}) & \omega_2 & \Omega_{32}\cos(k_{32}z - \omega_{32}t + \phi_{32}) \\ 0 & \Omega_{32}\cos(k_{32}z - \omega_{32}t + \phi_{32}) & \omega_3 \end{pmatrix}$$

Where

Equation 4.57: $$\Omega_{12} = \frac{d_{12}E_{012}}{\hbar},\ \Omega_{32} = \frac{d_{32}E_{032}}{\hbar},\ \delta_{12} = \omega_{12} - (\omega_2 - \omega_1),\ \delta_{32} = \omega_{32} - (\omega_2 - \omega_3)$$

We again assume that the wavelength is longer than the length scale of the electron wavefunction, make the rotating wave approximation, and perform the rotating wave transformation using the Q-matrix , summarized in the box below for convenience.

$$\begin{aligned}
&\frac{d}{dt}(\hat{Q}|\Psi\rangle) = \dot{\hat{Q}}|\Psi\rangle + \hat{Q}|\dot{\Psi}\rangle \\
&\hat{Q}|\dot{\Psi}\rangle = \frac{-i}{\hbar}\hat{Q}\hat{H}|\Psi\rangle \ \ (\textit{schrödinger equation}) \\
&= \frac{d}{dt}(\hat{Q}|\Psi\rangle) - \dot{\hat{Q}}|\Psi\rangle = \frac{-i}{\hbar}\hat{Q}\hat{H}\hat{Q}^{-1}\hat{Q}|\Psi\rangle \\
&\textit{define } |\tilde{\Psi}\rangle = \hat{Q}|\Psi\rangle \quad \textit{and} \quad \hat{H}' = \hat{Q}\hat{H}\hat{Q}^{-1} \\
&\textit{then } \frac{d}{dt}|\tilde{\Psi}\rangle = \frac{-i}{\hbar}\hat{H}'|\tilde{\Psi}\rangle + i\hat{M}|\tilde{\Psi}\rangle = \frac{-i}{\hbar}(\hat{H}' - \hbar\hat{M}) \\
&\textit{define } \hat{\hat{H}} = \hat{H}' - \hbar\hat{M} \\
&\textit{then } \frac{d}{dt}|\tilde{\Psi}\rangle = \frac{-i}{\hbar}\hat{\hat{H}}|\tilde{\Psi}\rangle
\end{aligned}$$

Figure 4.6: Boxed summary of rotating wave transformation for general wavefunction

In this case, we define:

Equation 4.58: $$\hat{Q} = \begin{bmatrix} e^{i\theta_1 t} & 0 & 0 \\ 0 & e^{i\theta_2 t} & 0 \\ 0 & 0 & e^{i\theta_3 t} \end{bmatrix}, \textit{where } \theta_1 = \omega_1,\ \theta_2 = \omega_{12} + \omega_1,\ \theta_3 = (\omega_{12} - \omega_{32}) + \omega_1$$

Our effective time independent Hamiltonian then becomes:

Equation 4.59: $$\tilde{H} = \begin{pmatrix} 0 & \frac{\Omega_{12}}{2} & 0 \\ \frac{\Omega_{12}}{2} & -\delta_{12} & \frac{\Omega_{32}}{2} \\ 0 & \frac{\Omega_{32}}{2} & -\Delta \end{pmatrix}$$

Since, for purposes of finding the refractive index, we are more interested in the steady-state behavior than the transient behavior of such a system, we now proceed directly to the density matrix calculation.

Equation 4.60: $$\dot{\tilde{\rho}} = \frac{-i}{\hbar}\left[\tilde{H}, \tilde{\rho}\right] + \dot{\tilde{\rho}}_{decay} = 0$$

Where

Equation 4.61: $$\tilde{\rho} = \begin{pmatrix} \tilde{\rho}_{11} & \tilde{\rho}_{12} & \tilde{\rho}_{13} \\ \tilde{\rho}_{21} & \tilde{\rho}_{22} & \tilde{\rho}_{23} \\ \tilde{\rho}_{31} & \tilde{\rho}_{32} & \tilde{\rho}_{22} \end{pmatrix} = \sum_m W_m \left|\tilde{\psi}_m\right\rangle\left\langle\tilde{\psi}_m\right| = \hat{Q}\hat{\rho}\hat{Q}^{-1},\ with \left|\tilde{\psi}_m\right\rangle = \hat{Q}\left|\psi_m\right\rangle$$

And we need the empirical decay matrix:

Equation 4.62: $$\dot{\tilde{\rho}}_{decay} = \begin{pmatrix} \frac{\Gamma}{2}\tilde{\rho}_{22} & -\frac{\Gamma}{2}\tilde{\rho}_{12} & 0 \\ -\frac{\Gamma}{2}\tilde{\rho}_{21} & -\Gamma\tilde{\rho}_{22} & -\frac{\Gamma}{2}\tilde{\rho}_{23} \\ 0 & -\frac{\Gamma}{2}\tilde{\rho}_{32} & \frac{\Gamma}{2}\tilde{\rho}_{22} \end{pmatrix}$$

We can now solve for all nine matrix elements of $\tilde{\rho}$ in steady state. The index of refraction for the beam at ω_{12} depends in particular on $\tilde{\rho}_{21}$, which is given by

Equation 4.63:

$$\rho_{21} = \frac{2\delta_{12}\Omega_{12}\Omega_{32}^2 - 2i\Gamma\delta_{12}\left(4\delta_{12}^2 - \Omega_{12}^2 - \Omega_{32}^2\right)}{\Omega_{12}^6 + 3\Omega_{12}^4\Omega_{32}^2 + 4\Gamma^2\delta_{12}^2\left(\Omega_{12}^2 + \Omega_{32}^2\right) + \left(-4\delta_{12}^2\Omega_{32} + \Omega_{32}^3\right)^2 + \Omega_{12}^2\left(16\delta_{12}^2\Omega_{32}^2 + 3\Omega_{32}\right.}$$

Plugging this into Equation 4.50 and Equation 4.52 gives us an explicit expression for the index and the absorption as functions of the frequency of the beam driving the $|\psi_1\rangle \, to \, |\psi_2\rangle$ transition. We plot the lineshape for the index expression (with most scale factors set to one) below:

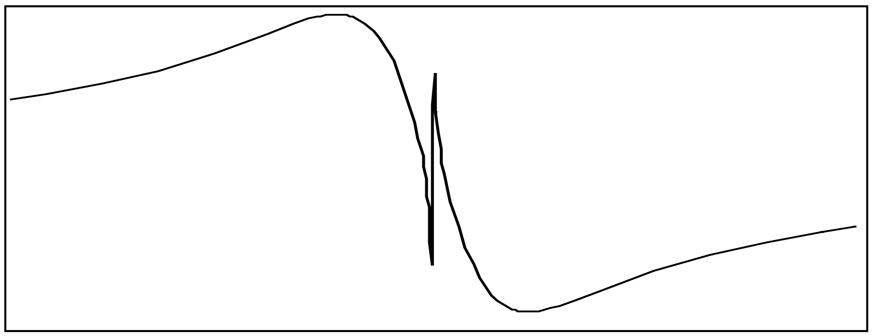

Figure 4.7: Lineshape of index of refraction vs. frequency for three level system with electromagnetically induced transparency.

For the absorption:

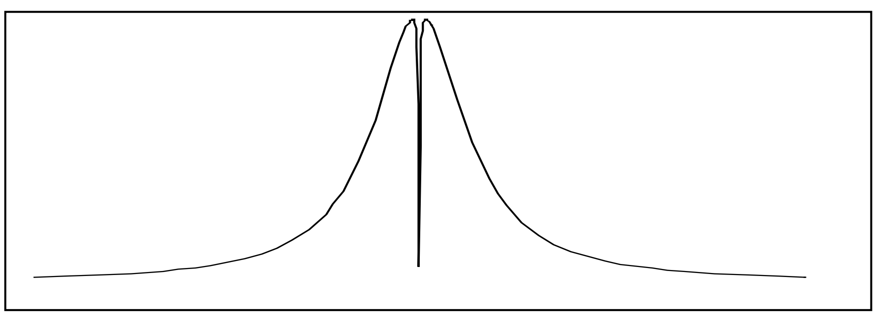

Figure 4.8: Lineshape of absorption coefficient vs. frequency for three level system with electromagnetically induced transparency.

In these plots we have set $\Omega_{32} = \Omega_{12} = 0.1, \; \Gamma = 1, \delta_{32} = 0$, and plotted the expressions as functions of δ_{12}. We see that, as expected, the index looks like the derivative of the absorption.

Using this technique, driving two-photon transitions in a three level Lambda system to create electromagnetically induced transparency, we have created a dispersion profile with steep positive slope, in a narrow spectral region over which the medium is transparent. The width of this region depends on the relative field strengths of the two beams and the decay rate. Pulses made up of frequency components within this linewidth will propagate at speeds much, much less than the free space speed of light, since the group index $n_g = 1 + \omega\left(dn/d\omega\right)$ is so large due to the steep slope of the index. This, then, is a slow light medium. We have achieved this condition experimentally in both sodium and rubidium vapor, as we will discuss later in the experimental results section.

There is, in some situations, a simpler way of handling this system mathematically. In Raman Gain, unlike EIT, we choose the average detuning of the two beams, δ_0, to be large, much larger than the linewidth of the excited state. This allows us to assume the population of the excited state is small, and to ignore any excited state decay processes. When the idea is to get gain, we want to minimize any residual absorption.

We further assume that the atoms have been optically pumped into one of the two metastable states. Ordinarily the populations of these two states are comparable, since they have almost equally long lifetimes and thermally (or otherwise) excited atoms can decay into both. However, if the atoms interact with an "optical pumping beam" which strongly couples one of these states to the excited state, then atoms which decay into that state will quickly transition back to the excited state, while atoms which decay into the other metastable state will stay there. The net result is that after a characteristic pumping time which depends on the strength and detuning of the pumping beam and on the decay rate of the excited state, the population of the state on which the pumping beam acts approaches zero while the state on which it does not approaches one. In the following analysis, we assume that the atoms interact first with the optical pumping beam and then with the Raman beams. Experimentally, the two beams are generally spatially separated, and the gain comes from atoms whose velocities take them through the optical pumping beam first and then into the Raman fields. Under these conditions, the behavior of the system is simpler.

For convenience, in this approach, we take the zero point of the energy of the system to be the same as the energy of the upper state. We will also name the upper state the $|\psi_0\rangle$ state rather than the $|\psi_2\rangle$ state as before ($|\psi_2\rangle$ will now designate the higher of the two ground states.). In this basis, then, we have

Equation 4.64:

$$\hat{H} = \hat{H}_0 + \hat{H}_1 = -\hbar\begin{bmatrix} 0 & 0 & 0 \\ 0 & \omega_1 & 0 \\ 0 & 0 & \omega_2 \end{bmatrix} - \hbar\begin{bmatrix} 0 & \Omega_{10}\left(e^{-i\omega_{10}t} + c.c\right) & 0 \\ \Omega_{10}\left(e^{i\omega_{10}t} + c.c\right) & 0 & \Omega_{20}\left(e^{-i\omega_{20}t} + c.c\right) \\ 0 & \Omega_{20}\left(e^{i\omega_{20}t} + c.c\right) & 0 \end{bmatrix}$$

and

Equation 4.65: $|\psi(t)\rangle = c_0(t)|\psi_0\rangle + c_1(t)|\psi_1\rangle + c_2(t)|\psi_2\rangle$ (where $|\psi_m\rangle$ has time dependence $e^{\omega_m t}$)

The amplitude of the excited state is then:

Equation 4.66: $\dot{c}_0(t) = i\Omega_{10}e^{-i\delta_1 t}c_1 + i\Omega_{20}e^{-i\delta_2 t}c_2 \;\; where\, \delta_j = \omega_{j0} - \omega_j$

We assume the population is all optically pumped into the lower ground state $|\psi_1\rangle$. Under that condition, we can integrate Equation 4.66 to get

Equation 4.67: $c_0(t) \approx -\frac{\Omega_{10}}{\delta_0} e^{-i\delta_1 t} c_1 \ where\, \delta_0 = (\delta_1 + \delta_2 / 2),\ \Delta = \delta_1 - \delta_2,\ and\ \delta_0 >> \Delta$

We have ignored decay from the excited state. We do, however, have to include transit time broadening effects, since they will be the dominant factor in determining the linewidth of the Raman gain. This must be found empirically and included by hand in our calculations.

For this reason, we write the equation of motion for the $|\psi_2\rangle$ state as

Equation 4.68: $\dot{c}_2(t) = -i\frac{\Omega_{10}\Omega_{12}^*}{\delta_0} e^{-i(\delta_1-\delta_2)t} c_1 - \Gamma c_2$

(where Γ is a phenomenological linewidth.)

We can solve Equation 4.68 to get

Equation 4.69: $c_2(t) = \left(\frac{\Omega_{10}\Omega_{20}^*}{\delta_0}\right)\frac{1}{(\delta_1 - \delta_2) + i\Gamma} e^{-i(\delta_1-\delta_2)t} c_1$

We can now calculate the density matrix element ρ_{02} directly from Equation 4.69 and Equation 4.67. We then recall that

Equation 4.70: $P = Nex_0\rho_{20} = \chi\varepsilon_0 E_{20}$

To obtain:

Equation 4.71: $\chi = -N\frac{|ex_0|^2}{2\hbar\varepsilon_0}\frac{|\Omega_{10}|^2}{\delta_0^2}\frac{1}{(\delta_1 - \delta_2) - i\Gamma} = \frac{M}{\nu\text{-}\nu_0 + i\gamma}, where\ \gamma = \frac{\Gamma}{2\pi}$

In a hot atomic gas we must also include Doppler broadening effects, but this calculation is sufficient to give us the shape of the dispersion. We plot the resulting index of refraction lineshape below:

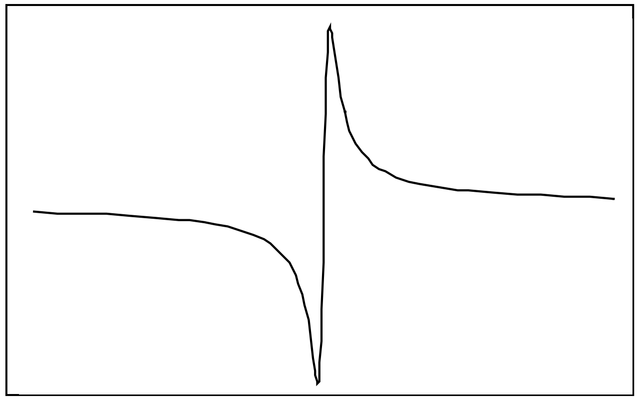

Figure 4.9: Index of refraction for a Raman gain feature

For the absorption, we get:

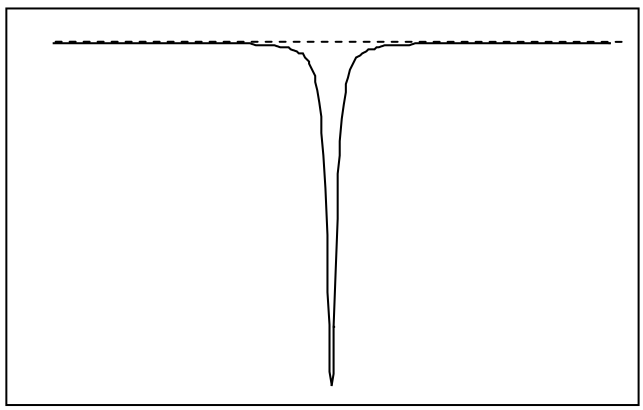

Figure 4.10: Absorption for a single Raman gain feature.
The absorption is less than zero because gain is negative absorption.

Note that the slope of the index profile is positive in the center. Raman gain, like EIT, creates a slow light medium. Ultimately this is because a gain feature has the same shape as a reduction in the absorption. Unlike the EIT dip, though, the amount of Raman gain is controllable. Greater optical pumping will lead to a larger amount of gain (and a deeper valley in the absorption profile) without affecting the linewidth. So the group velocity of this slow light medium is tunable, and pulses will be amplified rather than attenuated.

This result is useful in itself, but perhaps even more useful is the fact that Raman gain features can be combined.

We have followed the derivation in Reference 19 in deriving this result for the susceptibility of a three level medium under Raman gain. The experiment described there uses two beams, both of which are near resonant on the $|\psi_1\rangle \text{ to } |\psi_0\rangle$, transition, having frequencies $v_0 + \Delta$ and $v_0 - \Delta$. Our later experimental results will also use this configuration.

In this case, the total susceptibility is the sum of that due to each individual beam, so that

Equation 4.72: $$\chi(\nu) = \frac{M}{\nu\text{-}\nu_0 + \Delta\nu + i\gamma} + \frac{M}{\nu\text{-}\nu_0 - \Delta\nu + i\gamma}, \textit{where } \gamma = \frac{\Gamma}{2\pi}$$

The lineshape for the index is now:

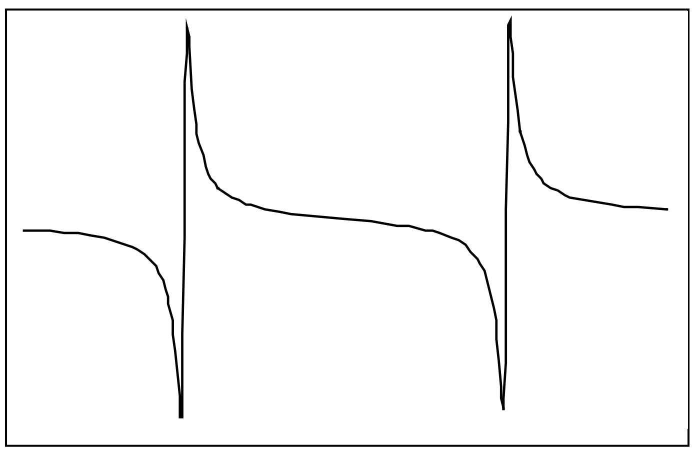

Figure 4.11: Index profile for a double Raman Gain feature. Note anomalous dispersion at center of profile.

The corresponding absorption lineshape is:

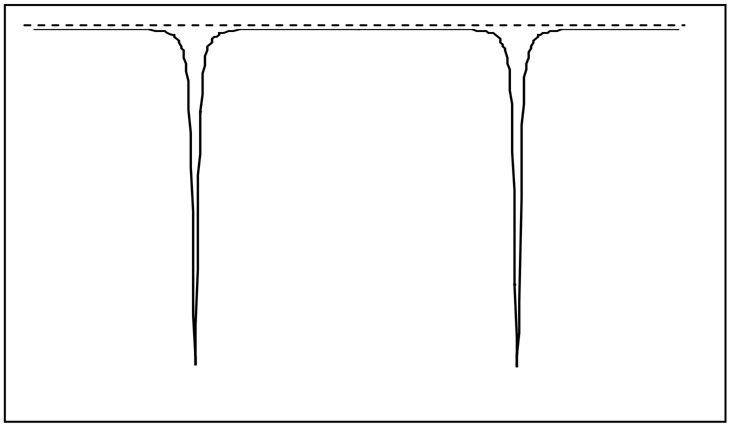

Figure 4.12: Absorption for a double Raman gain feature.
Note that gain is negative absorption.

Two things are noteworthy about this profile. The first is that the dispersion is anomalous (the slope of the index is negative) at the center of the profile. This is important because in nature this kind of dispersion generally occurs at frequencies at which the material is absorbing, as in the two-level profile. The second is that the dispersion is controllable. By changing the frequencies of the beams coupling the other leg of the Lambda system (which we will call the "Raman pumps") we can control the separation of those gain features. And by changing the amount of optical pumping, we can control their amplitude.

The transparency allows us to introduce this kind of medium into a cavity without introducing undue losses. (It also allows pulses to propagate through this kind of medium without significant attenuation.) The controllable slope allows us to fine tune the resonance properties of cavities (or the propagation velocity of pulses) which are interacting with this medium. In short, it is a tunable, low-loss fast-light material, and for that reason has many uses.

The experimental results section of this thesis includes experimentally measured dispersion profile of this type, with different pump frequencies and optical pumping levels. We will refer back to these theoretical results in the discussion of those experiments.

This chapter is not by any means exhaustive. Many other types of slow and fast light material exist besides those described here. These are theoretical descriptions of processes that take place in atomic gasses. However, gain, loss, and dispersion also occur in crystals and glasses, through processes such as photorefractive coupling and Brillouin scattering.

Though these are different physical processes, requiring different models to accurately describe, nevertheless they obey the same general principles. A gain feature or a reduction in absorption always leads to normal dispersion and slow light. An absorption, or a reduction in gain, or the region between two gain features, is always associated with anomalous dispersion, which will give rise to fast light if the group index is between zero and one. This is a consequence of the Kramers-Kronig relations described in the classical dispersion chapter, borne out by all of the classical and quantum mechanical models we have developed so far. Though other fast and slow light media exist, those we have described here share most of their important features.

CHAPTER 5 - INTERFEROMETRIC GYROSCOPES

We have seen how the resonance frequency of a cavity depends on its length. The relevant expression from the Cavity Review chapter is:

Equation 5.1: $$\omega_{res}[m] = \frac{2\pi c}{\lambda_{res}} = \frac{2\pi mc}{L} \quad m = integer$$

This relationship is the principle on which optical gyroscopes work. A rotation produces a change in the effective length of a ring cavity, and the resonant frequency of the cavity changes. In a passive cavity based gyroscope, that change in resonant frequency is measured through the change in transmission, or the frequency shift required to restore transmission of the input beam to on-resonance levels. In a ring laser based gyroscope, the laser output frequency can be measured very accurately, and the rotation is sensed as a change in this output frequency.

In this chapter we describe the relationship between rotation rate and effective cavity length, known as the Sagnac effect.

The simplest way to think about the effective length change of a cavity due to rotation is to imagine a circular cavity. This is achievable in practice with optical fibers or other waveguides, but it also serves as a good model for the behavior of cavities built of bulk optics and shaped like squares or triangles. Those polygon-shaped cavities can be analyzed with a path-integral approach. Though the path of light in a rotating polygonal cavity departs from the circle, the effects of these departures in general cancel out, and the phase the light picks up due to the rotation is the same as if it had traveled a circular path [20].

Therefore we will consider light traveling along a circular path.

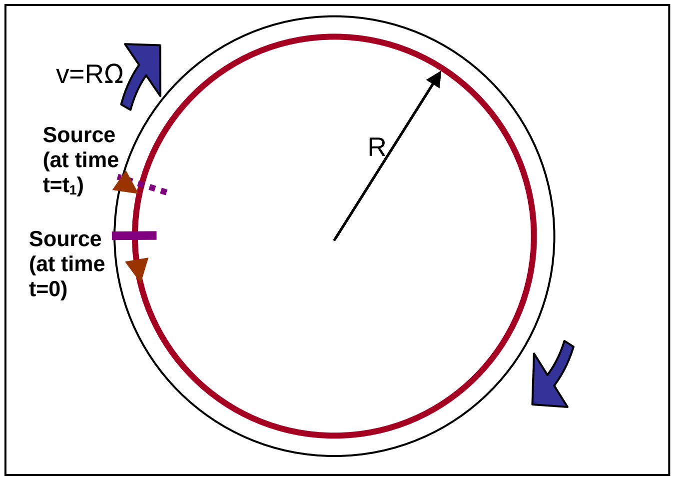

Figure 5.1: Circular cavity for optical gyroscope

Consider a phase front which leaves the source and travels around the cavity in the same direction as the cavity rotation. We might expect that, by the time it returns to the position of the source (and interferes with the light the source is still emitting) the source will have moved, making the effective path length for this phase front longer. By contrast, light traveling the direction opposite the rotation will encounter the source after traveling a shorter distance than in the stationary cavity.

This intuitive picture, however, fails to take into account the effect of the moving source on the velocity of the phase front it emits. If one imagines starting from a certain point on a carousel and walking around the edge of the carousel back to the starting point, it is easy to understand that within the rotating frame, the distance, and the travel time, is the same in either direction. An observer in the non-rotating frame would indeed say that the distances were different, but that observer would also measure the velocity of the person walking in the same direction as the rotation to be larger than that of the person walking in the direction opposing the rotation. The result would be that the person in the non-rotating frame would agree with the person in the rotating frame that the travel times were the same.

This kind of naïve, non-relativistic calculation cannot, for this reason, describe optical gyroscopes. Without relativity, there is no Sagnac effect. Light traveling in both directions would pick up the same phase, due to the difference in velocities.

In a relativistic calculation, on the other hand, the rotating and non-rotating observer may disagree on whether it takes the same amount of time to go clockwise as counter-clockwise around the carousel, but must agree on the speed of light. Clearly these are relevant distinctions for the case of the optical gyroscope.

Let us consider the problem again, this time using relativistic addition of velocities. Two phase fronts leave the source, traveling in opposite directions. According the special relativity, their velocities are given by:

Equation 5.2: $V_R^{\pm} = \dfrac{V_P \pm v}{1 \pm V_p v / c^2}$

Here the "plus" velocity belongs to the co-rotating beam, and the "minus" velocity to the counter rotating beam, $v = R\Omega$ is the velocity of the source, and V_p is the phase velocity of the light in the rotating frame. (We note, as we begin, that this analysis actually applies to any kind of wave, not just light. For instance, this same approach describes gyroscopes based on the interference of atomic wavefunctions, which we will discuss briefly in the context of the results of this calculation.)

The distance each phase front must travel before reaching the source is given by:

Equation 5.3: $L^{\pm} = 2\pi R \pm vT^{\pm}$

The time that this journey takes is thus:

Equation 5.4: $T^{\pm} = \dfrac{L^{\pm}}{V_R^{\pm}} = \dfrac{2\pi R \pm vT^{\pm}}{V_R^{\pm}}$

We can solve Equation 5.4 for $T^{\pm}$:

Equation 5.5: $T^{\pm} \mp \dfrac{vT^{\pm}}{V_R^{\pm}} = \dfrac{2\pi R}{V_R^{\pm}} \Rightarrow T^{\pm} = \dfrac{2\pi R}{V_R^{\pm} \mp v}$

Or for $L^{\pm}$:

Equation 5.6: $L^{\pm} = 2\pi R \pm v\left(L_{\pm}/V_R^{\pm}\right) \Rightarrow L^{\pm} = \dfrac{2\pi R}{\left(1 \mp v/V_R^{\pm}\right)}$

We can use this to calculate the difference in the effective cavity lengths for the co- and counter-propagating beams. We include a few intermediate steps of that calculation below:

Equation 5.7: $L^{+} - L^{-} = 2\pi R\left(\dfrac{1}{\left(1 - v/V_R^{+}\right)} - \dfrac{1}{\left(1 + v/V_R^{-}\right)}\right)$

Equation 5.8: $\Rightarrow L^{+} - L^{-} = 2\pi Rv\left(\dfrac{1/V_R^{-} + 1/V_R^{+}}{\left(1 - v/V_R^{+}\right)\left(1 + v/V_R^{-}\right)}\right)$

Equation 5.9: $1/V_R^{-} + 1/V_R^{+} = \dfrac{\left(1 - V_p v/c^2\right)\left(V_p + v\right) + \left(1 + V_p v/c^2\right)\left(V_p - v\right)}{\left(V_p - v\right)\left(V_p + v\right)}$

Equation 5.10: $\Rightarrow 1/V_R^{-} + 1/V_R^{+} = \dfrac{2V_p\left(1 - v^2/c_0^2\right)}{V_p^2 - v^2}$

Equation 5.11: $\left(1 - v/V_R^{+}\right)\left(1 + v/V_R^{-}\right) = \left(1 - \dfrac{v\left(1 + V_p v/c^2\right)}{V_p + v}\right)\left(1 + \dfrac{v\left(1 - V_p v/c^2\right)}{V_p - v}\right)$

Equation 5.12:

$$\Rightarrow \left(1 - v/V_R^{+}\right)\left(1 + v/V_R^{-}\right) = \left(\frac{V_p + v - v\left(1 + V_p v/c^2\right)}{V_p + v}\right)\left(\frac{V_p - v + v\left(1 - V_p v/c^2\right)}{V_p - v}\right)$$

Equation 5.13: $$\Rightarrow \left(1 - v/V_R^+\right)\left(1 + v/V_R^-\right) = \frac{V_p^2\left(1 - v^2/c^2\right)^2}{V_p^2 - v^2}$$

Equation 5.14: $$\Rightarrow\ L^+ - L^- = 2\pi Rv \frac{\dfrac{2V_p \cancel{\left(1 - v^2/c^2\right)}}{\cancel{V_p^2 - v^2}}}{\dfrac{V_p^2 \cancel{\left(1 - v^2/c^2\right)^2}}{\cancel{V_p^2 - v^2}}} \Rightarrow\ L^+ - L^- = \frac{4\pi Rv}{V_p} = \frac{4\pi R^2\, v/R}{V_p}$$

Equation 5.15: $$L^+ - L^- = \frac{4A\Omega}{V_p} \quad \text{where} \quad A = area\ of\ ring\ cavity,\ \Omega = rotation\ rate$$

We have thus verified that there is a real difference in lengths in the relativistic case, and that it is proportional to the rotation rate. This difference can be measured with a Sagnac interferometer, as illustrated in Figure 5.2.

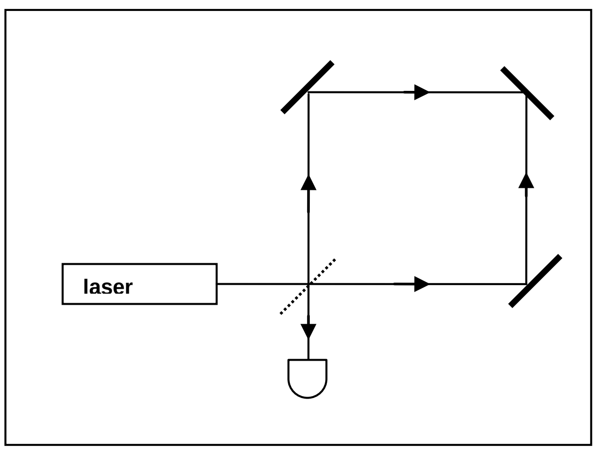

Figure 5.2: Sagnac Interferometer

The phase difference between the beam which has traveled clockwise and that which has traveled counterclockwise around the interferometer is

Equation 5.16: $$k\Delta L = \frac{4\pi}{\lambda}\frac{2A\Omega}{V_p}\ where\ A = area\ of\ interferomer$$

Such an interferometer is itself a type of gyroscope, because it is designed to sense phase differences which depend on rotation rate.

We note that there is a difference between the temporal phases of the co- and counter-propagating beams as well, but that this, unlike the spatial phase difference, does not depend on the phase velocity. This is because unlike the wavelength, the frequency of a wave is independent of its phase velocity.

Equation 5.17:

$$\Delta t_o = T^+ - T^- = 2\pi R\left[\frac{\left(V_R^- - V_R^+\right) + 2v}{\left(V_R^+ - v\right)\left(V_R^- + v\right)}\right] = 2\pi R\left[\frac{\dfrac{2v\left(V_p^2/c^2 - 1\right)}{1-\left(V_p v/c^2\right)^2} + 2v}{\dfrac{V_p^2\left(1-v^2/c^2\right)^2}{1-\left(V_p v/c^2\right)^2}}\right] = 2\pi R\left[\frac{2v\left(V_p^2/c^2 - \left(V_p v/c^2\right)^2\right)}{V_p^2\left(1-v^2/c^2\right)^2}\right]$$

Therefore:

Equation 5.18:

$$\omega\Delta t_0 = 2\pi R\,\omega\frac{2v}{c^2}\left[\frac{1}{\left(1-v^2/c^2\right)}\right] = 4\pi R^2\, v/R\frac{\omega}{c^2}\left[\frac{1}{\left(1-v^2/c^2\right)}\right] = \frac{4\pi}{\lambda}\left[\frac{2A\Omega}{c\left(1-v^2/c^2\right)}\right]$$

In the limit where $\left(v^2/c^2\right) << 1$ and $V_p \approx c$, the temporal and spatial phase differences are the same.

Though one could, as mentioned above, use a Sagnac interferometer as an optical gyroscope, this approach is not the most commonly used, because cavity-based gyroscopes, and especially laser-cavity gyroscopes, tend to give more precise results in practice, all other things being equal. While these Sagnac interferometer based gyroscopes measure the interference between two beams, a cavity-based gyroscope allows one to measure the interference between many passes, as described in the cavity review chapter, and is more sensitive to phase differences between those beams caused by changes in its length. We include this calculation of the phase difference here for completeness and as an aid to understanding the origin and physical meaning of the Sagnac effect.

As an aside, however, it is worth noting that these results do apply directly to atomic interferometer based gyroscopes. Atomic gyroscopes are configured as Mach-Zehnder interferometers rather than Sagnac interferometers, as illustrated below, but the only difference in the analysis is that the waves complete just half a circuit of the device before interfering, so that we have $L^{\pm} = \pi R \pm v\left(L_{\pm}/V_R^{\pm}\right)$ instead of $L^{\pm} = 2\pi R \pm v\left(L_{\pm}/V_R^{\pm}\right)$, which makes the length (and time) differences half as large.

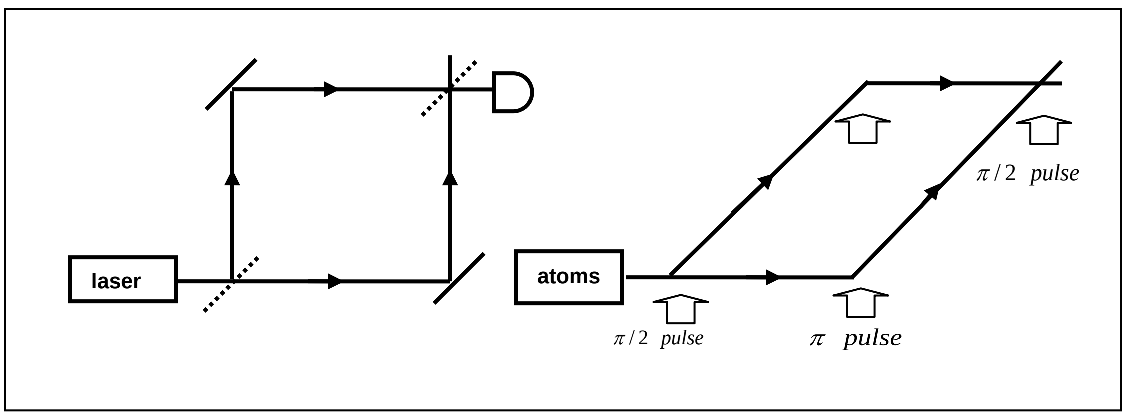

Figure 5.3: Mach-Zehnder interferometer for light and for atoms

For atoms, the relevant wavelength is given by

Equation 5.19: $$\hbar k = MV_p \Rightarrow \lambda = \frac{2\pi}{k} = \frac{2\pi\hbar}{MV_p}$$

So that

Equation 5.20: $$k\Delta L = \frac{4\pi}{\lambda}\frac{2A\Omega}{V_p} = \frac{2AM\Omega}{\hbar}$$

and the relevant frequency is given by

Equation 5.21: $$\hbar\omega = Mc^2 \Rightarrow \omega = \frac{Mc^2}{\hbar}$$

So that

Equation 5.22: $$\omega\Delta t_0 = \frac{2A\Omega M}{\hbar}\left[\frac{1}{\left(1-v^2/c^2\right)}\right]$$

We can compare these mass-dependent phase differences for atoms to the temporal and spatial phase differences for light, and find that the phase differences for atoms are approximately 10^{10} greater. (The comparison is between atomic interferometers and two-beam optical interferometers.) This is the reason for the interest in atom interferometer based gyroscopes. Implementing them in practice, and making these phase measurements with sufficient resolution, however, remains a significant barrier. Optical cavity based gyroscopes, which also improve on the two-beam interferometer design, if less dramatically, have proven much simpler to realize.

Equation 5.1, Equation 5.2, and Equation 5.6 provide all of the information we need to understand the optical cavity-based gyroscopes that will be the subject of the remainder of this discussion. We need to plug the expressions for the two different lengths into the expression for resonant frequency to find the difference between the resonant frequencies of the co- and counter- rotating beams in a ring cavity. Before we do so, however, we note that though the following analysis of the difference in resonant frequencies for co- and counter- rotating beams applies to both passive and laser cavities, this is detected differently in the two cases, as illustrated below.

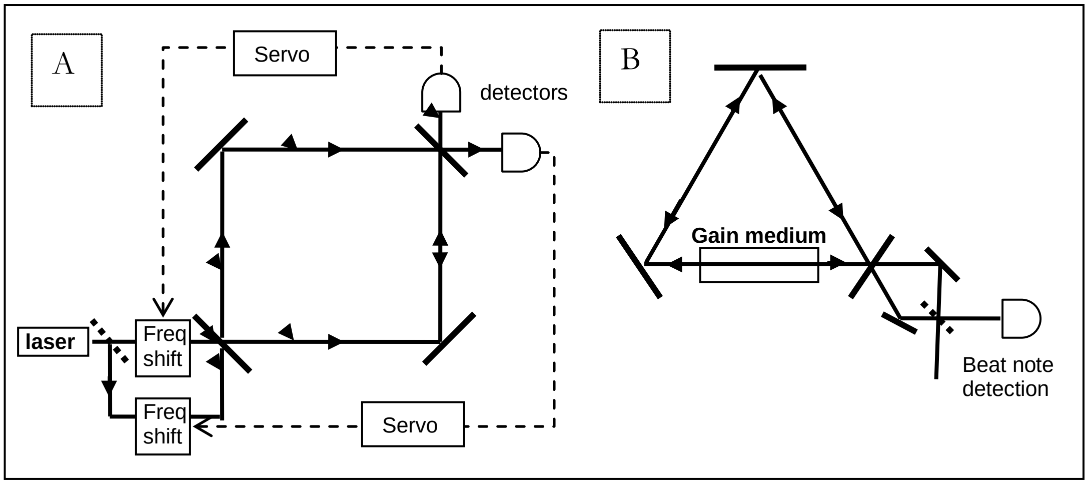

Figure 5.4: A) A four mirror ring cavity for passive optical gyroscope
B) A three mirror laser cavity for ring laser gyroscope

In a passive interferometer, a change in the resonant frequency of the cavity due to rotation means that a laser frequency which was resonant when the cavity was stationary becomes off resonant, in both directions. A servo lock system is used to shift the frequency of each beam independently until each resonates again. The servo control signal gives a measure of the necessary frequency shift, and thus of the difference between the resonant frequencies for the two directions.

In a laser cavity, there is no input beam to adjust. Instead, there is a gain material which fluoresces over a relatively broad spectrum, and only those frequencies which are resonant in the cavity will build up inside and be emitted as laser output. A single mode laser will emit one frequency in each direction, and if those frequencies are mixed at the output with a beamsplitter, the beat-note in the resulting intensity is a measure of the difference in the two frequencies, and can be detected directly.

The frequency difference will itself be almost the same in each case, as the resonance condition is the same in each case. The only distinction is that the laser cavity always has an intracavity medium, to provide the requisite gain, while the passive cavity may or may not contain a medium of some type. Any intracavity medium will have an index of refraction, and this will effect the propagation velocity, and thus the wavelength, of the input light. To make our model as general as possible, we will include the effects of an index of refraction in our calculations.

From Equation 5.2 we had $V_R^{\pm} = \dfrac{V_P \pm v}{1 \pm V_P v / c^2} = \left(c/n_0 \pm v\right)\left(1 \pm v/n_0 c\right)^{-1}$. Now if we assume $v/n_0 c$ is small, we can use the binomial expansion to move the factor containing that term out of the denominator in the second term in the expression for $V_R^{\pm}$. Then simplifying and dropping terms of order v^2, we arrive at

Equation 5.23: $$V_R^{\pm} \simeq c/n_0 \mp v(1 - 1/n_0^2) \equiv c/n_0 \pm v\alpha_F$$

where α_F is known as the Fresnel drag coefficient.

The resonant frequencies are:

Equation 5.24: $$\omega^{\pm} = \frac{2\pi N c}{n_0 V_R^{\pm} T^{\pm}} = \frac{c}{n_0} \frac{1}{V_R^{\pm}} \frac{2\pi N (V_R{}^{\pm} \mp v)}{P_0}$$

where N is an integer, $V_R^{\pm} T^{\pm} = P^{\pm}$ is the effective path length around the circle when it is moving, and P_0 is its stationary length, $2\pi R$.

If we assume that $v\alpha_F$ is small compared to c/n_0, then we can neglect that term where it appears in the denominator. Then the resonant frequencies are

Equation 5.25: $$\omega^{\pm} \simeq (V_R^{\pm} \mp v)\frac{2\pi N}{P_0} \equiv V_E^{\pm} \cdot \frac{2\pi N}{P_0}$$

The 'effective velocity,' $V_E^{\pm}$, we define in this equation depends on the index of refraction, as we can see if we write $V_R^{\pm}$ in terms of *n* according to Equation 5.23. But the index of refraction is itself a function of frequency. Therefore, in order for ω^{+} or ω^{-} to be resonant, we need:

Equation 5.26: $$V_E^{\pm} = \frac{c}{n(\omega^{\pm})} \mp v / n^2(\omega^{\pm}) = \frac{c}{n(\omega^{\pm})} . \left[1 \mp \frac{v}{n(\omega^{\pm})c}\right]$$

The full expression for the resonant frequencies of a rotating optical cavity filled with some material with index of refraction $n(\omega)$ is thus:

Equation 5.27: $$\omega^{\pm} = \frac{c}{n(\omega^{\pm})} . \left[1 \mp \frac{v}{n(\omega^{\pm})c}\right] \frac{2\pi N}{P_0}$$

We can solve this exactly for the resonant frequencies only if we know the exact functional form of $n(\omega)$. Alternatively, we can approximate it as a power series. If we keep only terms to first order in ω, and assume $v / n_0 c << 1$, and $|\Delta\omega / 2n_0 \left(\partial n / \partial \omega\right)|_{\omega_0}| << 1$ so that terms with a product of those two expression are negligible, then we can express $V_E^{\pm}$ in terms of the first derivative of $n(\omega)$ with respect to ω, then we can write

Equation 5.28: $$\omega^{-} - \omega^{+} \approx \frac{2\pi N}{P_0}\left(V_E^{-}(\omega^{-}) - V_E^{+}(\omega^{+})\right)$$
$$= \frac{2\pi N}{P_0} \frac{c}{n_o} \cdot \left[\left(1 + \frac{v}{n_o c} - n' \frac{\Delta\omega}{2}\right) - \left(1 - \frac{v}{n_o c} + n' \frac{\Delta\omega}{2}\right)\right]$$

where

Equation 5.29: $$\Delta\omega = \omega^{+} - \omega_0 = -(\omega^{-} - \omega_0) = \frac{1}{2}(\omega^{+} - \omega^{-})$$

and the resonant frequency for the empty cavity is

Equation 5.30: $$\omega_0 = \frac{2\pi N}{P_0}\frac{c}{n_o}$$

Writing the left hand side of the equation in terms of $\Delta\omega$ allows us to actually solve for it, and find what change in resonant frequency a rotation should induce in this cavity. The result is

Equation 5.31: $$\Delta\omega = \left[\left(\frac{2\pi N}{P_0}\frac{c}{n_o}\right)\frac{2v}{n_o c}\right]\left[1 + n'\left(\frac{2\pi N}{P_0}\frac{c}{n_o}\right)\right]^{-1}$$

This is the result we were seeking, an expression for the difference in resonant frequencies which is proportional to v, the rotational velocity of the ring cavity. In the absence of a material inside the cavity we have $n = 1$, and this simplifies to:

Equation 5.32:
$$\Delta\omega_0 = \frac{2\pi N c_0}{P_0}\frac{2v}{c\,n_0^2} = \frac{\omega_o}{c\,n_0}2\Omega R = \frac{\omega_o}{c\,n_0}\frac{4\Omega A}{P_0}, \text{ because } 2R = \frac{4A}{P_0} \quad (where\, A = \pi R^2)$$

Equation 5.33: $$\Delta\omega_0 = \frac{\omega_o}{c\,n_0}\frac{4\Omega A}{P_0}$$

The difference in resonant frequencies is, like the difference in phase, proportional to the rotation rate of the cavity. It is not proportional to the area in the same way, but rather to A/P_0, which scales with the radius of the ring cavity.

This frequency difference can be detected with either of the two schemes shown in Figure 5.4, more sensitively than the phase difference can be. Due to the necessarily narrow linewidth of a laser, the scheme shown in Figure 5.4B is generally the most sensitive, and it is this scheme which is used in commercial laser gyroscopes.

In the presence of the gain medium, however, the resonant frequencies are slightly different.

To see the effect of the medium clearly, we plug in $\Delta\omega_0 \equiv \frac{2\pi N}{P_0}\frac{2v}{n_0^2}$ into Equation 5.31, and write:

Equation 5.34: $$\Delta\omega = \left[\Delta\omega_0\right]\left[1+n'\left(\omega_0\right)\right]^{-1}$$

So the factor by which the splitting in the presence of a medium differs from that in the absence of a medium is.

Equation 5.35: $$1+n'\omega_0 = \frac{\Delta\omega_0}{\Delta\omega} = 1/n_g$$

This factor, $1/n_g$, is thus the effect of an index of refraction on the resonant frequencies of an optical cavity based gyroscope. We have assumed, here, that the medium fills the entire cavity. This explicit relationship between gyroscope sensitivity and group index is a new result, first published in Reference 21.

In the next section, we will examine the relationship between index of refraction and cavity resonance in general, and show that this gyroscope result is just a special case of a universal relationship between resonant frequency and cavity length in the presence of a refractive material. We will consider the case of a medium which does not fill the entire cavity at that time.

For now, we simply note that this calculation shows $\Delta\omega \propto 1/n_g$, so that a fast light material ($n_g < 1$) could enhance the sensitivity of a gyroscope to rotations, whereas a slow light material ($n_g > 1$) would decrease that sensitivity.

Of course, this enhancement diverges when n_g vanishes. This is due to the unrealistic assumption made above that the index varies linearly over all frequencies. In practice, the variation in the index is linear only over a limited bandwidth, Γ. When this is taken into account, the divergence is eliminated. The expression for the finite enhancement factor under such a condition is derived in Reference 21.

There are many other factors to consider in evaluating the potential of these media in improving optical gyroscopes. Reference 22 and Reference 23 give additional details on the behavior of conventional ring laser gyros. In particular they include noise analysis not considered in the preceding calculations. In the absense of noise, there is, in general, no need to enhance the frequency splitting between the two beams. Any rotation, however small, gives rise to some frequency splitting, and without noise that frequency splitting could always be detected. We will see in the next chapter that the introduction of a fast light material increases the noise on measurements of the resonant frequency of a passive cavity by a factor of $1/n_g$ as well. Since the sensitivity and the noise increase by the same factor, the signal-to-noise ratio is in this case unchanged. However, we will see in Chapter 7 that this is not the case for laser cavities containing fast light media.

We also consider these limitations, and others, in more detail in the next chapter.

CHAPTER 6 - INTRACAVITY DISPERSION

We have now reviewed optical cavities, dispersive media, and optical gyroscopes. More, we have shown that the sensitivity of optical gyroscopes filled with a dispersive material scales with the group index of the material. Now we will try to draw some general conclusions about the effects of intracavity dispersion.

The principle underlying all of these effects starts with the fact, established in the classical dispersion chapter, that the wavelength of light inside a medium can be different from its wavelength in free space, even though the frequency is unchanged. The degree to which the wave is compressed or expanded in the material depends on the index of refraction:

Equation 6.1: $\lambda = \lambda_{vacuum} / n = 2\pi c/(n\omega)$

In a cavity, the relevant quantity is the optical phase picked up after one round trip. If this phase is an integer multiple of 2π, all of the reflections will interfere constructively. The cavity output is a function of spatial phase, and the spatial phase depends on wavelength, and therefore on frequency. The spectral properties of the cavity — its linewidth, free-spectral range, and sensitivity to length changes — are all consequences of the relationship between phase and frequency. We observe, then, the effect of dispersion on this relationship:

Equation 6.2: $\phi = kL \Rightarrow \dfrac{d\phi}{d\omega} = \dfrac{dk}{d\omega} L = \dfrac{L}{v_g} = \dfrac{n_g L}{c}$

We saw a factor of n_g appear in our gyroscope calculations. It was not obvious, there, why the sensitivity of a gyroscope, operating in continuous wave mode, should depend on the group index of the material. We see now that the group index is really just a characteristic of the relationship between spatial phase and frequency. Since the location of a pulse is determined by the requirement that all of the frequency components add in phase, the group index does determine pulse propagation velocities. Its meaning, however, is broader than that. The quantity $d\omega / dk$ determines the properties of cavities as well as pulses, and is ultimately important in any calculation of the spectral consequences of spatial interference.

The resonance condition that the length of the cavity be an integer multiple of the wavelength can be stated, using the relationship of wavelength to frequency, as:

Equation 6.3: $L_{res} = \dfrac{2\pi Nc}{n(\omega)\omega}$

Where "N" is an integer. If the length of the cavity changes by an amount dL, the frequency which resonates in it will change by an amount $d\omega$, so that, assuming $n(\omega)$ is a continuously differentiable function:

Equation 6.4: $\dfrac{d\omega}{dL_{res}} = \left(\dfrac{dL_{res}}{d\omega}\right)^{-1} = -\dfrac{n^2(\omega)\omega^2}{2\pi Nc}\left(n(\omega) + \omega n'(\omega)\right)^{-1} = -\dfrac{\omega}{L_{res}} \dfrac{n(\omega)}{n_g(\omega)}$

From this it can be seen, as we saw with considerably more explicit calculation in the gyroscope case specifically, that a group index between zero and one will increase the sensitivity of the resonant frequency of a cavity to length changes, and a group index greater than one will decrease it. Fast-light-materials make for more sensitive cavities, in other words, and slow light materials make them less sensitive. This is a much simpler way to arrive at the conclusions we reached in the last chapter, and the conclusion is more general. The sensitivity enhancement has nothing to do with the Sagnac effect. The resonance frequency of the cavity changes more with any change in length, whatever the cause. The concept is illustrated below:

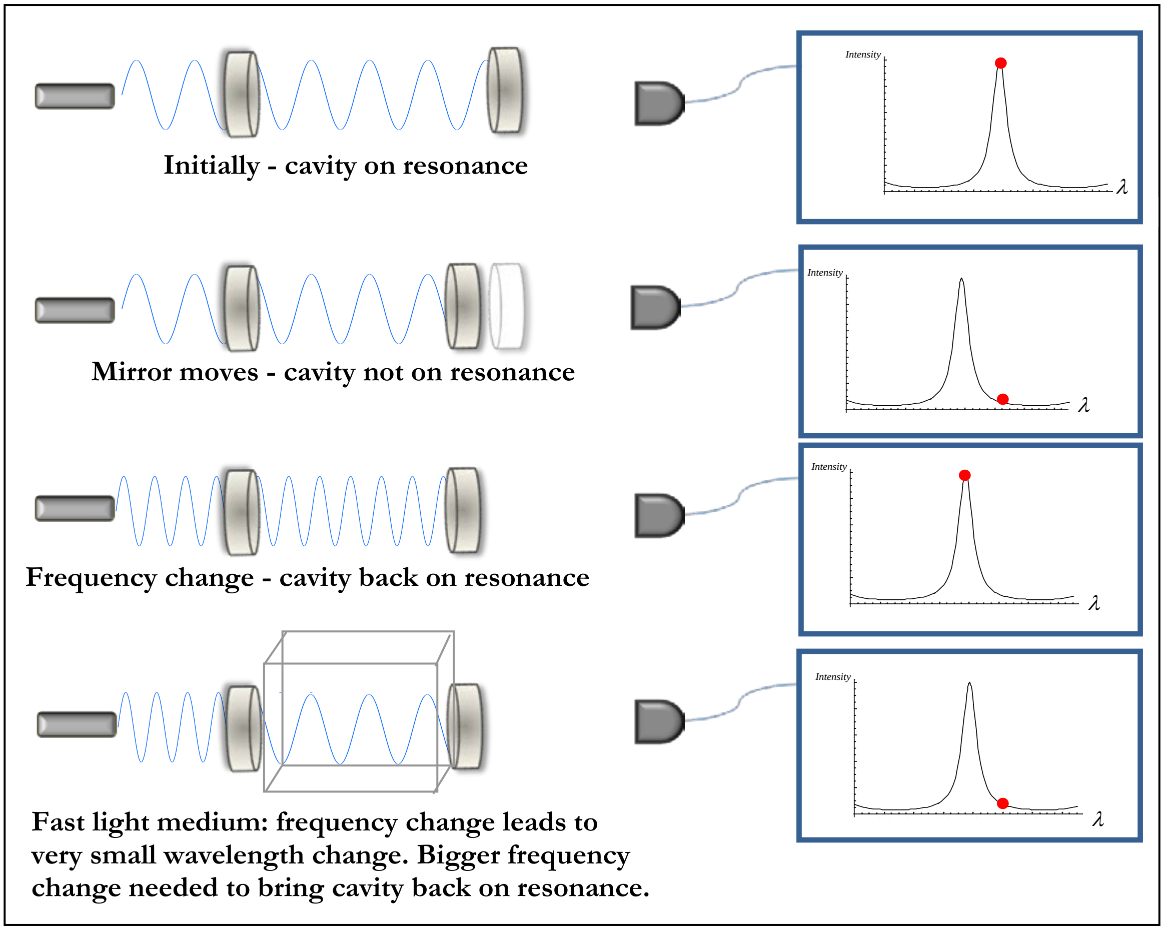

Figure 6.1: Effect of fast-light material on cavity sensitivity

Having established this effect on the sensitivity of the cavity, we now consider the effect of dispersion on the linewidth of the cavity. We begin by examining a special case.

Since it is possible for different frequencies of input light to experience different indices of refraction, it is possible to make arrangements such that a whole range of frequencies should have approximately the same wavelength inside the material, as illustrated below.

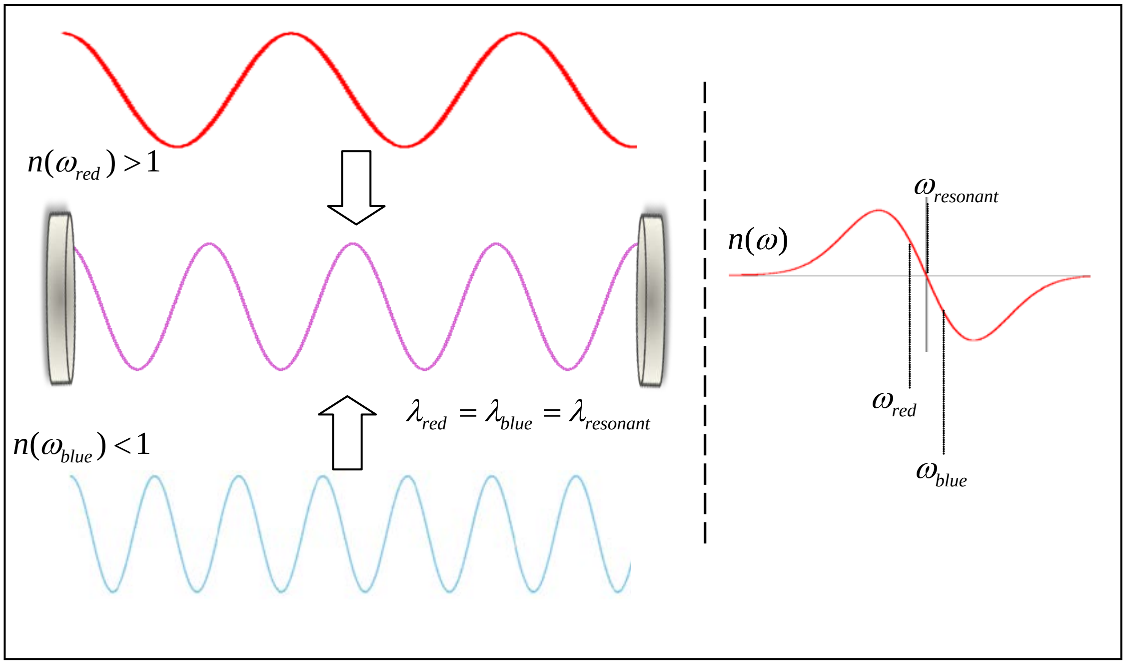

Figure 6.2: Index of refraction chosen to compress wavelengths longer than resonant and expand wavelengths shorter than resonant so that all frequencies within a particular range share the same, resonant wavelength. This is the principle of the "White Light Cavity."

The condition for this to happen is:

Equation 6.5: $$\left.\frac{\partial(n\omega)}{\partial\omega}\right|_{\omega_o} = 0 \;\Rightarrow\; \left.\frac{\partial n}{\partial\omega}\right|_{\omega_o} = -\frac{n_o}{\omega_o} \Rightarrow n_g \approx 1 + \omega_o \left.\frac{\partial n}{\partial\omega}\right|_{\omega_o} = 0$$

If we do find a material which fulfills this condition, and if the wavelength to which this range of frequencies corresponded happened to be resonant in a cavity, then we would expect that all frequencies within that range could resonate. Thus, the apparent linewidth of the cavity could be increased.

We call this condition "critically anomalous dispersion" (CAD). It is anomalous because a negative slope is required for the index, but it is a very particular and generally very small negative slope. Another name for this condition, proposed in Reference 24, is "Lambda compensation." The idea is that the change in the index compensates for the changes in frequency, to keep the wavelength constant. This scenario is illustrated below:

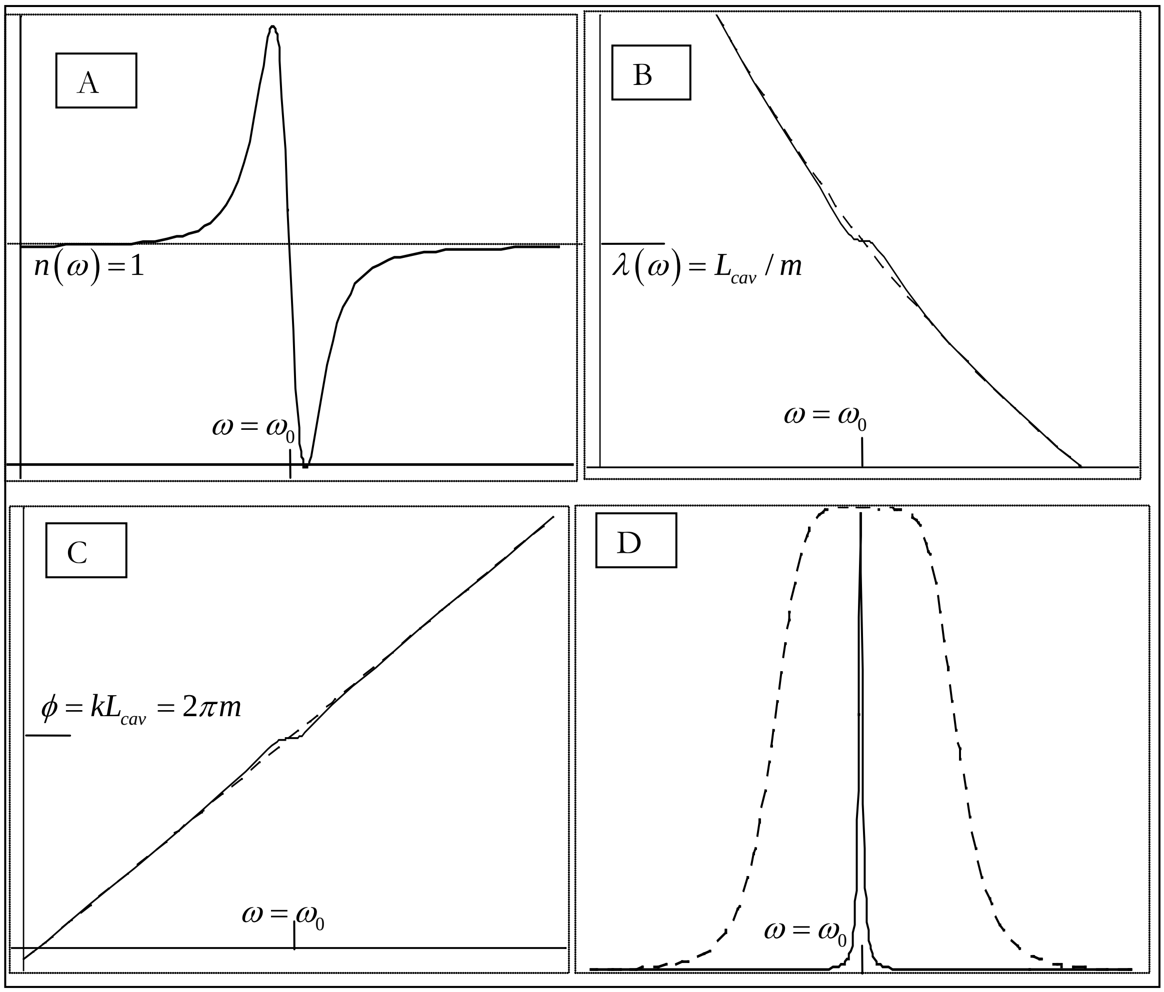

Figure 6.3: A) An index profile $n(\omega)$ with critically anomalous dispersion. B) Wavelength vs. frequency in the absence (dashed) and presence (solid) of CAD material. C) Propagation phase $\phi = nkL$ vs. frequency in the absence (dashed) and presence (solid) of CAD material. D) Transmission of a cavity as a function of frequency in the absence (dashed) and presence (solid) of a CAD material. Plots A-C are over the same frequency range (700-1300, with units chosen so that $c=10$, to show the flatness on the same scale as the $1/\omega$ lineshape for the wavelength.) Plot D is over a smaller range (990-1010) to show detail. The resonant frequency of the cavity is chosen to match the center frequency of the dispersion.

Note that the field build up, which is determined primarily by the reflectivity of the cavity mirrors, remains unaffected by this broadening. This is the principle of the 'white light cavity'.

Of course, the reverse is also possible. We can arrange for the wavelengths to be dramatically different for very close frequencies, inside another kind of medium, much more than what would happen in free space. In that case, a much smaller range of frequencies is going to resonate in the medium-filled optical cavity than would resonate in the empty cavity. The apparent linewidth of the cavity would then be highly reduced.

We can describe these effects quantitatively by stating the resonance condition for the cavity in terms of the phase difference between light that is entering the cavity and that which has completed one round trip. If that phase difference is a multiple of 2π, then the output of the cavity will reach its maximum value. We will consider the linewidth of the cavity to be the range of frequencies for which the output is at least half the input. The output will drop to half when the phase it has picked up after one round trip is:

Equation 6.6: $\phi_{1/2\max} = 2\pi N + \delta\phi_{1/2\max} = \frac{L}{c}\omega_0 + \frac{L}{c}\delta\omega_{1/2\max}$

Here N is an integer, ω_0 is the resonant frequency of the cavity, L is its length, and c is the free space velocity of light. The quantity $\delta\phi_{1/2\max}$ is the amount of excess phase that causes the output light level to drop to half its maximum value, and $\delta\omega_{1/2}$ is the linewidth of the cavity.

The phase light picks up as it travels on each round trip depends on the frequency of the light:

Equation 6.7: $\frac{d\phi}{d\omega} = \frac{d}{d\omega}\left(\omega\frac{n(\omega)L}{c}\right) = \frac{n(\omega)L}{c} + \omega\frac{dn(\omega)}{d\omega}\frac{L}{c}$

Here L is the round trip length of the cavity, c is the free space velocity of light, and $n(\omega)$ is the index of refraction of the material as a function of frequency. If we assume that the index depends *linearly* on the frequency over some range centered around a frequency ω_0, so that

$\delta\phi_{1/2max} = \frac{d\phi}{d\omega}\delta\omega_{1/2max}$ and that $n(\omega_0) \approx 1$, we can express the change in frequency necessary to give the change in phase which drops the cavity output to half:

Equation 6.8: $\delta\omega_{1/2\max} = \frac{c}{L}\left(1+\omega_0 n'\right)^{-1}\delta\phi_{1/2\max}$

where n' indicates the derivative of n with respect to ω, and is constant over the linear region, and ω_0 is the center frequency. One can see that the linewidth, $\delta\omega_{1/2\max}$, will be reduced if $(1+\omega n')$ is greater than one, and increased if $(1+\omega n')$ is between 0 and 1. This quantity is, again, the group index of the material. So these simplified calculations suggest that in order to create the broad linewidth cavity, we need a material with a group index of less than one, over some range of frequencies. And in order to create a cavity with a narrow linewidth, we need a material with a group index greater than one.

We conclude that a fast-light material has the effect of increasing the sensitivity of the cavity to changes in its length, and at the same time broadening the resonance.

The fact that the broadening with fast-light material does not come at the expense of a decrease in the intracavity intensity is important, which is determined solely by the reflectivities of the cavity mirrors, assuming there are no other losses. In other words, the cavity finesse remains unchanged[25] . Thus, with this technique, it is possible to have high finesse cavities with broad linewidths. Similarly, the narrowing with slow-light material does not entail an increase in the cavity storage time (and, therefore, the intracavity intensity), so that low finesse cavities with narrow linewidths are feasible.

These calculations raise a few questions about the CAD condition. Though it is easy to think conceptually about the idea of wavelength not changing with frequency, at least over some small bandwidth, it causes some problems mathematically. As $n_g \to 0$, both our linewidth and our sensitivity expressions blow up. Of course, this is primarily a result of the fact that we approximated $n(\omega)$ as a linear function, when, in practice, there are inevitably higher order contributions.

To understand the physical behavior of a system under the CAD condition, it is easiest to think physically. The exercise is useful in understanding the general problem as well.

For the sake of illustration, consider for a moment an impossible situation in which the group index for a material is exactly zero for all frequencies, that is, that the wavelength were a constant which did not vary at all with frequency. Suppose further that a cavity filled with such a material is resonant at that particular wavelength. We would find that every frequency we put into the cavity would resonate. The linewidth would be infinite. This would be the ideal 'white light cavity.' If we then changed the length of the cavity, we would not be able to make it resonate again no matter how much we changed our laser frequency. This is because we would not be changing the wavelength at all. The perfect white light cavity is also, in this sense, infinitely sensitive to length changes. In practice, the group index can vanish only over a limited bandwidth, Γ, which in turn limits the bandwidth of the white light cavity and the reduction in sensitivity to length changes. The details of the actual bandwidth of a white light cavity and the degree of reduction in sensitivity under realistic conditions are modeled mathematically in Reference 21. Alternatively, we can examine a graphical solution to the resonant frequency equation, such as that shown in Figure 6.4.

If we really want to show that fast light increases the sensitivity of a cavity to length changes, we must solve for the resonant frequency of the cavity and show how it depends on length, in the absence and the presence of fast light materials. The familiar equation for resonant frequency is:

Equation 6.9: $\omega_{res} = \dfrac{2\pi mc}{n(\omega_{res})L}$

This equation just says that the length has to be some integer multiple m of the wavelength, but we have written the wavelength out in terms of the frequency, and solved for that. Now because $n(\omega)$ can be a complicated function, not just a simple polynomial, it can be hard to solve this equation explicitly without making approximations. But we can always solve it graphically. We just re-write it:

Equation 6.10: $\omega_{res} n(\omega_{res}) = \dfrac{2\pi mc}{L}$

Then we define

$y_L = \omega_{res} n(\omega_{res}) = \mathit{Left\ Hand\ Side}$ and $y_R = \dfrac{2\pi mc}{L} = \mathit{Right\ Hand\ Side}$

We plot the left hand side of the equation and the right hand side of the equation separately, as functions of frequency, and where those two lines intersect, that is where the left hand side is equal to the right hand side. That is the frequency which is resonant. The right hand side is just a constant, determined by whatever value of L we pick. So it is a horizontal line. The left hand side depends on the index of refraction, and so may have a more complicated shape.

In Figure 6.4 we choose one particular length and plot the corresponding horizontal line. The left hand side is then plotted in red. The red line intersects the blue at a particular frequency, which is the resonant frequency for the length we chose in plotting that blue line. Next we choose a different length, get a different constant for the right hand side, and plot that in purple. The left hand side is the same; it does not depend on length. This red line intersects the purple at another particular frequency, which is the resonant frequency for the length we chose in plotting that purple line.

The resonant frequency for the larger length is at the location of the left dotted red line, and the resonant frequency for the smaller length is marked by the right dotted red line.

Finally, let us consider what it would be for an empty cavity. In that case the index is one, so plotting the left hand side gives a diagonal line. It crosses the line for the larger length at the frequency marked by the left dotted black line, and the line for the greater length at the frequency marked by the right dotted black line. The difference in the resonant frequencies for the two lengths is given by the distance from one dotted line to the other along the frequency axes.

We have found graphical solutions for four different pairs of lengths, illustrated in the four different plots below, for both the empty cavity and the CAD cavity. The two large plots are on the same scale, while the frequency axis for the two small plots spans a much larger range. The same index profile is assumed in all four cases, and the pairs of lengths have the same average value in all four cases. These plots illustrate the effect of the CAD condition on the sensitivity of the cavity, and are relevant for optical gyroscopes, with the two choices of length corresponding the different lengths of the co- and counter- rotating beams.

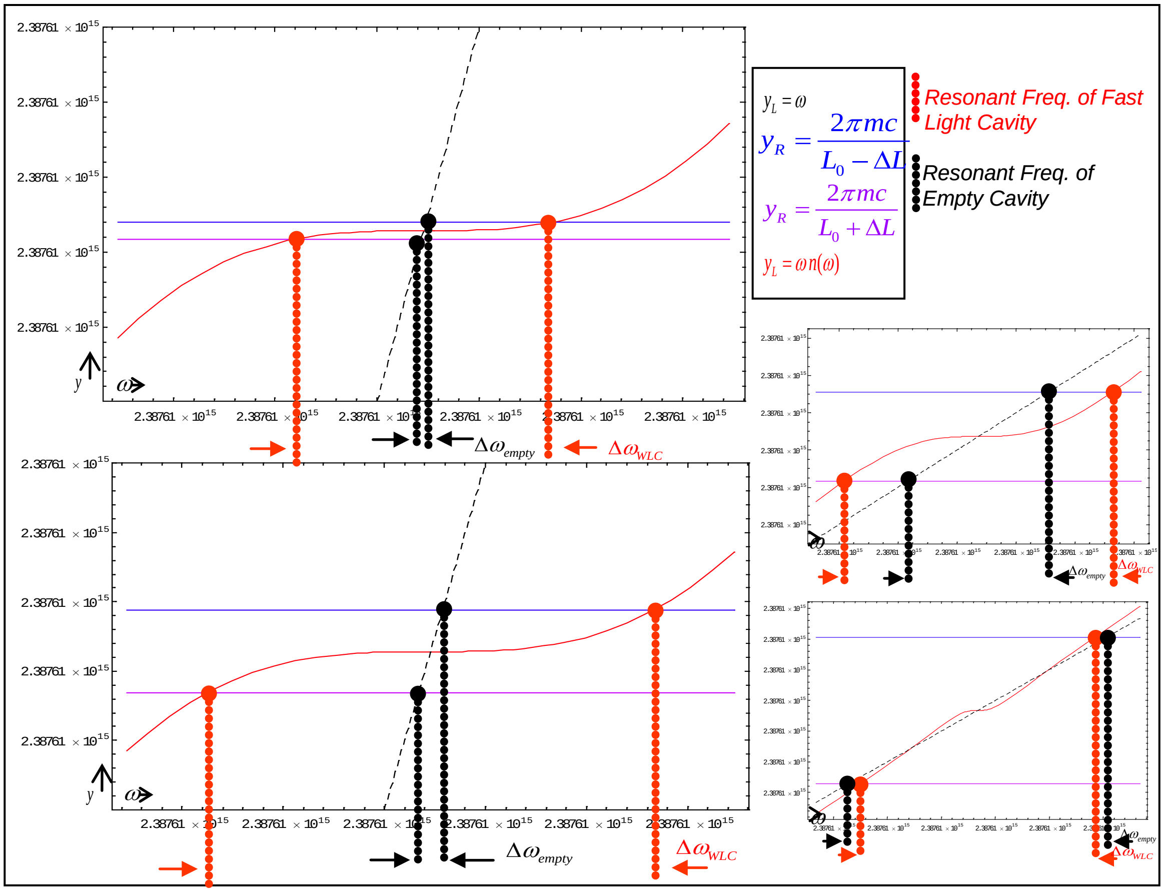

Figure 6.4: Graphical solutions for the resonant frequency of a cavity in the presence or absence of a CAD material. See text for details.

From this we can see that for the same change in length, the resonant frequency of the fast light cavity changes by a lot more in the CAD cavity case. We can also see the effect of the bandwidth limitation of our dispersion. If we plot the L.H.S and R.H.S. on a bigger frequency scale, (shown in the smaller figures) we can see that the y_L starts to turn around and get closer to the y_R. That's because eventually the index of refraction goes back to one. So the result is that for big differences in length, the resonant frequencies are not so different.

The upshot is, we only get big enhancements over the range where the slope of $\omega_{res} n(\omega_{res})$ (which is proportional to the phase) is very shallow. That is approximately the range over which the dispersion is linear.

Because we can make this slope arbitrarily close to zero, we can get an enhancement factor for small rotations that is as big as we like. But as soon as the resonant frequencies start to get outside of this flat range, the "enhancement" starts to drop off. So the tradeoff is this, the bigger the enhancement we want, the smaller the range of that enhancement, assuming that the bandwidth is fixed.

This represents a limitation, but even with this limitation, the effect is still potentially very useful. The parameters of the dispersion simply have to be chosen differently depending on whether the goal is to detect very small rotations or whether a modest enhancement over a broader range is more desirable.

However, there is another problem which does limit the usefulness of the passive fast light cavity for gyroscopes. The increase in sensitivity goes along with that same dispersion that gives the cavity broadening. They are two effects of the same cause; both result from making the wavelength vary only a tiny bit as the frequency changes. We have shown that the sensitivity of a cavity with this kind of medium is $1/n_g$ times the sensitivity of the empty cavity. Below is an illustration of the cavity transmission when we sweep the input frequency through the cavity resonance for an empty cavity, and then change the length by a little amount delta L, and another showing what happens if we do the same thing for the white light cavity.

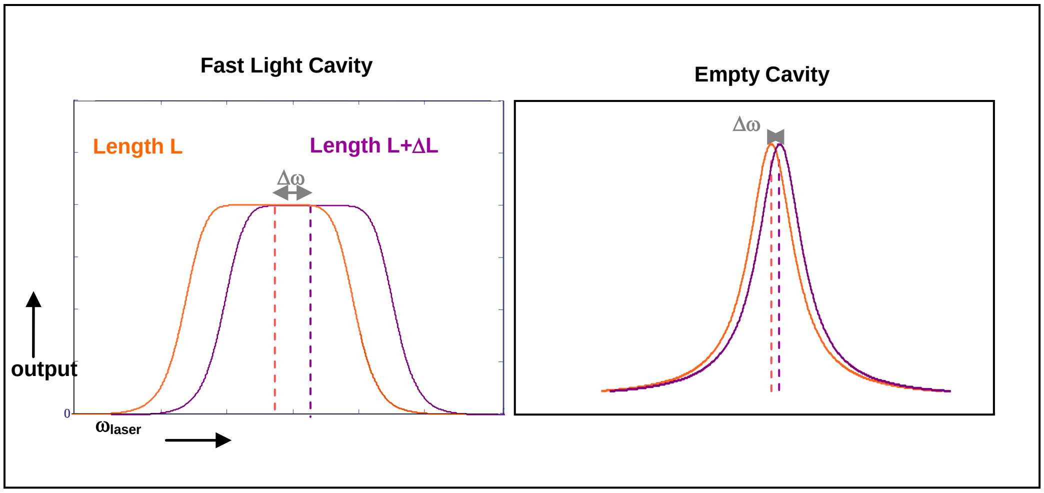

Figure 6.5: Transmission vs. frequency for idealized fast light cavity and for empty cavity, for the same two choices of length.

The broader linewidth means an increased uncertainty in any measurement of the resonant frequency. The white light cavity resonant frequency is more sensitive to length changes, but also more uncertain, and by the same factor. In a passive cavity, this results in an unchanged signal to noise ratio.

In practice, the situation is not quite so bad. The linewidth changes as the resonant frequency moves away from the center of the dispersion, so that a more realistic version of the shift for the WLC looks like Figure 6.6.

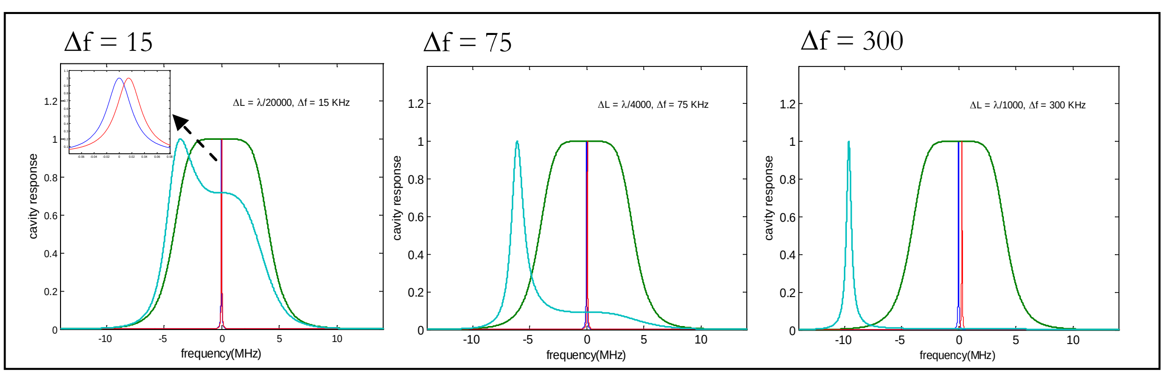

Figure 6.6: Shifting resonance of a White Light Cavity. Linewidth and sensitivity both change with frequency, shown with, and labeled by, the corresponding empty cavity splittings.

As we will see in a later chapter, however, there is a better way to get around this problem. In brief: the linewidth of a laser cavity is always very small. If we put the dispersive material into a cavity with gain, we can keep the sensitivity increase, but force the linewidth to be narrow. The experiments become a little harder, but the approach has other benefits as well, which we will discuss in the relevant chapter.

There are other applications, in particular in gravitational wave detection, in which the increased linewidth of the cavity is a desirable trait. These too, we discuss in their own chapter.

Before we conclude this general discussion, however, we must mention an important detail. All of the above analysis has assumed that the dispersive material filled the entire length of the cavity. The calculations for linewidth and sensitivity are only slightly modified if it does not, but we include them here for completeness. The CAD condition itself is modified as well. We emphasized above that if the medium fills the entire cavity, the CAD condition requires that the wavelength not vary with frequency. More fundamental, however, is the requirement that the phase not vary with frequency. If the medium fills only a portion of the cavity, those two conditions are distinct.

Below, we show some of the intermediate steps in the calculation of the linewidth of a cavity only partially filled by a dispersive medium. The length of the medium is l while the round-trip length of the cavity is L, and $n' = \left.\frac{dn}{d\omega}\right|_{\omega_0} = \frac{n_g - 1}{\omega_0}$

Equation 6.11: $$\phi = \omega\frac{(L-l)}{c} + \omega\frac{n(\omega)l}{c}; \qquad \delta\phi = \frac{d\phi}{d\omega}\delta\omega$$

Equation 6.12: $$\frac{d\phi}{d\omega} = \frac{(L-l)}{c} + \frac{n(\omega)l}{c} + \omega\frac{n'(\omega)l}{c}$$

Equation 6.13: $$\delta\phi_{1/2} = \left(\frac{(L-l)}{c} + \frac{n(\omega)l}{c} + \omega \frac{n'(\omega)l}{c} \right) \delta\omega_{1/2}$$

Equation 6.14: $$\delta\omega_{1/2} = \delta\phi_{1/2} \frac{c}{(L-l) + l\left(n(\omega) + \omega n'(\omega)\right)}$$

Equation 6.15: $$\delta\omega_{1/2} \simeq \delta\phi_{1/2} \frac{c}{L\left((1 + \frac{l}{L}\left(\mathrm{n}_g - 1\right) \right)} \; for\, n\left(\omega_0\right) \approx 1$$

The CAD condition is now

Equation 6.16: $n' = -\dfrac{L}{l\,\omega_0}$

If we assume the mirrors of the cavity have equal reflectivity "R" and calculate $\delta\phi_{1/2}$ as we did in Equation 2.14, we arrive at:

Equation 6.17: $$\delta\omega_{1/2} \simeq \cos^{-1}\left(\frac{4R - 1 - R^2}{2R} \right) \frac{c}{L\left((1 + \frac{l}{L}\left(\mathrm{n}_g - 1\right) \right)}$$

This expression is somewhat more general than the simpler expressions given above. The group index still plays a role, and still appears in the denominator, but modified by the fraction of the cavity length occupied by the material.

We can do a similar calculation for the sensitivity.

Equation 6.18: $$\omega = \frac{2\pi Nc}{(L-l) + n(\omega)l} \Rightarrow L = \frac{2\pi Nc}{\omega} + l(1 - n(\omega))$$

Equation 6.19: $$\frac{dL}{d\omega} = \frac{-2\pi Nc}{\omega^2} - n'(\omega)l$$

Equation 6.20: $$\frac{d\omega}{dL} = \frac{-\omega^2}{2\pi Nc} \left(\frac{1}{1 + n'(\omega)\omega \frac{l\omega}{2\pi Nc}} \right)$$

Equation 6.21:

$$\frac{d\omega}{dL} = \frac{-\omega^2}{2\pi Nc}\left(\frac{1}{1+n'(\omega)\omega\frac{l\omega}{2\pi Nc}}\right) = \left[\frac{d\omega}{dL}\right]_{empty}\left(\frac{1}{1-\left(n_g-1\right)l\left[\frac{d\omega}{dL}\right]_{empty}}\right)$$

Again this result is less transparent, but more general, and though the role of the group index is more complex, it is still important. The CAD condition given in Equation 6.16 yields maximum sensitivity, as we can see by plugging it into Equation 6.20.

This chapter concludes the theoretical background for intracavity dispersion. The succeeding chapters will cover, not the general principles, but specific applications of these effects.

CHAPTER 7 - DISPERSION IN ACTIVE CAVITIES

Self Consistency Equations

The problem may be stated simply – given a laser cavity which is partly filled by some dispersive medium, what will be the frequency of the laser output?

The question, though easy to ask, is not easy to answer. The reason is that the intracavity laser field generally has an effect on the dispersive medium. Consider a field that is resonant in a cavity containing some kind of medium. As the intracavity field begins to build up due to gain and constructive interference, the greater intensity modifies the susceptibility of the medium, and thus changes the phase shift the medium imparts. This may change the round trip phase for the field so that it is no longer equal to a multiple of 2π , which then destroys the resonance. All lasers have at least one dispersive element in them: the gain medium which distinguishes a laser cavity from a passive optical resonator. So this problem of the lasing field undermining its own resonant build-up is universal. We must resolve it if we wish to know how the frequency of any laser depends on the physical properties of the cavity and gain medium.

The general solution to this problem is to use a set of self consistency equations developed by Lamb[10] to describe the properties that a field which can exist in steady state must have. The first of the self consistency equations says that, in steady state:

$$\dot{E} = -\frac{1}{2}\frac{\nu}{Q}E - \frac{1}{2}\nu E \chi''(E,\nu) = 0$$

Therefore:

Equation 7.1: $$\chi''(E,\nu) = -\frac{1}{Q} \quad (\mathit{for}\ E,\nu \neq 0)$$

Since χ'' is proportional to the gain and $1/Q$ is proportional to the loss experienced by the beam on each round trip, this equation simply implies that in steady state the gain will be equal to the loss. The gain must initially be larger than the loss for lasing to occur; this condition is achieved by saturation of the gain medium.

If the medium is homogeneously broadened, for instance, assuming a lasing frequency that is not quite matched to the gain center frequency, we see the behavior illustrated in Figure 7.1, below. (See Reference 7.)

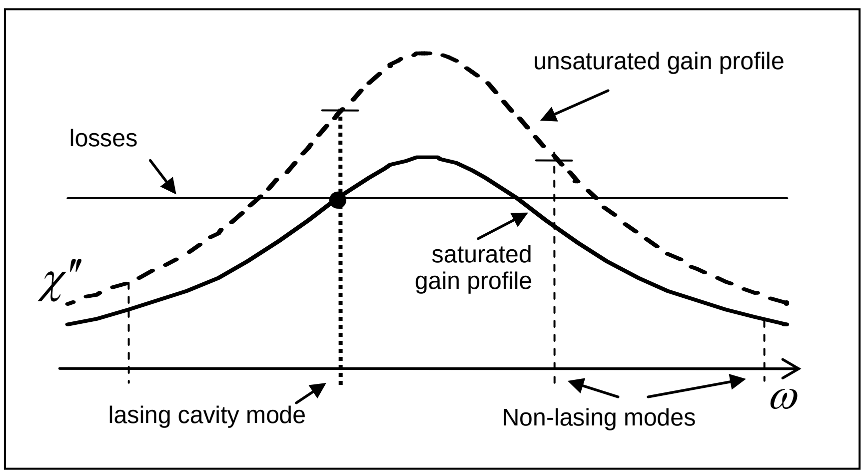

Figure 7.1: Saturation of homogeneous gain profile to satisfy self-consistency equations at lasing frequency.

There are several subtle points to be considered in the interpretation of a graph of this type which we will discuss later, but for now let us simply take it at face value. The gain causes the field to increase in magnitude on every pass around the cavity. As the field builds up, light that has passed once through the cavity adds with light which has passed twice, three times, one hundred times through the cavity, all in phase, and the total field strength increases as more and more reflections build up, each stronger than the last. Any physical gain medium is saturatable, however, and the increasing intensity causes a decrease in the gain. The steady state is reached when the gain at the frequency of the field is equal to the loss in the cavity. This figure also indicates why an ideal, homogeneous laser cannot have more than one lasing mode. The saturation which reduces the gain to the threshold for the mode closest to the gain center will reduce it below threshold for all of the other modes. (In practice this may not always be true; effects such as spatial hole burning complicate the behavior of real lasers and may result in multimode oscillation even with homogeneously broadened gain media. However, for now let us consider ideal cases.)

Any inhomogeneously broadened lasing medium, by contrast, can support multiple lasing modes. This is because the saturation does not reduce the gain over the whole profile, but only a relatively small frequency range around the lasing frequency. If the medium is inhomogeneously broadened, we may look at its gain profile as the sum of many narrower, homogeneously broadened gain profiles each centered at a different frequency. Any particular frequency of light will not lie within the gain bandwidth of most of the atoms in such a system. The gain due to these atoms will not, therefore, be decreased by the buildup of the field. It is for this reason that the gain will be saturated only for a small range around the resonating frequency. The result is referred to as spectral hole burning, illustrated below, for the case where multiple longitudinal cavity modes lie within the bandwidth of the inhomogeneously broadened gain.[7]

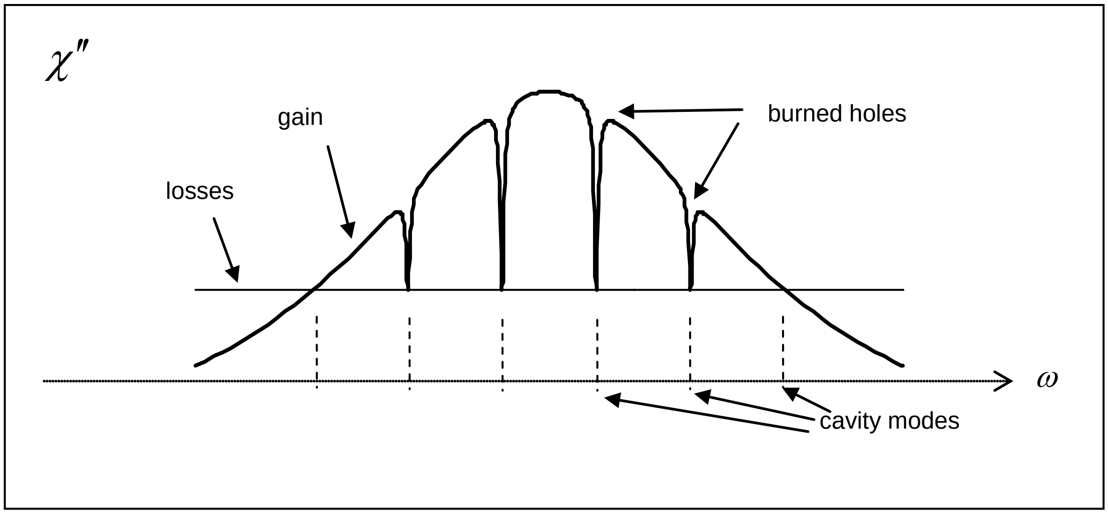

Figure 7.2: Saturation of inhomogeneous gain profile to satisfy self-consistency equations at lasing frequency or frequencies.

Equation 7.1 tells us that in each case, the homogenous and inhomogeneous, the gain profile must touch the loss line at the lasing frequency, but it does not tell us anything about the gain at other frequencies. It applies to both homogenously and inhomogeneously broadened media, but specifies just one point on the gain curve – the point at the lasing frequency. In addition, if the gain at a particular frequency is lower than the loss even without saturation effects then the laser cannot lase at that frequency at all, and Equation 7.1 does not apply.

Now let us consider the second of Lamb's self consistency equations:

$$\dot{\phi} = (\Omega - \nu) - \frac{1}{2}\nu\chi'\left(E,\nu\right) = 0$$

We can write this in the form

Equation 7.2: $$\nu = \frac{\Omega}{1 + \frac{1}{2}\chi'\left(E,\nu\right)} = \frac{\Omega}{n\left(E,\nu\right)}$$

This is equivalent to the statement that the round trip phase for the lasing field must be equal to a multiple of 2π. We can see this, in the case where the dispersive medium fills the cavity, by writing:

$$\phi_{rt} = n(E,\nu)\frac{\nu}{c}L = 2\pi m$$

Equation 7.3: $\nu = \dfrac{2\pi mc}{n(E,\nu)L}$

If E is known, this determines the resonant frequency with a medium filling the cavity. Setting n=1 shows that the resonant frequency for the empty cavity is

Equation 7.4: $\Omega = \dfrac{2\pi mc}{L}$

From comparing Equation 7.3 and Equation 7.4, we see that $\nu = \Omega / n\left(E,\nu\right)$, the second of the steady-state self-consistency equations, can be derived from the round-trip phase condition alone. This is the equation that describes mode pulling, also known as frequency pulling. Since for a gain medium n is less than one for frequencies below the gain center and greater than one for frequencies above the gain center, ν is always closer to the gain center frequency than Ω is, when the only dispersion is due to a gain peak.

We have been careful here to note explicitly the dependence of χ'' and χ', and thus of the gain and refractive index, on both E, the laser field amplitude, and ν, its frequency.

Since χ' depends on the field amplitude, the changes in gain caused by the increasing intensity are accompanied by changes in phase shift.

In a homogenously broadened medium, the effect of the saturation is simply to decrease the magnitude of χ' over the whole profile, as illustrated below in Figure 7.3

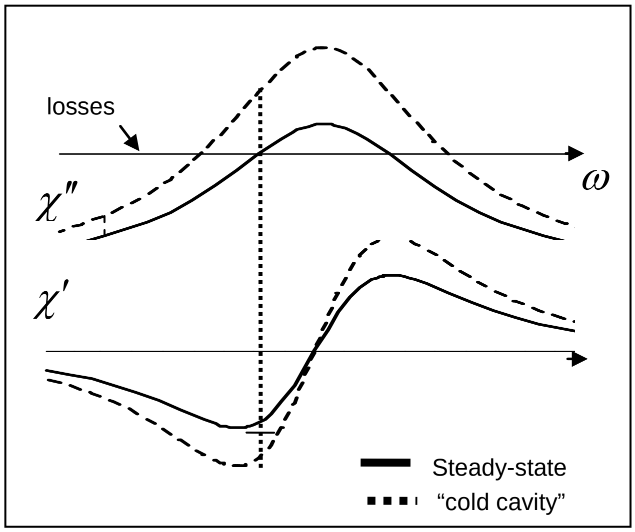

Figure 7.3: Saturation of homogeneous gain profile to satisfy self-consistency equations at lasing frequency or frequencies, and index profile corresponding to the saturated gain profile.

Note that the frequencies for which χ' is plotted here are not in general resonant in the cavity and cannot be sustained in steady state. Only the point at $\omega = \nu$ tells us anything about the phase shift that would be seen by a resonating beam.

At this point we will take a moment to consider the interpretation of this graph, and related graphs, a little more carefully. The χ' graph in Figure 7.3 is nothing more or less than a graph of $\chi'(E_L, \omega)$, where E_L is the field strength of the resonating intracavity beam, which we here hold constant while scanning the frequency. The χ'' graph, which is similar to Figure 7.1, similarly depicts $\chi''(E_L, \omega)$. When we have a material which is not in a cavity, these experiments are easy to perform. However, it is not possible to obtain either graph in Figure 7.3

experimentally for a homogeneously broadened gain medium which is inside a cavity. For this reason, we must be careful in interpreting all graphs of this type, whether for χ' or χ''.

Figure 7.1 and Figure 7.3, and several more graphs to come, are created by treating frequency as a variable that can be changed independently of field strength, but the cavity makes that impossible. If the cavity were to lase at any other frequency, it would have a different associated electric field in steady state. We might imagine introducing a second, non-resonant beam into the cavity at some other frequency to measure the susceptibility at that point, but the susceptibility for a medium interacting with two beams is not the same as the single-beam susceptibility equation we started from, though it may be very similar. This type of experiment would produce a graph very much like those we have displayed, but not identical. Finally, we may imagine turning off the saturating beam and then scanning a probe through the material. This would produce the best approximation of these graphs, but depending on the lifetimes of the states of the gain medium, there may be no way to scan fast enough, physically, to accurately reproduce them. Nevertheless, this type of graph is heuristically useful. It reminds us that the effect of saturation on a medium is generally not to flatten the frequency response of that medium, but simply to reduce the magnitude of that response. It reminds us that the real part of the susceptibility at the lasing frequency is not zero, but the intensity build up does reduce it from its "cold cavity" value – the value it has when the field is small, during the initial build up. The effect of the saturation by the lasing field is to deplete the population of the excited state. Fewer excited atoms interacting with the field means the material will produce a smaller response, and we will see a smaller phase shift. That the phase shift never entirely goes to zero when we are away from the peak is also natural. Driving an oscillator off-resonance always results in a phase lag in its response, regardless of how hard one drives it. The only way our homogeneously broadened material will produce zero phase shift for our lasing field is if that field is exactly on-resonance for the gain transition, in which case, the phase shift will always be zero.

The one point on this graph which is physically meaningful inside a cavity is the one we are really interested in, $\chi'(E_L, \nu)$, the susceptibility at the lasing frequency and field strength. This graph helps us picture how it will change as the cavity length is changed.

What about Figure 7.2? In that case, clearly we are not holding E constant at any particular E_L for all frequencies. To obtain Figure 7.2 experimentally, it seems that we would not only need to use free-space beams, but would really need, in this case multiple beams. Whatever constant-intensity probe we scan through this frequency range will only see those saturated holes if other beams are present, doing the saturating. On the other hand, we face the same problem that the susceptibility for an atom interacting with multiple beams includes effects more complicated than simple saturation. So Figure 7.2, though it is a common depiction of "hole burning," is not something we could expect to reproduce exactly (although we would see something very similar to it) with any real experiment, even outside a cavity. Nevertheless, Figure 7.2 is useful. It reminds us that the atoms with resonant frequencies which are not close to the lasing frequency are not in fact saturated by the lasing field. It also gives us a way to think about the contribution of those atoms to the phase shift the lasing field experiences.

Let us imagine that the χ'' illustrated in Figure 7.2 is the sum of a broad Lorentzian and four narrow, inverted Lorentzians. The associated χ' at any frequency is then determined by the sum of the phase shift due to that broad Lorentzian gain and the phase shift due to each of the narrow Lorentzian "absorption" features, as illustrated in Figure 7.4 below [26,27,28,29].

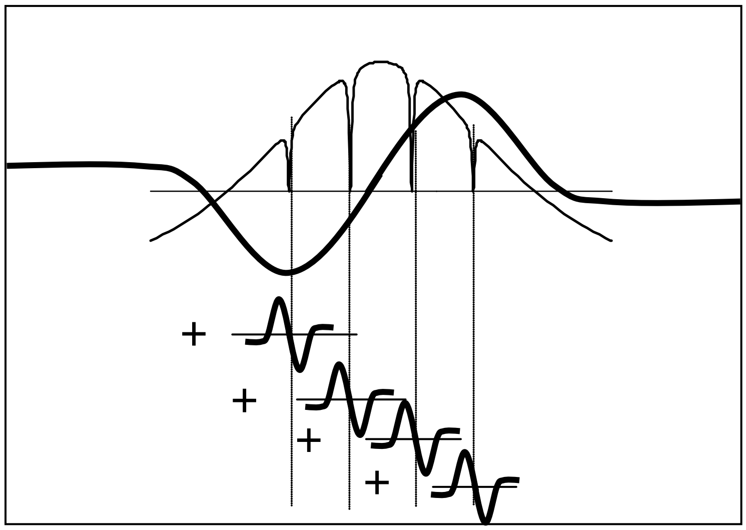

Figure 7.4: Saturation of inhomogeneous gain profile to satisfy self-consistency equations at lasing frequency or frequencies, and index profile corresponding the saturated gain profile.

The phase associated with a hole is zero at the exact center of that hole, but the contributions to the phase from holes burned at other frequencies may cause the phase to be different from that which would be associated with the gain alone. At any given frequency, in other words, the phase depends on the shape of the entire profile.

Now that we have an idea of what the self-consistency equations tell us, and do not tell us, about the shape of $\chi''(E,\nu)$ and $\chi'(E,\nu)$, let us try to solve them.

Equation 7.1 and Equation 7.2 comprise two equations in two unknown quantities. They can be simultaneously solved for E and ν if expressions for $\chi''(E,\nu)$ and $\chi'(E,\nu)$ are available.

Example: Lasing Frequency in a Homogeneously Broadened Gain Medium

Let us first consider the lasing frequency of a single mode ring laser, using a homogeneously broadened gain medium. We will approximate the susceptibility of this medium by using an expression for the absorption of a two-level system, with the sign changed. This has the correct mathematical form, in that it is a saturatable Lorentzian function. Simply sticking a negative sign on the standard (see Chapter 3) equation for the imaginary part of the susceptibility in a two-level system gives us:

Equation 7.5: $\chi'' = -\frac{N_i \hbar \Omega_{ri}}{\varepsilon_0 E^2}\left(\frac{\Omega_{ri}\Gamma_i}{2\Omega_{ri}^2 + \Gamma_i^2 + 4(\nu - \nu_0)^2}\right)$

$use\ \Omega_{ri} = \frac{\mu E}{\hbar}, \Gamma_i = \frac{\nu_0{}^2 \mu^2}{3\pi\varepsilon\hbar c^3}, \Rightarrow \mu^2 = \frac{3\pi\varepsilon_0 \hbar c^3 \Gamma_i}{\nu_0{}^2}\ \ and\ let\ \Omega^2 = \Gamma_i^2 \xi_i E^2 \ \Rightarrow\ \xi_i = \frac{3\pi\varepsilon_0 c^3}{\nu_0{}^2 \Gamma}$

Equation 7.6: $\chi'' = -H\left(\frac{1}{\xi_i B + 1 + 4\delta^2}\right)$

$where\ \ B = 2E^2;\ \ \delta = (\nu - \nu_0)/\Gamma_i,\ \ H = \frac{N_i \hbar \xi_i \Gamma_i}{\varepsilon_0}$

Starting with the corresponding expression for the real part of the susceptibility gives us:

Equation 7.7: $\chi' = -\frac{N_i \hbar \Omega_{ri}}{\varepsilon_0 E^2}\left(\frac{2\Omega_{ri}(\nu_0 - \nu)}{2\Omega_{ri}^2 + \Gamma_i^2 + 4(\nu_0 - \nu)^2}\right)$

Therefore:

Equation 7.8: $\chi' = 2\delta H\left(\frac{1}{\xi_i B + 1 + 4\delta^2}\right)$

Figure 7.5, below, shows the unsaturated gain profile $-\chi''(B=0,\delta)$ plotted on the same axes as $1/Q$.

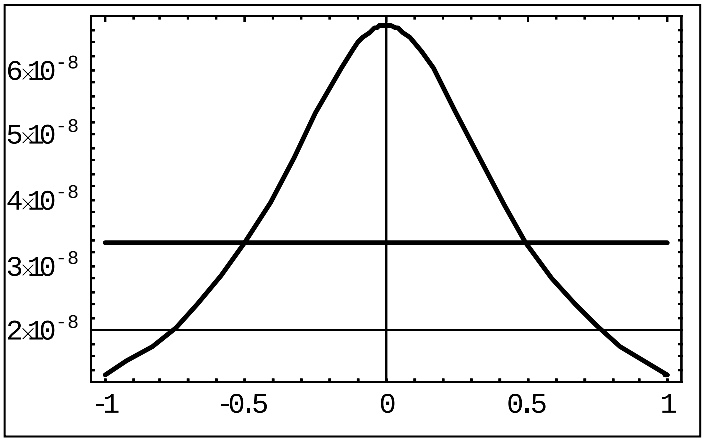

Figure 7.5: Homogeneously broadened unsaturated gain $-\chi''(B=0,\delta)$ and (constant) loss as a function of frequency

Similarly we may plot $\chi'(B=0,\delta)$, to get an idea of its unsaturated shape:

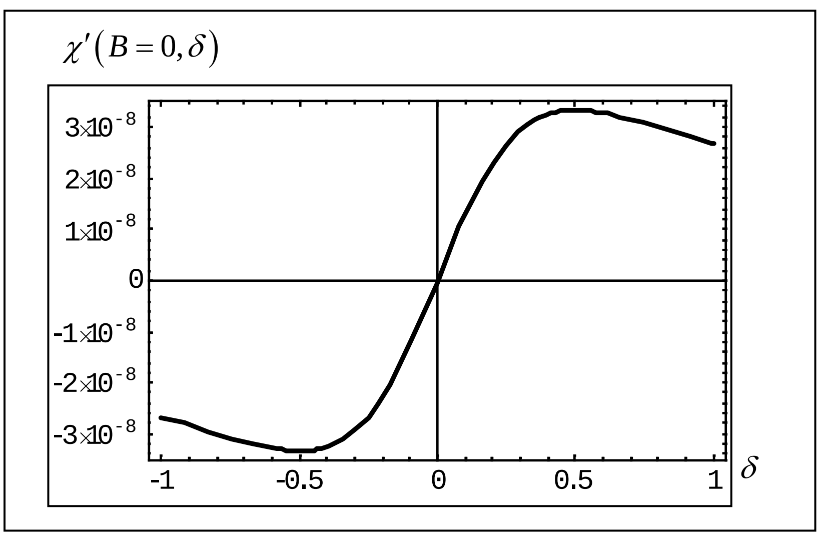

Figure 7.6: Dispersion profile $\chi'(B=0,\delta)$ corresponding to homogeneously broadened unsaturated gain

The values for the constants used in these plots and all those to follow in this section are given in the table below.

```
H=2/Q;
Q=m*F;
F=300;
m=10^5;
Γ =10^7;
ω0 =2* π *3.8*10^14;
ξe =0.00005864869566283799`
```

We can plug these non-dimensionalized expressions for $\chi''(B,\delta)$ and $\chi'(B,\delta)$ into Equation 7.1 and Equation 7.2 (though we must express the frequencies in these equations in the same non-dimensionalized way). From the $\chi''(B,\delta)$ equation, we find

Equation 7.9: $B = \dfrac{HQ-(1+4\delta^2)}{\xi_i}$

This is proportional to the steady-state intensity. Plotting that (and remembering that delta equals one when $(\nu-\nu_0)=\Gamma$) gives us the inverted parabola illustrated in Figure 7.7, below:

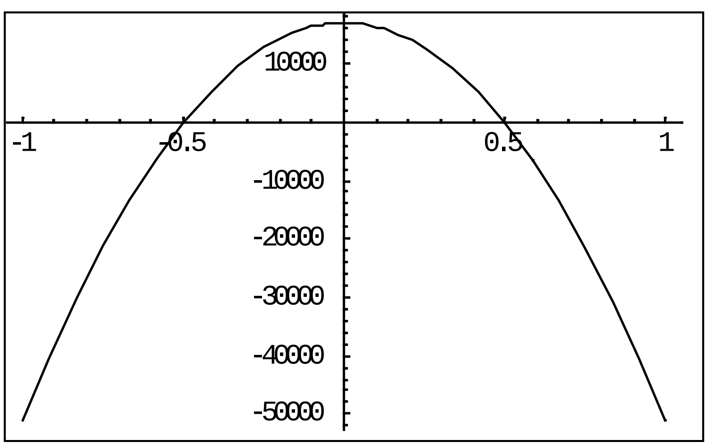

Figure 7.7: Plot of $B = 2E^2$ as a function of frequency corresponding to homogeneously broadened unsaturated gain

Note that Figure 7.7 shows B is negative for values of δ greater than 0.5. Since B represents the intensity, which cannot physically be negative, this is an indication that we are applying the equation in a regime where it is meaningless. Comparing Figure 7.7 and Figure 7.5, we see that the frequency range over which the unsaturated gain is greater than the loss matches the frequency range over which we get positive numbers for the intensity. The equation only applies to a lasing cavity, and the cavity can only lase if the initial gain is greater than the loss.

Plugging the expression $B(\delta)$ in Equation 7.9 into the expression for $\chi'(B,\delta)$ in Equation 7.7 gives us

Equation 7.10: $$\chi' = 2\delta\left(\frac{1}{Q}\right) = 2\frac{(\nu-\nu_0)}{\Gamma}\left(\frac{1}{Q}\right)$$

This is a linear function which goes to infinity and or negative infinity for large detunings, a result which will not sound so unphysical if we keep in mind that the equations we used to calculate this expression apply only over the region from $\delta = -1/2$ to $\delta = 1/2$. $\chi'(\delta)$ is plotted below, in Figure 7.8.

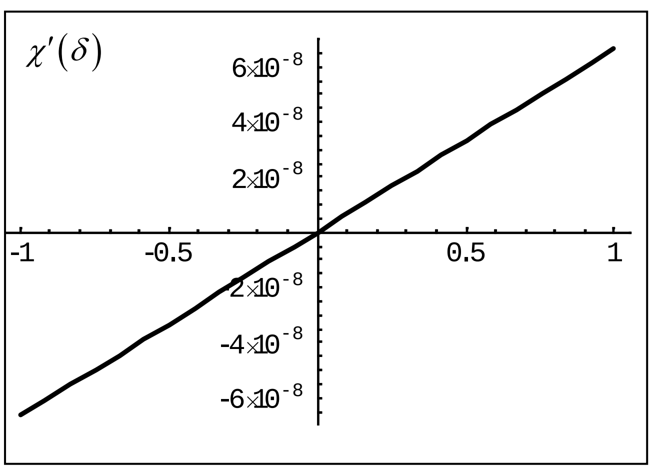

Figure 7.8: Plot of lasing dispersion $\chi'(\delta)$ as a function of lasing frequency in saturated gain medium.

Note that what we have plotted here, $\chi'(\delta)$, is not in the usual sense a dispersion profile. It is not a dispersion profile for the same reason that the plot in Figure 7.9 (below) of $\chi''(\delta)$ is not a gain profile:

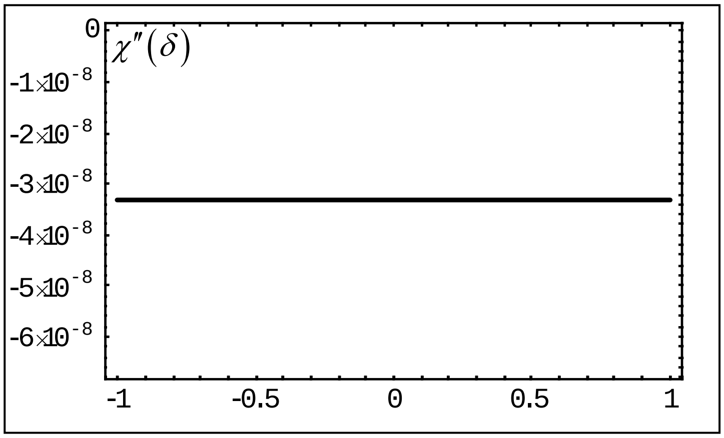

Figure 7.9: Plot of saturated gain $\chi''(\delta)$ as a function of lasing frequency

The straight line at -1/Q reflects the fact that, whatever the gain profile may look really like (in this case, like Figure 7.1), it is equal to 1/Q at the lasing frequency, and every frequency which we are considering here is a lasing frequency. We can change the lasing frequency by changing the cavity length, but we will always dynamically change χ'' as well in doing so, to make it equal to -1/Q. They are not, as before, graphs of $\chi''(E_L,\omega)$ and $\chi'(E_L,\omega)$ for constant values of E_L. In our previous graphs, E_L was chosen to be the steady state lasing intensity for a particular frequency, but was then held constant as we plotted the functions for other frequencies. Instead, these are graphs of $\chi''(E(\nu),\nu)$ and $\chi'(E(\nu),\nu)$. Each value of ν actually corresponds to a different cavity length, and gives rise to a different steady state field strength.

These plots of χ'' and χ', since they do not represent a real gain and dispersion profile but rather map out this dynamic response to changes in cavity length, are not subject to the

Kramers-Kronig relations, and are furthermore not physically meaningful outside the lasing bandwidth of $-.5\Gamma \text{ to} .5\Gamma$.

We will call the variation of χ' with lasing frequency, plotted in Figure 7.8, the "lasing dispersion" to distinguish it from what we will call the "natural dispersion" given by the variation of $\chi'(\omega)$ as plotted, for instance, in Figure 7.3.

What these plots, Figure 7.8 and Figure 7.9, do show is that even though the gain may have the same value at any lasing frequency, no matter what the profile, the real part of the susceptibility will vary with the lasing frequency.

Finally, we can plug Equation 7.10 into Equation 7.2 and solve for a relationship between the lasing frequency ν and the length.

$$(\Omega-\nu)-\frac{1}{2}\nu\chi'=0$$

(From Equation 7.2)

$$(\Omega-\nu)-\nu\left(\frac{(\nu-\nu_0)}{\Gamma Q}\right)=0$$

(Plugging in Equation 7.10)

As it turns out, solving this for ν, while perfectly possible, is not very enlightening, due to its quadratic form. Let us solve it instead for the empty cavity resonance frequency Ω.

Equation 7.11: $$\Omega=\nu\left(\frac{(\nu-\nu_0)}{\Gamma Q}+1\right)=\frac{2\pi mc}{L}$$

This tells us a length corresponding to any lasing frequency we choose, assuming we know the Q of our cavity and the center frequency of our gain and its linewidth, and assuming that our lasing medium has the single homogeneously broadened gain profile that we assumed in our model. We could, as noted, also solve this quadratic equation for ν if we wish, and then choose the solution that is physically meaningful, and express ν in terms of the length directly by recalling that :

$$\Omega = \frac{2\pi mc}{L}$$

(From Equation 7.4)

In this way we can now calculate by exactly how much our cavity mode is "pulled."

This simple calculation points the way toward our goal of using dispersion to enhance the sensitivity to length changes of a resonating single-mode cavity.

Example: Lasing Frequency with Inhomogeneously Broadened Gain

We explained at the beginning of the chapter that in an inhomogeneously broadened medium, a hole is burned in the broadened gain profile at any lasing frequency, and that because saturation does not reduce the gain over the entire profile in this type of medium, there may be more than one lasing frequency. We claimed that the susceptibility of this type of system can be modeled by treating the gain in the system as the sum of a single broad gain profile and narrower effective absorption profiles centered around each lasing frequency, adding up to give a net gain equal to the loss in the cavity (at the lasing frequency.) The natural dispersion profile is then, as illustrated in Figure 7.4, the sum of the dispersion profiles due to the gain peak and those due to the dips. At any given lasing frequency, the contribution to the total χ' from the effective absorption induced by that lasing field at that frequency is zero, because the lasing frequency will necessarily be at the center of the dip it induces, and thus at the zero-crossing of the associated dispersion. Therefore the total χ' experienced by a lasing mode is the sum of the χ' associated with the broad gain profile, and that associated with the effective absorptions induced by *other* lasing modes (or by any other hole burning mechanisms, such as mirror-image hole burning in two-mirror cavities.[7])

Let us now imagine an inhomogeneously broadened laser which lases in just one mode. This may be because the cavity free spectral range is broad enough compared with the gain profile that only a single mode experiences sufficient gain, or it may be because frequency-selective intracavity elements are used to impose losses on the other modes. In any case, it is a single-mode laser.

In this case, since there are no other lasing modes, we must conclude that the lasing dispersion is in fact identical to the natural dispersion. Why? The gain profile, under the lasing condition, looks exactly like the unsaturated gain profile except that it has a single dip at the lasing frequency. The net χ'_{net} is the sum of the χ'_{gain} due to the unsaturated gain and the χ'_{dip} associated with that dip, $\chi'_{net} = \chi'_{gain} + \chi'_{dip}$. The phase shift associated with the dip is always zero at the lasing frequency, $\chi'_{dip}(\nu) = 0$, so that at the lasing frequency, $\chi'_{net} = \chi'_{gain}$.

In this case, the profile we plot for $\chi'(E(\nu), \nu)$ should be identical to that which we would get by holding E constant ($E = E_L$)as we have been doing so far in this section.. This method will not work for experimentally determining the lasing dispersion of a homogeneous laser, but it will allow us to experimentally determine the lasing dispersion of an inhomogeneous laser.

The fact that the lasing dispersion is identical to the natural dispersion in an inhomogeneously broadened medium makes such a laser, in some senses, much easier to understand and model.

For instance, consider the following gain medium. This is a plot of the type described in detail above, in which the lasing frequency is constant, but a hypothetical weak probe is scanned to observe the unsaturated gain profile and the "hole" burned by the lasing beam.

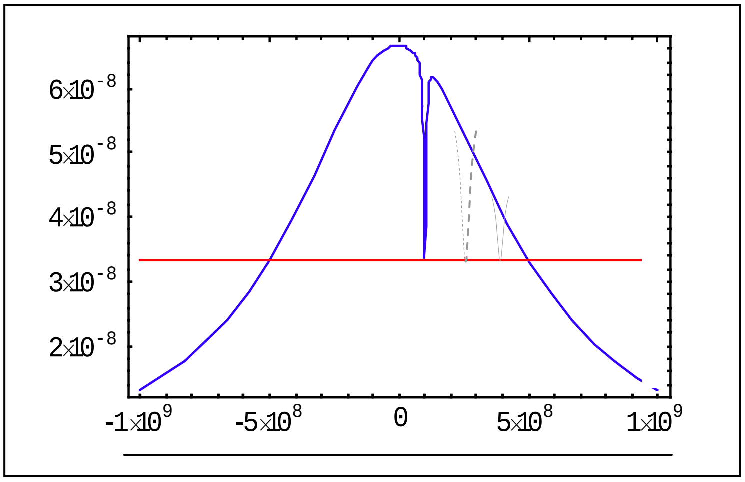

Figure 7.10: Profile of $\chi''\left(\delta_{probe}\right)$ for inhomogeneously broadened medium with spectral hole burned by the lasing beam. Spectral holes corresponding to other cavity lengths as shown as dotted lines.

Plotting the real part of the susceptibility for a similar hypothetical probe beam produces something which has the lineshape of the negative derivative of this function, as we would expect from the Kramers-Kronig relations:

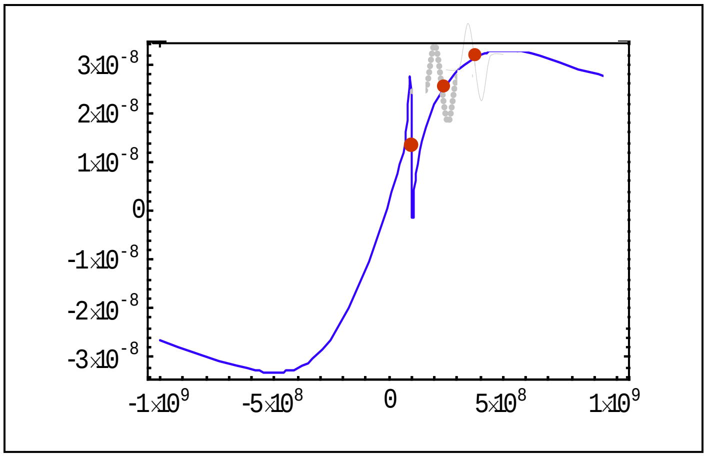

Figure 7.11: Profile of $\chi'\left(\delta_{probe}\right)$ for inhomogeneously broadened medium with dispersion corresponding to spectral hole burned by the lasing beam. Dispersion effects due to spectral holes at other frequencies, corresponding to other cavity lengths shown as dotted lines.

The only way to scan the frequency of the lasing beam is to change the length of the cavity. Plotting the gain at the lasing frequency as a function of the lasing frequency, rather than that of a hypothetical probe, produces the same kind of straight line at -1/Q that we saw in Figure 7.9.

Plotting the real part of the susceptibility as a function of the *lasing* frequency, however, produces a profile which lacks any sign of the "kink" due to the spectral hole. Indeed, since the spectral hole is in a different location for each point on this graph, it would be impossible to identify a frequency at which such a kink should occur. However, in this case the graph as a function of lasing frequency is otherwise identical to that for the plot of the hypothetical probe frequency in all other respects. This is different than what we saw in the homogeneous case.

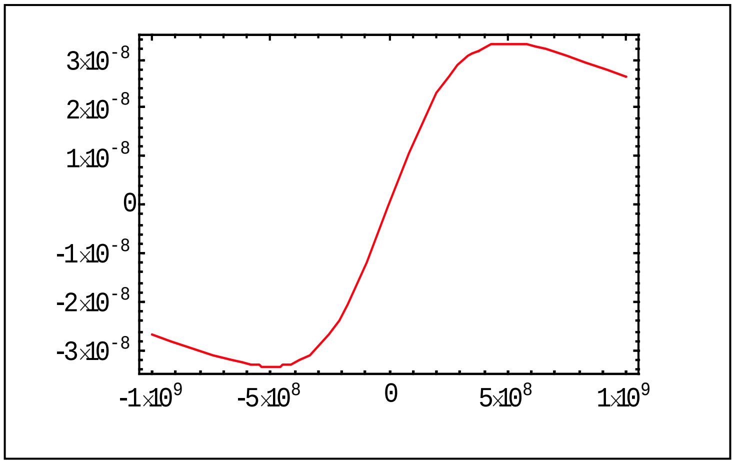

Figure 7.12: Profile of $\chi'\left(\delta_{lasing}\right)$ for inhomogeneously broadened medium

Of course, if the laser is multi-mode, the effect of the spectral holes burned by the other lasing modes does have to be taken into account, and this is also the case if the lasing is bidirectional, and the counter-propagating beam lases at a different frequency, as in a gyroscope.

Sensitivity to Length Changes

Let us recall how the resonance frequency of an empty cavity changes when the cavity length is changed. We can take the derivative of Equation 7.4 with respect to L to find:

Equation 7.12: $$\frac{d\Omega}{dL} = \frac{-2\pi mc}{L^2}$$

This expression tells us the local slope of $\Omega(L)$ at a given L value, but it is sometimes more convenient to specify a value of Ω rather than L. Knowing L, of course, determines Ω. In fact, we can simply substitute $L = \dfrac{2\pi mc}{\Omega}$ into Equation 7.12 to find:

Equation 7.13: $$\frac{d\Omega}{dL}=\frac{-2\pi mc}{\left(\frac{2\pi mc}{\Omega}\right)^2}=\frac{-\Omega^2}{2\pi mc}$$

Alternatively, we could have solved Equation 7.4 for L, taken the derivative with respect to Ω, and inverted the result:

$$L=\frac{2\pi mc}{\Omega}$$
$$\frac{dL}{d\Omega}=\frac{-2\pi mc}{\Omega^2}$$

Equation 7.14: $$\frac{d\Omega}{dL}=\frac{-\Omega^2}{2\pi mc}$$

This gives us the same expression, and this is the approach we will use later.

What this expression tells us, however we arrive at it, is how much the resonance frequency of the cavity changes when its length is changed. We have defined this rate of change of resonance frequency as the *sensitivity,* S, of the cavity. Throughout this paper, "sensitivity" refers to the sensitivity of the resonance frequency to changes in the cavity length. The sensitivity of an empty cavity is given by:

Equation 7.15: $$S_{empty}\equiv d\Omega/dL$$

We would like to know what effect a dispersive medium has on this sensitivity. In particular, we would like to know the ratio

Equation 7.16: $$R_S\equiv\frac{S_{dispersive}}{S_{empty}}=\frac{dv/dL}{d\Omega/dL}$$

Ideally, we would like a general expression which applies to any type of dispersion. We can find this expression directly from Equation 7.2, by taking the derivative with respect to L.

$$(\Omega-\nu)-\frac{1}{2}\nu\chi'(E,\nu)$$

(from Equation 7.2)

Taking the derivative of each term, we get

Equation 7.17: $$\left(\frac{d\Omega}{dL}-\frac{d\nu}{dL}\right)-\frac{1}{2}\left(\frac{d\nu}{dL}\chi'(E,\nu)+\nu\frac{d\chi'(E,\nu)}{dL}\right)=0$$

It is worth pausing here to describe what is meant by $d\chi'/dL$. If we change the length of our laser cavity, we will change the empty cavity resonant frequency Ω. If Ω changes, then the lasing frequency and field amplitude ν and E which were simultaneous solutions for Equation 7.1 and Equation 7.2 with the original Ω, will no longer solve Equation 7.2. If we change L, in other words, we are forced to solve Equation 7.1 and Equation 7.2 all over again for new values of ν and E , and when we plug those new values of ν and E into the expression for $\chi'(E,\nu)$ we will get a new value for χ', Every different L corresponds to a different $\chi'(E,\nu)$, and hence it is meaningful to try to take a derivative $d\chi'/dL$.

However, because the mechanism by which L changes χ' is indirect, it is also natural to write this derivative in terms of the way in which each changes with respect to ν.

Equation 7.18: $$\frac{d\chi'}{dL}=\frac{d\chi'}{d\nu}\frac{d\nu}{dL}$$

$$\left(\frac{d\Omega}{dL}-\frac{d\nu}{dL}\right)-\frac{1}{2}\left(\frac{d\nu}{dL}\chi'(E,\nu)+\nu\frac{d\chi'}{d\nu}\frac{d\nu}{dL}\right)=0$$

$$\frac{d\nu}{dL}\left(1+\frac{1}{2}\chi'+\frac{1}{2}\nu\frac{d\chi'}{d\nu}\right)=\frac{d\Omega}{dL}$$

Equation 7.19: $$R_S=\frac{d\nu/dL}{d\Omega/dL}=\frac{1}{\left(1+\frac{1}{2}\chi'+\frac{1}{2}\nu\frac{d\chi'}{d\nu}\right)}$$

Equation 7.19 is the key result of this section. It tells us how we may enhance the sensitivity of a lasing cavity by manipulating the susceptibility of the intracavity medium. We can make R_s larger than one, which means our dispersive cavity is more sensitive than our empty cavity, if the quantity in the denominator is less than one.

At this point we must note that the quantity in the denominator bears a striking resemblance to another quantity which is frequently used in optics.

As we have discussed earlier, the velocity with which a pulse propagates in a medium, or group velocity, is in general given by $v_g=c/n_g$, for a pulse with a center frequency of ω_0

Equation 7.20: $$n_g=n(\omega_0)+\left.\frac{dn}{d\omega}\right|_{\omega_0}\omega$$

This equation is derived, for instance in Reference 9. Recalling that $n(\omega)=1+\chi'(\omega)/2$ and that therefore $dn/d\omega=(1/2)d\chi'/d\omega$, we see that the expression for group index n_g is almost identical to the denominator of R_s.

The difference is that the frequency ν in Equation 7.19 has a specific meaning. It is the lasing frequency of the cavity, a solution to the self-consistency equations.

In particular, we must again distinguish carefully between the graph of the lasing dispersion $\chi'(\nu)$ displayed in Figure 7.8 and the graph of the natural dispersion $\chi'(\omega)$ displayed in Figure 7.3. Figure 7.3 assumes a fixed cavity length and fixed electric field strength. It is a physical response function which must obey the Kramers-Kronig relations (taking into account the saturation effects). It is the susceptibility that a weak probe would see if it were combined with the intracavity beam through a beamcube, allowed to co-propagate with it through the medium, and then reflected out of the cavity by a second beam cube before completing a full round trip. This hypothetical non-resonating weak probe could be of any frequency, and its frequency could be scanned independent of the length of the cavity, unlike the lasing frequency. If this weak probe were pulsed, the group index of the pulse would depend on the local slope of $\chi'(\omega)$ as depicted in Figure 7.3.

In Figure 7.8, on the other hand, the electric field strength and the length of the cavity are assumed to change as ν is scanned. Each ν on this graph is a steady-state lasing mode for a different cavity length.

The group velocity of a pulse made up only of lasing modes would indeed depend on the slope of a graph of $\chi'(\nu)$ produced the same way as the graph depicted in Figure 7.8 (recall that $\delta = \nu / \Gamma$). However Figure 7.8 itself actually depicts $\chi'(\nu)$ for a homogeneously broadened gain medium, which can only support a single lasing mode, so though we can calculate the quantity $1+\frac{1}{2}\chi'+\frac{1}{2}\nu\frac{d\chi'}{d\nu}$ for this medium, we cannot ever interpret it as a group velocity for this particular case.

The only way the denominator of R_s can be interpreted as a group velocity, then, is if the cavity contains an inhomogeneously broadened gain medium which supports multiple lasing modes. In such a cavity, pulses may be supported in steady-state. Every frequency component of the pulse would be a lasing mode of the cavity. This is the case, for example, for the pulses in mode-locked lasers[7]. If the laser gain medium is inhomogeneously broadened, the denominator of R_s can be interpreted as the velocity of such a pulse. Group velocities greater than c have been experimentally observed in such lasers.[30],[31]

Example: Sensitivity of Laser with Homogeneously Broadened Gain

Let us return now to the example of the laser with the single homogeneously broadened gain peak. We have seen how its steady state susceptibility, both real and imaginary, vary with lasing frequency, in Figure 7.8 and Figure 7.9. Let us consider the effect of this variation in $\chi'(\nu)$, the lasing dispersion, on the sensitivity of the laser:

$$\chi' = 2\delta\left(\frac{1}{Q}\right) = 2\frac{(\nu-\nu_0)}{\Gamma}\left(\frac{1}{Q}\right)$$

(From Equation 7.10)

$$\frac{d\chi'}{d\nu} = \frac{2}{\Gamma Q}$$

$$R_S = 1\Big/\left(1+\frac{1}{2}\chi'+\frac{1}{2}\nu\frac{d\chi'}{d\nu}\right) = 1\Big/\left(1+\frac{(\nu-\nu_0)}{\Gamma}\left(\frac{1}{Q}\right)+\frac{\nu}{\Gamma Q}\right)$$

Equation 7.21: $$R_S = 1\Big/\left(1+\frac{1}{\Gamma Q}(2\nu-\nu_0)\right)$$

For any $\nu > \nu_0/2$, that denominator is greater than one. Keep in mind that all of these expressions are derived from Equation 7.2, which is only valid over the range $\delta = -0.5$ to $\delta = 0.5$ or $\nu = \nu_0 - \Gamma/2$ to $\nu = \nu_0 - \Gamma/2$, and it becomes obvious that for optical frequencies and realistic transition linewidths, $R_s < 1$, meaning that the dispersive cavity is, in this case, less sensitive than the empty cavity.

We can see this graphically too. In Equation 7.11 we solve the self-consistency equations for Ω. But since $L = 2\pi mc/\Omega$, we can also write:

Equation 7.22:
$$L = 2\pi mc \Big/ \nu\left(\frac{(\nu - \nu_0)}{\Gamma Q} + 1\right)$$

We can plot this over the linewidth of the gain (remembering that the physical region is only been $\delta = -0.5$ and $\delta = 0.5$) to see how the relationship between length and lasing frequency differs in the dispersive-medium cavity and the empty one.

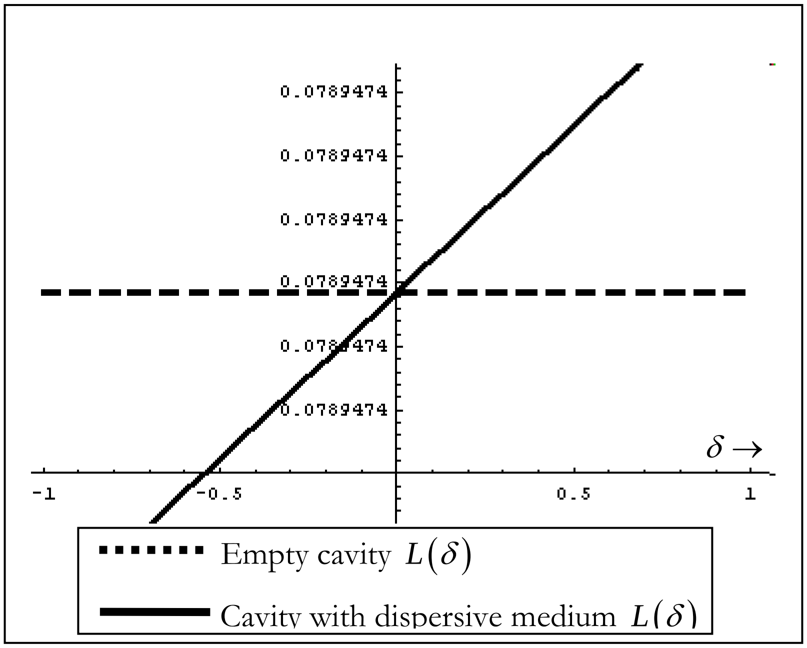

Figure 7.13: Length of cavity as a function of cavity resonant frequency, for empty cavity and cavity with dispersive medium.

The thing to note about this graph is that $dL/d\delta$ is greater for the cavity with the dispersive medium than it is for the empty cavity. This implies that $d\delta/dL\left(=1/\left(dL/d\delta\right)\right)$ is smaller for the cavity with the dispersive medium than in is for the empty cavity. And that means that a change in the length of the dispersive cavity causes a smaller change in resonance frequency than a change in the length of the empty cavity. Thus a laser cavity with this type of homogeneous gain is, in this sense, less suited for use in optical gyroscopes than an empty cavity would be due to the mode pulling effect of the gain. Of course, in reality practical considerations such as the narrowness of the laser linewidth in comparison to that of an empty cavity, and the fact that it automatically adjusts to changes in its length, make it a much better solution in spite of this problem.

We can compare the derivatives of these graphs plotted vs. frequency as well, to note how much less sensitive the laser gyro is for any given choice of resonant frequency. We will define this ratio as

Equation 7.23: $$R_{S(freq)}\left(\omega_{res}\right)=\frac{dL_{empty}/d\omega_{res}}{dL_{dispersive}/d\omega_{res}}$$

where $\omega_{res}=\Omega$ for the empty cavity and $\omega_{res}=\nu$ for the cavity with the dispersive medium. It is comparable to the ratio R_s defined in Equation 7.21. Specifically, R_s compares those derivatives for a common value of L, comparing empty and medium-filled cavities of the same length, which resonate at different frequencies. $R_{S(freq)}$, on the other hand, compares the derivatives for a common value of the resonance frequency, comparing empty and medium-filled cavities of different lengths, which resonate at the same frequency. Both are useful metrics, (and both give very similar numeric values in this case) but R_s is simpler to calculate analytically, while $R_{S(freq)}$ is simpler to graph, being simply the ratio of the slopes of the lines plotted in Figure 7.13. The curvature of those lines is not obvious on this scale, but the graph in Figure 7.14 below demonstrates that those slopes, and the ratio between them, do in fact vary slightly with frequency.

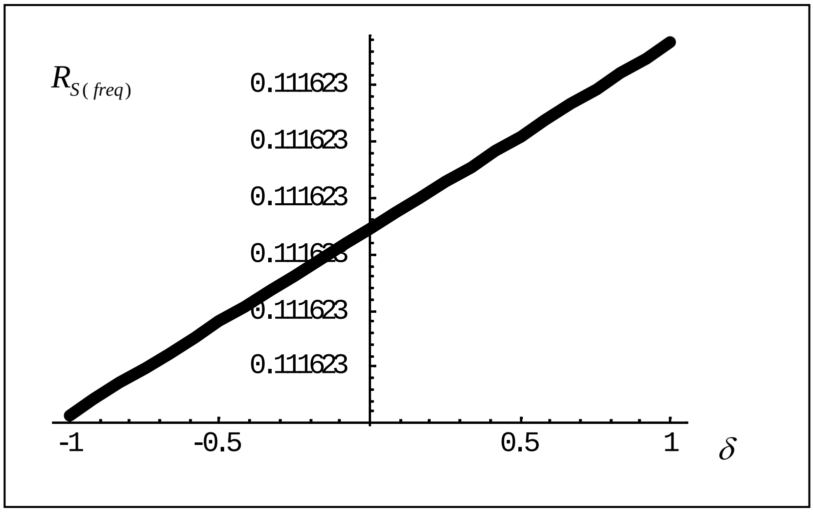

Figure 7.14: The ratio $R_{S(freq)}$ of the slopes of the solid and dotted lines in Figure 7.13

For all of the meaningful values (again, between $\delta = -0.5$ and $\delta = 0.5$) we see that the medium filled cavity is much less sensitive to length changes than the empty cavity. This ratio remains always less than one. Ideally, for a laser gyroscope, we would prefer that this ratio (or the related ratio R_s, depending on how we choose to compare the cavities) be greater than one. In fact we would prefer it to be as large as possible.

Example: Sensitivity of a Laser with Inhomogeneously Broadened Gain

Because the lasing dispersion is identical to the natural dispersion in a single-mode, inhomogeneously broadened laser (see the Example: Lasing Frequency with Inhomogeneously Broadened Gain section) we can take the derivatives required by Equation 7.19 easily.

Equation 7.24: $$R_s = \frac{1}{\left(1+\frac{1}{2}\chi'(\nu)+\frac{1}{2}\nu\frac{d\chi'(\nu)}{d\nu}\right)} = \frac{1}{\left(1+\frac{1}{2}\chi'(\omega)+\frac{1}{2}\omega\frac{d\chi'(\omega)}{d\omega}\right)\bigg|_{\omega=\nu}}$$

This relationship holds for inhomogeneously broadened gain media only.

For example, consider a medium with the inhomogeneously broadened gain profile illustrated below.

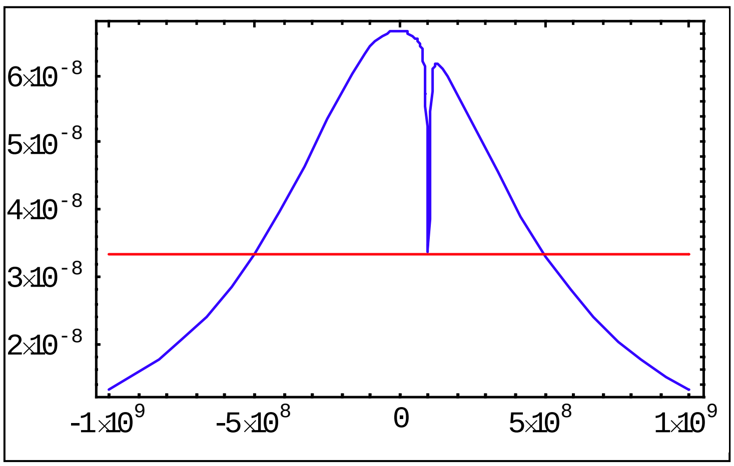

Figure 7.15: Inhomogeneously broadened gain profile as a function of hypothetical probe frequency (depicted with spectral hole burned by lasing beam.)

In this case, the corresponding index profile, as a function of lasing frequency, has the lineshape of the negative derivative of that gain profile (without the hole). We can plot the length as a function of resonant frequency for the lasing cavity and the empty cavity:

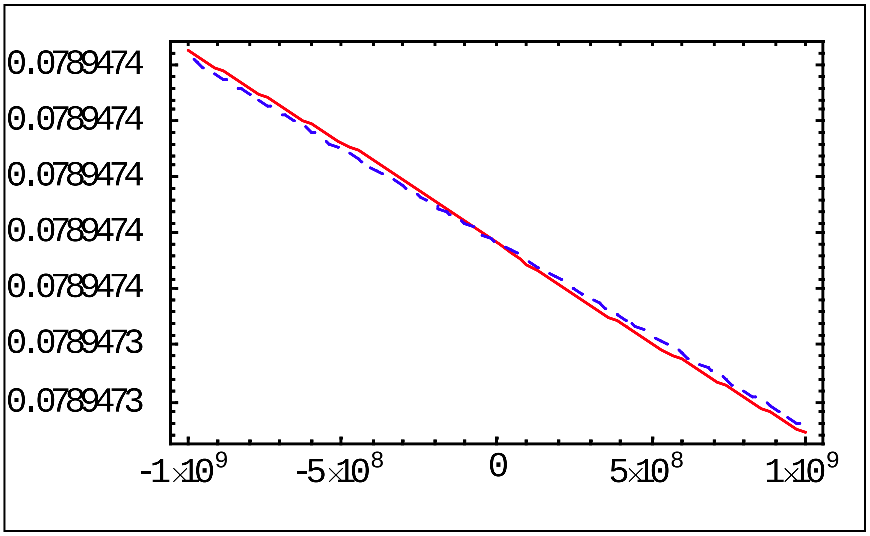

Figure 7.16: Cavity length as a function of resonant frequency for empty cavity (dashed) and inhomogeneously broadened laser (solid)

Finally, we can plot the ratio of the slopes of these lines as a function of frequency.

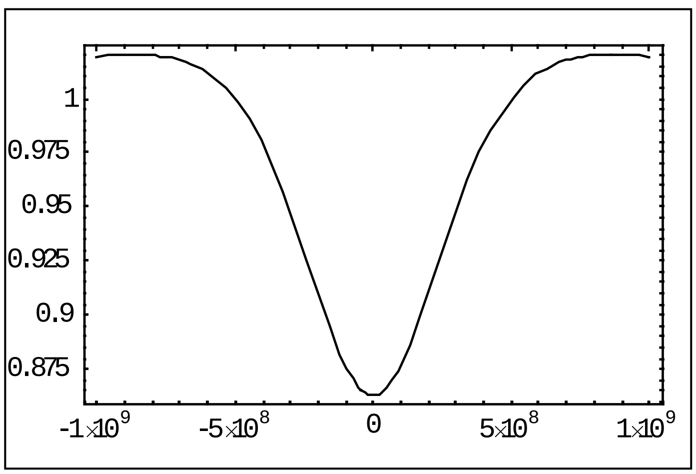

Figure 7.17: Ratio of sensitivity of resonant frequency for laser cavity in an example homogeneously broadened medium to that of an empty cavity, as a function of frequency.

We conclude that the mode-pulling due to the gain peak actually makes laser gyroscopes slightly less sensitive than empty cavities for small rotations, though this disadvantage is more than balanced by other advantages.

Example: Sensitivity of a Laser with Inhomogeneously Broadened Gain and Dip

We have seen that the ratio R_s given by Equation 7.21 depends on what we have called the "lasing dispersion" of the medium, the variation in χ' as a function of lasing frequency ν (which cannot be altered independently of the cavity length.)

We have also seen that a "natural dispersion" profile with a positive slope, i.e., normal dispersion, such as that depicted in Figure 7.6 and associated with a gain peak, gives rise to a lasing dispersion which also has a positive slope, as depicted in Figure 7.8. For this reason we might expect that what we need in order to get a sensitivity enhancement (an increase in R_s) is a medium which has an anomalous natural dispersion. If this gives rise, by the process described in the "Self-Consistency Equations" section, to an anomalous lasing dispersion, i.e. a $d\chi'(\nu)/d\nu < 0$ then we can make the denominator of the expression in Equation 7.21 less than one, which would make $R_s > 1$.

We need an anomalous lasing dispersion, and an anomalous natural dispersion is the obvious place to start.

How can we achieve an anomalous natural dispersion? Generally, anomalous dispersion is associated with either 1) an absorption feature, 2) a dip in a gain profile, i.e., a local reduction in gain, or 2) the valley between two gain peaks. All of these are very similar physically, of course. We have seen that with the inhomogeneously broadened medium, the lasing dispersion is identical to the unsaturated dispersion, so we put a dip in the gain, and solve for the depth which will give the appropriate dispersion:

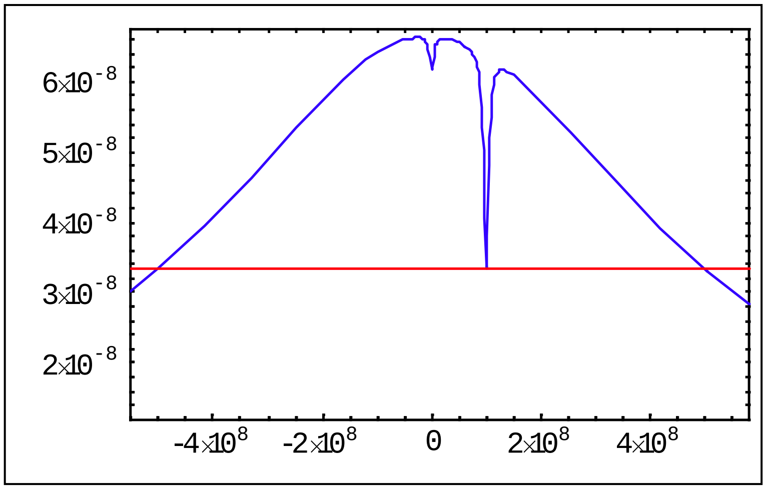

Figure 7.18: Homogeneously broadened gain profile with dip chosen to give dispersion satisfying CAD condition, and a spectral hole.

The resulting dispersion, for a hypothetical probe, would have a kink in it due to the burned hole.

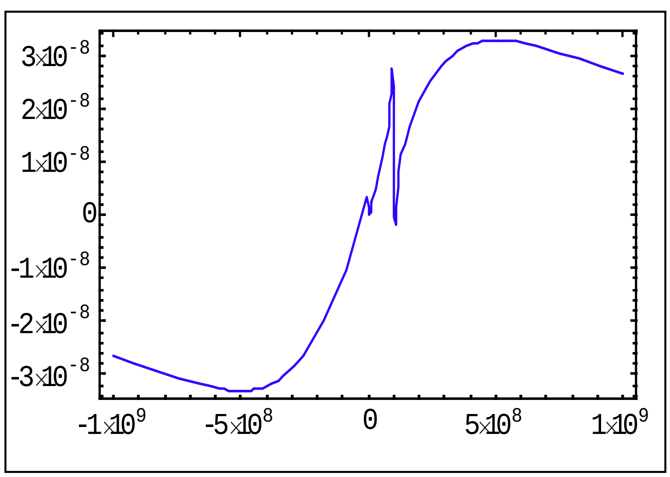

Figure 7.19: Dispersion profile for a hypothetical probe scanned through homogeneously broadened gain profile with spectral hole.

The corresponding lasing dispersion is unaffected by the spectral hole, but still features the small region of anomalous dispersion due to the dip in the inhomogeneous gain profile.

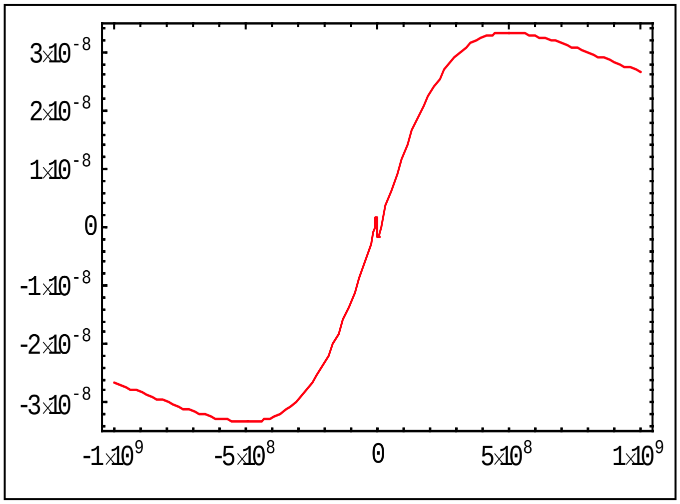

Figure 7.20: Lasing corresponding to homogeneously broadened gain profile with small dip

We can verify that with this type of profile, $\omega_{lasing} n\left(\omega_{lasing}\right)$ still has the region of shallow or zero slope which we saw in the last chapter corresponding to a slow change of phase with frequency and thus to an increased sensitivity.

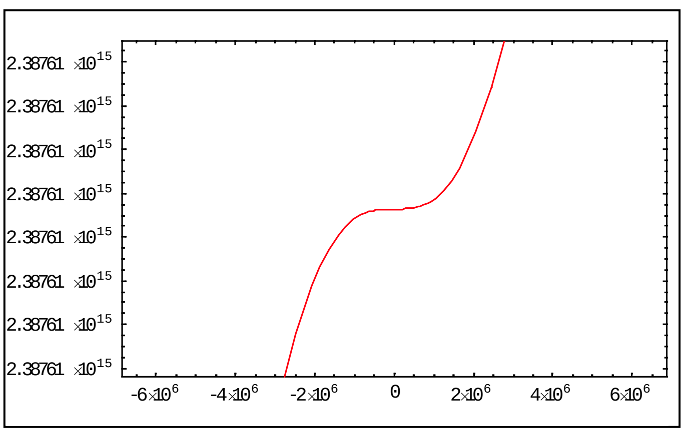

Figure 7.21: $\omega_{lasing} n(\omega_{lasing}, E_{lasing})$, proportional to spatial phase as a function of lasing frequency, is constant over some bandwidth. This shows that the inhomogeneously broadened medium will have the same sensitivity as we saw for the passive WLC, though the linewidth is necessarily narrow.

This suggests strongly that a profile which would give us sensitivity enhancement in the passive case will also give us sensitivity enhancement if the cavity lases.

This is one way of checking the sensitivity. The method described in the previous section of relating the length of the cavity to the lasing frequency also works for this system, and gives the desired result.

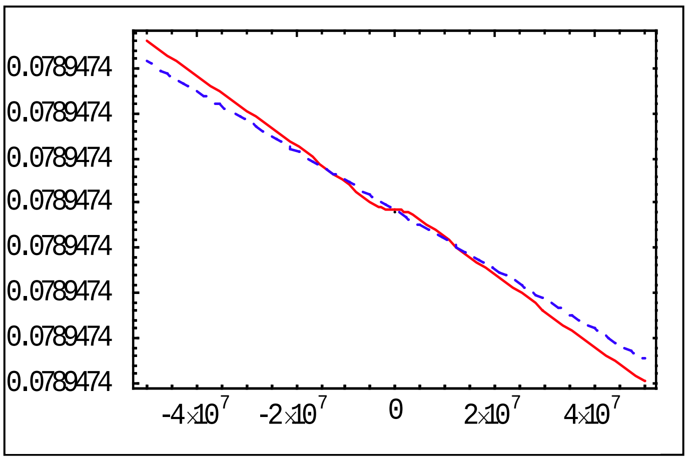

Figure 7.22: Cavity length as a function of resonant frequency for empty cavity (dashed) and inhomogeneously broadened laser with a dip (solid)

Comparing the ratio of the derivatives of these lengths with respect to lasing frequency confirms that enhancement of the type which we derived for passive cavities is achievable in laser cavities too, at least in this inhomogeneously broadened case. (The ratio approaches infinity as the slope of that solid line approaches zero.)

Example: Laser with Homogeneously Broadened Gain and Dip

Let us imagine starting with a homogeneously broadened gain profile somewhat broader in bandwidth than what we have been simulating so far, and imagine that we insert into the cavity along with this gain medium a second, absorbing medium, with an absorption bandwidth that is a small fraction of our gain bandwidth. This has the effect of causing a reduction in the net gain at certain frequencies, centered at the center frequency of the gain. The net susceptibility would be the sum of the susceptibilities of the two media.

Equation 7.25: $$\chi'' = -G\left(\frac{1}{\xi_e B + 1 + 4\delta^2/\Gamma_e^2}\right) + H\left(\frac{1}{\xi_i B + 1 + 4\delta^2/\Gamma_i^2}\right)$$

where now $\delta = (\nu - \nu_0)$, $G = N_e \hbar \xi_e \Gamma_e / \varepsilon_0$, $H = N_i \hbar \xi_i \Gamma_i / \varepsilon_0$, $\xi_j = \frac{\Omega_{r,j}^2}{\Gamma_j^2 E^2} = \frac{3\pi\varepsilon_0 c^3}{\nu_0^2 \Gamma_j}$ $B = 2E^2$,

Equation 7.26: $$\chi' = 2G\delta\left(\frac{1/\Gamma_e}{\xi_e B + 1 + 4\delta^2/\Gamma_e^2}\right) - 2H\delta\left(\frac{1/\Gamma_i}{\xi_i B + 1 + 4\delta^2/\Gamma_i^2}\right)$$

As we did in Figure 7.5 and Figure 7.6, we can plot these with $B = 0$ to get an idea of their unsaturated shape. Those plots are shown in Figure 7.23 and Figure 7.24 below. These plots are from $-\Gamma_e \, to \, \Gamma_e$ (since this time we have not non-dimensionalized the equations). Note that as before the laser equations only apply over regions where $-\chi''(B=0,\delta)$ is greater than $1/Q$, i.e., in this case, from -5×10^8 to 5×10^8 .

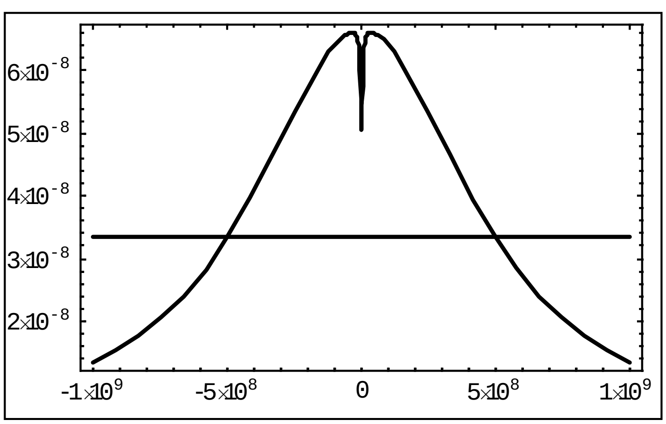

Figure 7.23: Unsaturated, homogeneously broadened profile $\chi''(B=0,\delta)$ with a narrow dip

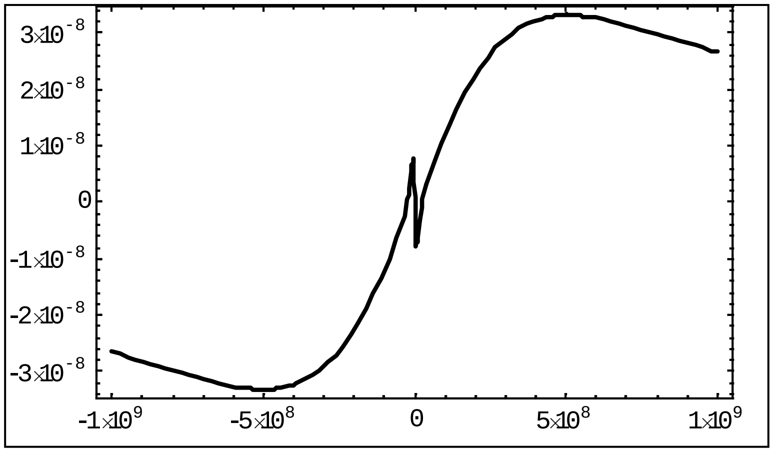

Figure 7.24: Unsaturated dispersion $\chi'(B=0,\delta)$ corresponding to homogeneously broadened gain profile with a dip

The values for the constants used in these plots and in all the plots to follow in this section are given in the table below:

```
G=2/Q;
H=(G-1/Q)/2;
Q=m*F;
F=300;
m=10^5;
Γi =10^7;
Γe =100* Γi ;
ω0 =2* π *3.8*10^14;
ξe = ξi  *(.2865034);
c=3*10^8;
me=9.10938188*10^(-31);
hbar=6.62606896*10^(-34)/(2* π );
ec=1.602176 487*10^(-19);
μ = hbar*ec^2/(2*me*ν0);
ξi = μ^2/(hbar^2*Γi^2)
```

Now we follow exactly the same procedure as in the previous example. We plug this into Equation 7.1 and solve for B as before. The resulting equation for B is much messier than Equation 7.9 and happens to be quadratic in B, but if we plot them (plots that are analogous to

Figure 7.7), one of them, shown in Figure 7.25 below turns out to be negative over the relevant frequency range, which is unphysical, since B is proportional to the intensity. The other, shown in Figure 7.26, has the sort of shape we might expect. The dip in the middle reflects the fact that it takes less intensity to bring the already lower effective gain at the center down to the level of $1/Q$. The two solutions for B are plotted from $\delta = -\Gamma_e$ *to* $\delta = \Gamma_e$:

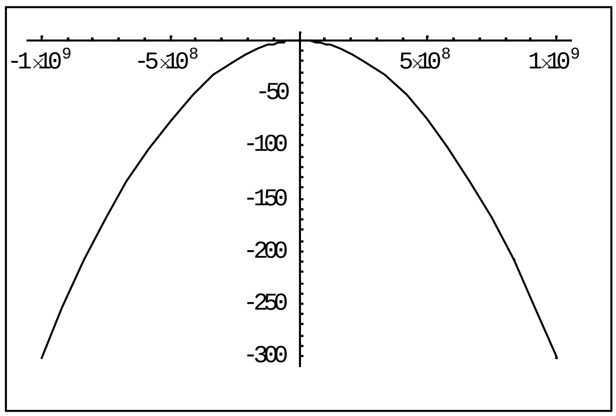

Figure 7.25: The quantity B, proportional to intensity, as function of frequency – unphysical solution

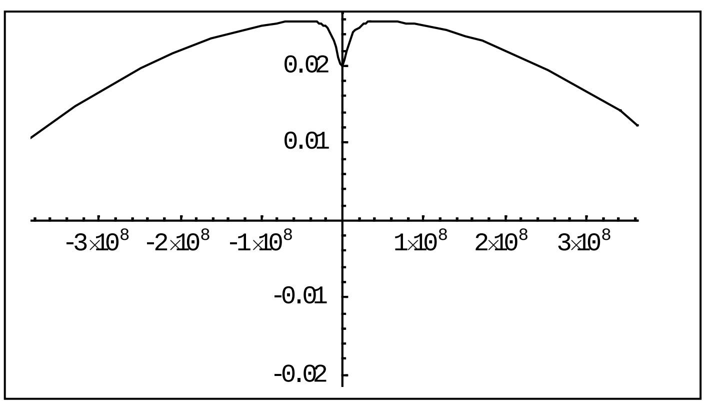

Figure 7.26: The quantity B, proportional to intensity, as function of frequency – physical solution

We will keep the positive solution for B and plug that into Equation 7.26. The resulting plot of the lasing dispersion is analogous to Figure 7.8.

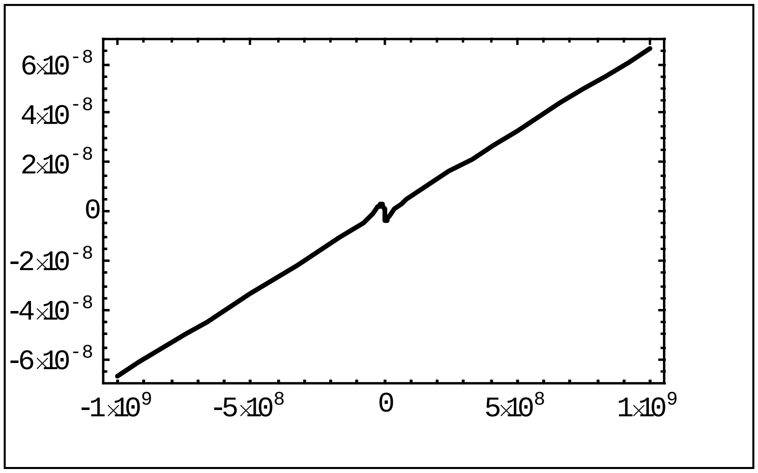

Figure 7.27: Real part of susceptibility as a function of lasing frequency for example system

The graph of the imaginary part of the susceptibility, under lasing conditions, of course looks identical to Figure 7.9, since the lasing gain is always a straight line at the loss value.

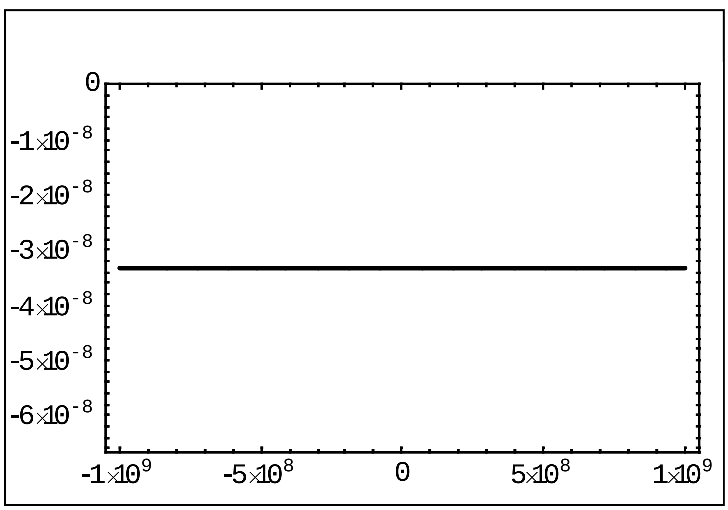

Figure 7.28: Imaginary part of susceptibility as a function of lasing frequency for example system

The expression relating the lasing frequency to the empty cavity resonant frequency is not as simple in this case as in the single-gain case, but we do not really need such an expression. In Figure 7.27 we have all we need to calculate R_s or $R_{S(freq)}$.

Let us first plot the change in length as a function of resonant frequency, in analogy with Figure 7.13, and see what qualitative conclusions we can draw. In this case, in order to show detail, we will only plot the results over the smaller range of $\delta = -1.2\Gamma_i$ to $\delta = 1.2\Gamma_i$, as shown in Figure 7.29, below.

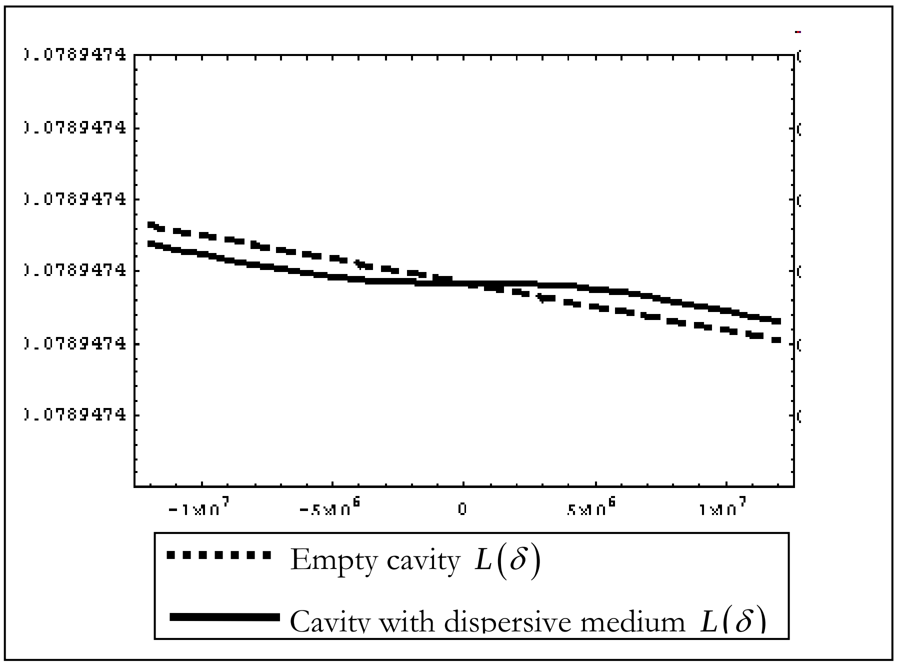

Figure 7.29: Cavity length as a function of resonant frequency for empty cavity and example laser cavity

Note that the length changes more slowly with resonant frequency in the dispersive-medium cavity case than in the empty cavity case. This implies that, as we hoped, the resonant frequency changes more quickly with changes in length, i.e. a small $dL/d\nu$ implies a large $d\nu/dL$. Let us finally plot the ratio $R_{S(freq)}$, over the range of that dip in the gain only, $\delta = -\Gamma_i$ to $\delta = \Gamma_i$

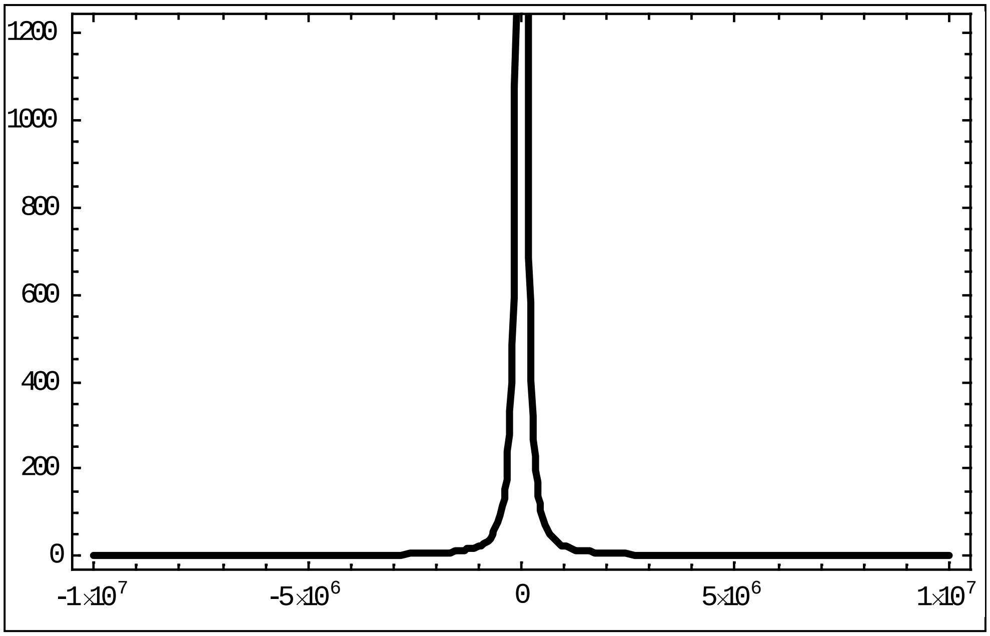

Figure 7.30: Ratio of sensitivity of laser to that of an empty cavity, $R_{S(freq)}$, plotted from $\delta = -\Gamma_i$ to $\delta = \Gamma_i$ for example laser.

The top of that plot will not fit on this scale. Again, there is no physical reason why the ratio cannot be infinite, since the plot for $L(\delta)$ can be completely flat, mathematically. In this case, numerical analysis gives a maximum value of $R_{S(freq)}$ is 1.35932×10^7.

This large ratio would seem to indicate that we have succeeded in creating a model for a more sensitive gyroscope. But there are two problems. One is the small enhancement range. As can be seen from Figure 7.30, the sensitivity falls off rapidly with frequency. This, however, could be an advantage, as small length changes would be detectable due to the large enhancement, but large length changes would not be outside the dynamic range of the device, as discussed in the Intracavity Dispersion chapter. The other problem is that the peak value of this ratio is very, very sensitive to a parameter over which we may not have much physical control, the ratio of ξ_e / ξ_i. If we take all of the other parameters as constants, and vary this ratio only, we find that, the very tall peak depicted in Figure 7.30 occurs only for critical values of that ratio. If, on the other hand, we allow G and H to vary, we can arrange for that peak to occur at other values of ξ_e / ξ_i. This is only a problem in the homogeneously broadened case.

We give a brief, numerical overview of the dependence of the sensitivity ratio on the ratio ξ_e / ξ_i , below. This ratio is ultimately determined by the ratio of the strength of the interaction which causes the dip (it may be due to a different medium than that which provides the background gain) and that which causes the gain.

Let us consider the maximum value of the ratio R_s ($R_{s\text{-max}}$) in $-10 < \delta < 10$ as function of ξ_i/ξ_e for various choices of the depth of the dip in a background gain which we will assume, for this calculation, to have a constant maximum value of G. We find that for each choice of H, the calculated $R_{s\text{-max}}$ varies strongly with ξ_i/ξ_e. For example, in a medium with H=2, changing ξ_i/ξ_e from 0.453333353 to 0.453333363 induces a considerable change of $R_{s\text{-max}}$: from 1.1×10^7 to 7.8×10^6. Therefore, it is instructive to normalize $R_{s\text{-max}}$ by its maximum (R_0) in order to graphically compare $R_{s\text{-max}}$'s for different H's. In Fig.1, the normalized $R_{s\text{-max}}$ are plotted as a function of ξ_i/ξ_e. For illustration, we consider $Q=3\times10^7$, Γ_i=10MHz and λ_0=780nm ($\lambda_0=2\pi c/\nu_0$ where c is speed of light in vacuum). As shown in Figure 7.31 $R_{s\text{-max}}$ changes very rapidly within narrow range of ξ_i/ξ_e. Therefore, in order to significantly enhance the frequency shift compared to the empty cavity if one has a fixed maximum gain and absorption, and if the dip is provided by different atoms than the gain, one must carefully choose two media whose dipole strengths can yield the appropriate ξ_i/ξ_e for maximum $R_{s\text{-max}}$.

If, however, the parameter H is not fixed, changing that value will cause shifts in the maximum ξ_i/ξ_e , as shown in Figure 7.31 below, for four different values of H.

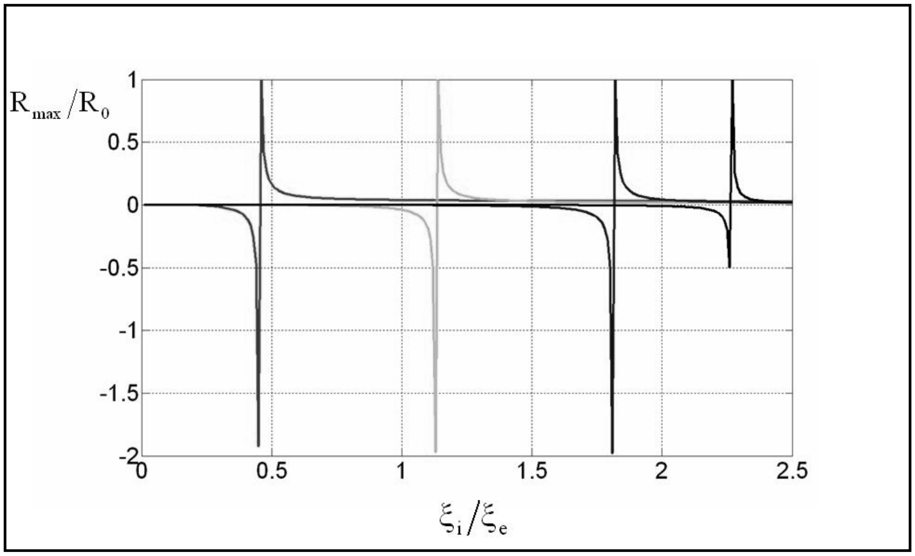

Figure 7.31: Dependence of sensitivity on ξ_i/ξ_e , shown for four different dip depths (H= 2, 5, 8, 10, with G=10 in all cases)

There is one more complication, however. Let us say that for each choice of H we choose the ξ_i/ξ_e which maximizes $R_{s\text{-max}}$ and then plot $R_S(\delta)$, like we plotted in $R_{S(freq)}$ in Figure 7.30. We would find that the variation in H actually causes the peak to move away from $\delta = 0$. This offset is illustrated in Figure 7.32 below, for a variety of choices of H.

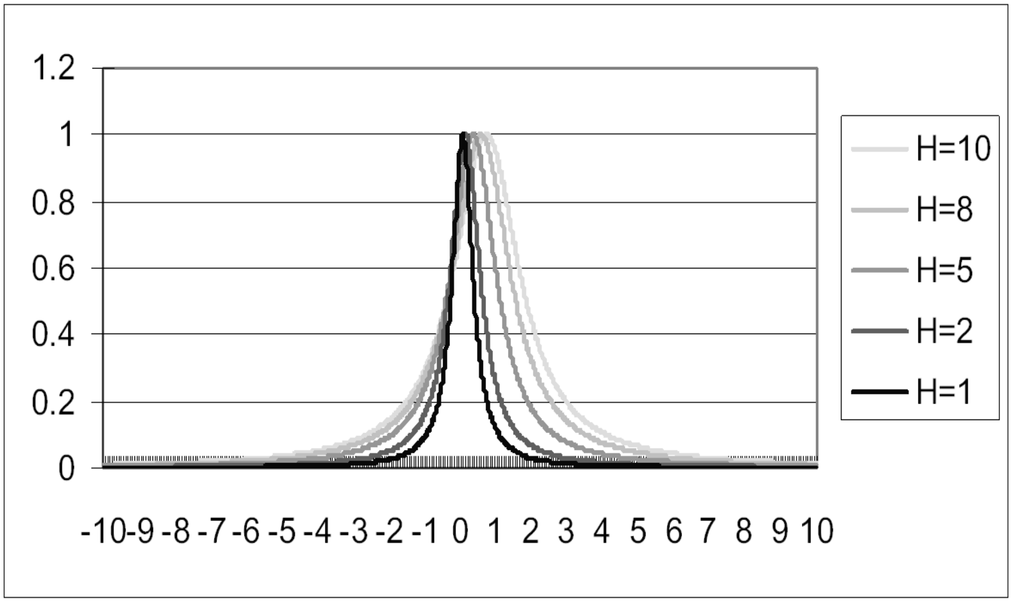

Figure 7.32: $R_S(\delta)$ for different values of H, G=10 in all cases

The graph in Figure 7.32 indicates that the centers of the curves are shifted from the field resonance with the absorption medium i.e. δ=0, and the full width at half maximum (FWHM) of R broadens as the absorption dip deepens from H=2 to 10.

The center shift and the FWHM broadening effects can be understood mathematically by examining the derivatives $dR_s/d\delta$ and $d\chi'/d\delta$. Recalling $\Gamma = \Gamma_i$ and $\nu/\Gamma = \delta + \nu_0/\Gamma$, differentiation of Figure 7.28 with respect to δ gives us

Equation 7.27: $$\frac{dR}{d\delta} = -\frac{\left[d\chi'/d\delta + (1/2)(\delta + \nu_0/\Gamma_i)\left(d^2\chi'/d\delta^2\right)\right]}{\left[1 + (1/2)\chi' + (1/2)(d\chi'/d\delta)(\delta + \nu_0/\Gamma_i)\right]^2}$$

The ratio R reaches maximum (R_{max}) when $dR/d\delta = 0$. We can set this expression equal to zero, and solve for δ to find the location of the maximum. Differentiating the resulting equation for

δ_{max} as a function of H tells us how the location of this maximum depends on the depth of the hole.

More work remains to be done in exploring these dependences for any particular system if we wish to use a laser with a homogeneously broadened gain profile as a gyroscope.

Laser Gyroscopes

These results imply that we may achieve the same sensitivity in lasers, whether based on homogeneously or inhomogeneously broadened gain media, that we have seen in passive cavities. The two types of gain media present different challenges, and ultimately the details of real, physical systems will determine how well the approach works for gyroscope applications. This is the motivation for our experimental work in this area.

We will not go into detail here about the affects of the fast light medium on laser frequency noise. These details can be found in Reference 32. However, we do wish to make one important point. The primary source of frequency noise for most lasers is mirror jitter, and we might expect that the fast light medium would increase the sensitivity of lasers to such jitter, thus, again, increasing the noise by the same factor as the sensitivity. However, laser gyroscopes do not involve direct frequency measurements, but rather measurements of the beat note between counter propagating modes, as illustrated in Figure 5.4. Mirror jitter, thermal effects, and other macroscopic noise sources affect both beams, and this common-mode noise cancels out, when one measures the beat frequency. The only noise on such a measurement is quantum noise, and Reference 32 shows that this is unaffected by the fast light material.

CHAPTER 8 - GRAVITATIONAL WAVE DETECTION

Astronomers and optical scientists have often worked together to do astronomy, and gravitational wave (GW) astronomy will not be an exception. GW detectors are not optical devices in the sense that telescopes are, but the most promising of them use interferometers to sense gravitational radiation by virtue of its effect on laser light here on earth [33]. Here we deal with the optics of laser interferometric GW detectors. We analyze the frequency response and sensitivity for several potential designs, including a proposed modification that uses a White Light Cavity (WLC) to enhance the sensitivity-bandwidth product. We previously demonstrated a WLC experimentally in rubidium[25], and have also explored photorefractive crystals as a potential medium for adapting the technique for use at the working wavelength of LIGO.[34,35] We review the theory of the WLC and show mathematically the advantages it can offer for LIGO-type GW detectors.

When light travels through a region of space over which a GW is also propagating, the latter causes a periodic variation in the phase of the light field. [36] Mathematically, light with this kind of phase modulation may be described as a sum of plane waves of different frequencies. The largest frequency component is the carrier, which is just the frequency of the light when the modulation amplitude is set to zero. The next largest are the two first order sidebands: a Plus-Sideband at the carrier plus the modulation frequency, and a Minus-Sideband at the carrier minus the modulation frequency.[37] Higher order sideband frequencies exist; however, when the modulation is small, as in the case of GWs, their amplitudes are negligible. The problem of detecting GWs may be reduced to the problem of detecting these sideband frequencies.

The difficulty lies in the fact that the amplitudes of these sideband frequency components are very small, and that they are expected to be separated generally by less than a hundred kilohertz, and in some cases by only tens or hundreds of hertz, from the carrier frequency. These sidebands, then, cannot be separated out from the carrier by means of the usual techniques for filtering light. Prisms and diffraction gratings will not resolve such tiny frequency differences, and even Fabry-Perot cavity filters are less than ideal for this purpose, as they would have to have linewidths down to tens of hertz and very high transmissivity on resonance, so as not to further attenuate the already weak sidebands.

Fortunately we can take advantage of a very convenient property of gravitational radiation: the fact that the modulations it causes along one axis are exactly out of phase with the modulations along a perpendicular axis.[38] We can therefore use an interferometer to separate out the carrier and the sidebands. Both Michelson and Sagnac interferometers have been proposed for this purpose. We discuss the Sagnac case in reference [39]. Here, we will discuss GW detectors that are variations on the Michelson interferometer.

If we arrange the arms of the interferometer along the x and y axes, and the path lengths are chosen correctly, then at one port the carrier light from the x-axis will exactly cancel the carrier light from the y-axis so that we get no carrier frequency light out. The interferometer is on a dark fringe for the carrier. The sidebands, however, having been created by phase modulations with opposite signs, will interfere constructively at this same port.[37] This means that we can have only the sideband light exiting one port of a Michelson interferometer under the dark fringe condition. Detecting light at that port, in theory, indicates the presence of a GW.

In practice the situation is more complicated. Most of the time light at this dark port only indicates vibrations in the interferometer mirrors or other sources of noise. A great deal of work has been done to minimize noise and to lock the interferometer on a dark fringe condition,[37] but we would also like to maximize the amplitude of the sideband light falling on the detector. One way of doing that, due to the nature of GWs, is to make the arms of the interferometer very long [33].

Another approach involves the use of optical cavities within the interferometer. If the resonance linewidth of the cavities used is too small, however, then our attempts to use them to enhance the sensitivity of the GW detector will also entail narrowing its linewidth. For this reason, the ideal detector may use a White Light Cavity, to get the benefits of cavity enhancement described below, without correspondingly narrowing the linewidth of the detector. A WLC, as we have discussed, resonates over a broader range of frequencies than what its length and finesse would ordinarily entail..

The remainder of this chapter is organized as follows. The "Design Concepts" section discusses several GW detector designs that have been proposed, starting from the basic Michelson interferometer configuration. The "General Model for Michelson-based GW Detectors " section gives a general derivation of the frequency response of devices of this type, including those described in the preceding section. The "White Light Cavities" section discusses the effect of a dispersive medium on that frequency response, and in particular, the effect incorporating WLCs into the design. We conclude in the "Summary" section with a review of our results.

Design Concepts

There are a variety of ways to use cavities to improve the response of the Michelson-interferometer based GW detector. One of the simplest is to add additional mirrors in each arm of the interferometer so as to turn each arm into a Fabry-Perot cavity, as illustrated in Figure 8.1, below.

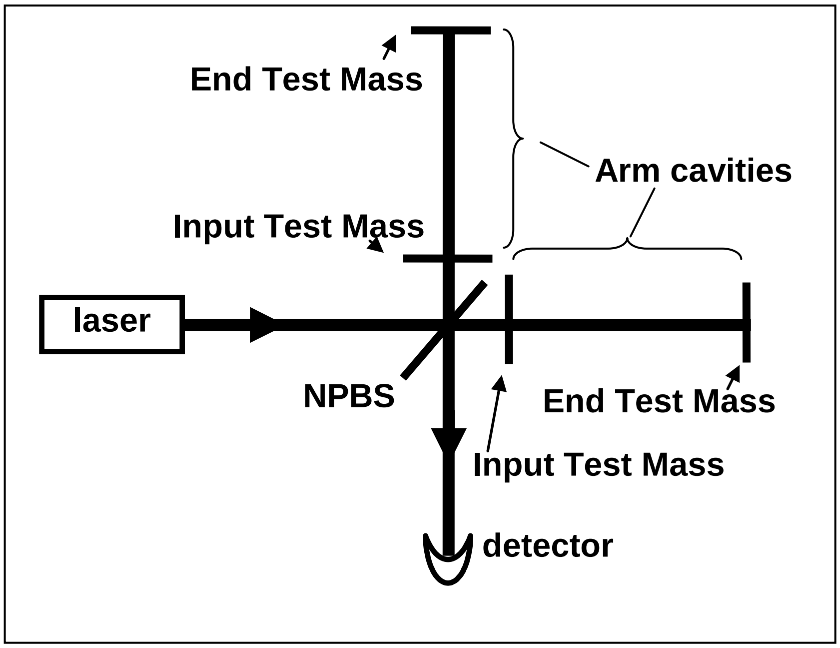

Figure 8.1: Michelson interferometer with arm cavities.

Sideband light is produced from the carrier on each pass as it bounces around the arm cavities. However, though the effect is similar to the use of longer cavity arms, we cannot simply model this as a system with longer effective lengths for the arms. We must take into account the inference effects of multiple bounces within these arm cavities.

We might choose to make the arm cavities resonant for the carrier frequency, for instance. This would allow us to increase the amplitude of the carrier frequency field in the arms by a potentially large factor. Since the sideband field is proportional to the carrier field, the amount of sideband light produced in the arms would then be increased by this same factor.

However, the sideband light itself would also undergo multiple reflections within the arm cavities. If the frequency separation between one of the sidebands and the carrier were greater than the resonance linewidth of the cavity, then the multiple reflections of this sideband would interfere destructively. The same conclusion would apply to the other sideband as well, and the signal at the output would be small. Similarly, we might tune the arm cavities to resonate the sidebands, but the carrier would then interfere destructively, making the net signal small.

One way to avoid this trade-off is to place the input mirrors outside the arms of the interferometer, as illustrated in Figure 8.2, below:

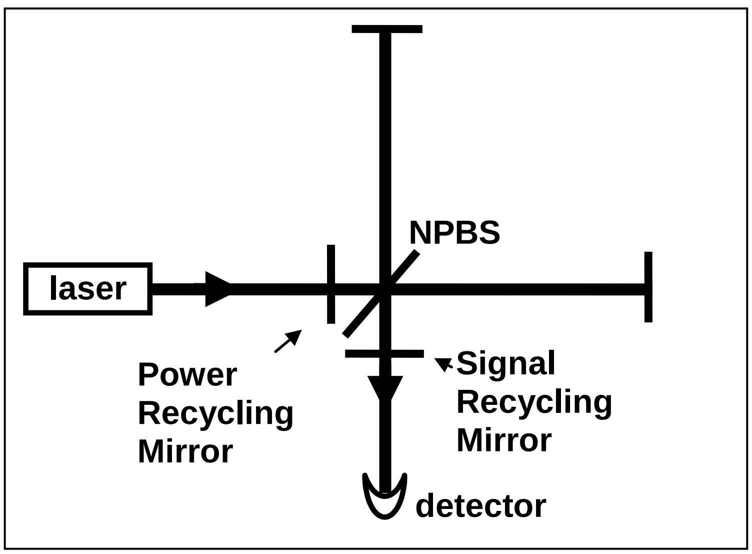

Figure 8.2: Michelson Interferometer with dual recycling

In this configuration, assuming the interferometer is held on the dark fringe condition, the carrier light will only be incident on the mirror labeled Power Recycling Mirror (PRM). It will undergo multiple reflections inside both arms, as if there had been an input mirror in each. Similarly, the sideband frequency light will be reflected back into the arms by the Signal

Recycling Mirror (SRM). This Dual Recycling arrangement allows both the carrier and one or both of the sidebands to resonate, within separate but overlapping optical cavities. The disadvantage of this scheme is that the beamsplitter is inside the optical cavity in which the carrier resonates. The current design for Advanced LIGO proposes a circulating power in the arms of 800kW [40]. This amount of power causes thermal distortion and noise on the beamsplitter.

A third option is to combine these two designs, as illustrated in Figure 8.3, below.

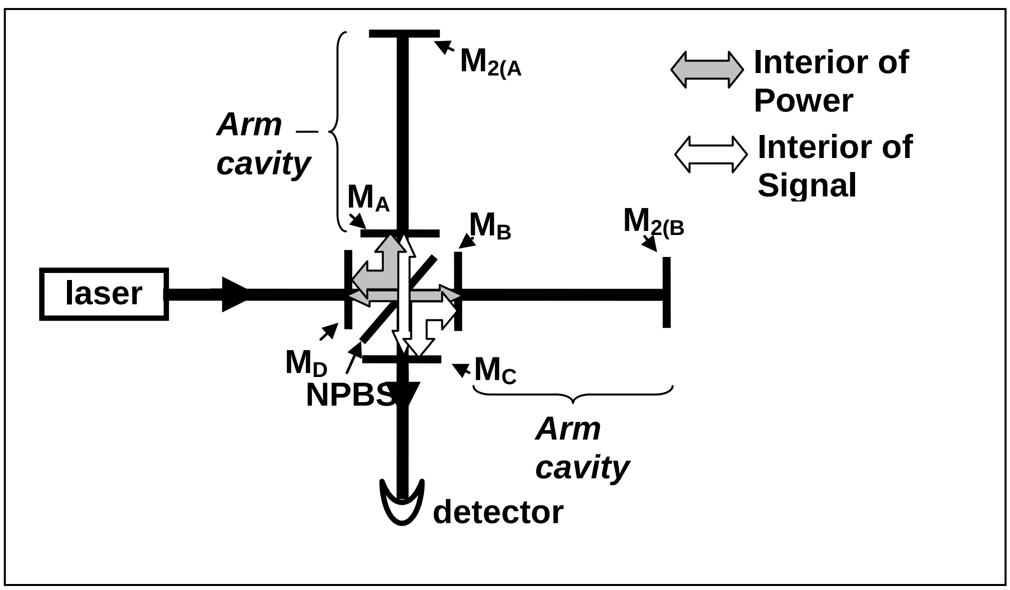

Figure 8.3: Michelson Interferometer with dual recycling and arm cavities

This system, though it comprises many overlapping compound cavities, is not much more difficult to analyze than the simpler version from Figure 8.1, under certain conditions. If the two arm cavities are completely identical, with the reflectivity and position relative to the beamsplitter for the mirrors M_A and $M_{2(A)}$ being exactly the same as those for mirrors M_B and

$M_{2(B)}$, then we may cease to distinguish between the end test masses $M_{2(A)}$ and $M_{2(B)}$, and refer simply to M_2.

Likewise, since we have assumed M_A and M_B are identical, we might simply refer to M_{AB} to indicate either one of these input test mass mirrors. Carrier light that is incident on either one from the arms will then travel toward M_D , so long as the interferometer is locked on a dark fringe. Having reflected off of M_D it will then travel back to one of the mirrors M_{AB}, and then back toward M_D again, so that a cavity is formed. We will refer to this cavity as the Power Recycling Cavity (PRC).

The sideband light, likewise, travels from M_{AB} to M_C and back again, so that the sidebands experience a different cavity than the carrier. We will refer to this cavity as the Signal Recycling Cavity (SRC).

In general, any Fabry-Perot cavity may be treated, from the outside, as a mirror that has a frequency dependent reflectivity. Therefore, we treat the PRC, comprising M_{AB} and M_D, as a single compound mirror M_{1CAR}, because it is the compound mirror which reflects the carrier back into the arms. Likewise, we treat the SRC, comprising M_{AB} and M_C, as a single compound mirror M_{1SB}, because it is the compound mirror which reflects the sidebands back into the arms.

The total system may then be modeled as a single Fabry-Perot cavity, with one mirror M_2 having a reflectivity equal to that of the end test masses M_{2A} and M_{2B}, and one mirror M_1, whose reflectivity is frequency dependent, equal to that of the compound mirror M_{1CAR} for carrier frequency light, and equal to that of the compound mirror M_{1SB} for sideband frequency light. The length of this effective cavity is equal to the distance between M_A and M_{2A} (or equivalently, between M_B and M_{2B}).

The model is illustrated in Figure 8.4 below:

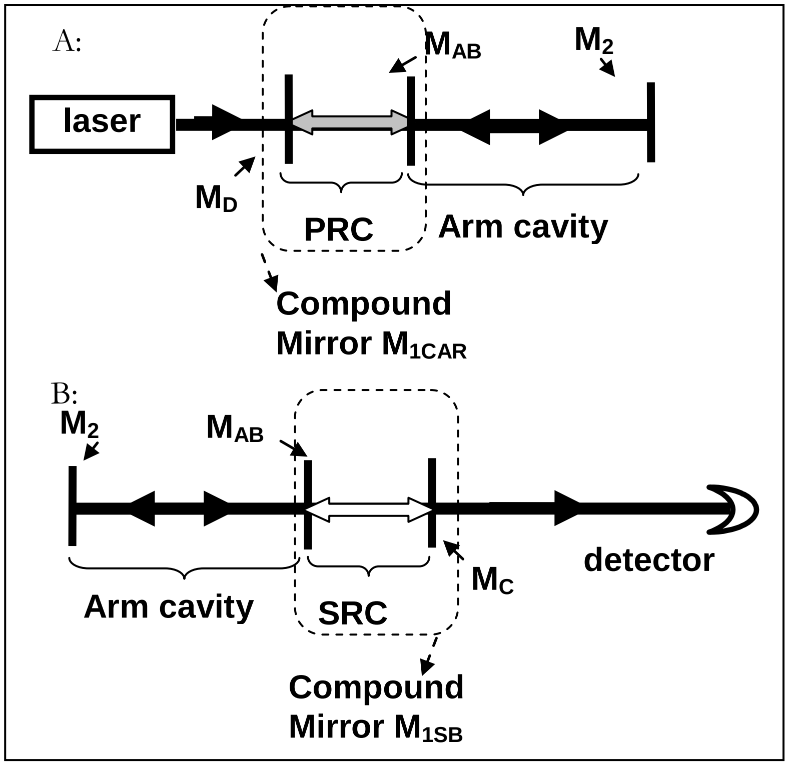

Figure 8.4: A) Effective path for carrier through system illustrated in Figure 8.3 B) Effective path for GW sideband through system illustrated in Figure 8.3

Just as in the case illustrated by Figure 8.1, we must choose the length of the arm cavities to resonate either one of the sidebands or the carrier. However, we have the choice, thanks to the fact that we now have tunable compound mirrors, to make the finesse different for the sidebands than for the carrier. The next section analyzes the behavior of this system in mathematical detail. In this section, however, we first summarize the results qualitatively.

There are two different modes of operation for this device[41]. In both, we choose the reflectivity of M_{1CAR} to be high (by tuning the PRC length and making the reflectivity of M_C high) and choose the length of the arms so that the carrier is resonant in the arm cavities. Since the sidebands necessarily have different wavelengths than the carrier, they will be off resonant in the arm cavities. Therefore, if we do not want the output signal to be nullified by the destructive interference of the sideband light in the arms, we must either lower the reflectivity of the compound output coupler M_{1SB}, (by tuning the SRC) broadening the arm cavity linewidth enough to allow the sidebands to survive, or try to tune the phase the light picks up on reflection from this compound mirror to bring the sideband light back to resonance in the arms.

The idea of lowering the finesse of the arm cavities for the sidebands by using a near-resonant cavity as an output coupler is termed Resonant Sideband Extraction (RSE) [42]. The SRC is much shorter than the arm cavities, on the order of 50 m[43] as opposed to 4000 m, and has a correspondingly broader linewidth – at least 30 kHz even with the highest reflectivity mirror choices we have used in the models in the next section. For realistic choices of mirror reflectivities, if the length of the SRC is chosen such that the carrier frequency would resonate in it, we find that GW sidebands within the spectrum of interest are also transmitted effectively. This mode of operation, with the length of the SRC chosen to resonate carrier frequency light, is conventionally known as tuned or symmetrically tuned mode. It is symmetric in the sense that sidebands spaced equally above and below the carrier frequency transmit equally. The technique allows us to build up the carrier field in the cavities, increasing the amplitude of our output signal, without destroying the sideband fields. The response is peaked at zero gravitational wave frequency but is relatively broadband, as we will see.

In the other mode, we attempt to adjust the phase of the reflectivity of the compound output coupler such that at least one sideband frequency is resonant in the arm cavities. Changing this reflectivity has no effect on the resonance of the carrier; for which only the PRC reflectivity is relevant. Again, because the SRC linewidth is broad enough to encompass the range of GW sidebands of interest, the phase of this reflectivity is relatively uniform over the spectrum of interest. In general it will exactly offset the excess phase (or the phase deficit) picked up in propagating through arm cavity only for a sideband of a particular frequency. The linewidth of this resonance depends on the magnitude of the reflectivity associated with this phase, but also on the length of the arm cavities. Making the reflectivity of the SRC higher increases the sideband field at the resonant frequency and thus the sensitivity of the detector at that frequency, but due to the great length of the arm cavities, the result is that the detector bandwidth becomes narrower than the spectrum of interest. This mode is conventionally known as detuned or asymmetrically tuned operation. Only sidebands created by a narrow range of GW frequencies, determined largely by the arm length we have chosen, are detectable in this mode. The amount of light falling on the detector is, however, higher in this narrowband mode, when the appropriate GW frequency is present, than it would be in the broadband mode for that same frequency.

Though this system offers better response in both modes than that depicted in Figure 8.1 , and eliminates many of the heating problems posed by that depicted in Figure 8.2, it still forces us to choose between high sensitivity and low bandwidth, or high bandwidth and low sensitivity. The WLC proposal that will be described in the "White Light Cavities" section would allow us to have the sensitivity of the narrowband mode over a spectrum as wide as that offered by broadband mode, so that a WLC-enhanced LIGO type interferometer might offer the best of both worlds.

The system depicted in Figure 8.3 is also a more general case of those depicted in Figure 8.1 and Figure 8.2. If we model it mathematically and find its response, we may recover the response for the systems depicted in Figure 8.1 and Figure 8.2, or for a simple Michelson interferometer with no cavities, by setting the reflectivities of the appropriate mirrors equal to zero. In the next section, we develop this general model.

General Model for Michelson-based GW Detectors

B.J. Meers[44] first modeled this system in 1989, but his model is not given in a form that lends itself to the analysis of the effect of a WLC on the system. Furthermore, in the course of developing the model, he makes certain assumptions about mirror reflectivities and resonance conditions which render his final expression less than general. We will essentially follow his method in deriving the frequency response of the system illustrated in Figure 8.3, but we will adopt a slightly different notation and avoid assuming any particular operating condition.

As Meers did, we will denote the reflectivity of the compound mirror M_{1CAR} by R_{1C}. This is not to be confused with the reflectivity of the mirror labeled M_C, which we will denote simply by R_C. We will denote the reflectivity of the compound mirror M_{1SB} by R_{1S}. Whereas he uses R_{1S} and R_{1C} to denote only the amplitude of the reflectivity, we will allow them to be complex numbers, giving information about both the amplitude and the phase of light reflected off the SRC and PRC, respectively. We can calculate these reflectivities from basic theory of a Fabry-Perot cavity, keeping in mind that they are frequency dependent quantities wherever we use them.

The first step in the derivation is to quantify the effect of a GW on light. Let us choose our coordinates such that the effect of the GW on the metric of space time is described by[38]

Equation 8.1: $ds^2 = dx^2(1+h\cos\omega_g t) + dy^2(1-h\cos\omega_g t) + dz^2 - c^2dt^2$

Along the path of a light wave, ds = 0. Let us assume we have light propagating along the x-axis. Then:

Equation 8.2: $dx^2(1+h\cos\omega_g t) = c^2 dt^2 \quad \Rightarrow \dfrac{dx}{dt} \approx c(1-\dfrac{h}{2}\cos\omega_g t)$

The phase the light accumulated as it travels is given by:

Equation 8.3:

$$\phi_x = \int_{x_1}^{x_2} k\,dx = \int_{t-\tau}^{t} k\frac{dx}{dt}dt = \int_{t-\tau}^{t} kc\left(1-\frac{h}{2}\cos\omega_g t\right)dt$$

$$\Rightarrow \boxed{\phi_x = \omega\tau - \frac{\omega h}{\omega_g}\sin\left(\frac{\omega_g\tau}{2}\right)\left(\frac{e^{i\omega_g(t-\tau/2)}+e^{-i\omega_g(t-\tau/2)}}{2}\right)}$$

The calculation for a beam traveling along the y-axis is identical, except that we use $\dfrac{dy}{dt} = c(1+\dfrac{h}{2}\cos\omega_g t)$.

Equation 8.4: $\Rightarrow \boxed{\phi_y = \omega\tau + \dfrac{\omega h}{\omega_g}\sin\left(\dfrac{\omega_g\tau}{2}\right)\left(\dfrac{e^{i\omega_g(t-\tau/2)}+e^{-i\omega_g(t-\tau/2)}}{2}\right)}$

Of course $\omega\tau$ is the phase that the light would pick up in the absence of GWs. We define $\phi_{prop} = \omega\tau$ as the ordinary propagation phase. In our model, we assume that light traveling along one of the coordinate axes under the influence of GWs picks up a multiplication factor expressed as $e^{i\phi_x} = e^{i\phi_{prop}}e^{i\delta\phi_x}$ $\cong$ $e^{i\phi_{prop}}\left(1+i\delta\phi_x\right)$ (where $\delta\phi_x = \phi_x - \phi_{prop}$) or as

$e^{i\phi_y} \cong e^{i\phi_{prop}}\left(1+i\delta\phi_y\right)$ (where $\delta\phi_y = \phi_y - \phi_{prop}$). By using these approximations, we are assuming that the modulation is small enough that the carrier power is effectively undepleted.

First we will consider the amplitude of the carrier field. Let us assume that a field with amplitude E_0 enters through M_{1CAR}, which has a transmissivity T_{1C} and a reflectivity R_{1C} at the carrier frequency. The field, after entering and reflecting off of either arm-end mirror M_2 (which has a reflectivity R_2) returns to the PRC with an amplitude.

Equation 8.5: $E_1 = E_0 T_{1C} R_2 e^{-2ik_c L}$ (where L is the length of the arm-end cavity)

This field now reflects off of M_{1CAR}, and then off of M_2 again, returning to the PRC now with an amplitude

Equation 8.6: $E_2 = E_0 T_{1C} R_2^2 R_{1C} e^{-4ik_c L}$

After each reflection thereafter the field picks up the same factor of $R_{1C} R_2 e^{-2ik_c L}$. The steady state field is the sum $\left(\sum_N E_N\right)$ over all bounces. Therefore in steady state the carrier frequency field inside is

Equation 8.7: $E'_{car} = E_0 T_{1C} R_2 e^{-2iNk_C L} \sum_{N=1}^{\infty}\left(R_2 R_{1C} e^{-2ik_C L}\right)^{N-1}$

Again, we have neglected the depletion of the carrier due to the modulation, in this model. Now the sideband fields being continually produced from this steady-state carrier are given, under the approximation described above, by

Equation 8.8: $E_{SB} = E'_{car} e^{i\omega t} e^{i\phi_{prop}} (1 + i\beta\left(e^{i\omega_g(t-\tau/2)} + e^{-i\omega_g(t-\tau/2)}\right)$ where $\beta = \dfrac{h\omega}{\omega_g}\sin\left(\omega_g \tau/2\right)$

These fields also reflect within the arm-end cavity. Considering only the component at frequency $\left(\omega + \omega_g\right)$, we see that its initial amplitude is

Equation 8.9: $E_{+_1} = E'_{car} e^{i\omega t} e^{-2ik_c L}\, i\beta e^{i\omega_g(t-\tau/2)}$

Here we have used $\phi_{prop} = -2ik_c L$. This field reflects off the SRC and experiences a reflectivity R_{1S}. After another round trip the amplitude is

Equation 8.10: $$E_{+_2} = E'_{car} e^{i\omega t} i\beta e^{i\omega_g(t-\tau/2)} R_{1S} R_2 e^{-2i\left(\frac{\omega+\omega_g}{c}\right)L_S} e^{-2ik_c L}$$

Note that $\left(\omega + \omega_g\right)/c = k_+$, the wavenumber of the sideband. We have, in this expression, introduced another variable L_S, which is the length of the cavity in which the sidebands are propagating. In the case illustrated by Figure 8.3 and Figure 8.4, this L_S is the same as L, equal to the distance between the end test mass, M_2, and the input test masses, M_{AB}. However, in the case illustrated by Figure 8.2, these are two distinct numbers, with L_S being equal to the sum of the distance from the end test mass to the beamsplitter and that from the beamsplitter to the signal recycling mirror, and L being equal to the sum of the distance from the end test mass to the beamsplitter and that from the beamsplitter to the power recycling mirror. After n passes, then, the total field is

Equation 8.11:
$$E'_+ = \left(\sum_n E_{+_n}\right) = E'_{car} e^{i\omega t} i\beta e^{i\omega_g(t-\tau/2)} \sum_{n=1}^{\infty} R_{1S}^{n-1} R_2^{n-1} e^{-2i(n-1)(\omega+\omega_g)L_S/c} e^{-2ik_c L}$$

Doing the geometric series sums for E'_{car} and E'_+, we find that the output field transmitted through the SRC, $E_+ = E'_+ T_{1S}$ is given by

Equation 8.12:
$$\frac{E_+}{E_o e^{i\omega t}} = \frac{T_{1S} T_{1C} R_2}{1 - R_2 R_{1C} e^{-2ik_C L}} \frac{i(h\omega/\omega_g)\sin(\omega_g \tau/2) e^{-2ik_C L} e^{i\omega_g(t-\tau/2)} e^{-2ik_c L}}{1 - R_{1S} R_2 e^{-2i(\omega+\omega_g)L_S/c}}$$

The notation here is slightly different from that used by Meers[44], but the result agrees with his provided we define $2L/c = \tau$, $\delta_C = (-2\omega L/c) \bmod 2\pi$ and $\delta_S = (-2\omega L_S/c) \bmod 2\pi$. By leaving the expression in terms of the separate wavenumbers of the sidebands and carrier, however, we leave ourselves the option of easily including dispersive effects in this calculation at the next stage.

For the Minus-Sideband, the expression is the same, except with $\omega_g \to -\omega_g$, and with R_{1S} potentially taking on a different value, since it is a frequency dependent reflectivity. These amplitudes do not tell us the frequency response of our device directly, however. In practice, the sidebands are detected by allowing a small amount of carrier frequency light to leak through, and detecting the beat signal. To find the total response of the interferometer we need to calculate the amplitude of that beat signal:

Equation 8.13:
$$\delta I = E_L E_+^* + E_+ E_L^* + E_L E_-^* + E_- E_L^*.$$

Here E_L is the carrier frequency field with which we are mixing our sidebands:

Equation 8.14: $$E_L = (A/E_0)e^{i(\omega t+\phi)}$$

In order to do this sum, it is convenient to change our notation slightly. Let $R_{1C} = r_{1C}e^{\phi r_{1C}}$, and let $R_{1S_+} = r_{1S_+}e^{\phi r_{1S_+}}$ be the reflectivity of the SRC at the Plus-Sideband frequency, while $R_{1S_-} = r_{1S_-}e^{\phi r_{1S_-}}$ is the reflectivity of the SRC at the Minus-Sideband frequency. In general, lower case letters for the reflectivity or transmissivity will now be used to denote the magnitude only. We also choose to insert a couple of multiplicative factors equal to one, marked with square brackets. With this convention the equation above may be rewritten as:

Equation 8.15:

$$\frac{E_+}{E_o e^{i\omega t}} = \frac{t_{1S_+}e^{\phi_{t1S_+}}t_{1C}e^{i\phi_{t1C}}r_2 ih\omega\sin\left(\omega_g\tau/2\right)e^{i\omega_g\left(t-\tau/2\right)}}{\omega_g}\frac{e^{-2ik_CL}\left[e^{i\phi_{r1C}}e^{-i\phi_{r1C}}\right]}{\left(1-r_2r_{1C}e^{i\phi_{r1C}-2ik_CL}\right)}\frac{e^{-2ik_cL}\left[e^{i\phi_{r1S_+}}e^{-i\phi_{r1S_+}}\right]\left[e^{-2ik_+L_S}e^{2ik_+L_S}\right]}{\left(1-r_2r_{1S_+}e^{i\phi_{r1S_+}}e^{-2ik_+L_S/c}\right)}$$

These additional factors allow us to make use of the identity $\frac{e^{i\phi}}{1-\rho_1\rho_2e^{i\phi}}$ $= \frac{e^{i\phi}-\rho_1\rho_2}{\left(1-\rho_1\rho_2\right)^2\left(1+F'\sin^2\left(\phi/2\right)\right)}$, where $F' = \frac{4\rho_1\rho_2}{\left(1-\rho_1\rho_2\right)^2}$, in order to write the output in terms of a cavity finesse. We will use F'_C for the finesse of the cavity as experienced by the carrier frequency light, F'_{S_+} for the Plus-Sideband and F'_{S_-} for the Minus-Sideband.

We now have

Equation 8.16:

$$\frac{E_+}{E_o e^{i\omega t}} = \frac{t_{1S_+} t_{1C} r_2 i h\omega \sin\left(\omega_g \tau/2\right)}{\omega_g}\left(\frac{e^{-2ik_C L + i\phi_{1rC}} - r_2 r_{1C}}{\left(1-r_2 r_{1C}\right)^2\left(1+F_C' \sin^2\left(\frac{-2k_C L + \phi_{r1C}}{2}\right)\right)}\right)\left(\frac{e^{-2ik_+ L + i\phi_{1rS_+}} - r_2 r_{1S_+}}{\left(1-r_2 r_{1S_+}\right)^2\left(1+F_{S_+}' \sin^2\left(\frac{-2k_+ L_S + \phi_{r1S_+}}{2}\right)\right)}\right)$$

$$\times e^{i\omega_g (t-\tau/2)} e^{\phi_{t1S_+}} e^{i\phi_{t1C}} e^{-i\phi_{r1C}} e^{-2ik_C L} e^{-i\phi_{r1S_+}} e^{2ik_+ L_S}$$

We would like to separate out the part of this expression that represents the sideband resonance in arms. To this end, we define

Equation 8.17: $$\xi_\pm = \frac{t_{1C} t_{1S_\pm} r_2 h\omega \sin\left(\omega_g \tau/2\right)}{\omega_g \left(1-r_2 r_{1C}\right)^2 \left(1-r_2 r_{1S\pm}\right)^2}$$

This contains all of the scaling information which is independent of the length of the arms. And we let

Equation 8.18: $$Be^{i\phi_B} = \frac{e^{-2ik_c L + i\phi_{r1C}} - r_2 r_{1C}}{1+F_C' \sin^2\left(k_c L - \phi_{r1C}/2\right)}$$

Now B and ϕ_B carry the information about the magnitude and phase of the carrier field in the arm cavities. With this notation,

Equation 8.19: $$\frac{E_+}{E_0 e^{i\omega t}} = i\xi_+ B\left(\frac{1-r_2 r_{1S_+} e^{2ik_+ L - i\phi_{r1S+}}}{1+F_{S_+}' \sin^2\left(k_+ L_S - \phi_{r1s_+}/2\right)}\right) e^{i\omega_g (t-\tau/2)} e^{i\phi_{eff}} e^{i\phi_{t1S_+}} e^{i\phi_B}$$

where $\phi_{eff} = \phi_{t1C} - \phi_{r1C} - 2ik_C L$

With this expression and some trigonometric identities, it is now relatively straightforward to calculate the total response of our device. In keeping track of the phase of the carrier, it proves convenient to define $\phi_{net} = \left(\phi_{eff} - \phi + \phi_B\right)$. We also replace τ with $2L/c$ at this point so as to make all length dependence explicit. We find:

Equation 8.20:

$$E_+E_L^* + E_+^*E_L = \frac{-2AB\xi_+}{1+F'_{S_+}\sin^2\left(k_+L_S - \phi_{r1S_+}/2\right)}$$
$$\times\left[\sin\left(\omega_g\left(t-\frac{L}{c}\right)+\phi_{t1S_+}+\phi_{net}\right) - r_2r_{1S_+}\sin\left(\omega_g\left(t-\frac{L}{c}\right)+\phi_{t1S_+}+\phi_{net}+2k_+L_S-\phi_{r1S_+}\right)\right]$$

Finally, we choose

Equation 8.21: $\phi_C = \phi_{net} - \pi/2 = \phi_{t1C} - \phi_{r1C} - 2k_cL - \phi + \phi_B - \pi/2$

This variable keeps track of the total phase of the carrier, and the term $\pi/2$ allows us turn our sine functions into cosine functions. Note that the unsubscripted ϕ comes from assuming our sidebands were beating with a carrier frequency field of the form $E_L = (A/E_0)e^{i(\omega t+\phi)}$. We will assume that this phase is controllable, and that we can always choose it so that the output is optimum. The signal from our device is then

Equation 8.22:

$$\begin{aligned}
\delta I &= E_LE_+^* + E_+E_L^* + E_LE_-^* + E_-E_L^* \\
&= 2AB\left[\left(\frac{\xi_+\cos\left(\omega_g\left(t-L/c\right)\right)}{1+F'_{S_+}\sin^2\left(k_+L_S-\phi_{r1S_+}/2\right)}\right)\left(r_2r_{1S_+}\cos\left(2k_+L-\phi_{r1S_+}+\phi_{t1S_+}+\phi_C\right)-\cos\left(t_{1S_+}+\phi_C\right)\right)\right. \\
&\quad+\left(\frac{\xi_+\sin\left(\omega_g\left(t-L/c\right)\right)}{1+F'_{S_+}\sin^2\left(k_+L_S-\phi_{r1S_+}/2\right)}\right)\left(-r_2r_{1S_+}\sin\left(2k_+L-\phi_{r1S_+}+\phi_{t1S_+}+\phi_C\right)+\sin\left(t_{1S_+}+\phi_C\right)\right) \\
&\quad+\left(\frac{\xi_-\cos\left(\omega_g\left(t-L/c\right)\right)}{1+F'_{S_-}\sin^2\left(k_-L_S-\phi_{r1S_-}/2\right)}\right)\left(r_2r_{1S_-}\cos\left(2k_-L-\phi_{r1S_-}+\phi_{t1S_-}+\phi_C\right)-\cos\left(t_{1S_+}-\phi_C\right)\right) \\
&\quad\left.+\left(\frac{\xi_-\sin\left(\omega_g\left(t-L/c\right)\right)}{1+F'_{S_-}\sin^2\left(k_-L_S-\phi_{r1S_-}/2\right)}\right)\left(r_2r_{1S_-}\sin\left(2k_-L-\phi_{r1S_-}+\phi_{t1S_-}+\phi_C\right)-\sin\left(t_{1S_-}+\phi_C\right)\right)\right] \\
&\equiv P\cos\left(\omega_g\left(t-L/c\right)\right)+Q\sin\left(\omega_g\left(t-L/c\right)\right)
\end{aligned}$$

To find the magnitude of this signal, then, we have only to add the amplitudes of the sine and cosine terms in quadrature.

Equation 8.23: $|\delta I| = \sqrt{P^2 + Q^2}$

This rather complicated expression gives the full response of the system illustrated in Figure 8.3, if we set $L_S = L$. In the limit where $r_{1S_+} = r_{1S_-} = r_{1C}$, this also gives the response of the simpler system illustrated in Figure 8.1. Finally, this expression can give us the response of the system illustrated in Figure 8.2 as well, where $L_S \neq L$, $r_{1S_\pm}$ is equal to the reflectivity of the SRM, and, r_{1C} is equal to that of the PRM.

A GW detector, in the configuration illustrated in Figure 8.3 and described by the above equation, has two basic modes of operation, as previously discussed. In the narrowband mode, the SRC is tuned to be far off resonance for the sidebands, so that the reflectivity of the SRC is high, and therefore the finesse of the arm cavities is high for the sidebands. A length is chosen for the arm cavities so that a sideband of a corresponding wavelength will resonate. The PRC is tuned to near resonance for the carrier, so that the finesse of the arm cavity for the carrier is low enough to prevent destructive interference from reducing the carrier amplitude. In the broadband mode, the SRC is tuned to be near resonant so that its transmission is high, and its reflectivity low. The arm length is chosen so that the carrier will resonate, and the finesse of the arm cavities for the carrier is made large by tuning the PRC far off resonance.

Below, the response for the two cases, calculated using the equation above, is plotted. Compare these graphs with those shown in reference 42 for a similar system with different reflectivity and length parameters. We display the response both with the currently planned Advanced LIGO value for the SRM reflectivity R_C and with a higher reflectivity, to illustrate the effect on the signal response. The higher reflectivity allows much larger signal responses but with much narrower bandwidths.

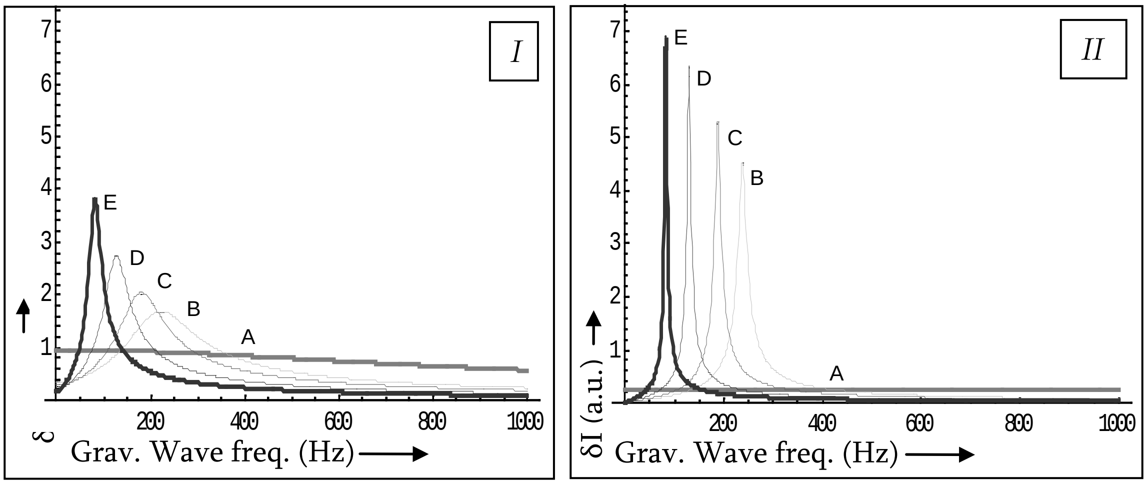

Figure 8.5: I) Output signal as a function of gravitational frequency for a GW detector of the type illustrated in Figure 8.3, using the Advanced LIGO parameters of reference 43, under different operating conditions. The tuned mode response is normalized to one at zero frequency II) The same but with the signal recycling mirror transmissivity decreased from 0.2 to 0.02. For both graphs, the detunings are given by: A) 0 deg [tuned mode] B) 20 deg C) 25.2 deg D) 36 deg E) 54 deg

The values presented in the table below were used in calculating the response.

```
r2 =  .9999;
kc = 2*π/((1064*10^(-9));
c = 3*10^8;
w = kc*c;
h = 10^(-12);
A = 1/25.65;
rD = sqrt(1-.03);
tD = sqrt(.03);
rC = sqrt(1-.2);
tC = sqrt(.2);
rAB =sqrt(1-.014);
tAB =sqrt(.014);
a = .991;
m = 5.420675*10^7;
Lprc = 2*m*π/kc;
φc = -φt1splus at fg = 0;
n = 3.75446*10^9; L = (n*2*π + φr1c/2)/(kc);
LsrcSymMD0 = (2*π*(10.53157*10^7) + π)/(2*kc)
```

Both h, the amplitude of the GW, and A, the amplitude of the homodyning beam, are simple scale factors in these equations, appearing only as multiplicative constants. Their values are arbitrarily adjusted to normalize the response one for the tuned case at zero GW frequency. The lower case "a" is the factor by which the field is assumed to be reduced on each pass through the SRC due to losses, and multiplies the reflectivity of the SRM in the Fabry-Perot calculations of the SRC reflectivity.

The variables r_2, r_{AB}, t_{AB}, r_C, t_C, r_D, and t_D, represent the reflectivity and transmissivity of the mirrors labeled M_2, M_{AB}, M_C and M_D, respectively, in Figure 8.3 and Figure 8.4 . These values are taken from reference 40, and are the currently planned values for the Advanced LIGO system.

LsrcSymMD0 represents the symmetrically tuned ("mode 0") length of the SRC. The reflectivity of the SRC is calculated from standard Fabry-Perot theory using one of these two values for the length of the cavity. In these calculations, the fact that one of the cavity mirrors has its substrate facing inwards must be taken into account. This alters the phase of the reflectivity of that mirror by 180 degrees, and thus alters the resonant length. The same is true of the PRC. Again, the SRC need not be 100% transmitting and is not, even on resonance due to the mismatch in R_{AB} and R_C. The more reflective the SRC is, the higher the signal will be, so long as the reflectivity of the SRC is still small enough to allow the relevant sideband spectrum to fit within the bandwidth of the arms. The transmissivity of the SRC, though not one, is nevertheless maximized for the chosen mirror reflectivities in these tuned mode plots. The reflectivity is higher, and the transmissivity lower, in detuned mode, but the magnitude cannot be chosen independently from the phase. This reflection phase could run between zero and 2π if the mirrors R_{AB} and R_C were matched, but this would mean lowering the reflectivity to zero in tuned mode, which would not be ideal. The attempt to resonate higher frequency sidebands in detuned mode therefore comes at the expense of the signal in tuned mode operation, and the mirror reflectivities R_{AB} and R_C are chosen with this tradeoff in mind.

Clearly hybrid modes of operation exist, with different choices for the lengths of the SRC and PRC and different choices for the phase of the carrier frequency beam with which the sidebands beat, but these two cases are enough to give a general idea of the behavior in the broadband tuned mode vs. narrowband detuned mode using the Advanced LIGO parameters.

White Light Cavities

Having written the output of the device in terms of the sideband wavenumbers k_+ and k_-, we are now in a position to include easily the effects of dispersion on the system. The effect of the medium is to change the wavelength of light within it, so that $\lambda_{medium} = \lambda_{vacuum} / n$, where n is the index of refraction of the medium. Equivalently, we may multiply the wavenumber by n, i.e. $k_{medium} = n k_{vacuum}$.

If we had a Fabry-Perot cavity of length L, the propagation phase that the light would ordinarily pick up on traveling from one end to the other is

Equation 8.24: $\theta_{vacuum} = kL$ (where $k = k_{vacuum}$)

If, however, we assume a cavity of length L partially filled by a medium of length l, that phase becomes

Equation 8.25: $\theta = k\left(L - l\right) + n\left(\omega\right) k\, l$

The phase picked up by light making one round trip in the cavity is then

Equation 8.26: $\theta_{r.t.} = 2k(L-l) + 2\,n(\omega)\,k\,l$

Assuming the light does not pick up any additional phase shifts as it propagates, the resonance condition is

Equation 8.27: $\theta_{r.t.} = 2\pi m \;\; (\textit{for integer } m)$

If the light does pick up some phase shift, e.g. by reflecting off of a phase shifting mirror, then the resonance condition is altered so that the total phase picked up is equal to $2\pi m$, and the round trip propagation phase is equal to $2\pi m$ minus the extra phase due to the reflection.

In either case, resonance requires that the round trip phase $\theta_{r.t.}$ be equal to some predetermined constant. In free space, there would be only one value of ω which would fulfill the resonance condition. In a medium, however, we may have $\theta_{r.t.}$ depend on ω in a non-linear way. If we require that

Equation 8.28: $\left.\frac{d\theta_{r.t.}}{d\omega}\right|_{\omega_0} = 0$

at some frequency ω_0, then the round trip phase will not change with frequency at all for very small deviations from ω_0, and will change by very small amounts for some range of frequencies around ω_0. If ω_0 happens to be the resonant frequency of the cavity, then a range of frequencies around ω_0 will also be very close to resonance. The key to making a WLC is to make this range sufficiently large that the cavity resonates over a much wider bandwidth than it would if it were empty.

Substituting $k = \omega / c$ into Equation 8.26 (since k here is the vacuum wavenumber), and taking the derivative, we find

Equation 8.29:
$$\left.\frac{d\theta_{r.t.}}{d\omega}\right|_{\omega_0} = \left[\frac{d}{d\omega}\left(2\frac{\omega}{c}(L-l)+2n(\omega)\frac{\omega}{c}l\right)\right]_{\omega_0}$$
$$\approx 2\left(\frac{L}{c}+\left.\frac{dn}{d\omega}\right|_{\omega_0}\frac{\omega_0}{c}l\right) \quad \left(if\ n(\omega_0)\approx 1\right)$$

Therefore the condition $\left.\frac{d\theta_{r.t.}}{d\omega}\right|_{\omega_0} = 0$ requires that

Equation 8.30: $\left.\frac{dn}{d\omega}\right|_{\omega_0} = \frac{-L}{l}\frac{1}{\omega_0}$

The simplest model for a WLC assumes an index of refraction which is linear with regard to ω and has a slope given by the equation above:

Equation 8.31: $n(\omega) = 1 + \frac{-L}{l}\frac{1}{\omega_0}\left(\omega-\omega_0\right)$

More complete models might assume $n(\omega)$ has the lineshape of the derivative of a Lorentzian, and choose the coefficients in the equation for this lineshape to give the appropriate slope at the center, or even more realistically, reproduce the lineshape of an index due to double gain peaks **Error! Bookmark not defined.**, for example, again with coefficients chosen such that the index has the appropriate slope between the two peaks.

Whichever functional form of $n(\omega)$ we choose, we may plug it into Equation 8.25 to find its effect on the phase of light propagating through the cavity. The linear form of $n(\omega)$, for instance, gives

Equation 8.32:
$$\begin{aligned}\theta &= k(L-l)+\frac{-L}{l}\frac{1}{\omega_0}(\omega-\omega_0)(kl)\\ &= k(L-l)+\frac{-L}{k_0}(k-k_0)(k)\end{aligned}$$

where $k_0=\omega_0/c$ and k is the vacuum wavenumber. All standard Fabry-Perot cavity analysis still applies, provided we use this expression for the propagation phase of light traveling from one end to the other of the cavity.

In general, in order to find the effect of changing the arm cavities into WLCs, on a LIGO type GW detector, we can make the following substitutions:

Equation 8.33:
$$\begin{aligned}&k_+L_S \rightarrow k_+(L_S-l)+n(k_+)k_+l\\ &k\_L_S \rightarrow k\_(L_S-l)+n(k\_)k\_l\\ &k_cL_S \rightarrow k_c(L_S-l)+n(k\_)k\_l\end{aligned}$$

Where $n(k)$ has the appropriate slope at the resonant frequency. Note that these expressions imply that we are placing the medium in the cavity of length L_S. In the type of system illustrated in Figure 8.3, where $L_S=L$, this means the medium must be placed in the arms of the interferometer. In the case illustrated by Figure 8.2, however, the medium may be placed between the beamsplitter and the Signal Recycling Mirror. In any case, we want to place it in whatever cavity stores the sidebands and has a length on the order of 4 km, in order to broaden the ordinarily very narrow linewidth associated with such a long resonator.

In the expressions above, we have used the linear form of $n(\omega)$, without indicating a turn-around point for the index function. Using more realistic functional forms of $n(\omega)$ gives a more realistic analysis of the behavior of the system. In Figure 8.6, we plot the effects on the output of the interferometer using a slightly more complex model for the index, which assumes its lineshape is that of the derivative of a Lorentzian with a linewidth of approximately 16kHz, with the scaling of the Lorentzian function chosen to give an appropriate slope to the index function at the center. The bandwidth will, in practice, depend on the specific choice of dispersive material. In our experimental demonstrations of the WLC[25], we have seen a linear bandwidth approximately 5 MHz which is considerably broader than the GW bandwidth of interest, 0 to 50 KHz. For these simulations, however, we have chosen to assume a narrower linewidth in order to show clearly the effect of the material for gravitational sideband frequencies near or outside of that linear bandwidth. For convenience we have chosen $l = L$ for these plots.

In general a WLC produces the same peak response as an empty cavity, but with a broader bandwidth. However, in the plots below the peak WLC response is twice as large as the peak detuned mode response. This is because in the WLC gravitational wave detector, both GW sidebands resonate instead of just one.

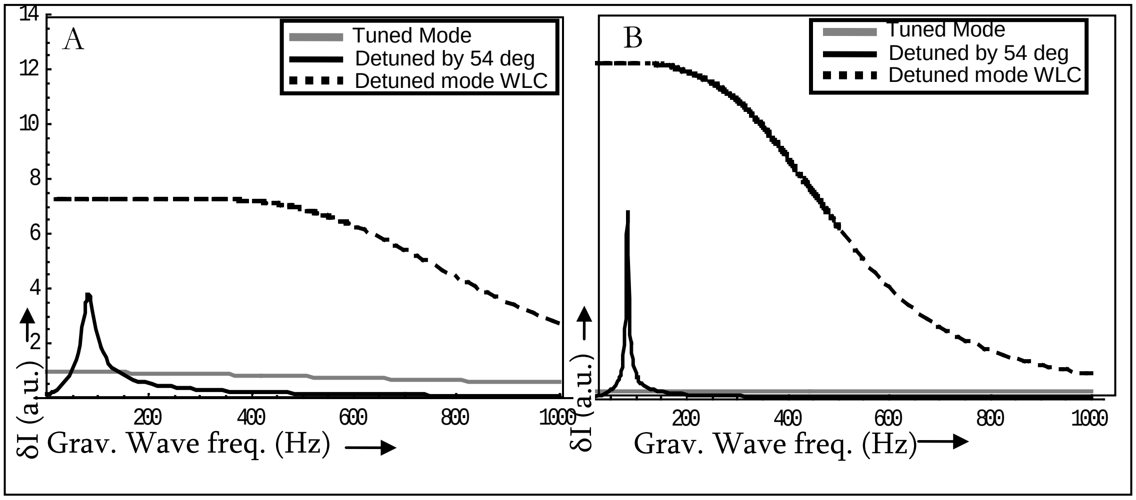

Figure 8.6: A) Tuned mode response, detuned mode response, and detuned mode response with WLC for a cavity/interferometer with Advanced LIGO reflectivities and lengths. B) The same, but using an SRM with a transmissivity of t_c^2=0.02 instead of t_c^2=0.2 as in Advanced LIGO. In both graphs the dispersive material is chosen to have $dn/d\omega = -L/(\omega_0 l)$ over a linewidth of approximately 1600 Hz centered around that resonant frequency, but the output begins to fall when the other sideband is no longer within the linear region.

These graphs illustrate that the WLC-based GW detector isn't just broader in bandwidth than the currently planned Advanced LIGO model, but potentially much more sensitive as well, since the mirror reflectivities could be optimized for sensitivity in narrowband mode instead of for bandwidth. The maximum peak sensitivity as a function of detuning becomes half the maximum broadband sensitivity, with the addition of a WLC.

The cases illustrated above are for the Advance LIGO type detector illustrated in Figure 8.3. We have also carried out the derivation, and developed the frequency response graph, for the type of detector illustrated in Figure 8.2, with and without a WLC. This system is similar to that for which we have already plotted the output, except that the finesse of the arm cavities for the SBs cannot be dynamically controlled – it is given by the reflectivity of the SRM and does not vary with its position. Nevertheless, the behavior in detuned mode is very similar. Incorporating a WLC again gives a broadband response equal to twice the peak value of the narrowband response, since with the WLC, both sidebands will resonate along with the carrier. This is illustrated in Figure 8.7. In this case, it is worth noting that again, increasing the reflectivity of the SRM increases the sensitivity of the detector without compromising the bandwidth, so that with the incorporation of a WLC, a detector of this type can be made far more sensitive, for a given carrier power, than would be feasible without the WLC.

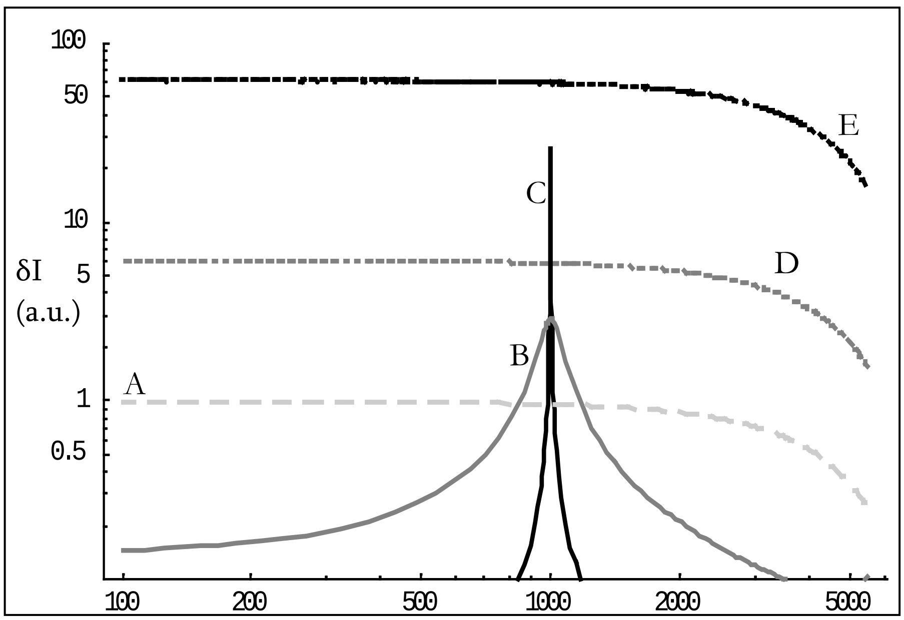

Figure 8.7: A) $r_{SRM} = 0$, B) Detuned mode, $r_{SRM} = \sqrt{1-0.1}$, C) Detuned mode, $r_{SRM} = \sqrt{1-0.001}$ D) Same as B but with WLC E) Same as C but with WLC

As discussed in reference 39, this simpler type of design may in fact be more suitable for use with a WLC than the design illustrated by Figure 8.3. In this configuration, illustrated by Figure 8.2, the dispersive medium may be placed outside of the interferometer arms, between the beamsplitter and the signal recycling mirror. In this case, the beam power within the medium can be smaller, since the high power carrier is not incident on the medium in this configuration. The design illustrated by Figure 8.2 also requires a simpler control system, with fewer cavities to lock. It does suffer from the issues regarding the heating of the beamsplitter as described earlier, and is slightly less flexible.

One other option, discussed in [45], is to add yet another mirror to the design illustrated in Figure 8.2, between the signal recycling mirror and the detector. The idea there was to recover some of the same flexibility as that offered by the design illustrated in Figure 8.3, in that the sidebands would again reflect off of a compound output coupler, the reflectivity of which can be tuned to give whatever finesse we choose for the cavity which stores the sidebands in the arms, while still allowing both a sideband and the carrier to resonate in the arms.

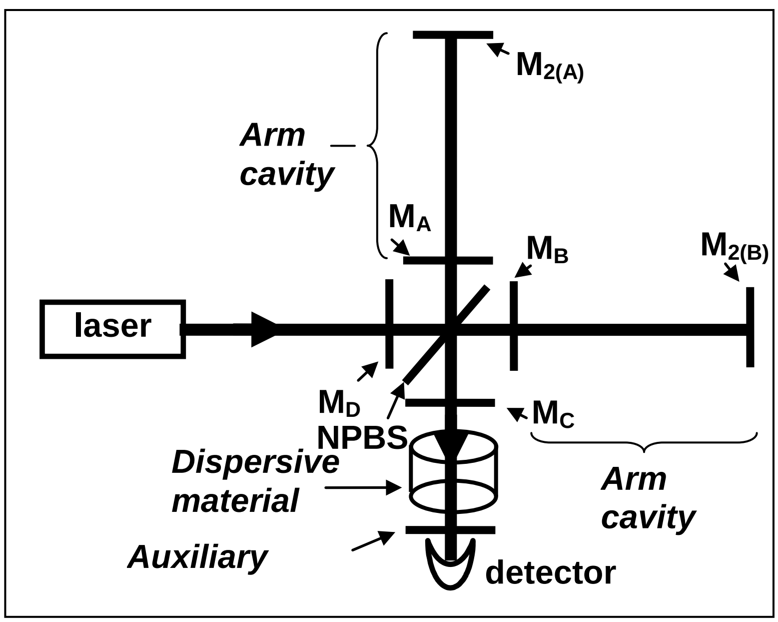

Figure 8.8: Dual recycling system with auxiliary signal recycling mirror, allows for large carrier build-up in arms, low power on primary beamsplitter, and, if the reflectivity of M_C is matched to that of M_{AB}, for high finesse signal recycling over broad band using WLC.

We may also consider adding the extra mirror in front of the detector to the system illustrated in Figure 8.3. This approach may offer special advantages if combined with a WLC. If

M_{AB} and M_C have matched reflectivities and if the distance between them is such that the carrier is resonant, and the linewidth broad enough that the relevant range of sidebands resonate as well, these two mirrors effectively disappear from the system. The cavity they form is transparent to the sideband light and causes no effective phase shift. The sidebands then encounter the final mirror, in front of the detector, and are reflected back through the transparent cavity again into the arms. This system is, as far as the sidebands are concerned, the same as that modeled in Figure 8.2. However, it allows the power in the arms to be kept high while keeping the power on the beamsplitter low. Finally, it allows us to place the dispersive medium outside of the interferometer arms, between the two mirrors which lie between the beamsplitter and the detector.

We simulated this situation with $r_C = r_{AB} = \sqrt{1-0.014}$ for two different values of the auxiliary mirror reflectivity. The distance between M_{AB} and M_C was reduced to 0.5 m, while the distance between M_C and the auxiliary mirror was chosen to be ~0.57m. The results, with and without the anomalously dispersive material, are shown below. In this plot the linewidth of the Lorentzian of which the index lineshape is the derivative has been chosen to be broader, approximately 160kHz.

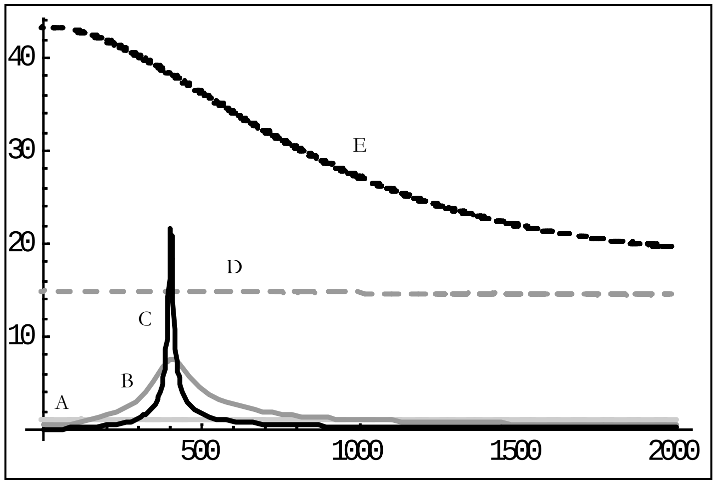

Figure 8.9: Response functions for the system depicted in Figure 8. A) $r_{AUX} = 0$, no dispersive material B) $r_{AUX} = \sqrt{1-0.02}$, no dispersive material. C) $r_{AUX} = \sqrt{1-0.002}$, no dispersive material D) Same as B but including material with critically anomalous dispersion at location shown in Figure 8. E) Same as C but including material with critically anomalous dispersion at location shown in Figure 8.8**.**

Alternative designs[46] using other optical systems to vary the reflectivity of the SRM can be treated in the same way. We have presented here a general analysis which can be used to describe the frequency response, and the effect of a WLC on it, for any variation on the basic Michelson design. We have elsewhere proposed a design incorporating the WLC into a Sagnac interferometer [39]. We believe that any of these designs can benefit from the incorporation of a workable WLC.

Conclusion

Almost all Michelson-based GW detectors can be described by equation 22 of this document. This equation follows from basic Fabry-Perot theory, provided the arms of the interferometer are identical, and involves treating some pairs of mirrors as a single compound mirror with a frequency dependent reflectivity, in certain cases.

The effect of introducing a medium into such a system is to change the propagation phase of the light within the long arm cavities. If the medium has a negative dispersion with a slope given by Equation 8.30, that propagation phase will not vary with frequency over some range, and the resonance bandwidth of the cavity will be broadened. This will have the effect, for all of the variations on the Michelson interferometer that we have discussed, of both broadening the bandwidth of the detector and increasing its sensitivity to some degree by preventing destructive interference within the cavity.

The method given here for calculating the effect of a WLC on any Michelson-based GW detector allows us to consider a variety of different designs, each with its own advantages and disadvantages. The potential benefits of a WLC are great enough that we believe the possibility should be a factor in future design discussions, and we have tried here to provide the tools necessary for evaluating those designs.

CHAPTER 9 - EXPERIMENTAL RESULTS

Having covered the theoretical background for and theoretical results of our research in the preceding chapters, we now turn our attention to the experimental results. These are presented in roughly chronological order.

Electromagnetically Induced Transparency

Our earliest experiment was an attempt to realize a controllable dispersion profile using the electromagnetically induced transparency process described in the quantum mechanical dispersion chapter. The purpose of this experiment was to get a sense of some of the experimental constraints of using dispersion in hot atomic for dispersion in gyroscopes, to determine the feasibility of the approach.

The experimental set-up is shown below:

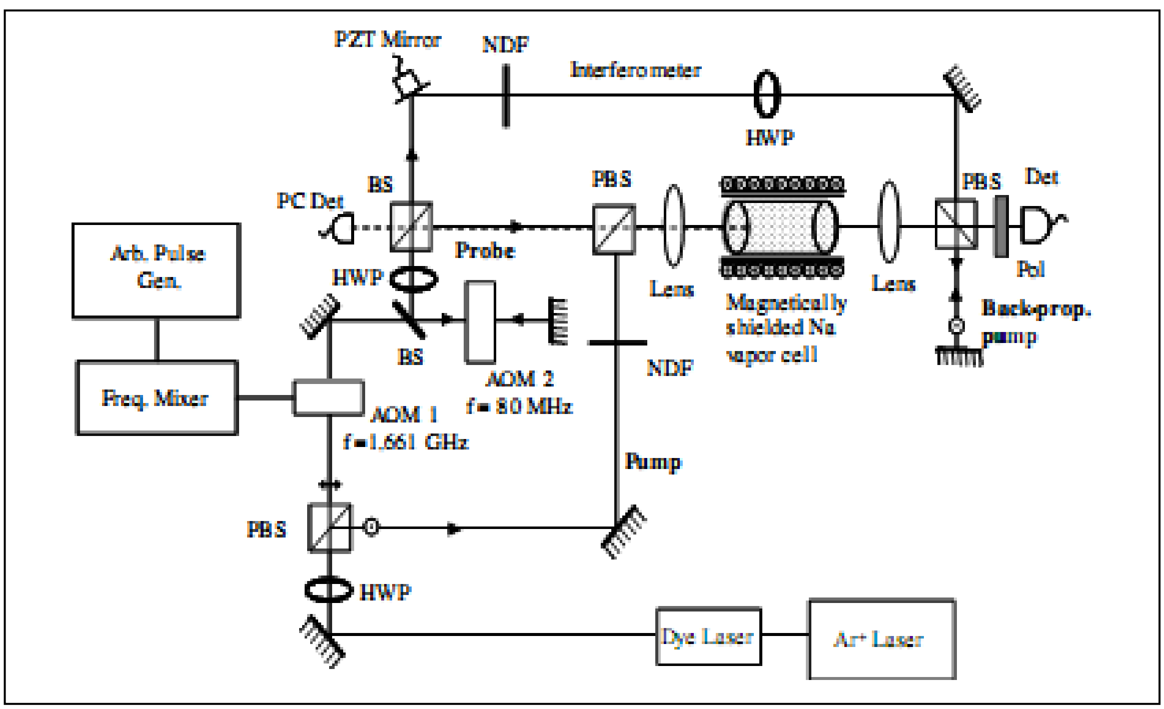

Figure 9.1: Experimental setup used to observe EIT, slow-light and PC in Na vapor. HWP = half-wave plate; PBS = polarizing beam splitter; NDF = neutral density filter; AOM= acousto-optic modulator; Pol = polarizer; and Det = detector.

The pump and probe beam couple two metastable sodium ground states, to create a lambda system like that described earlier. When the probe beam is scanned, Electromagnetically Induced Transparency is observed. The theoretical lineshape calculated for EIT in the Quantum Dispersion chapter is reproduced below:

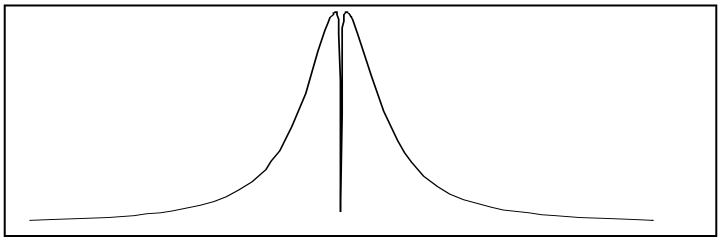

Figure 9.2: Lineshape of absorption coefficient vs. frequency for three level system with electromagnetically induced transparency.

The dip in the absorption of the probe when its detuning matches that of the pump corresponds to an increase in the amount of transmitted light. The linewidth of that transparency depends in part on the power in the pump beam. Below are our experimental observations of that increased transmission at the center frequency, for several pump powers.

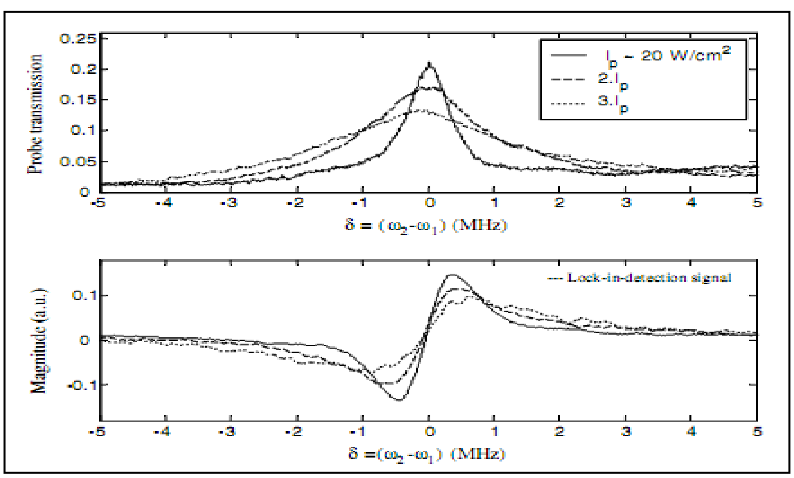

Figure 9.3: Variation of EIT line width with pump intensity: (a) detector output; and (b) lock-in-detection signal.

The lock in detection signal is a measurement obtained by modulating the probe beam at a given frequency and then demodulating the output. This signal is in general lower in noise than the direct signal.

Having produced the EIT, and shown that we could vary its linewidth, our next task was to attempt to measure the associated index profile. This we did using a homodyne method based on the Mach–Zehnder interferometric configuration, as shown in Figure 9.1. The probe beam was split, and the portion which was not sent through the cell traversed an approximately equivalent path length outside the cell. The reference beam and the transmitted EIT signal were combined at the output with a beamsplitter. They interfered, and the phase difference between the two interfering beams due to the dispersion was given by

Equation 9.1: $\Delta\phi = (2\pi/\lambda)\left[n(\omega)-1\right]L$

The resulting intensity falling on the photodiode was then

Equation 9.2: $I_D \propto 2\left|E_p\right|\left|E_{ref}\right|\cos\left(\Delta\phi+\phi_{ref}\right)$

where E_p and E_{ref} are the amplitudes of the probe and the reference, respectively, L is the active interaction length, and ϕ_{ref} is the phase of the reference beam. A piezo-mounted mirror was used to adjust the path length of the free-space beam so that $\phi_{ref} = \pi/2$. Under this condition, the signal from the detector was directly proportional to $\Delta n(\omega)\left[= n(\omega)-1\right]$ for $\left|k\Delta n(\omega)L\right| \ll 1$. This approximation is valid if $\left|\Delta n\right| \ll 10^{-6}$, a condition which is generally fulfilled for media of this type. Since this set-up is essentially just a Mach-Zehnder interferometer, it is very sensitive to vibrations. The probe frequency scan had to be very rapid (1 KHz) in order to produce sufficiently high signal to noise ratio – the major noise sources were all at lower frequencies

Figure 9.4 shows the output of the photodiode, and, and thus the index variation, as a function of the difference frequency δ.

We measured the slope of the index at the center of the dispersion profile to be $\left(dn/d\omega\right)\big|_{\delta=0}\left(\approx 1.89\times 10^{-13} rad^{-1}s\right)$. This slope corresponds to a group velocity of $v_g \approx c/607$. We also verified that our total refractive index variation, measured in this way, was small enough to justify our approximation. This measurement gives a maximum $\Delta n \approx 1.89\times 10^{-7}$ over a bandwidth Δf = 1MHz.

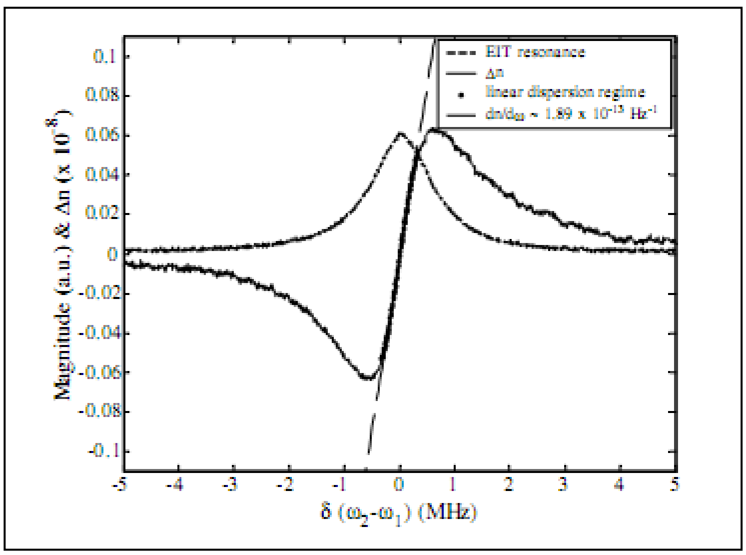

Figure 9.4: Interferometrically measured refractive index variation associated with EIT dispersion.

To verify our measurements of the group velocity and group index, we measured the delay time for a pulse within this dispersion bandwidth. The probe was pulsed, and the pulse was split at the beamsplitter. The difference in arrival time for the reference pulse and the pulse which propagated through the medium was measured. The results are shown below:

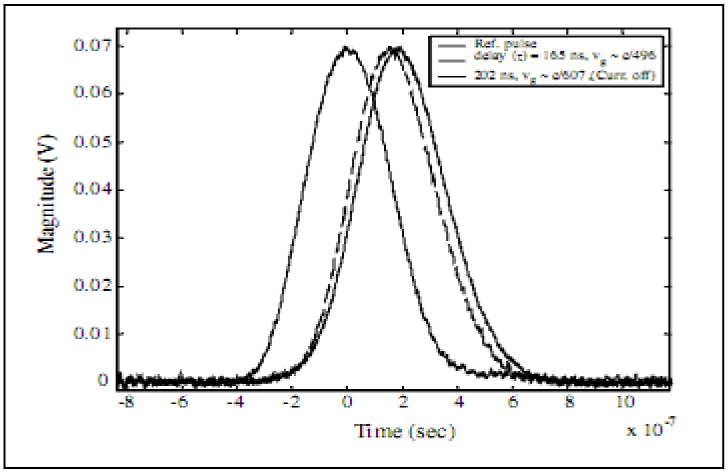

Figure 9.5: Probe pulse slowing using EIT induced dispersion in sodium vapor.

The presence of unwanted magnetic fields due to the heating coils caused some of the dephasing and linewidth broadening in the system, and thereby reduced the group velocity. We therefore made measurements of the delay time with and without the coils turned on. The maximum delay time, ~202 ns, was measured with the coils temporarily off. The value of v_g corresponding to this time delay is ~c/607, which agrees very well with our previous measurement.

Further details of this experiment can be found in Reference 47. These basic results were sufficiently promising to encourage us to pursue the matter further.

Intracavity Slow-Light

The next step was to study the effects of dispersive media on cavities. We moved to rubidium as our lambda system, and experimented with both slow and fast light dispersion profile. The results of the intracavity slow light experiments are presented first.

This experiment shows for the first time that the cavity sensitivity really does vary with the group index in the way described in the Intracavity Dispersion chapter.

Demonstrating that dependence is the primary purpose of the experiment. The motivation, ultimately, is to create a cavity with increased sensitivity using a fast light profile. However, the reduced-sensitivity due to slow light demonstrated here may prove useful in its own right. For example, highly stable cavities have applications in laser frequency stabilization, squeezed light production, and in other any process that relies on narrow linewidth, low loss optical cavities immune to external perturbations.

In this experiment, the intracavity medium was a 10 cm long rubidium vapor cell. The cavity itself was a four mirror ring cavity, with a 100 cm perimeter. The empty cavity finesse was measured to be approximately one hundred, and the linewidth, approximately 3 MHz. One mirror is epoxied to a piezoelectric transducer (PZT), which is used to actively lock the cavity length. The relevant levels for the Lambda-system are those coupled by the D_2 transitions of ^{85}Rb vapor. The probe and the pump were produced by the same Ti:Sapphire, split into two beams which were separately frequency shifted by AOMs. This is important because the beams must be coherent in order for the EIT process to occur. The probe was aligned to resonate in the cavity, and the pump was combined with the resonating probe using a polarizing beam splitter (PBS). It was split from the probe again after co-propagating with it through the cell by another PBS. The pump was orthogonally-polarized. A voltage ramp was sent to the voltage controlled oscillator (VCO) to sweep its RF output. This RF output, amplified, produces the acoustic wave in the AOM, and its frequency determines the probe frequency shift, so that this voltage ramp corresponds to a probe frequency scan. The probe AOM was used in a double-pass configuration so that the frequency could be scanned without misaligning the probe beam. A flipper mirror inside the cavity allowed us to monitor, when necessary, the probe field under the EIT condition without cavity interference effects. The pump frequency is chosen, and the probe frequency ω_0 is initially tuned to two-photon resonance condition. The lock beam which counter propagates to the probe is chosen to have a frequency which differs from it by an integer number of free spectral ranges of the cavity (and this frequency difference is tuned until resonance is observed in both beams simultaneously.) The cavity length is locked the resonance of the lock-beam, and thus, indirectly, to the resonant length for the probe. This allows us to control the cavity length and the probe frequency separately. This scheme is illustrated below.

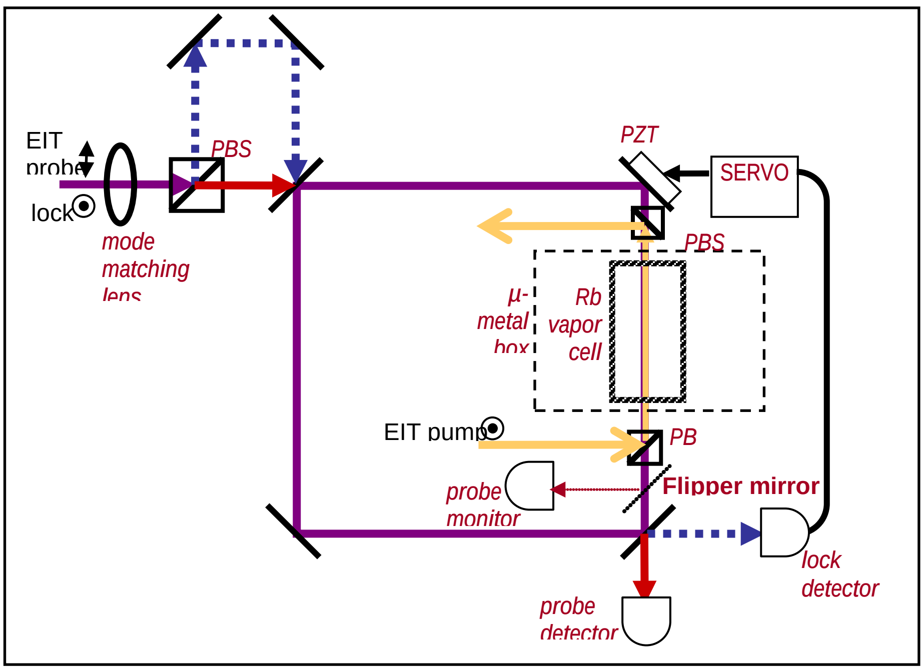

Figure 9.6: Experimental set-up for intracavity EIT experiment. PZT = piezoelectric transducer, PBS=Polarizing Beam Splitter. The μ-metal box is for magnetic shielding.

The linewidth of the cavity containing the vapor cell, in the absence of EIT, was measured to be about 8 MHz, vs. about 3 MHz with no cell. This broadening is to be expected, since the absorption in the vapor represents an additional loss in the cavity. When the pump is switched on, we measure the EIT-affected cavity linewidth (~ 1.5 MHz) to be nearly five times narrower than what we observed without the pump. Others have observed this effect before[48].

The modified cavity linewidth $\delta\omega'_{1/2}$ can be written, combining our calculations from the cavity review section and the intracavity dispersion section, as:

Equation 9.3: $\frac{\delta\omega'_{1/2}}{\delta\omega_{1/2}} = \left|(\sin^{-1}\left[\frac{1-R\rho}{2\sqrt{R\rho}}\right]/\sin^{-1}\left[\frac{1-R}{2\sqrt{R}}\right])/[1+\left(n_g-1\right).\frac{\ell}{L}]\right|, \quad n_g \equiv 1+\omega.\left.\frac{\partial n}{\partial\omega}\right|_{\omega=\omega_o}, \quad \rho \equiv e^{-\frac{\alpha\ell}{2}}$

where $\delta\omega_{1/2}$ is the empty cavity linewidth, n_g is the group index, R is the reflectivity of each of the beam-splitters, and α is the loss coefficient.

If (i.e., n_g=1), then the linewidth is broadened due to the loss induced attenuation. This attenuation has no effect, however, on the sensitivity of the cavity.

Figure 9.7b shows a simulation illustrating the narrowing, obtained by using an analytic expression for $n(\omega)\left(=\sqrt{1+\mathrm{Re}[\chi]}\right)$ and $\alpha(=[\mu_o\omega^2/k^2]\mathrm{Im}[\chi])$, where χ is the susceptibility. A close match to the observed broadening is obtained for the estimated values of the experimental parameters.

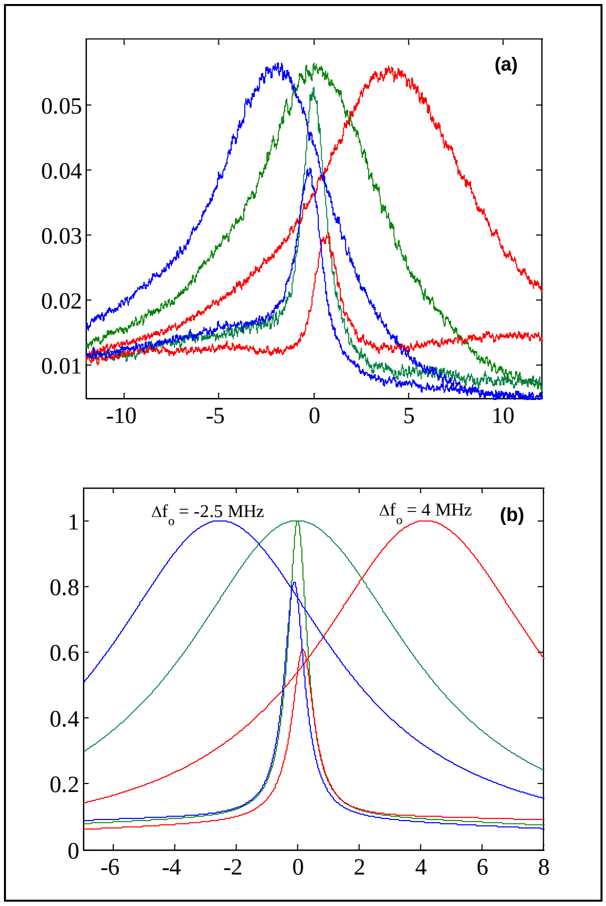

Figure 9.7: (a) Experimental results showing linewidth narrowing and reduced shift in cavity resonance for Δf_o = -2.5, 0 and 4 MHz respectively (b) theoretical model for cavity response (Cavity linewidth = 8 MHz, EIT Linewidth = 1 MHz, L/l= 10 and $n_g \approx 50$). In the figures, the horizontal axis represents the frequency in MHz and the vertical axis represents the cavity transmission in arbitrary units.

Next, we describe the effect of the cavity length variation on its resonance frequency. Figure 9.7a shows the shift in the center of cavity resonance both in the presence and in the absence of the medium dispersion, as L is changed. L is changed by changing lock frequency ω_c away from its original value. In the absence of dispersion, the cavity resonant frequency thus changes by $\Delta\omega = \omega_c - \omega_o$. However, in the presence of dispersion, the resonant frequency is shifted by a *smaller* amount $\Delta\omega'$.

The magnitude of this shift is a measure of the sensitivity of the cavity. We have predicted theoretically that it should be given by

Equation 9.4: $\Delta\omega_o^{'} = \Delta\omega_o / [1 + (n_g - 1).(\ell / L)]$

where $\Delta\omega_o$ is the shift in frequency for the empty cavity and $\Delta\omega_o'$ for the cavity with the dispersive medium. We predicted that the frequency shift should also be inversely proportional to n_g, and scaled by (L/ℓ). This effect is related to what is commonly called frequency-pulling[10]. However, it has not been studied experimentally or discussed in the context of sensitivity modification.

Figure 9.8 shows a sequence of such results when the resonance frequency of the cavity is gradually changed from ω_o.

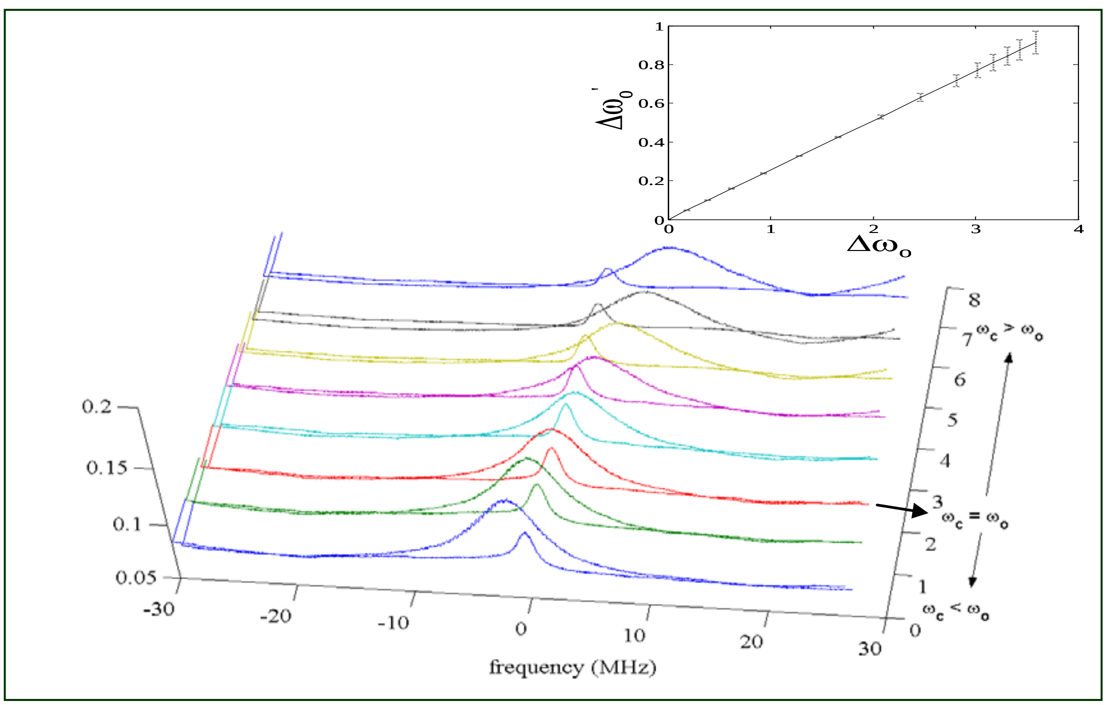

Figure 9.8: Cavity resonances with (narrow) and without (broad) the effect of the intra-cavity medium dispersion. The inset in the figure shows measured frequency shifts corresponding to the peaks of resonances, illustrating reduced sensitivity to length change. The straight line superimposed on the data represents the fit to Equation 9.4

In this figure we can see both the linewidth and sensitivity modifications. We also see that amplitude of the transmitted signal for the cavity with EIT is reduced with increasing $\Delta\omega_o$ (or ΔL). This is because at the resonant frequency of the cavity does not necessarily correspond to the center of the EIT transmission, and the EIT transmission is not 100%. If the shift $\Delta\omega_o'$ (corresponding to a given $\Delta\omega_o$) exceeds the EIT linewidth, the signal level corresponding to maximum probe transmission for the loaded-cavity resonance is further reduced. It is also important to note that, once the cavity resonant frequency is outside the EIT bandwidth, $\Delta\omega_o'$ is no longer determined strictly by the expression in Equation 9.4. This is because Equation 9.4 assumes a constant group index. In practice, the dispersion becomes non-linear and the group index varies with frequency once $\Delta\omega_o'$ becomes comparable to the EIT linewidth (~ 1 MHz). To model this situation we must resort to graphical methods like those described in the Intracavity Dispersion chapter.

This experiment provides evidence for our theoretical prediction of the dependence of linewidth and sensitivity on group velocity. It suggests very strongly that the fast light gyroscope is a promising technology. Further details can be found in Reference 49.

Intracavity Fast-Light

The next step is to try to produce a fast light medium with a dispersion profile having the appropriate slope, to measure the cavity broadening and sensitivity enhancement.

In order to produce the dispersion, we use the bi-frequency Raman gain described in the Quantum Mechanical Dispersion chapter, and illustrated below.

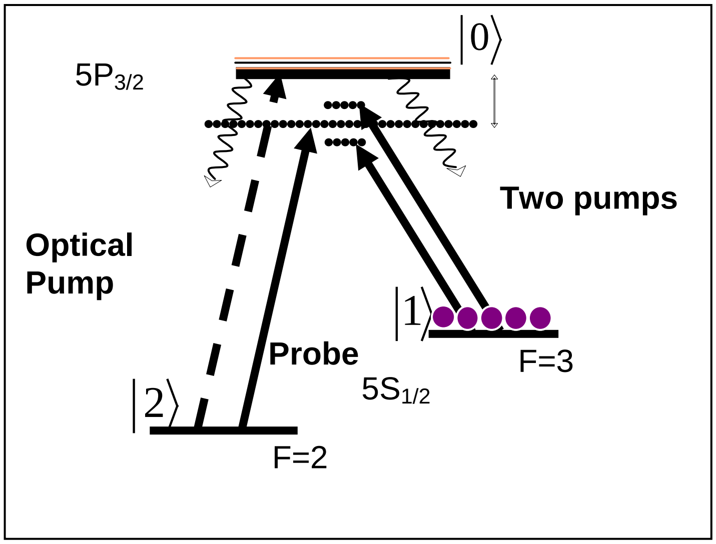

Figure 9.9: Energy level diagram for bi-frequency pumped Raman gain in Rubidium

The experimental setup for the white-light cavity is shown in Figure 9.10. The same 10 cm long Rubidium vapor cell is placed inside the same 100 cm long cavity, which consists of four mirrors with two plane mirrors as input and output ports, and two concave mirrors. The empty cavity finesse and linewidth are again about 100 and 3 MHz. The Lambda system configuration and lock process for the cavity are the same. An incoherent optical pump from a diode laser is used to create a population inversion between the ground states, and the average detuning of the pumps and probe is chosen to be larger than the linewidth of the transition.

In this case, two pump beams of different frequencies are both injected into the cavity to generate closely spaced gain lines, as described in the Quantum Dispersion chapter. These pump beams are derived from the same Ti:Sapph laser, again using a beamsplitter and two different AOMs. The optical pump beam follows almost the same path as the Raman pumps (which co-propagate) except that 1) it travels in the opposite direction, and 2) it is spatially separated by approximately a millimeter, so as not to interfere with the three level system. The atoms which transit through the optical pumping beam and are pumped into the appropriate state before interacting with the Raman beams are the source of the gain signal. This set-up is depicted in Figure 9.10.

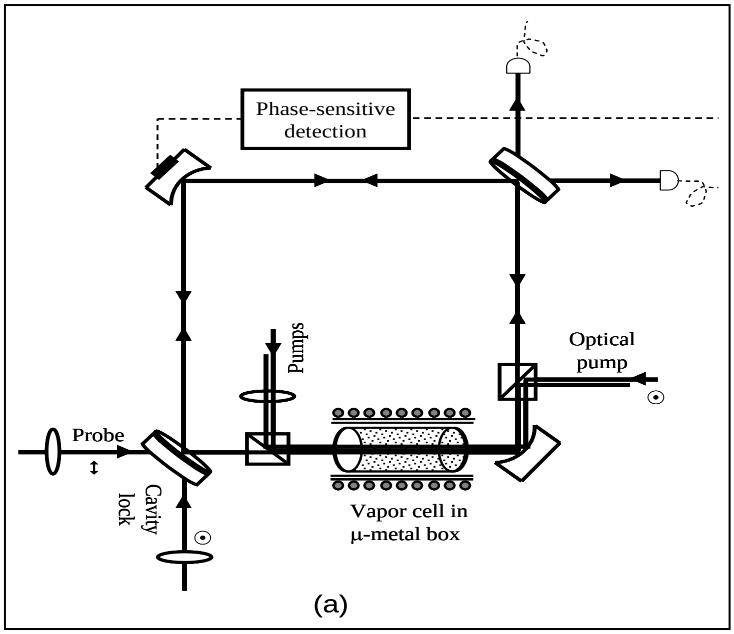

Figure 9.10: Schematic of the experimental set-up for the white-light cavity

The probe experiences gain when its detuning matches that of either of the two Raman pumps – the average frequency of which differs from the center frequency of the probe gain by the splitting of the metastable states which we are using in Rb^{85} (3.0357 GHz). The probe frequency is scanned through the gain profile using the same AOM set in a double-pass configuration. The magnetically shielded vapor cell is heated to nearly a steady temperature of $60^{o}C$ using heating coils carefully wound with current passing both directions, to produce a negligible magnetic field.

As discussed in the Quantum Mechanical Dispersion chapter, Raman gain is most efficient when the average frequency of the probe and the pump fields is detuned below

Doppler resonance so that the probe does not get significantly absorbed in the cell even in the absence of the pump beams.

We first measured directly the dispersion as seen by the probe field. We flipped up the flipper mirror in order to observe the probe beam without cavity interference effects. The measurement was made, this time, using a heterodyne technique involving a reference beam produced by frequency shifting a fraction of the probe beam outside the cavity using a 40 MHz AOM. The signal from the reference beam detector and that from the probe detector were mixed electronically and the result passed through a low-pass frequency filter, to demodulate the rf signal. This allowed us to measure the dispersion in the atomic medium in a way less subject to vibration noise. The basic scheme is illustrated below:

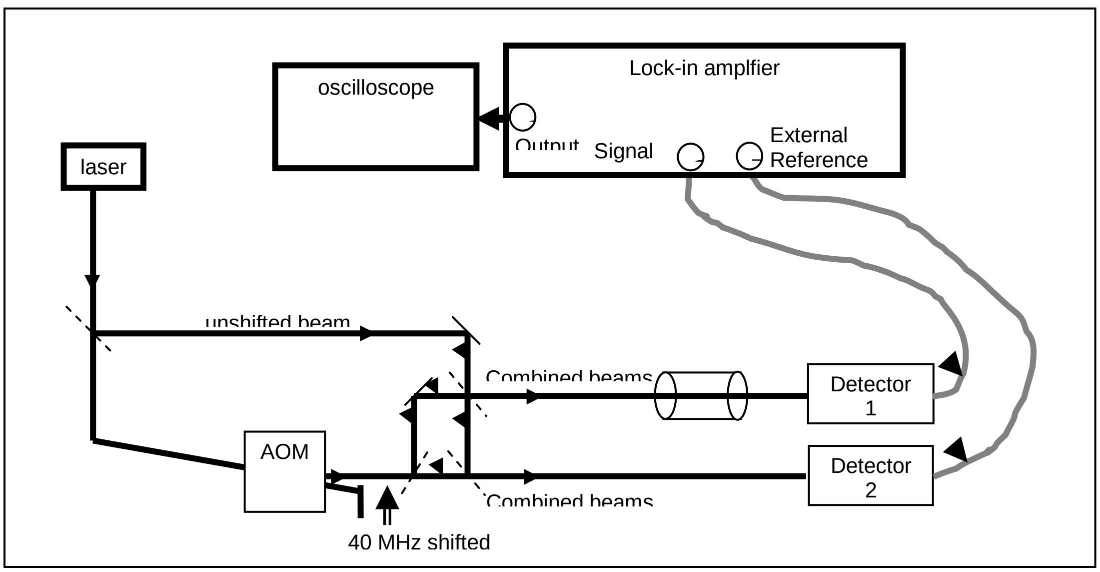

Figure 9.11: Heterodyne detection scheme for low-noise dispersion measurements.

The signal from Detector 1 is

Equation 9.5:
$$\begin{aligned}\left|Ae^{i\omega t-i\phi(\omega)}+Be^{i(\omega+\Omega)t+\delta\phi_1}\right|^2 &= A^2+B^2+AB\left(e^{-i\Omega t-i\delta\phi_1-i\phi(\omega)}+e^{i\Omega t+i\delta\phi_1+i\phi(\omega)}\right)\\ &= A^2+B^2+2AB\left(\cos\left(\Omega t+\delta\phi_1+\phi(\omega)\right)\right)\end{aligned}$$

And from Detector 2:

Equation 9.6:
$$\left|Ce^{i\omega t}+De^{i(\omega+\Omega)t+i\delta\phi_2}\right|^2=C^2+D^2+CD\left(e^{-i\Omega t-i\delta\phi_2}+e^{i\Omega t+i\delta\phi_2}\right)$$
$$=C^2+D^2+2CD\left(\cos\left(\Omega t+\delta\phi_2\right)\right)$$

If the signal from Detector 2 is sent through a high pass filter to remove the D.C. terms, we are left with:

Equation 9.7: $Det2_{filtered}=2CD\left(\cos\left(\Omega t+\delta\phi_2\right)\right)$

A lock-in amplifier shifts the filtered Detector 2 signal by a controllable phase, and multiplies the two signals, so that we have:

Equation 9.8:
$$Det2_{filtered,shifted}*Det1=\left(2CD\left(\cos\left(\Omega t+\delta\phi_2+\phi_{shift}\right)\right)\right)*\left(A^2+B^2+2AB\left(\sin\left(\Omega t+\delta\theta_1+\phi\left(\omega\right)\right)\right)\right)$$

$$=\left(2CD(A^2+B^2)\left(\cos\left(\Omega t+\delta\phi_2+\phi_{shift}\right)\right)\right)$$
$$+2AB\left(\sin\left(\Omega t+\delta\theta_1+\phi\left(\omega\right)\right)\right)\left(2CD\left(\cos\left(\Omega t+\delta\phi_2+\phi_{shift}\right)\right)\right)$$

$$=\left(2CD(A^2+B^2)\left(\cos\left(\Omega t+\delta\phi_2+\phi_{shift}\right)\right)\right)$$
$$+\frac{4ABCD}{2}[\sin\left(2\Omega t+\delta\phi_2+\phi\left(\omega\right)+\phi_{shift}+\delta\theta_1\right)$$
$$+\sin\left((\delta\theta_1-\phi_{shift}-\delta\phi_2)+\phi\left(\omega\right)\right)]$$

This product has three terms, one at 2Ω, one at Ω, and one at D.C. We use a low-pass filter to keep only the DC term.

Equation 9.9: $Lock-in\ output=\frac{4ABCD}{2}[\sin\left((\delta\theta_1-\phi_{shift}-\delta\phi_2)+\phi\left(\omega\right)\right)]$

We adjust ϕ_{shift} by hand until $\delta\theta_1-\phi_{shift}-\delta\phi_2=0$, so that the final signal, sent to the storage oscilloscope, is $S_{scope}=2ABCD[\sin\left(\phi\left(\omega\right)\right)]$.

For small $\phi(\omega)$,

Equation 9.10: $$sin(\phi(\omega)) \approx \phi(\omega), and\, \phi(\omega) \propto \Delta n$$

In this way we were able to get less noisy and more repeatable results than with the homodyne approach.

We experimented with the possibility of achieving very small negative dispersion slopes ($n_1 \sim 3 \times 10^{-16}$ rad^{-1} sec), which are necessary to produce the CAD condition when the dispersive medium fills an appreciable fraction of the cavity. These slopes have been achieved with gain of less than a factor of two. This low gain prevents our passive cavity from turning into a laser.

The dispersion and gain measurements produced in this way were modulated at a frequency which corresponded to the difference frequency between the two pump beams, as illustrated below:

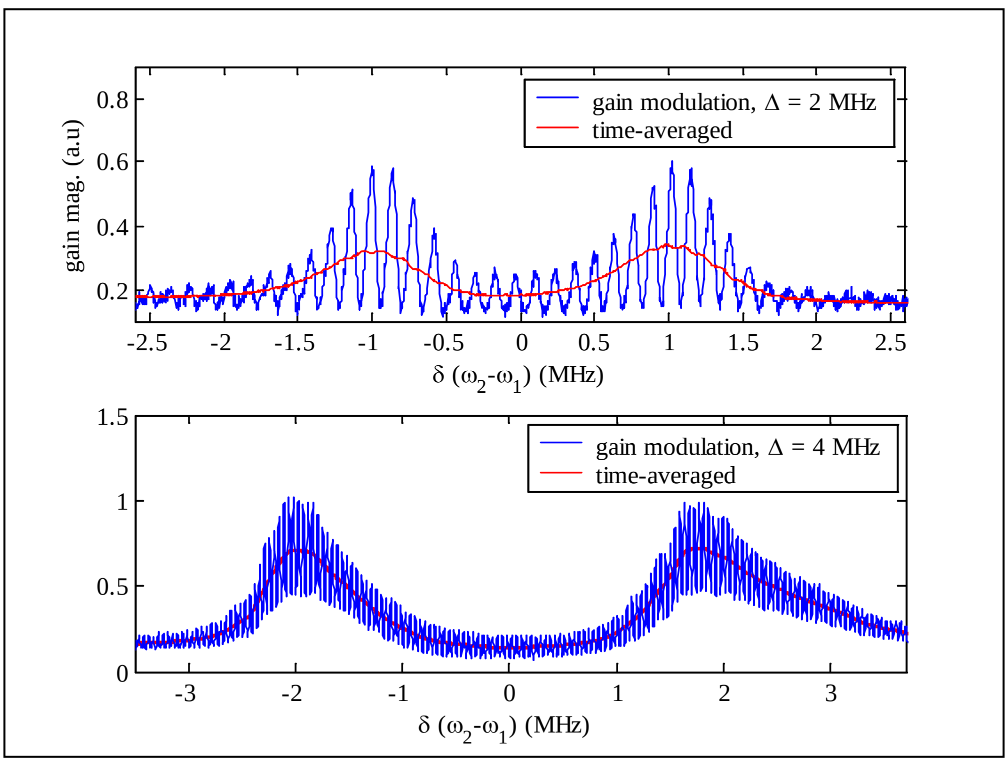

Figure 9.12: Gain modulation using bi-frequency pumps with (a) Δ = 2 MHz (b) Δ = 4 MHz.

We attribute this temporal variation to interference between the two pumps within the material. We can time average the output to eliminate these fast oscillations.

The corresponding dispersion signals vary around zero rather than 1, because in this heterodyne case, as in the homodyne case, they are proportional to Δn rather than n. The measured dispersion profile corresponding to $\Delta = 2$ MHz is shown below.

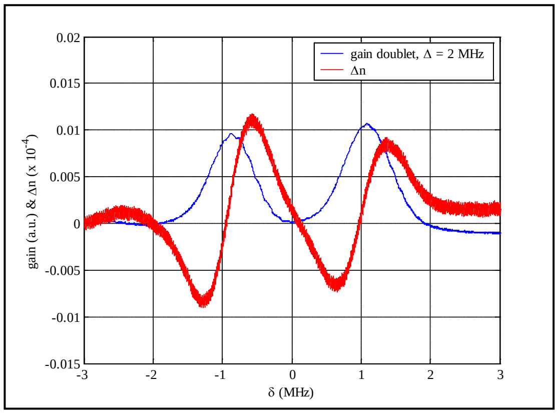

Figure 9.13: Measured dispersion ($\partial n/\partial\omega \sim -2.65 \times 10^{-13}$ rad sec^{-1}, $n_g \sim 639$) associated with bi-frequency Raman gain using the heterodyne technique.

As we change the separation of the two pump frequencies, the slope of the index of refraction changes:

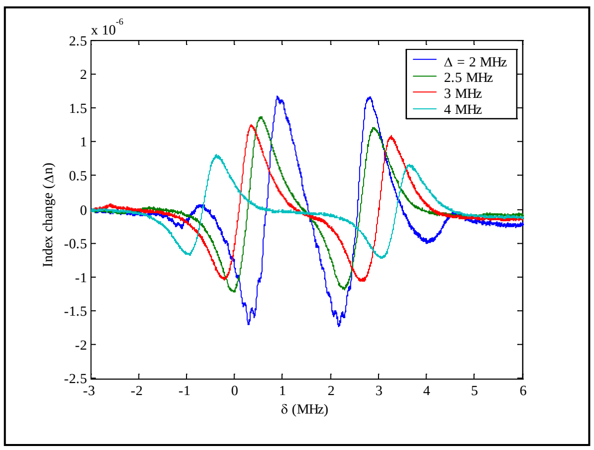

Figure 9.14: Heterodyne measurement mapping variation in dispersion slope with pump separation Δ (a) 2 MHz, $\partial n/\partial\omega = -1.08\times10^{-12}$ rad sec^{-1}, $n_g = -2608$ (b) 2.5 MHz, $\partial n/\partial\omega = -1.4\times10^{-13}$ rad sec^{-1}, $n_g = -337.3$ (c) 3 MHz, $\partial n/\partial\omega = -8.05\times10^{-14}$ rad sec^{-1}, $n_g = -193.5$ (d) 4 MHz, $\partial n/\partial\omega = -4\times10^{-15}$ rad sec^{-1}, $n_g = -8.66$. These measurements were done over a bandwidth $\Delta f = 0.5$ MHz.

We can also affect the slope of the index by varying the pump power to vary the amount of gain:

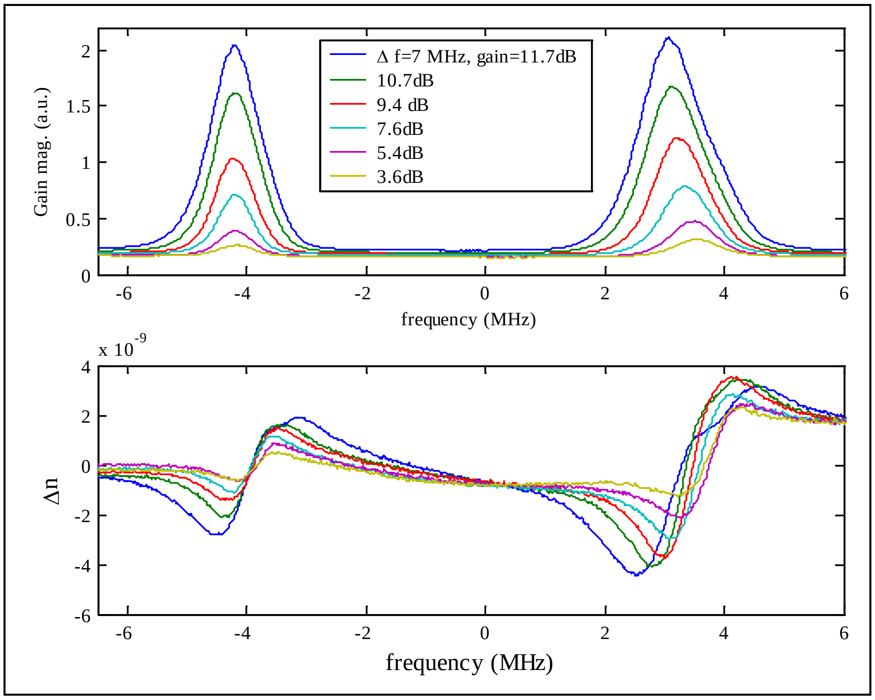

Figure 9.15: Measured dispersion profiles associated with gain doublets for varied gain magnitude and Δf = 7 MHz. For 3.6 dB gain, first-order dispersion slope is estimated to be – 8.7 x 10-16 rad-1.sec, that corresponds to n_g = 0.66

We then flip down the flipper mirror and observe the effect of the dispersion on the cavity resonance by scanning the probe frequency. The result is shown in Figure 9.16.

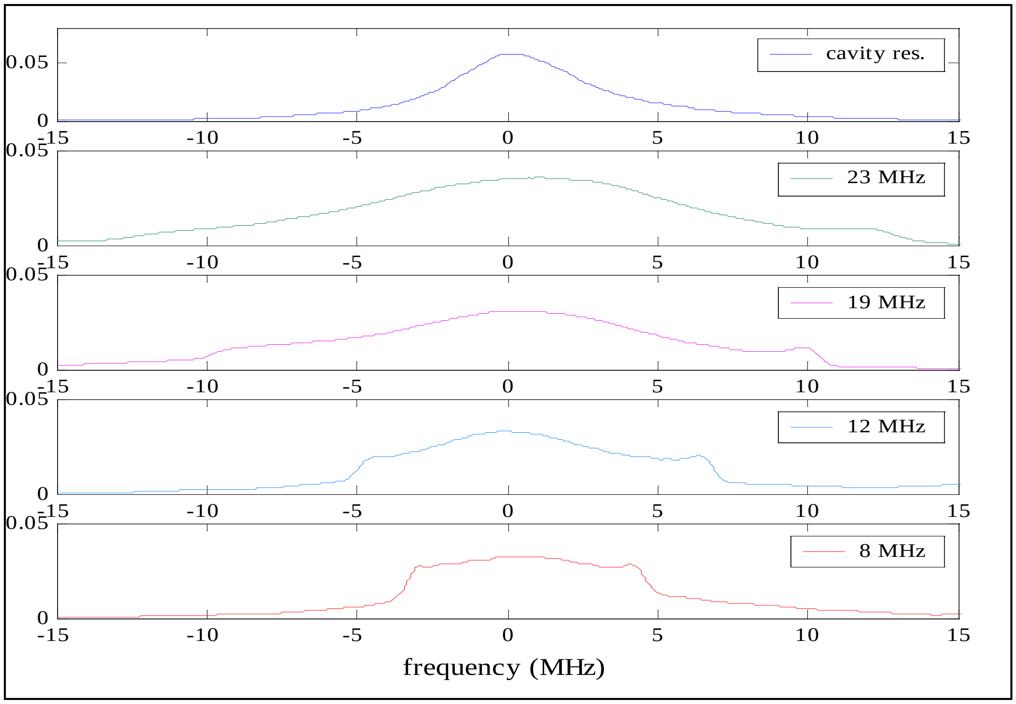

Figure 9.16: Experimental results showing broadened cavity response for gain doublets with varying gain separation.

Figure 9.16 shows different cavity resonances for different frequency separations between the gain lines. When the gain separation was increased, the amount of gain was also increased by increasing the pump intensity, in an attempt to keep the slope of the dispersion constant.

Although the increased linewidth can be clearly seen from this data, we were not able to produce a truly uniform output at large frequency separations. We were limited by the amount by which we could increase our gain, in practice.

In future experiments, we can attempt to remedy this by adjusting different experimental parameters such as the atomic density, the cell length, and the bandwidths of the AOMs used for generating the pumps.

The cavity linewidth (Figure 9.16) with the pumps turned off but the cell in place was, as mentioned above, approximately 8 MHz due to extra loss introduced by intra-cavity elements and residual medium absorption.

These data also show a probe transmission near white-light conditions that is somewhat lower than the peak cavity transmission in the absence of gain. The factor by which the cavity transmission is reduced from the empty cavity case remains nearly the same when the white-light effect is observed with increasing gain separations, and therefore increasing bandwidths, so we conclude that the increase in bandwidth does not correspond to a reduction in the finesse. We attribute the decrease in peak transmission to possible additional absorption loss in probe transmission caused by optical pumping effects resulting from detuned Raman pumps. Future experiments can be designed to mitigate this problem.

Recall that the theoretical response for a WLC is limited only by the dispersion bandwidth.

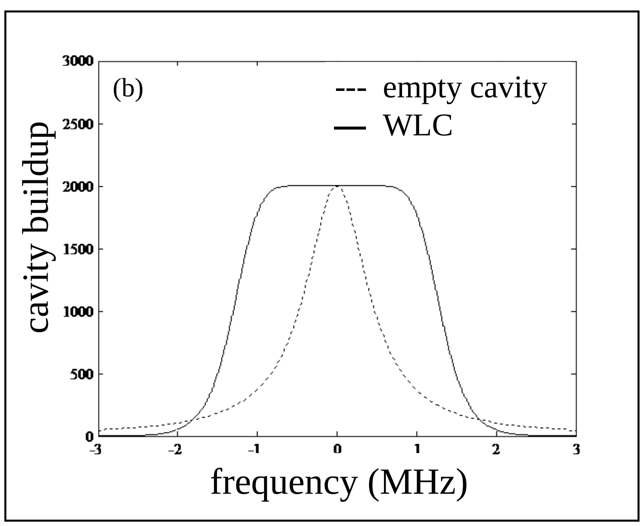

Figure 9.17: Simulated cavity resonance shows white-light effect for n_g = -9 obtained using gain-doublets with Γ = 7.95 MHz. The cavity buildup (x 2000) with WLC is maintained

For comparison, Figure 9.17 shows a simulated example of WLC response for an internal cavity build-up approximately 10^3 and $(L/\ell) = 10$. Negative dispersion with $n_g \approx -9$ (which is required to produce the CAD condition with these length choices) is produced by considering gain lines (linewidth ~ 1 MHz) with a frequency separation of 7.95 MHz. Theoretically, the broad cavity resonance should be observed without sacrificing any of the build-up factor. However, our simulations also show non-uniform response similar to the experimental results in Figure 9.16 when the dispersion slope differs from the exact white-light condition.

Figure 9.18 shows a comparison of the measured linewidth for white-light response from our experimental data with the estimated linewidth from our model.

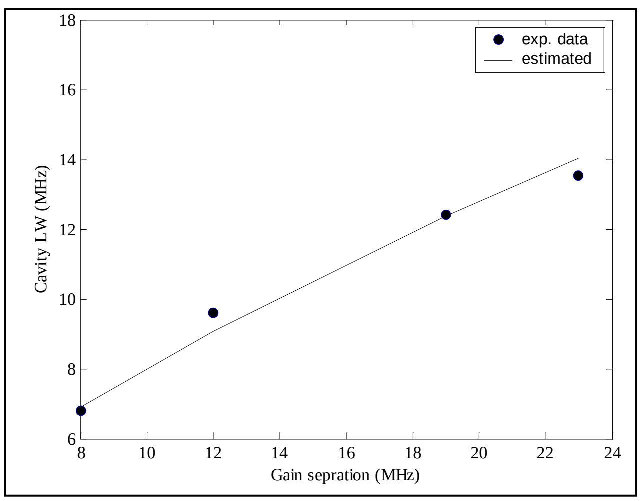

Figure 9.18: Comparison between the estimated WLC linewidth and the actual linewidth measured from experimental data in Figure 9.16

We attempted to use this apparatus to demonstrate the enhancement in sensitivity to cavity length change as well. Because the enhancement factor decreases with increasing values of the empty-cavity frequency shift, $\Delta\omega_o$ (as seen in the Intracavity Dispersion chapter) and because the value of the loaded-cavity frequency shift, $\Delta\omega_o^{'}$ (i.e., the enhanced shift) must be less than the dispersion bandwidth, we were not able to shift the cavity length by a small enough ΔL reliably, and we were not able to see this effect. A resonator that has a much higher finesse and a more precise voltage supply for the PZT should make it possible. However, we are not, at this time, pursuing that experiment, because simply demonstrating the enhanced sensitivity of a passive WLC would not be directly useful for rotation sensing, due to the signal to noise ratio problem described at the end of the Intracavity Dispersion Chapter.

Passive fast-light cavities of this kind are not in themselves useful for gyroscopes. The additional noise on the resonant frequency measurements introduced by the increased linewidth means that the signal to noise ratio remains the same. The increased linewidth is itself of interest for LIGO, as discussed in the Gravitational Wave Detection chapter, however, the LIGO detectors do no operate at the rubidium wavelength. This experiment therefore, while relevant to both applications, is not directly applicable to either. We were therefore motivated to attempt to realize similar dispersion profiles in photorefractive crystals, because photorefractive are available with responses at LIGOs working wavelength of 1064 nm, and to realize slow light in a depletion regime, which could be adapted to yield the appropriate dispersion inside a laser cavity. We present the results of the depletion-regime measurements first.

Fast-Light in Depletion Regime

We might use the double Raman Gain technique described above to produce fast light in a laser cavity. The cavity field, acting as a Raman probe, would experience gain in an intracavity rubidium cell at two different frequencies, and would experience the negative dispersion necessary for enhancing the rotational sensitivity of the ring laser in between those frequencies. However, for this scheme to work, the two pump fields producing Raman gain would each have to be coherent with the probe field, and would have to be of greater intensity than the probe field.

This is not easily achievable experimentally. A beam derived from the output of a laser cavity cannot be stronger than the intracavity field. We can imagine using the laser output, shifted in frequency by an AOM, to injection-lock a diode laser, and amplifying the diode laser output to produce pumps stronger than the intracavity field. This introduces a whole new laser into the system, however, and still presents serious challenges.

A simpler alternative to this scheme is to use the weaker laser output beam as the Raman probe and the stronger intracavity beam as the Raman pump. The weaker beam would be derived from the laser output, and thus automatically coherent with the intracavity beam, but would be frequency shifted so as to stay at a constant even as the laser output frequency changes. The idea is to change the cavity resonant frequency without changing the center frequency of the dispersion. Under these circumstances, the intracavity field, acting as a Raman pump, would experience depletion by the probe beam when the intracavity frequency is equal to ω_{probe}. This frequency dependent loss should create a controllable anomalous dispersion around ω_{probe}. It is the dispersion associated with such a depletion which we seek to measure in this experiment. This scheme does not require additional lasers and lends itself naturally to creating dispersion for relatively high powered beams.

The atomic transitions used in the experiment are illustrated in Figure 9.19.

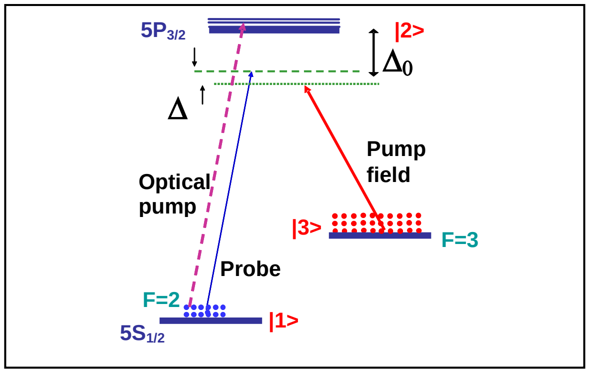

Figure 9.19: Energy levels in D2 line of 85Rb used in Raman gain and depletion experiment.

The optical pump produces the Raman population inversion as described in the Quantum Mechanical Dispersion Chapter and in the bi-frequency pumped Raman gain experiments detailed above. The probe experiences Raman gain in the presence of the pump. During the Raman transition, the pump energy is depleted as the energy in the probe field is increased. The gain at the probe frequency is associated with a positive dispersion, due to the Kramers-Kronig relations, while the depletion at the pump frequency is associated with a negative dispersion.

Our experiment uses the same kind of spatially non-overlapping incoherent optical pump shown in the earlier experimental diagrams, and a moderate intensity Raman pump. The relevant Rubidium energy levels are also the same.

Below, Figure 9.20 shows the schematic of our experimental setup.

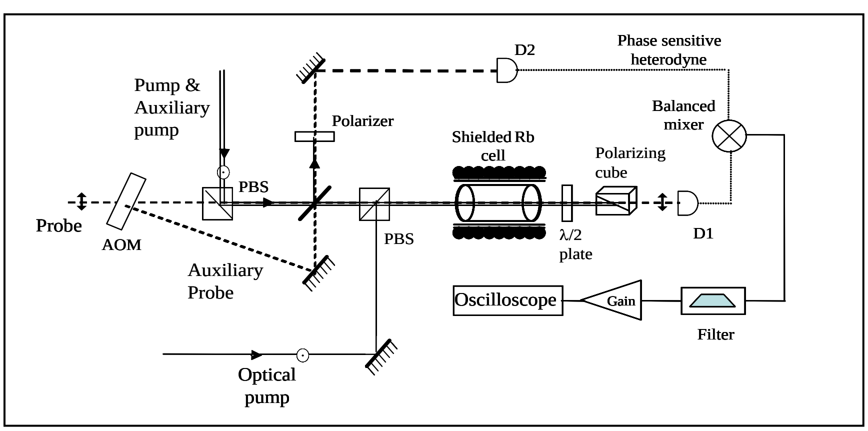

Figure 9.20: Experimental arrangement. PBS: polarizing beam splitter, AOM: acousto-optic modulator, D: photodiode

The probe and pump laser beams are frequency shifted by separate AOMs. The frequency difference between them is matched, as usual, to the metastable hyperfine state splitting (3.0357 GHz) in Rb^{85}. A beam from a tapered amplifier diode laser, which need not be coherent with the Raman beams and does not overlap with them, is used as an optical pump to populate the upper metastable state. Raman gain at the probe frequency is observed when its frequency is scanned, with a maximum where its detuning from resonance matches that of the pump. The pump and probe beams are linearly polarized, and orthogonal.

The rubidium cell is of the same type as those used in the previous experiments.

In order to achieve maximum probe gain, the average frequency detuning Δ_o of the laser fields for the Raman transition was varied by tuning the laser frequency away from the $5S_{1/2}$ (F = 3) - $5P_{3/2}$ (F′ = 4) transition while the probe signal was observed. The most efficient gain corresponded to a detuning close to 1 GHz below the transition. Figure 9.21a shows the gain in the probe and a corresponding depletion of the pump beam.

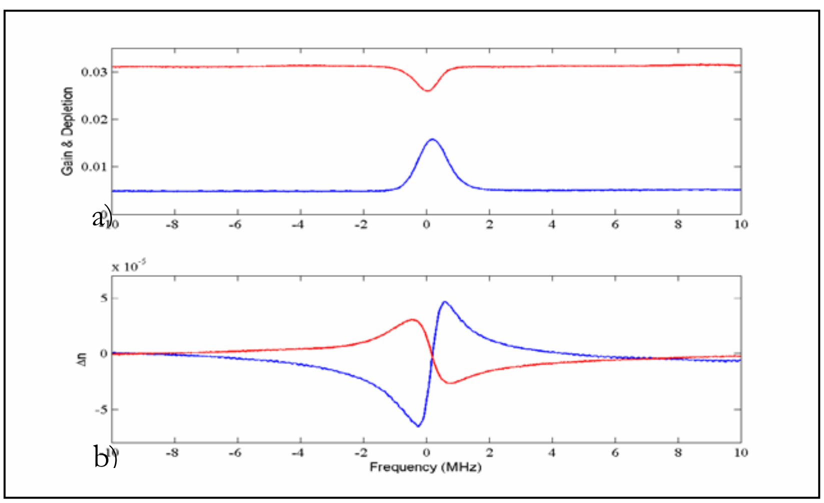

Figure 9.21: (a) Measured gain and depletion for Raman Pump (red) and Raman Probe (blue) (b) corresponding dispersions measured using the heterodyne technique

The same heterodyne technique described above was used to measure the resulting dispersion (Figure 9.21b). The slight differences between these measurements and those discussed above can be seen from the description of the process in Reference 50:

> A non-resonant reference beam was produced by frequency shifting a fraction of the probe beam by 80 MHz, using an AOM. This is then divided in two parts, one of which was combined with the probe that experiences Raman gain and the other with the unperturbed fraction of the probe that does not propagate through the cell. These two heterodyne signals are detected using two fast photodetectors. The phase difference between the two rf signals varies in response to probe dispersion as the probe frequency is scanned around the gain resonance. A mixer with low phase–noise and a low-pass frequency filter are used to demodulate the rf signal from the detectors. The amplitude of the demodulated signal is proportional to the refractive index variation in the dilute atomic medium. A similar heterodyne technique is used to measure the dispersion due to pump depletion in Fig. 3b [here Figure 9.21b], using an auxiliary frequency shifted pump beam shown by the dashed line in Fig. 2 [here Figure 9.20]. This beam is blocked during probe dispersion measurement, but turned on during the pump dispersion measurement. The polarizer and the half-wave plate in both the unperturbed and the perturbed beam paths are also rotated to measure the pump dispersion using the same experimental arrangement. The dispersion is observed to be negative in comparison with the probe.

Due to the positive slope of the dispersion profile at the probe frequency, we expect a group velocity less than the free space velocity of light for pulses centered at the probe frequency. Meanwhile, the group velocity for a pulse at the pump frequency should be greater than c due to the negative slope of the dispersion at that frequency.

To test this simultaneous slow and fast light effect, we pulsed these beams and measure the group velocities directly.

The beams were pulsed using an RF switch on the VCO which drives the relevant AOM. The switch could be turned off and on with TTL pulses from a digital pulse generator, creating nearly rectangular pulses at the frequency of the output of the AOM. Square pulses, unfortunately, have many frequency components outside the dispersion bandwidth. The VCO output was therefore passed through a mixer and multiplied with a low-pass filtered TTL pulse.

The resulting pulses had smooth rise and falling edges. They also had a two lobed shape which is evident in Figure 9.22 and Figure 9.23.

The shapes of the pump pulse and the probe pulse are different, because two different frequency mixers were used. We had relatively limited control over these shapes with the available equipment, but so long as they were composed primarily of frequency components within the relevant bandwidth, their shapes were unimportant. Figure 9.22 shows the delay and gain experienced by the probe pulse. The peak of the pulse clearly emerges later in the presence of gain.

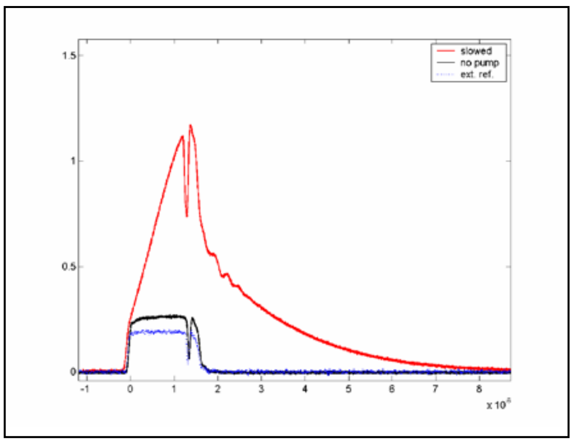

Figure 9.22: Slowed probe pulse due to Raman gain induced positive dispersion. The transmission of the probe in the absence of the pump is shown by the black line, and the transmission when the pump beam is on, by the red line. For reference, we also recorded a pulse which was routed around the cell and experienced no dispersion, shown in blue. The smaller amplitude is due to the imperfect beam splitter used to separate this pulse from the pulse which was sent through the medium.

Figure 9.23 shows similar data for the pump pulse. The blue line is the observed pump pulse in the absence of the probe beam, and the red line represents the propagation of the pump when the probe beam is on. We clearly see the effect of the depletion by the probe. Here the arrival time difference is less dramatic, but still clear. The solid red line shows the reduction in amplitude due to the depletion of the pump beam: a slight advancement at the leading edge, a more significant one at the trailing edge, and approximately 20nS at the central feature.

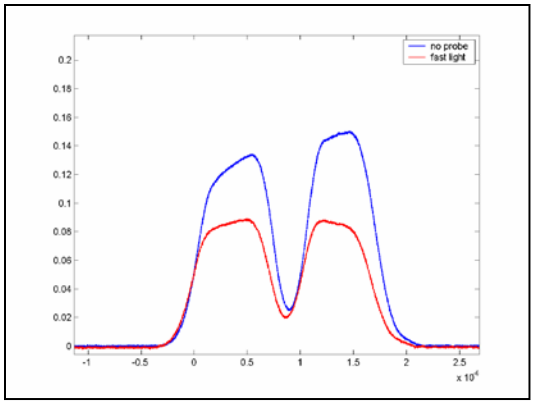

Figure 9.23: Advancement of pump pulse (fast light) due to Raman depletion induced negative dispersion

This data shows that the same medium may simultaneously act as a slow light medium for pulses centered at one frequency and a fast light medium for pulses centered at a different frequency.

If a gain depletion of this kind is used in place of a gain doublet, the anomalous dispersion for the depleted pump is accompanied by a normal dispersion for the amplified probe. This property may be of interest in itself. However, the primary purpose of this experiment is as a proof-of-principle for the proposed method of creating anomalous dispersion for a laser gyroscope.

Further details of this experiment can be found in reference 50.

Fast-Light in Photorefractive Crystal

This white light cavity realized with rubidium vapor, as described above, is not useful for gravitational wave detection in its present form. The properties of rubidium are such that we can only produce the required gain at wavelengths near 780 nm, whereas the wavelength of the lasers used in gravitational wave detectors such as LIGO is 1064 nm. However, the basic principle of producing dispersion by creating two gain peaks can still be applied – all that is necessary is a material in which gain can be produced at wavelengths near 1064nm. The best candidates for such a material are photorefractive crystals, which diffract light from a pump beam into the path of a probe whenever the two are at the same frequency, thus producing gain on the probe.[51] The use of these crystals to create controllable dispersion profiles for applications such as slow light has already been investigated in some detail [52,53,54].

We have experimentally demonstrated that gain at two frequencies can be produced with a photorefractive crystal, and observed the corresponding dispersion profiles for frequencies around those gain peaks. This confirms that photorefractive crystals could potentially produce the kind of dispersion we need for a white light cavity at frequencies where rubidium vapor cannot be used.

We used a laser at 532 nm and frequency shifted part of it by 40 MHz using an AOM. We split both the unshifted and shifted beams into "pump" and "probe" beams, which for this experiment were equally strong. The probe beams were combined and reflected off of a piezo-mounted mirror onto the barium titanate (BTO) crystal, but one of the two probe beams was always blocked during the experiment. The pump beams were combined and directed onto the crystal by ordinary mirrors, making an angle of approximately fifteen degrees with the probe beams, as illustrated in Figure 9.24. Both pump beams were always on during the experiment.

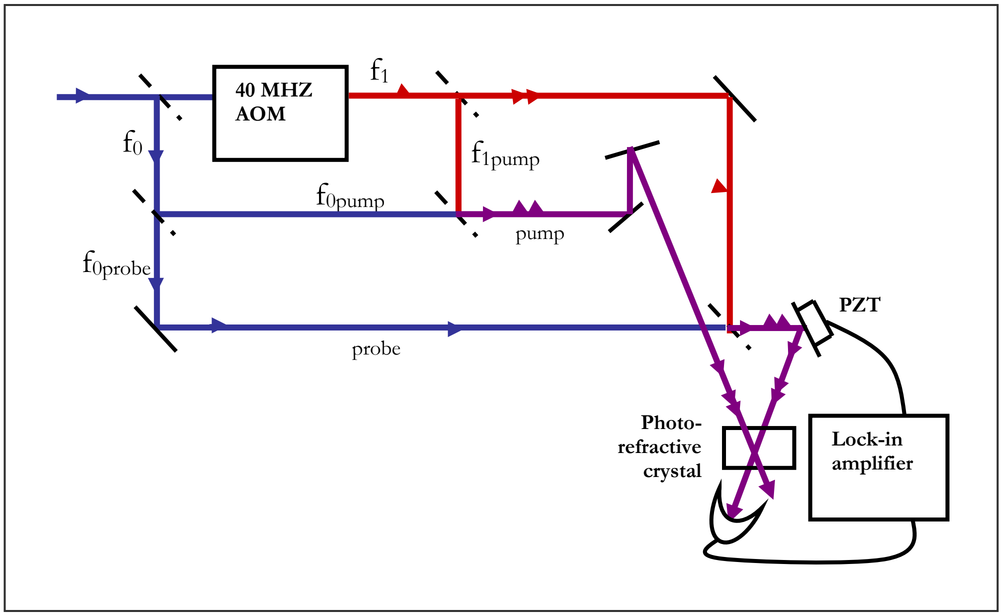

Figure 9.24: Experimental set-up for bi-frequency gain and dispersion measurement in photorefractive crystal

Our expectation was that the photorefractive crystal would produce gain in the probe whenever the frequency of the probe matched that of either of the two pump beams. Ideally, to verify that we could produce gain at either frequency when both pumps were on simultaneously, we would like to have had a single probe beam, and scanned its frequency over a range including both pump frequencies. For this trial, however, with our pump beams 40 MHz separated, we were able to scan only a small range around the frequency of the unshifted pump, and a small range around the frequency of the shifted pump.

We did this by first blocking the shifted probe beam, and then scanning the other, unshifted, probe beam over a few hertz by moving the piezo-mounted mirror, causing the position of the mirror to vary quadratically so that its velocity varied linearly, producing a linear frequency scan on the probe beam through the Doppler effect. We observed gain when the frequency of the probe matched that of the unshifted pump. Next, we blocked the unshifted probe beam, unblocked the shifted one, and repeated the scanning procedure. We again observed gain, when the frequency of the probe matched that of the shifted pump.

Our scan range was small because the gain peaks produced by the photorefractive crystal are narrow, on the order of a few hertz. To see the shape of the peak and corresponding dispersion profile, we had to scan the probe over that kind of narrow frequency range, which was only possible for us using the Doppler shifting mirror described. The piezo on which the mirror is mounted, however, has a limited range of motion, and we could not use it to create Doppler shifts as large as 40 MHz. This is why we simply switched to a probe beam which was already 40MHz shifted in frequency and scanned that in order to see the second gain peak. Unfortunately this method leaves us without information about the shape of the dispersion profile for frequencies in between the two peaks. In future versions of the experiment, we intend to shift the second pump by only a few hertz, rather than 40 MHz, using a second piezo mounted mirror with a linear sweep in position, creating a constant Doppler shift on the second pump beam. This should allow us to see the whole profile at once when scanning our probe.

Another issue with this particular experiment was the response time of the crystal. Photorefractive crystals do not, in general, produce gain instantaneously once the pump and probe frequencies are matched. One has to wait for the two beams to "write" the grating in the crystal which produces the diffraction, and the amount of time that takes depends on a number of factors, including the type of crystal and the strength of the beams. Then too, the grating takes time to disappear, if the writing beams are shifted in frequency again or turned off. If we could scan the probe frequency sufficiently slowly, waiting longer than the response time before measuring the intensity of the probe and moving onto the next point on the frequency axis, this response time would not be an issue. But the crystal we were using had a very slow response time, on the order of five seconds, and it was not practical to scan the probe so slowly with the method we were using. Therefore, as we scanned the probe frequency, instead of seeing a normally shaped gain peak, we saw one distorted by a slow rise and fall time. The voltage on the piezo varied parabolically during a scan window (when we took the data) and then was held constant for a period before being varied again. The clearest evidence for the time constant effect was the fact that the gain signal was not constant during the period when the piezo was not moving, and thus the Doppler shift zero, the two frequencies equal), but built up with a slow rise time.

This effect is similar to effect of an RC filter circuit – if the input voltage is changed, it takes time for the output voltage to respond.

The signal that we saw using a crystal with a slow response time is the same as that which we would have seen if we used a crystal which could respond instantaneously but then filtered the detector output through an RC circuit. The effect, either way, would be that a change in the frequency of one of the beams would take time to cause a change in the signal. So in order to overcome this problem, we modeled the system in this way, as if the detector signal from a fast crystal had simply been filtered by an RC circuit.

The equation describing our system is then

Equation 9.11: $$V_{in}(t) = V_{out}(t) + \tau \frac{dV_{out}}{dt}$$

where τ is the time constant, equal to RC in a real RC circuit, but related in the crystal to the time it takes to create the grating, rather than to a literal resistance or capacitance.

Equation 9.11 clearly shows the mathematical relationship between the output voltage which we saw on the oscilloscope, and the hypothetical "input" voltage, that is, the voltage we would see if our system could respond instantaneously. In order to see what our signal would look like if the response time of our crystal were not an issue, we have to take the output voltage we get from the detector, and from it derive that hypothetical input voltage. We constructed a circuit that could do this, which is diagrammed in Figure 9.25.

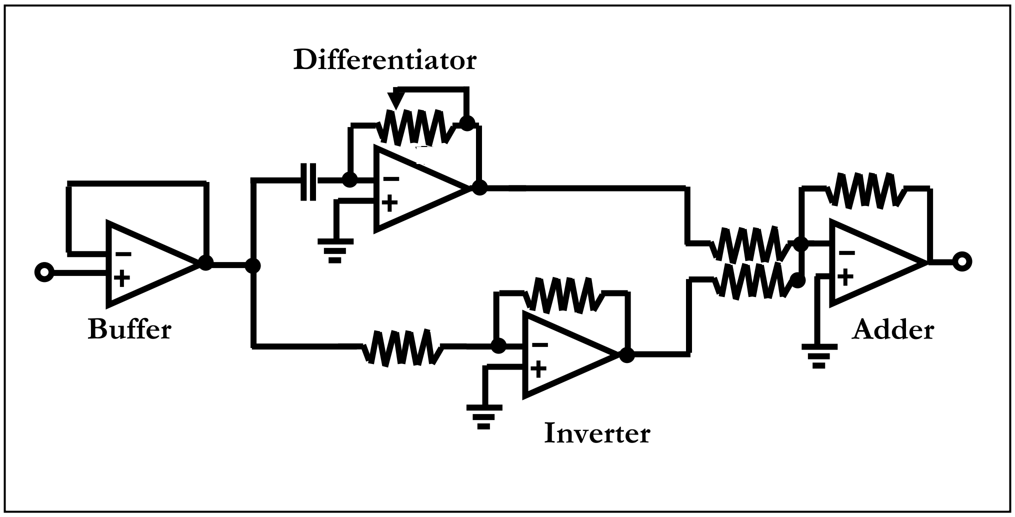

Figure 9.25: Design of circuit which compensates for slow response time of photorefractive crystal

The output of this circuit is related to its input by:

Equation 9.12: $$V_{out}(t) = -\left(V_{in}(t) - \tau \frac{dV_{in}}{dt} \right)$$

In other words, the effect of this circuit is the opposite of that of an RC filter circuit. They undo each other. We tested this by putting a variety of voltage waveforms, triangular, square, and sinusoidal into the RC filter circuit, and then passing the output of that through our compensation circuit, to verify that we could in this way, recover the original waveform. If the RC circuit is described as a filter which suppresses (but cannot entirely eliminate) the high frequencies of signals passed through it, the compensator circuit can be thought of as undoing this by amplifying those high frequencies. So long as the time constants of the two circuits are matched, the exact frequencies which were initially suppressed will be amplified by the compensator.

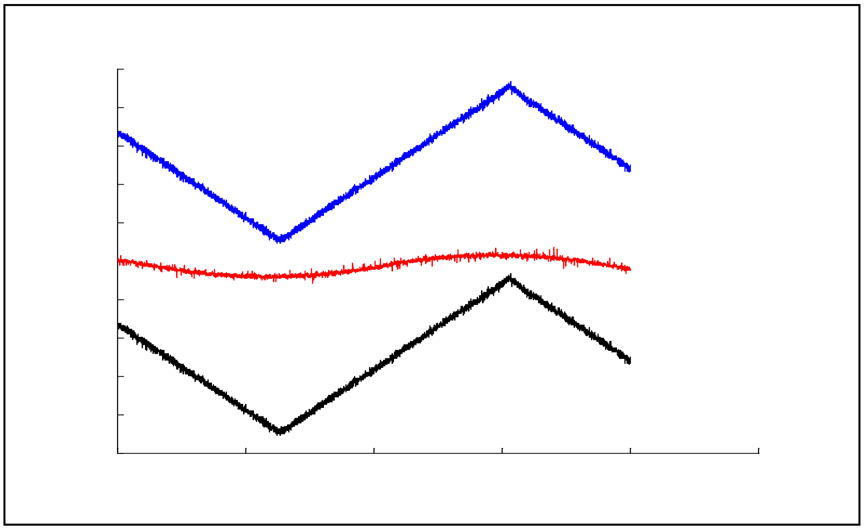
Figure 9.26: Input waveform (blue), filtered waveform (amplified by a factor of 30 to show shape), restored waveform (output of circuit)

We therefore fed the output from our detector through this compensator circuit, and adjusted the time constant of the compensator circuit until we had a signal which was unchanged during the time during which the piezo was not moving, a property we knew that the signal should have, if not for the slow time constant. Once we had this compensator circuit in place, we saw peaks which had their maximum value when the frequencies were matched, as we would expect.

We then measured the dispersion by introducing a 1 kHz modulation onto the position of the piezo mounted mirror, using the local oscillator from a lock-in amplifier. This additional phase modulation on the beam creates sideband beams which interfere with the probe, such that the intensity signal on the detector has a beat note. The phase of this beat signal depends upon the phase of the probe beam, and thus upon the index of refraction it experiences while passing through the crystal. The phase of the beat note can be detected by mixing the detector signal with a reference channel and then filtering with the lock-in amplifier. The result of this is a demodulated signal, the amplitude of which is proportional to phase of the probe beam. Scanning the frequency of the probe while recording this signal allows us to map out the index of refraction of the material as a function of frequency.

That data is presented in figure 4.

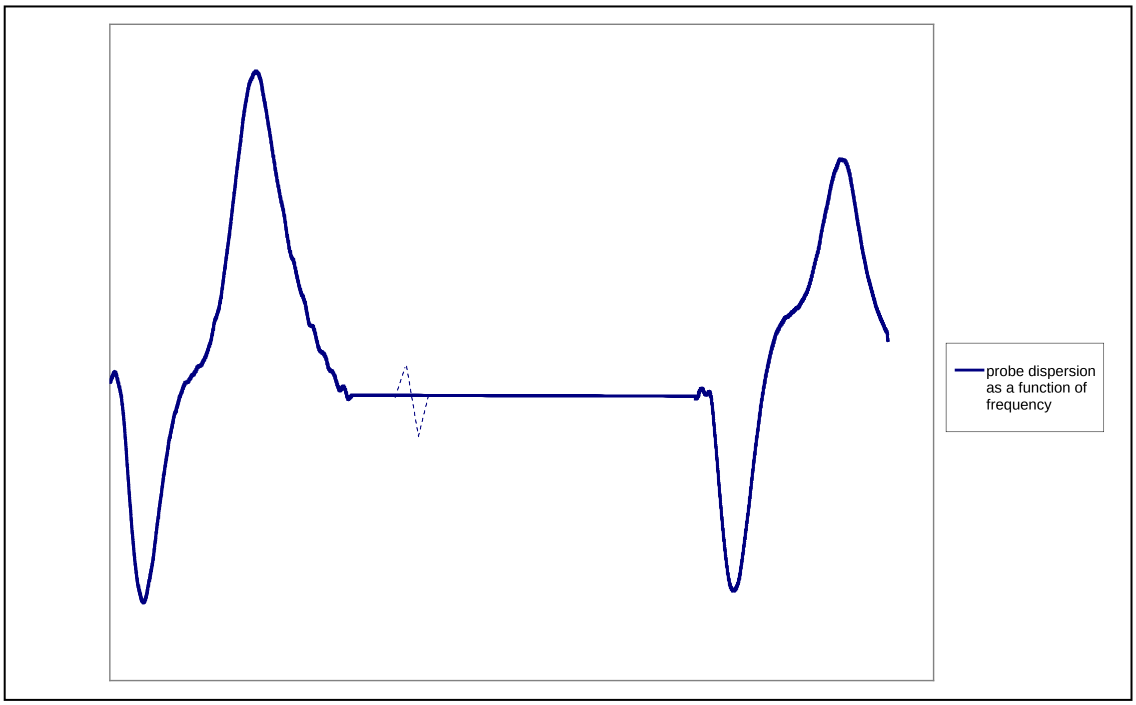

Figure 9.27: Probe dispersion around unshifted (left) and shifted (right) pump frequencies. Broken line represents 40 MHz separation between the two gain regions

The broken line represents the 40 MHz which really separate these two dispersion profiles, for which we do not have data. In addition, these two profiles have been scaled and shifted so that we can represent them on the same graph; in reality the unshifted pump and probe beam were stronger and produced a slightly higher gain peak and corresponding dispersion. Finally, we observed that these profiles actually showed the effects of the time constant to a certain extent in spite of the compensator circuit, flattening out only slightly after the piezo had returned to rest. Our compensator was set to correct for the crystal rise-time response only – the additional signal filtering done by the lock-in amplifier, as well the different fall time of the crystal (it takes a different amount of time for the grating to disappear than to form) were uncompensated.

The data nevertheless clearly shows a dispersion with a general shape that corresponds to that which we would expect from a gain peak. The fact that this dispersion can be measured around either pump frequency, while both pump frequencies are present, leads us to conclude that with the appropriate crystal and the appropriate pump beams, the kind of double-gain dispersion profile necessary for a white light cavity can be created.

This experiment is a proof of principle, showing that photorefractive crystals can be used to create a double-peaked gain profile similar to that which we created in rubidium using Raman gain, with a corresponding similar anomalous dispersion profile. This is encouraging. It means that the same approach which we used to create a white light cavity at 780 nm can be used to create one at the wavelengths used in LIGO and other gravitational wave detectors, with photorefractive crystals rather than rubidium vapor acting as the gain medium.

While we intend to do further experiments with pumps more closely spaced in frequency and a probe scan which can measure the dispersion in the region between them directly, and eventually repeat this with a different (perhaps faster response time) crystal, at a laser wavelength of 1064 nm, we believe this data is sufficient to show that the approach is worth pursuing. Further details of this experiment and a related experiment performed by our colleagues at Texas A&M University can be found in Reference 34.

CHAPTER 10 - CONCLUSIONS

New methods of controlling dispersion discovered by researchers studying slow and fast light may prove themselves very useful, not only for their effects on pulse propagation, but for their effects on interferometric sensors. By allowing us to change the relationship between frequency and spatial phase, these materials give us a new kind of freedom in the design of interferometric sensors.

Here we have addressed just two potential applications: ring laser gyroscopes and gravitational wave detection. Others are studying related uses of these techniques[55].

We have confirmed experimentally and theoretically[49] that putting a slow light medium into a cavity narrows its linewidth and causes its resonance frequency to change very little when the length of the cavity is changed, and that this narrowing and sensitivity modification varies inversely with the group index. We have also confirmed experimentally[25] and theoretically[6] that putting a fast light medium into a cavity broadens its linewidth, and that the degree of broadening is controllable. We have shown theoretically that a fast light medium in a cavity will increase the sensitivity of its resonance frequency to length changes, and have shown explicitly that this result applies even to optical gyroscopes[21], where the 'length change' is essentially equivalent to the effect of rotation. We are working on using these results to design more sensitive ring laser gyroscopes.

We have shown that the technique can be generalized, that the relevant dispersion profiles can be realized in photorefractive crystals as well as in atomic gasses, and that they can be implemented in spectral regimes with gain, depletion, or transparency.

Future work suggested by this research includes new approaches to gravitational wave detection, exploiting the increased sensitivity of the active fast-light cavity, and further experimental and theoretical study of these "superluminal lasers."

So far all of the experimental results bear out our theoretical predictions, and the prospects for these technologies are promising.

REFERENCES

[1] W. Demtröder, *Laser Spectroscopy: Basic Concepts and Instrumentation,* Springer, New York, NY, (2003)

[2] M. Xiao, Yong-quing Li , Shao-zheng Jin, and J. Gea-Banacloche., "Measurement of Dispersive Properties of Electromagnetically Induced Transparency in Rubidium Atoms." Phys. Rev. Lett. **74**, 666, (1995).

[3] Lene Hau, S.E. Harris, Zachary Dutton, and Cyrus H. Behroozi, "Light speed Reduction to 17 Metres per Second in an ultracold atomic gas." Nature **397**, 594, (1999).

[4] R.W. Boyd and D.J. Gauthier, "'Slow' and 'Fast' Light," Progress in Optics **43**, 497, (2002).

[5] Wang, L. J.; Kuzmich, A.; Dogariu, A. "Gain-assisted superluminal light propagation". Nature. 406, 277, (2000).

[6] M. Salit, G.S. Pati, K. Salit, and M.S. Shahriar, "Fast-Light for Astrophysics: Super-sensitive Gyroscopes And Gravitational Wave Detectors," Journal of Modern Optics, 54, 2425 – 2440 (2007)

[7] A. E. Siegman, *Lasers*, University Science Books, Sausalito, CA (1986)

[8] B. E. A. Saleh, M. C. Teich, *Fundamentals of Photonics*, Wiley-Interscience, Malden, MA (2007)

[9] E. Hecht, *Optics*, Pearson Education Limited, Upper Saddle River, NJ (2001)

[10] M. Sargent, M. O Scully, W. E. Lamb, *Laser Physics*, Westview Press, Boulder, CO, (1974)

[11] J.S. Toll, "Causality and the Dispersion Relation: Logical Foundations," Physical Review, **104**, 1760-1770, (1956).

[12] C.G.B. Garrett and D.E. McCumber, "Propagation of a Gaussian Light Pulse Through an Anomalous Dispersion Medium," Physical Review A, **1**, 305-313, (1970)

[13] M. D. Stenner, D. J. Gauthier, and M. A. Neifeld, "The speed of information in a 'fast-light' optical medium," *Nature* **425**, 695-698 (2003)

[14] M W. Mitchell and R. Y. Chiao, "Negative group delay and 'fronts' in a causal system: An experiment with very low frequency bandpass amplifiers," Physics Letters A, **230**, 133-138 (1997)

[15] J.C. Garrison, M.W. Mitchell, R.Y. Chiao, E.L. Bolda, "Superluminal Signals: Causal Loop Paradoxes Revisited," Physics Letters A **245**, 19-25 (1998)

[16] P. Meystre, M. Sargent, *Elements of Quantum Optics*, pp. 60-62, Springer, 1998

[17] M. O. Scully, M. S. Zubairy, *Quantum Optics*, Cambridge University Press, Cambridge (1997)

[18] K.R. Salit, "Optical Switching via Quantum Interference Effects in a Multilevel Atomic System," PhD Dissertation Northwestern University, AT 3331160 at http://www.proquest.com/en-US/products/dissertations/individuals.shtml (2008)

[19] A. Dogariu, A. Kuzmich, and L. J. Wang, "Transparent Anomalous Dispersion and Superluminal Light Pulse Propagation at a Negative Group Velocity," Physical Review A,63, no. 5, id. 053806

[20] S. Chu, in *Coherent Atomic Matter Waves - Les Houches Vol 72*, edited by R. Kaiser, C. Westbrook and F. David, Springer, Berlin (2001)

[21] M.S. Shahriar, G.S. Pati, R. Tripathi, V. Gopal, M. Messall and K. Salit, "Ultrahigh Precision Absolute and Relative Rotation Sensing using Fast and Slow Light", Physical Review A 75 (5): Art. No. 053807 (2007).

[22] W.W. Chow, J. Gea-Banacloche, and L.M. Pedrotti, "The Ring Laser Gyro," Reviews of Modern Physics, **57**, 61-104, 1985

[23] M. Hereld and D.Z. Anderson, "Beat Frequency Locking in a Passive Ring Laser Gyroscope," SPIE Vol 487, p 33, *Physics of Optical Ring Gyros*, (1984)

[24] R.-H. Rinkleff, and A.Wicht, "The Concept of White Light Cavities Using Atomic Phase Coherence," Physica Scripta. Vol. **T118**, 85–88 (2005)

[25] G.S. Pati, M. Messall, K. Salit, and M.S. Shahriar, "Demonstration of a Tunable-Bandwidth White Light Interferometer using Anomalous Dispersion in Atomic Vapor," Phys. Rev. Lett. 99, 133601 (2007)

[26] C.S. Liu, B.E. Cherrington, and J.T. Verdeyen, Dispersion Effects in a High-Gain 3.39 micron He-Ne Naser," Journal of Applied Physics, **40**, 3556-3569, (1969).

[27] W.R. Bennett Jr, "Hole Burning Effects in a He-Ne Optical Maser," Physical Review, **126**, 580-594, (1962)

[28] H. Greenstein, "Theory of a Single-Mode Gas Laser," Physical Review, **175**, 438

[29] B.K. Garside, "Mode Pulling in Ring Lasers," IEEE Journal of Quantum Electronics, Vol **QE-5**, 97 (1969)

[30] F.R. Faxvog, C.N.Y Chow, T. Bieber, and J.A. Carruthers, "Measured Pulse Velocity Greater than c in a Neon Absorption Cell," Applied Physics Letters, **17,** 192-193, (1970)

[31] F.R. Faxvog and J.A. Carruthers, "Pulse Velocity and Mode Pulling in a Laser with Equally Spaced Modes," Journal of Applied Physics, **41**, 2457-2458, (1970)

[32] M.S. Shahriar, M. Salit, and J.H. Shapiro, "Model for beat noise in a fast-light enhanced ring laser gyroscope", (http://lapt.eecs.northwestern.edu/preprints/beat-noise-in-FRLG.pdf)

[33] J. Hough, B.J. Meers, G.P. Newton, N.A. Robertson, H. Ward, B.F. Schutz, I.F. Corbett, and R.W.P. Drever, "Gravitational Wave Astronomy -- Potential and Possible Realisation", Vistas in Astronomy **30**, 109 (1987)

[34] H. N. Yum, M. Salit, G. S. Pati, S. Tseng, P. R. Hemmer, and M. S. Shahriar, "Fast-light in a Photorefractive Crystal for Gravitational Wave Detection," Optics Express, **16**, 20448-20456, (2008)

[35] Q. Sun, M. S. Shahriar, M. S. Zubairy, "Slow light and fast light in a photorefractive crystal" , http://lapt.eecs.northwestern.edu/preprints/slow-fast-prc.pdf

[36] F.I. Cooperstock and V Faraoni, "Laser-Interferometric Detectors of Gravitational Waves", Class. Quantum Grav. **10**, 1189, (1993)

[37] E.D. Black, R. N. Gutenkunst, "An introduction to signal extraction in interferometric Gravitational Wave detectors", Am. J. Phys. **71**, 365 (2003).

[38] J.B. Hartle, *Gravity: An Introduction to Einstein's General Relativity*, Addison Wesley, San Francisco, (2003)

[39] M.S. Shahriar and M. Salit, "Application of Fast Light in Gravitational Wave Detection with Interferometers and Resonators," Journal of Modern Optics, **55**, 3133 – 3147, (2008)

[40] LIGO Laboratory / LIGO Scientific Collaboration, "Advanced LIGO Reference Design: LIGO-060056-08-M", http://www.ligo.caltech.edu/docs/M/M060056-08/M060056-08.pdf , 23 May 2007

[41] K. A. Strain, G. Müller, T. Delker, D. H. Reitze, D. B. Tanner, J. E. Mason, P. A. Willems, D. A. Shaddock, M. B. Gray, C. Mow-Lowry, and D. E. McClelland, "Sensing and control in dual-recycling laser interferometer gravitational-wave detectors," Applied Optics **42**, 1244 (2003).

[42] J. Mizuno, K.A. Strain, P.G. Nelson, J.M. Chen, R. Schilling, A. Rudiger, W. Winkler and K. Danzmann, "Resonant. sideband extraction: a new configuration for interferometric gravitational wave detectors," Physics Letters A **175**, 273-276, (1993)

[43] LIGO Laboratory / LIGO Scientific Collaboration, "AdvLIGO Interferometer Sensing and Control Conceptual Design: LIGO-T070247-01-I" http://lhocds.ligo-wa.caltech.edu:8000/advligo/ISC_Requirements_and_Conceptual_Design_Review?action=AttachFile&do=get&target=T070247-01.pdf

[44] B.J. Meers, "The Frequency Response of Interferometric Gravitational Wave Detectors", Physics Letters A **142**, 465, (1989)

[45] B. J. Meers and K. A. Strain, "Wave-front Distortion in Laser-interferometric Gravitational-wave Detectors", Phys. Rev. D **43**, 3117 (1988).

[46] Gl. de Vine, D. A. Shaddock, and D. E. McClelland, "Experimental demonstration of variable-reflectivity signal recycling for interferometric gravitational-wave detectors", Optics Letter **27**, 1507 (2002)

[47] R. Tripathi, G.S. Pati, M. Messall, K. Salit and M.S. Shahriar, "Experimental constraints of using slow-light in sodium vapor for light-drag enhanced relative rotation sensing," Optics Communications. **266**, 604-608, (2006)

[48] M. M. Kash, V. L. Sautenkov, A. S. Zibrov, L. Hollberg, G. R. Welch, M. D. Lukin, Y. Rostovtsev, E. S. Fry, M. O. Scully, "Ultraslow Group Velocity and Enhanced Nonlinear Optical Effects in a Coherently Driven Hot Atomic Gas", Phys. Rev. Lett. **82**, 5229 (1999).

[49] G.S. Pati, M. Salit, K. Salit, M.S. Shahriar, "Demonstration of displacement–measurement–sensitivity proportional to inverse group index of intra-cavity medium in a ring resonator,"Optics Communications, **281**, 4931–4935 (2008)

[50] G. Pati, M. Salit, K. Salit, S. Shahriar, "Simultaneous Slow and Fast Light Effects Using Probe Gain and Pump Depletion Via Raman Gain in Atomic Vapor," Submitted to Optics Express (2009)

[51] T.J. Hall, R. Jaura, L.M. Connors, P.D. Foote, Prog. in Quantum Electronics, **10**, 77 (1985)

[52] Z. Deng, D.-K. Qing, P. Hemmer, C. H. R. Ooi, M. S. Zubairy, and M. O. Scully, " Time-Bandwidth Problem in Room Temperature Slow Light," Phys. Rev. Lett. **96**, 023602 (2006).

[53] E. Podivilov, B. Sturman, A. Shumelyuk, and S. Odoulov, " Light Pulse Slowing Down up to 0.025 cm/s by Photorefractive Two-Wave Coupling," Phys. Rev. Lett. **91**, 083902 (2003).

[54] A. Shumelyuk, K. Shcherbin, S. Odoulov, B. Sturman, E. Podivilov, and K. Buse, " Slowing Down of Light in Photorefractive Crystals with Beam Intensity Coupling Reduced to Zero" Phys. Rev. Lett. **93**, 243604 (2004).

[55] Z. Shi and R. W. Boyd, "Slow-light Interferometry: Practical Limitations to Spectroscopic Performance," JOSA B, **25**, Issue 12, pp. C136-C143